Synthesis, Characterization, and Reactivity of First Row Dipyridylazaallyl Transition Metal Complexes

by Brenda Ann Frazier

SYNTHESIS, CHARACTERIZATION, AND REACTIVITY OF FIRST ROW DIPYRIDYLAZAALLYL TRANSITION METAL COMPLEXES

A Dissertation

Presented to the Faculty of the Graduate School

of Cornell University

In Partial Fulfillment of the Requirements for the Degree of

Doctor of Philosophy

by

Brenda Ann Frazier

August 2010

SYNTHESIS, CHARACTERIZATION, AND REACTIVITY OF FIRST ROW DIPYRIDYLAZAALLYL TRANSITION METAL COMPLEXES

Brenda Ann Frazier, Ph. D.

Cornell University 2010

A series of tertiary amines, i.e. **HAr$_2$pyN**, **HArpy$_2$N**, **BrAr$_2$pyN**, and **BrArpy$_2$N**, containing at least one pyridyl arm were prepared, and oxidative addition of **BrAr$_2$pyN**, and **BrArpy$_2$N** with Ni(COD)$_2$ afforded two diamagnetic Ni(II) complexes, ((BrAr)ArpyN)NiBr (**1-Ni**) and (Arpy$_2$N)NiBr (**2-Ni**). The disproportionation of Fe{N(TMS)$_2$}$_2$(THF) in the presence of **BrArpy$_2$N** afforded (Arpy$_2$N)FeBr (**2-Fe**); however, C-N bond cleavage, not disproportionation, was observed upon treating Cr{N(TMS)$_2$}$_2$(THF)$_2$ with **BrArpy$_2$N**. Unusual optical properties were characteristic of the resulting complex, (smif)CrN(TMS)$_2$ (**4-Cr**), (smif = (2-py)CHNCH(2-py)).

Exposure of 1st-row transition metal complexes with the smif ligand produced a new homologous series of optically dense complexes, (smif)$_2$M (M = V (**6-V**); Cr (**6-Cr**); Mn (**6-Mn**); Fe (**6-Fe**); Co (**6-Co**); Ni (**6-Ni**)). Oxidation chemistry afforded three [(smif)$_2$M](OTf) complexes (M = Cr (**7-Cr**); Mn (**7-Mn**); Co(**7-Co**)). Physical and electronic properties for the series were investigated by NMR, EPR, UV-vis, and XAS (pre K-edge) spectroscopies along with X-ray crystallography, electrochemistry, and SQUID magnetometry. SQUID and XAS data helped elucidate the electronic structures obtained from the density functional theory calculations. Large absorptivities ($\varepsilon \sim 18{,}000 - 60{,}000$ M^{-1}cm^{-1}) were observed in the UV-vis spectra for the complexes and have been attributed to intraligand transitions between $CN_{aza}C^{nb}$ and smif π^* orbitals. Efforts to synthesize (smif)$_2$Ti via salt metathesis under reducing

conditions afforded varying ratios of four titanium(II) complexes: lithium[(κ-C,N^{am},N^{im},N^{py}_3-1,2-bis(pyridin-2-yl)-2-(pyridin-2-ylmethyleneamino)ethyl)(pyridin-2-ylmethideyl)amido)Ti(smif)] (**10-Ti**), $(smif)_2$Ti (**11-Ti**), (smif)(dpma)Ti (**12-Ti**), (κ-N^{am},N^{py}_2-2,3,5,6-tetrakis(pyridin-2-yl)piperazin-1-yl)(smif)Ti (**13-Ti**).

Reactivity of the coordinated azaallyl moiety in the smif ligand was probed after treatment of $Fe\{N(TMS)_2\}_2(THF)$ with one equivalent of smifH afforded a solution of (smif)$FeN(TMS)_2$ (**14-Fe**), which dimerizes in the solid state to form a bridging tetra-substituted piperazine bis-amide ligand, **[14-Fe]$_2$**. Solid-state and solution dynamics indicated reversible C-C bond coupling of the smif backbone, thereby provoking an exploration of reactivity for the azaallyl moiety with unsaturated organic molecules. Exposure of **14-Fe** to di-(p-tolyl)acetylene yielded the [3+2] cycloaddition product, **29-Fe**. Attempts to prevent C-C bond formation by methylating the backbone led to acid-base chemistry of the azaallyl moiety.

BIOGRAPHICAL SKETCH

The author was born in Pittsburgh, Pennsylvania on April 25, 1983 to Donald and Debra Frazier. Growing up in the City of Champions, she quickly became a supporter of the "Black and Gold." When she was not cheering for her teams – Steelers, Penguins, and Pirates – or playing volleyball, she was curled up with her biology, physics, and chemistry books. Her high school organic teacher made chemistry fun and exciting through personal anecdotes and demonstrations, thereby sparking a burning desire to continue studying organic chemistry.

After graduating from North Allegheny High School, Brenda pursued a chemistry degree at Washington & Jefferson College. Her desire to be an organic chemist was squandered while she participated in the Research Experience for Undergraduates Program at The University of Michigan during the summer of 2004. Under the tutelage of Professor Omar Yaghi and Nathan Ockwig, his graduate student, she discovered the joys of being an inorganic chemistry: pretty colors, various forms of spectroscopy, and crystal structures. She graduated summa cum laude with a B. A. in Chemistry from Washington & Jefferson College in 2005.

Brenda pursued graduate studies in chemistry at Cornell University under the guidance of Professor Pete Wolczanski. After synthesizing a new homologous series of complexes, gazing at the intensely colored solutions, and obtaining countless crystal structures, she completed her Ph. D in Inorganic Chemistry in June 2010. She has accepted the challenge of teaching chemistry at Northern New Mexico College.

To Dad and Mom

ACKNOWLEDGEMENTS

First and foremost, I would like to thank my advisor, Pete Wolczanski, for training me as a scientist, always challenging me to improve, and preparing me for academia. He has bestowed upon me the value of teachable moments and his wisdom of teaching in a classroom setting. I aspire to be a great teacher like him in the future. I have been truly blessed to be a member in Pete's group, and I am honored to have Pete as my chemical father, mentor, and friend.

I would like to thank my committee members, Paul Chirik and Brian Crane. I am very grateful for Paul's contributions as he has provided me with interesting experiments to perform and allowed me to use their new lab equipment for characterization. Brian is thanked for not only teaching me how to apply inorganic chemistry to biological systems, but also for showing me how to challenge engineering students with general chemistry.

This dissertation would not have been possible without the hard work of several collaborators. I am forever indebted to Emil Lobkovsky for his amazing talent in X-ray crystallography because he was able to solve structures on single crystals that were "two-dimensional" and "way too small" to yield publishable data. I would like to give a special thanks to toluene for being the best crystallization solvent. Karsten Meyer, Susanne Mossin, Suzanne Doucette, and Carola Vogel are thanked for their experimental assistance in obtaining solid state magnetic data, EPR data, and reliable elemental analyses. I appreciate Carsten Milsmann for teaching me how to fit my SQUID data. Thomas Cundari, Garnet Chan, Johannes Hachman are thanked for their calculational contributions and providing electronic structures. Frank Neese is thanked for helping fit the EPR data for $(smif)_2Cr$. I would like to thank Serena DeBeer for her assistance with XAS spectroscopy and insightful conversations that helped elucidate a few electronic structures. Héctor Abruña and Mitk'El Santiago-Berrios are thanked for

their expertise in electrochemistry. I am deeply grateful to Ivan Keresztes for his vast knowledge of NMR spectroscopy. His willingness to teach me 2-D spectroscopy and excitement in working together to solve the 15 pyridine rings are greatly appreciated. The Chirik group, in particular Jonathan Darmon, is thanked for training me to use the Mössbauer spectrometer and Gouy balance.

I am particularly thankful for the chemistry building staff. In particular, I would like to thank Dave Wise for expertise in glassblowing and reminding me that "hot glass looks like cold glass." Dave Neish and Larry Stull are thanked for immediately responding to our laboratory needs, keeping morale up, great conversations, and most importantly for their friendship. I would like to thank Josh Wakeman, a fellow country kid, for his kindness is letting us know when our liquid nitrogen dewars had arrived and also for great conversations and daily entertainment. I appreciate the phone calls from Denise Wurtenberg that notified us when our precious packages arrived. Ralph Personius is thanked for helping us keep our lab and gloveboxes running. It was my pleasure to share the first floor hallway and endless stories with Sharon Calhoun, Vonnie Ellis, and Sharon de Roos.

The Wolczanski group members, both past and present, are thanked for providing an amazing working environment and training me to be a successful synthetic inorganic chemist. I would like to thank Mike Marshak and Matt Chambers for providing endless entertainment between Monday night karaoke and Group Therapy. Dr. Dave Manke, my hero, is thanked for being an awesome mentor and a great friend. He introduced me to Columbo and Boston Legal, showed me how to be "BIG FUN," taught me the "Black Magic" of crystallizing compounds, and encouraged me to succeed. It was my honor to spend five years with my chemical siblings, Elliott Hulley and Emily Volpe. I am forever indebted to Elliott for his insightful discussions about chemistry and life. I appreciate that he was always there

with a Cherry Coke to cheer me up on a bad day or when something went awry in the lab. Emily is commended for being the nicest person on the planet as well as a fun companion on trips home. I always knew that I could count on Emily to bring out the best in any situation. It has been my pleasure to train and work with Erika Bartholomew, Wes Morris, and Valerie Williams. Erika proved to be a great labmate, wonderful friend, and great dinner date, whether dinner was prepared at a local restaurant or in my kitchen following Betty Crocker's recipes. I enjoyed watching Steelers Games with Wes at Uncle Joe's. I am encouraged by Valerie's zeal for chemistry and willingness to help others. I will always remember the enlightening group conversations during coffee and lunch breaks. I know they will become great chemists under Pete's watchful eye, and I am pleased to leave the lab in such great caring hands. I would like to give special thanks to Tom Ruttledge for his friendship, love for Wednesday night beers and wings, and being a superb mentor.

I am fortunate to have had fantastic classmates who were not only skilled in chemistry, but also talented in the art of throwing great parties. I will forever cherish the memories created from our Friday/Sunday night dinners, recruiting weekends, A and B exam celebrations, Halloween parties, and the return of the Jersey kids.

Finally, I am deeply grateful to my parents, family, and Dave Kuiper for their love, support, and encouragement. My parents showed me how to work hard and strive for excellence. My siblings have provided comic relief with their "real life" stories as well as new places to vacation. I am forever thankful for my best friend, Dave, who provided a never-ending source of entertainment and humor through random stories and well-planned Kuiper jokes. He has challenged me to continually grow as a scientist and keep my eyes focused on my goals.

TABLE OF CONTENTS

LIST OF FIGURES

LIST OF TABLES

LIST OF SCHEMES

CHAPTER 1

First-Row Transition Metal Complexes Containing Aryl Chelates and the Discovery of the smif, 1,3-di-(2-pyridyl)-2-azaallyl, Ligand*

Introduction

Many organic transformations require the use of transition metal catalysts, and the best catalyst systems available often contain 2nd or 3rd-row transition metals. For instance, olefin metathesis chemistry is ruled by ruthenium and molybdenum catalysts,[1,2,3] whereas palladium complexes dominate the field of coupling reactions: C-C (e.g. Suzuki,[4,5] Heck,[6,7,8] and Sonogashira[9]) and C-N (e.g. Buchwald-Hartwig[10,11,12]) bond formations (Figure 1.1). Most catalysts are easily synthesized and tuning of catalyst properties may be done via ligand modifications. All of the catalysts utilized for the aforementioned organic transformations undergo 2 e^- processes, which are required for the oxidative addition and reductive elimination steps often invoked in catalytic cycles.

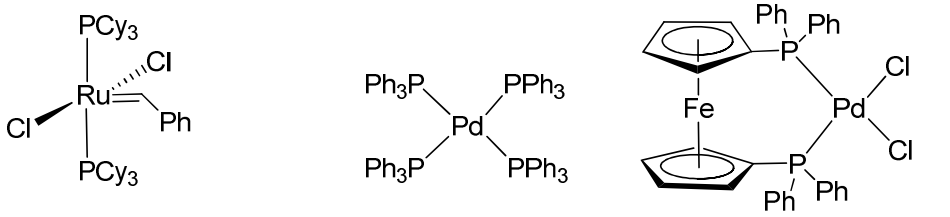

Grubb's 1st Generation Catalyst | Suzuki Catalyst | Buchwald-Hartwig Catalyst

Figure 1.1. Examples of olefin metathesis and cross-coupling catalysts.

Ideally, a transition metal catalyst system should be cost effective, non-toxic, and easily synthesized. First-row transition metals are often cheaper than 2nd and 3rd-row metals and are also less toxic; therefore, rigorous purification steps required in drug syntheses utilizing 2nd and 3rd-row transition metal catalysts can be avoided

* Reproduced with permission from: Frazier, B. A.; Wolczanski, P. T.; Lobkovsky, E. B. *Inorg. Chem.* **2009**, *48*, 11576-11585. Copyright 2009 American Chemical Society.

through a switch for the first-row.[13,14] First-row transition metal compounds are not frequently used as catalysts, in part because of the weak fields exhibited by these complexes, which often lead to 1 e- chemistry that can be detrimental for metathesis or cross coupling reactions.[15] The challenge remains to generate 1st-row transition metal complexes possessing a field strong enough to effectively undergo 2 e^- processes, such as oxidative addition and reductive elimination, as observed by 2nd and 3rd-row catalysts.

First-row transition metal complexes exhibiting strong fields often contain carbon-based ligands.[16,17,18] Metal-aryl bonds are particularly appealing and should impart strong fields since sp^2-C's generate better orbital overlap than corresponding O- and N-based ligands ($S_C > S_N > S_O$). They also do not undergo β-H eliminations, which are prevalent in sp^3 carbon-based ligands. From an electronic standpoint, C-based ligands are favored over O- and N-based ligands as angular overlap theory shows stronger fields arise from better orbital overlap and a smaller energy gap, ΔE_{ML}, between metal 3d orbitals and ligands and . (Figure 1.2).[19]

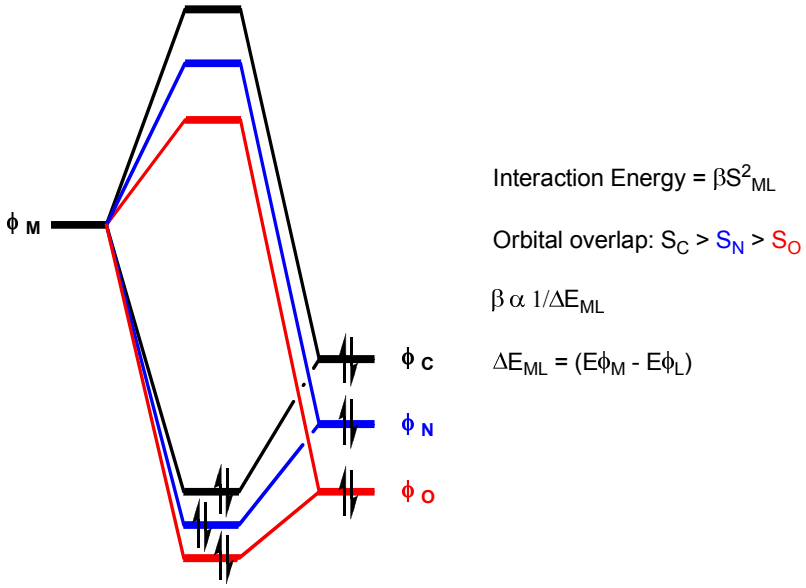

Figure 1.2. Angular overlap arguments predict that C-based ligands should generate stronger fields than O- and N-based ligands based on orbital overlap and interaction energy.

Initial research efforts probed the use of potentially tetradentate, tertiary amines as ancillary ligands to generate the target compounds, **A** and **B** (Figures 1.3, 1.4). **A** possesses a ligand coordinated κ-C,N_{py},N_{py},N_{am} with the incorporation of a single metal-aryl bond, whereas **B** contains two metal-carbon bonds and displays κ-C,C,N_{py},N_{am} coordination. The remaining coordination site (X/L) was designated as a location for either a halide, lending toward future reactivity, an alkylidene, or a labile coordinating ligand.

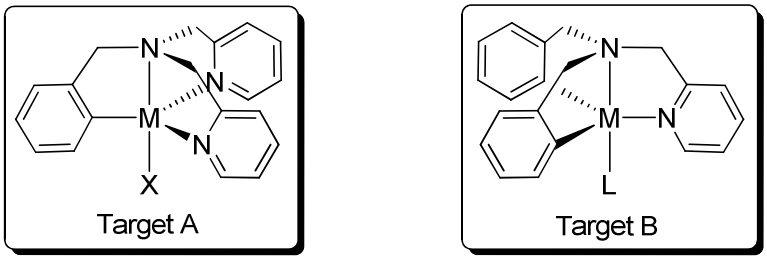

Figure 1.3. Target compounds.

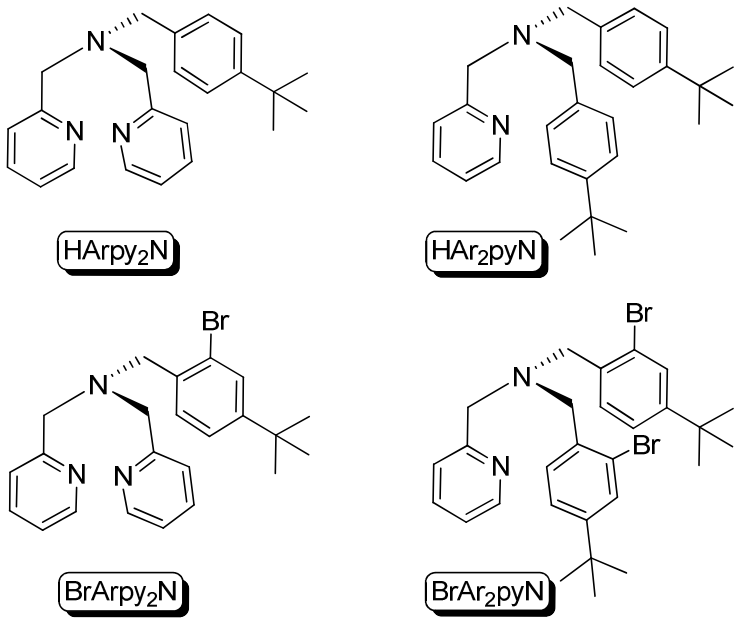

Figure 1.4. Ligands for heterolytic CH bond activation (**HArpy$_2$N** and **HAr$_2$pyN**) and oxidative addition (**BrArpy$_2$N** and **BrAr$_2$pyN**).

Each tertiary amine ligand was specifically designed with hopes of installing at least one metal-aryl bond and generating strong fields in the resulting transition metal complexes. Ligand chelation would be directed by the incorporation of 'hooks,' i.e. an amine nitrogen and pyridine ring nitrogens. These 'hooks' would coordinate the ligands in such a fashion as to prepare the complex for the future metal-aryl bond.

Metal-aryl bonds may be incorporated via heterolytic CH bond activation for **HAr$_2$pyN** and **HArpy$_2$N**[20,21] and oxidative addition of aryl bromide bonds in **BrAr$_2$pyN** and **BrArpy$_2$N**.[22,23] Recent research efforts, particularly in our laboratories,[21] have shown that electrophilic metal centers can invoke CH bond activations. This process maintains the metal's oxidation state and is rather atom efficient, often only involving the loss of HX. Oxidative addition is a simple route for installing a metal-aryl bond, yet it requires finding an appropriate M(0) source.

Results and Discussion

Synthesis of tetradentate ligands. Treatment of 2-(aminomethyl)pyridine and di-(2-picolyl)amine with substituted benzyl bromides[24] afforded tetradentate ligands (Scheme 1.1). These ligands were synthesized on 4 - 15 g scales and isolated as yellow crystalline solids in good yields, 62 - 76 %. **HArpy$_2$N** and **HAr$_2$pyN** were synthesized for heterolytic CH bond activation while **BrArpy$_2$N** and **BrAr$_2$pyN** were prepared for oxidative addition of the aryl-bromide bond. Substitution *meta* to the activation site, where X = H or Br, was intended to not only increase product solubility, but also to protect the future metal-aryl bond.

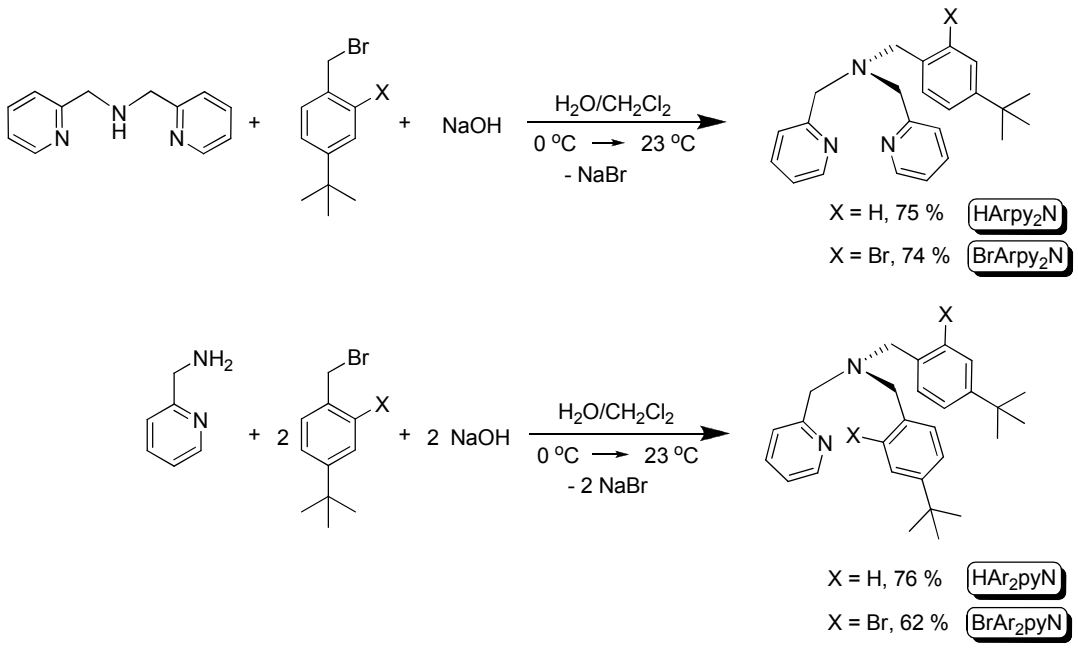

Scheme 1.1. Syntheses for tetradentate ligands, **HArpy$_2$N**, **BrArpy$_2$N**, **HAr$_2$pyN**, and **BrAr$_2$pyN**.

Heterolytic CH Bond Activation Attempts. All attempts to utilize various electrophilic M(II) sources, such as triflates, or M(II) halides to induce heterolytic CH bond activation of **HArpy$_2$N** and **HAr$_2$pyN** were unsuccessful. Treatment of M(II) halides led to the formation of adducts, e.g. {κ-N_{py},N_{am}-HAr$_2$pyN}MCl_2, where M = Fe, Co, and Ni. These compounds were not characterized as the desired CH bond activation was not observed, even at elevated temperatures. Subsequent investigations focused on oxidative addition methods to generate metal-aryl bonds.

Oxidative Addition Generates Metal-Aryl Bonds. A. Nickel. To prevent the insertion of a carbonyl into the future metal-aryl bond, noncarbonyl containing 1st-row transition metal complexes were explored. Initial efforts focused on using $Ni(COD)_2$,[25] a soluble Ni(0) source possessing labile ligands. Oxidative addition to yield a Ni(II) compound was observed. Treatment of $Ni(COD)_2$ with one equivalent of **BrAr$_2$pyN**

in THF yielded the corresponding diamagnetic compound, {κ-C,N_{py},N_{am}-(2-pyridylmethyl)N(CH_2(4-^{t}Bu-phenyl-2-yl))(CH_2(4-^{t}Bu-phenyl-2-Br))}NiBr (((BrAr)ArpyN)NiBr, **1-Ni**). **1-Ni** was isolated in 96 % yield as orange crystals (Scheme 1.2). Unfortunately, all attempts to install the second metal-aryl bond under reducing conditions resulted in the reductive elimination and intramolecular aryl-aryl coupling of the ligand, thus generating a seven-membered ring, and presumably Ni(0). Aryl-aryl coupling with nickel complexes is well documented,[26,27] and the reductive elimination to form the ring was not surprising.

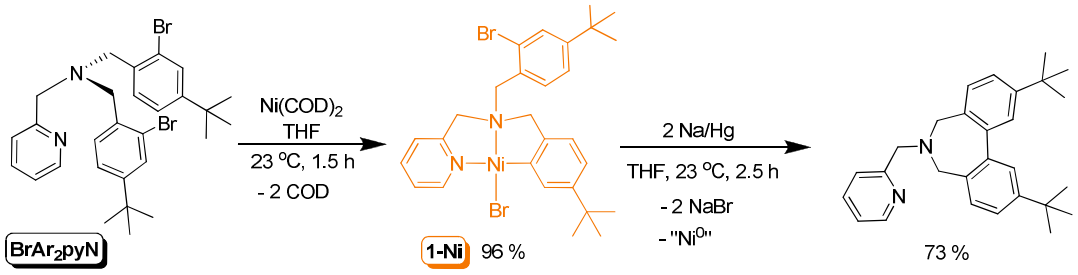

Scheme 1.2. Synthesis of ((BrAr)ArpyN)NiBr (**1-Ni**) and conversion to intramolecular aryl-aryl coupled ligand.

Oxidative addition studies with nickel focused on the use of **BrArpy$_2$N** in the hope of installing one metal-aryl bond, and examining subsequent reactivity. Treatment of Ni(COD)$_2$ in benzene with **BrArpy$_2$N** yielded the diamagnetic, Ni(II) oxidative addition product, {κ-C,N_{py},N_{py},N_{am}-(2-pyridylmethyl)$_2$N(CH_2(4-^{t}Bu-phenyl-2-yl))}NiBr ((Arpy$_2$N)NiBr, **2-Ni**). Orange needles of **2-Ni** were isolated in 67 % yield (Scheme 1.3). **2-Ni** is depicted as a trigonal bipyramid with κ-C,N_{py},N_{py},N_{am} ligation based upon the C_s symmetry observed in the ^{1}H and ^{13}C{^{1}H} NMR spectra. However, the compound may undergo a rapid exchange of the 2-pyridylmethyl groups through the square planar complex shown in Scheme 1.3. Further reactivity was not investigated as thermolysis of **2-Ni** revealed the unexpected intermolecular aryl-aryl

coupling of the ligand, which was presumably accompanied by the disproportionation of nickel. The development of neutral hexadentate ligands from aryl-aryl coupling may be beneficial for other coordination chemistry, but our research focus shifted toward other 1st-row transition metals.

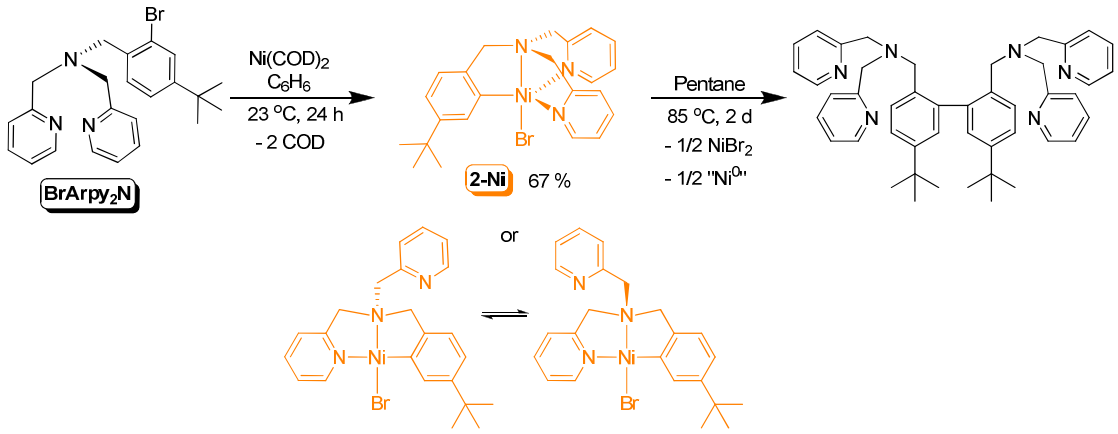

Scheme 1.3. Synthesis of ($Arpy_2N$)NiBr (**2-Ni**) and conversion to intermolecular aryl-aryl coupled ligand.

B. Iron. The search for noncarbonyl Fe(0) sources led to studying the reactivity of **$BrAr_2pyN$** and **$BrArpy_2N$** with Rieke iron[28] and "$Fe(PMe_3)_4$,"[29] in addition to complexes capable of behaving like Fe(0) sources, e.g. $(dmCh)_2Fe$ (dmCh = dimethylcyclohexadienyl).[30] However, these reactions were unsuccessful in yielding the desired targets. Subsequent efforts concentrated on disproportionating Fe(II) sources into ⅓ Fe(0) and ⅔ Fe(III). Unfortunately, the disproportionation attempts with Fe(II) halides were unsuccessful even upon thermolysis, presumably due to a lack of solubility, thereby warranting the use of a soluble Fe(II) source, i.e $Fe\{N(TMS)_2\}_2(THF)$.[31] Treatment of $Fe\{N(TMS)_2\}_2(THF)$ in Et_2O with **$BrArpy_2N$** generated a dark green solution, $Fe\{N(TMS)_2\}_3$,[32] from which {κ-C,N_{py},N_{py},N_{am}-(2-pyridylmethyl)$_2$N(CH_2(4-^{t}Bu-phenyl-2-yl))}FeBr (($Arpy_2N$)FeBr, **2-Fe**), was isolated as red needles in 16 % yield (Scheme 1.4). When considering the disproportionation of

$Fe\{N(TMS)_2\}_2(THF)$, the low yield of paramagnetic **2-Fe** was approximately 50 % of the anticipated yield. The ^1H NMR spectrum of **2-Fe** observed in THF-d_8 displayed 18 paramagnetic peaks, which may be rationalized by the slight twist observed in the crystal structure of **2-Fe** preventing the mirror plane required for true C_s symmetry. Crystals of **2-Fe** were insoluble in non-coordinating solvents, such as C_6D_6 and toluene-d_8. A more convenient, higher yielding synthesis to **2-Fe** (Scheme 1.4) was pursued after the structure of **2-Fe** was elucidated via X-ray crystallography. Exposing $FeBr_2$ in THF with an equivalent of **BrArpy$_2$N** for 6 h yielded the paramagnetic, yellow adduct, $\{\kappa$-N_{py},N_{py},N_{am}-(2-pyridylmethyl)$_2$N(CH_2(4-^{t}Bu-phenyl-2-Br))$\}FeBr_2$ ((BrArpy$_2$N)$FeBr_2$, **3-Fe**), in excellent yield (97 %). The reduction of **3-Fe** in THF with two equivalents of sodium amalgam over the course of 6 h afforded **2-Fe** in 91 % yield.

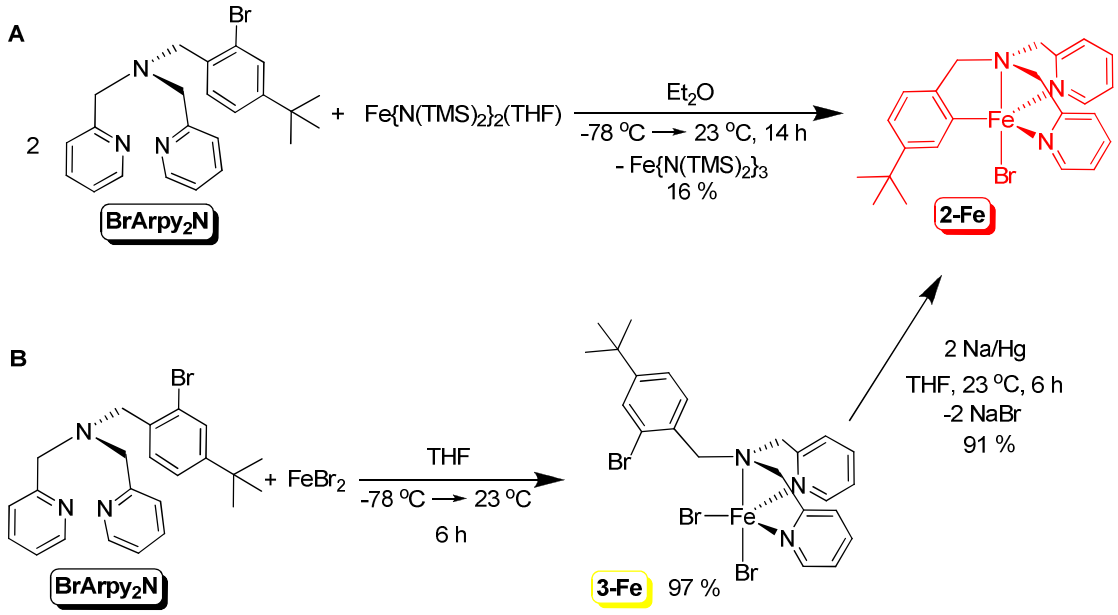

Scheme 1.4. Synthetic routes to **2**-Fe via disproportionation, **A**, and reduction of the adduct, **B**.

Characterization of (Arpy$_2$N)Fe (2-Fe): X-ray Crystal Structure. Single crystal, X-ray diffraction quality, red rods were obtained from toluene. Select

crystallographic and refinement data for **2-Fe** are listed in Table 1.1. Pertinent bond distances and angles are listed in Table 1.2. The solid state structure, shown in Figure 1.5, is a slightly distorted trigonal bipyramid with equatorial angles around the expected 120 ° (∠N2-Fe1-N3 = 110.77(16) °, ∠N2-Fe1-C15 = 117.34(18) °, ∠N3-Fe1-C15 = 117.07(18) °) while the axial bromide and amine nitrogen span an angle of 169.10(11) ° around the iron. The chelation angles of the ligand are all less than 90 °, i.e. ∠N1-Fe1-N2 = 75.47(15) °, ∠N1-Fe1-N3 = 75.19(15) °, ∠N1-Fe1-C15 = 80.07(17) °, resulting in a slight twist of the amine ligand preventing true C_s symmetry for **2**-Fe and tilting the chelates away from the amine: ∠Fe1-N2-C2 = 116.5(3) °, ∠Fe1-N2-C6 = 125.3(4) °, ∠Fe1-N3-C8 = 117.6(4) °, ∠Fe1-N3-C12 = 122.5(3) °, ∠Fe1-C15-C14 = 113.0(4) °, and ∠Fe1-C15-C16 = 131.8(4) °. Due to the acute bite angles of the ligand, all angles between the ligand and the bromide are greater than 90 °, i.e. ∠Br1-Fe1-N2 = 99.77(11) °, ∠Br1-Fe1-N3 = 97.86(12) °, ∠Br1-Fe1-C15 = 110.75(14) °. The amine is pyramidal, possessing iron-nitrogen-carbon angles around 106 ° (∠Fe1-N1-C1 = 106.7(3) °, ∠Fe1-N1-C7 = 108.0(3) °, ∠Fe1-N1-C13 = 105.5(3) °). The iron-bromide and iron-carbon bond distances of 2.5352(9) Å and 2.068(5) Å are normal. Bond lengths consistent with an sp^3(N)-sp^3(C) assignment are observed for the amine nitrogen-methylene carbons: d(N1-C1) = 1.461(6) Å, d(N1-C7) = 1.466(6) Å, d(N1-C13) = 1.467(6) Å. Iron-pyridine nitrogen distances, 2.149(4) Å and 2.156(4) Å, are shorter than the iron-amine nitrogen bond length of 2.276(4) Å.

Table 1.1. X-ray crystallographic data for ($Arpy_2N$)FeBr (**2-Fe**) and (smif)CrN($TMS)_2$ (**4-Cr**).

	2 - Fe	**4 - Cr**
Formula	$C_{23}H_{26}N_{43}BrFe$	$C_{18}H_{28}N_4Si_2Cr$
Formula weight	480.23	408.62
Crystal system	Orthorhombic	Triclinic
Space group	*P* bca	$P\bar{1}$
Z	8	2
a (Å)	13.0576(12)	8.0101(4)
b (Å)	16.9655(11)	11.5495(5)
c (Å)	20.0495(18)	11.9921(7)
α (°)	90	95.2630(10)
β (°)	90	91.093(4)
γ (°)	90	107.584(4)
V (Å^3)	4441.5(6)	1051.84(9)
ρ_{calc} g/cm^3	1.436	1.290
μ (mm^{-1})	2.491	0.666
temp (K)	173(2)	173(2)
λ (Å)	0.71073	0.71073
final R indices [$I > 2\sigma(I)$][a,b]	$R_1 = 0.0501$	$R_1 = 0.0405$
	$wR_2 = 0.0906$	$wR_2 = 0.0783$
R indices (all data)[a,b]	$R_1 = 0.1101$	$R_1 = 0.0689$
	$wR_2 = 0.1100$	$wR_2 = 0.0928$
GOF[c]	1.000	1.001

[a] $R_1 = \Sigma||F_o| - |F_c|| / \Sigma|F_o|$.

[b] $wR_2 = [\Sigma w(|F_o| - |F_c|)2/\Sigma wF_o{}^2]^{1/2}$.

[c] GOF (all data) = $[\Sigma w(|F_o| - |F_c|)^2/(n - p)]^{1/2}$, n = number of independent reflections, p = number of parameters.

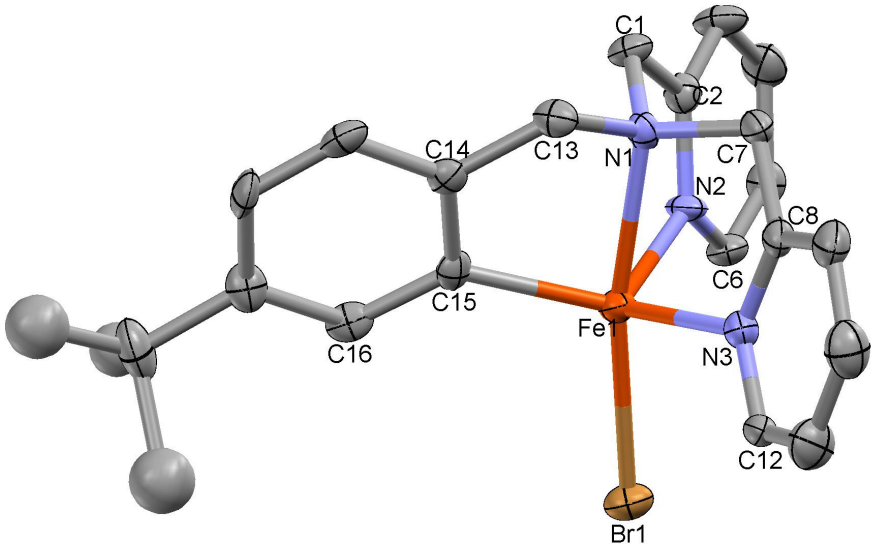

Figure 1.5. Molecular structure of ($Arpy_2N$)FeBr (**2-Fe**). Thermal ellipsoids are at 50 % probability level, and all hydrogens have been removed for clarity. The disordered ^{t}Bu group (two staggered positions, one shown above) was refined isotropically.

Table 1.2. Selected interatomic distances and angles for ($Arpy_2N$)FeBr (**2-Fe**).

Bond Distances (Å)		Bond Angles (°)	
Fe1 - N1	2.276(4)	N1 - Fe1 - Br1	169.10(11)
Fe1 - N2	2.149(4)	N2 - Fe1 - N3	110.77(16)
Fe1 - N3	2.156(4)	N2 - Fe1 - C15	117.34(18)
Fe1 - C15	2.068(5)	N3 - Fe1 - C15	117.07(18)
Fe1 - Br1	2.5352(9)	N1 - Fe1 - N2	75.47(15)
N1 - C1	1.461(6)	N1 - Fe1 - N3	75.19(15)
N1 - C7	1.466(6)	N1 - Fe1 - C15	80.07(17)
N1 - C13	1.467(6)	Fe1 - N2 - C2	116.5(3)
		Fe1 - N2 - C6	125.3(4)
		Fe1 - N3 - C8	117.6(4)
		Fe1 - N3 - C12	122.5(3)
		Fe1 - C15 - C14	113.0(4)
		Fe1 - C15 - C16	131.8(4)
		Br1 - Fe1 - N2	99.77(11)
		Br1 - Fe1 - N3	97.86(12)
		Br1 - Fe1- C15	110.75(14)
		Fe1 - N1 - C1	106.7(3)
		Fe1 - N1 - C7	108.0(3)
		Fe1 - N1 - C13	105.5(3)

Magnetism of (Arpy$_2$N)FeBr (2-Fe). The paramagnetic ^{1}H NMR spectrum prompted an investigation into the temperature dependence of the molar susceptibility of **2-Fe** (Figure 1.6). SQUID magnetometry revealed a μ_{eff} of 5.3 μ_B at 293 K, consistent with a high spin (S = 2) ground state for Fe(II). The value is slightly higher than the spin-only value of 4.90 μ_B presumably due to contributions from orbital angular momentum and spin-orbit coupling. The magnetic moment values observed between 0 K and 50 K may be attributed to zero field splitting (ZFS). Apparently, one metal-aryl bond was not capable of invoking a field strong enough to produce a low spin (S = 0) or even an intermediate spin (S = 1) metal center.

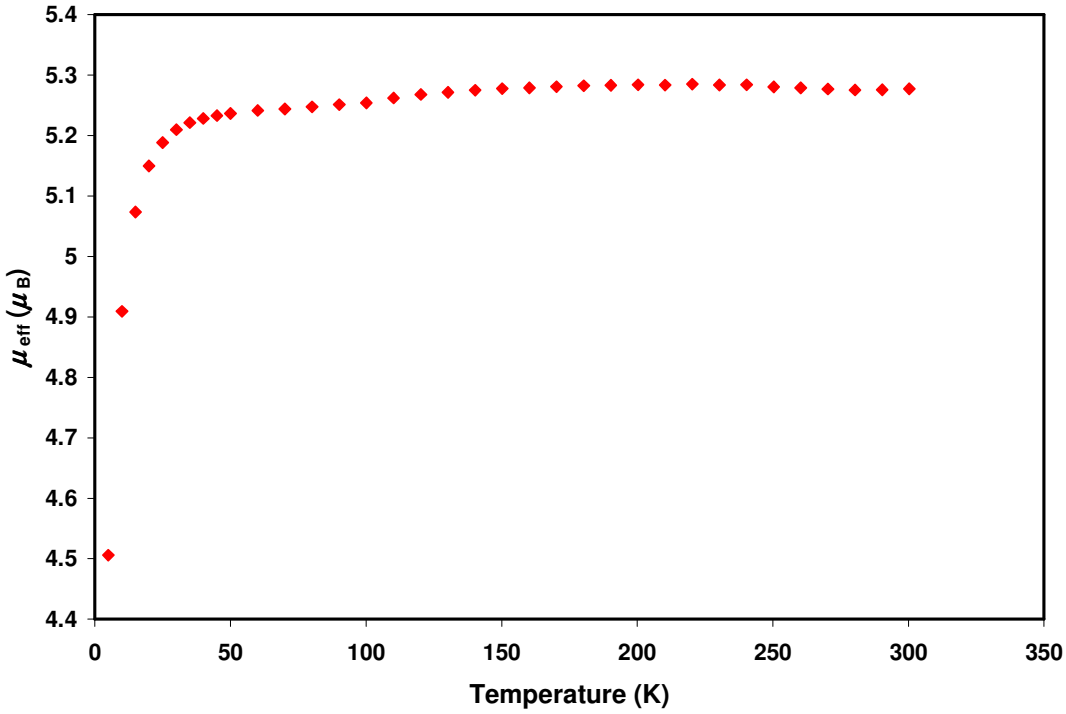

Figure 1.6. SQUID data for (Arpy$_2$N)FeBr (**2-Fe**): Magnetic moment (μ_{eff} in μ_B) as a function of T (K).

C-N Bond Cleavage and the Synthesis of (smif)CrN(TMS)$_2$. After observing the disproportionation of Fe{N(TMS)$_2$}$_2$(THF)[31] from Fe(II) to ⅓ Fe(0) and

⅔ $Fe\{N(TMS)_2\}_3$,[32] investigations shifted toward inducing the same disproportionation from the corresponding chromium analog, $Cr\{N(TMS)_2\}_2(THF)_2$.[33,34] Treatment of $Cr\{N(TMS)_2\}_2(THF)_2$ with **BrArpy$_2$N** in Et_2O generated an intense deep green solution from which, {κ-N_{py},N_{py},N_{aza}-(1,3-di-(2-pyridyl)-2-azaallyl)}$CrN(TMS)_2$ ((smif)$CrN(TMS)_2$, (**4-Cr**)) was isolated as dark green crystals in 52 % yield (eq. 1.1).

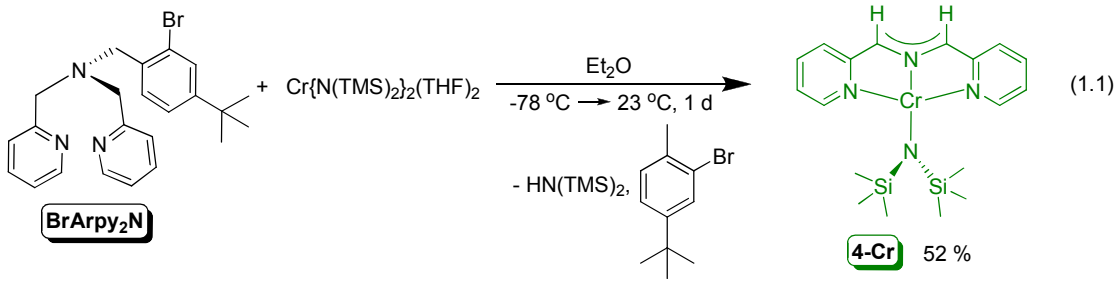

(1.1)

The ^1H NMR spectrum acquired in C_6D_6 of the dark green solid revealed six paramagnetic peaks. Single crystal X-ray diffraction studies established the structure of **4-Cr** and revealed an unusual C-N bond cleavage, or amine debenzylation, of **BrArpy$_2$N** leading to the formation of the 1,3-di-(2-pyridyl)-2-azaallyl ligand, dubbed "smif", instead of the anticipated trigonal bipyramidal oxidative addition product. ^1H NMR spectroscopy revealed that the reaction filtrates contained 2-bromo-4-*tert*-butyltoluene, a precursor to the benzyl bromide used in the synthesis of **BrArpy$_2$N**, and hexamethydisilazane, $HN(TMS)_2$. An alternative route to synthesize (smif)$CrN(TMS)_2$ was established (eq 1.2). Slow addition of a solution of 1,3-di-(2-pyridyl)-2-azapropene, **smifH**,[35] to $Cr\{N(TMS)_2\}_2(THF)_2$ in Et_2O at 23 °C produced a very intense, deep emerald green solution containing **4-Cr** and $HN(TMS)_2$. **4-Cr** was isolated in a good yield (74 %).

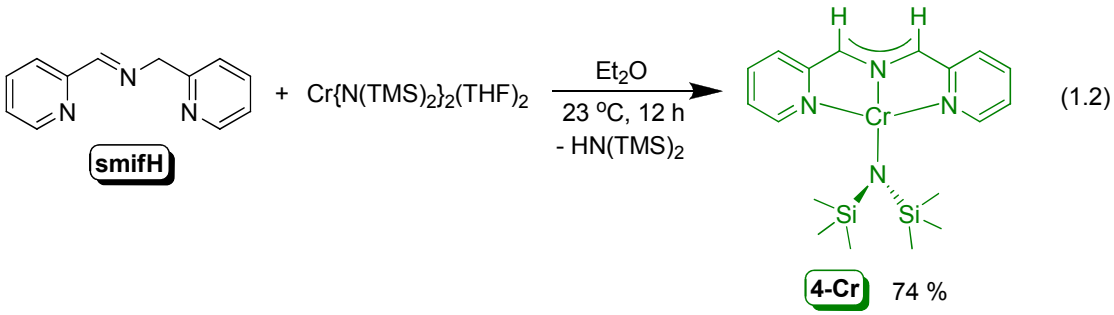

(1.2)

Characterization of (smif)CrN(TMS)$_2$ (4-Cr): X-ray Structure. Single crystal, X-ray diffraction quality, dark green hexagonal blocks were obtained from pentane. Select crystallographic and refinement data for **4-Cr** are listed in Table 1.1, and pertinent bond distances and angles are listed in Table 1.3. The solid state structure of **4-Cr**, shown in Figure 1.7, depicts a nearly square planar Cr(II) compound containing an amide, N(TMS)$_2$, perpendicular to the plane produced by the smif ligand. Pyridine nitrogens span an angle of 157.07(6) ° (N1-Cr1-N3) around chromium. Similar to **2-Fe**, the azaallyl chelate of **4-Cr** has acute bite angles, i.e. ∠N2-Cr1-N1 = 78.80(6) ° and ∠N2-Cr1-N3 = 78.35(6) °, rendering the corresponding angles between the amide nitrogen and pyridine rings obtuse: ∠N4-Cr1-N1 = 101.04(6) ° and ∠N4-Cr1-N3 = 101.74(6) °. The bond distances on the azaallyl backbone are considerably shorter than those observed for **2-Fe** (~ 1.46 Å) and are consistent with a delocalized anion: d(N2-C6) = 1.332(2) Å, d(N2-C7) = 1.320(2) Å. As observed in **2-Fe**, the pyridine rings are "tilted" away from the metal center: ∠Cr1-N1-C1 = 129.05(12) °, ∠Cr1-N1-C5 = 112.12(12) °, ∠Cr1-N3-C8 = 113.02(12) °, ∠Cr1-N3-C12 = 129.57(13) °. The structure of **4-Cr** deviates slightly from a true square plane as the asymmetric amide (∠Cr1-N4-Si1 = 110.97(7) °, ∠Cr1-N4-Si2 = 122.23(7) °) is canted out of the plane of the molecule shown by the $N_{aza}CrN_{am}$ angle of 168.76(6) °. These distortions may result in the attenuation of the *trans*-influence between the azaallyl and amide. Chromium-nitrogen bond distances are relatively

close even though the nitrogens are very different. The chromium-pyridine nitrogen distances are the longest at 2.0887(14) Å and 2.0864(15) Å for Cr1-N1 and Cr1-N3, respectively. The anionic nitrogens yield the shortest distances from chromium with the amide at 2.0260(12) Å and the azaallyl-nitrogen 2.0416(14) Å away.

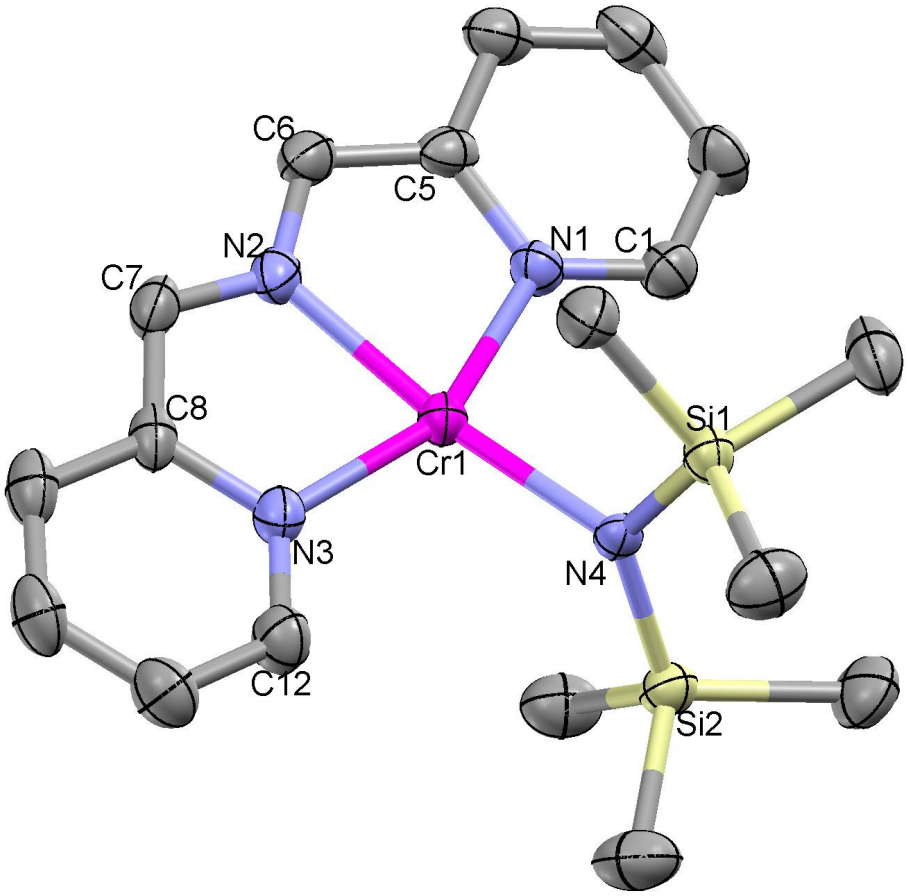

Figure 1.7. Molecular structure of (smif)CrN(TMS)$_2$ (**4-Cr**). Thermal ellipsoids are at 50 % probability level, and all hydrogens have been removed for clarity.

Table 1.3. Selected interatomic distances and angles for (smif)CrN(TMS)$_2$ (**4-Cr**).

Bond Distances (Å)		Bond Angles (°)	
Cr1 - N1	2.0887(14)	N1 - Cr1 - N3	157.07(6)
Cr1 - N2	2.0416(14)	N2 - Cr1 - N1	78.80(6)
Cr1 - N3	2.0864(15)	N2 - Cr1 - N3	78.35(6)
Cr1 - N4	2.0260(12)	N4 - Cr1 - N1	101.04(6)
N2 - C6	1.332(2)	N4 - Cr1 - N3	101.74(6)
N2 - C7	1.320(2)	N2 - Cr1 - N4	168.76(6)
		Cr1 - N1 - C1	129.05(12)
		Cr1 - N1 - C5	112.12(12)
		Cr1 - N3 - C8	113.02(12)
		Cr1 - N3 - C12	129.57(13)
		Cr1 - N2 - C6	115.65(13)
		Cr1 - N2 - C7	115.77(13)
		Cr1 - N4 - Si1	110.97(7)
		Cr1 - N4 - Si2	122.23(7)
		C6 - N2 - C7	128.48(17)

Magnetism of (smif)CrN(TMS)$_2$ (4-Cr). Temperature dependence studies of the molar susceptibility commenced after the observation of a paramagnetic ^{1}H NMR spectrum for **4-Cr** (Figure 1.8). SQUID magnetometry data revealed a μ_{eff} of 4.7 μ_B at 293 K, consistent with the expected high spin Cr(II), S = 2 ground state. Similar to **2**-Fe, the magnetic moment values decrease below 50 K and may be attributed to ZFS. The ZFS is large due to the substantial deviation from spherical symmetry in square planar **4-Cr**.

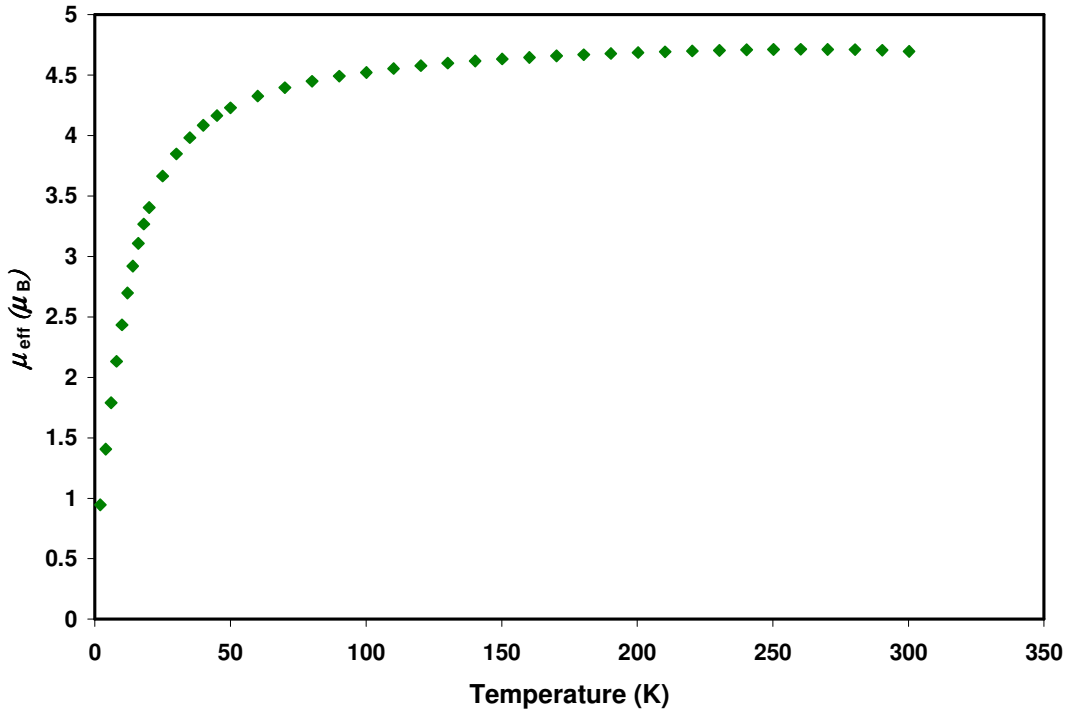

Figure 1.8. SQUID data for (smif)CrN(TMS)$_2$ (**4-Cr**): Magnetic moment (μ_{eff} in μ_B) as a function of T (K).

UV-vis Spectrum of (smif)CrN(TMS)$_2$ (4-Cr). A solution of (smif)CrN(TMS)$_2$ (**4-Cr**) in benzene yields a very intense, deep emerald green solution. Strong absorptions in the red and blue regions are observed in the UV-vis spectrum, shown in Figure 1.9, thereby permitting transmission of the deep emerald green color. The UV-vis spectrum possesses four main features. The strongest absorption occurs in the high energy regime, 396 nm (ε ~ 27,000 M^{-1} cm^{-1}). Three very intense absorptions are also observed at lower energy with extinction coefficients ~ 17,000 M^{-1} cm^{-1} (581 nm, ε ~ 17,000 M^{-1} cm^{-1}; 627 nm, ε ~ 19,000 M^{-1} cm^{-1}; 675 nm, ε ~ 15,000 M^{-1} cm^{-1}). Calculations for related complexes, e.g. (smif)$_2$M, where M = V, Cr, Mn, Fe, Co, Ni, suggest that these observed absorptions may be attributed to and dominated by intraligand (IL) transitions between the azaallyl $CN_{aza}C^{nb}$ orbitals to pyridine π* orbitals. Additionally, underlying metal-to-ligand charge transfer (MLCT)

bands may also play a role in the observed intensities as the calculations also show that the azaallyl $CN_{aza}C^{nb}$ orbital is energetically close to the metal 3d orbitals.

Related smif compounds also possess similar features in their UV-vis spectra, particularly the lower energy absorptions. These features observed for **4-Cr** occur at 581 nm (17,210 cm^{-1}), 627 nm (15,950 cm^{-1}), and 675 nm (14,820 cm^{-1}), and they are separated by 1,130 cm^{-1} and 1,260 cm^{-1}. These bands may be attributed to the progression of the vibronic coupling of a single electronic IL transition. In an ideal progression, the energy gap between transitions is identical. A sharp absorption at 1140 cm^{-1}, possibly resulting from a bending vibration of the backbone $CN_{aza}C$ that is capable of coupling to the electronic IL transition, was observed in the in IR spectrum of **4-Cr**.

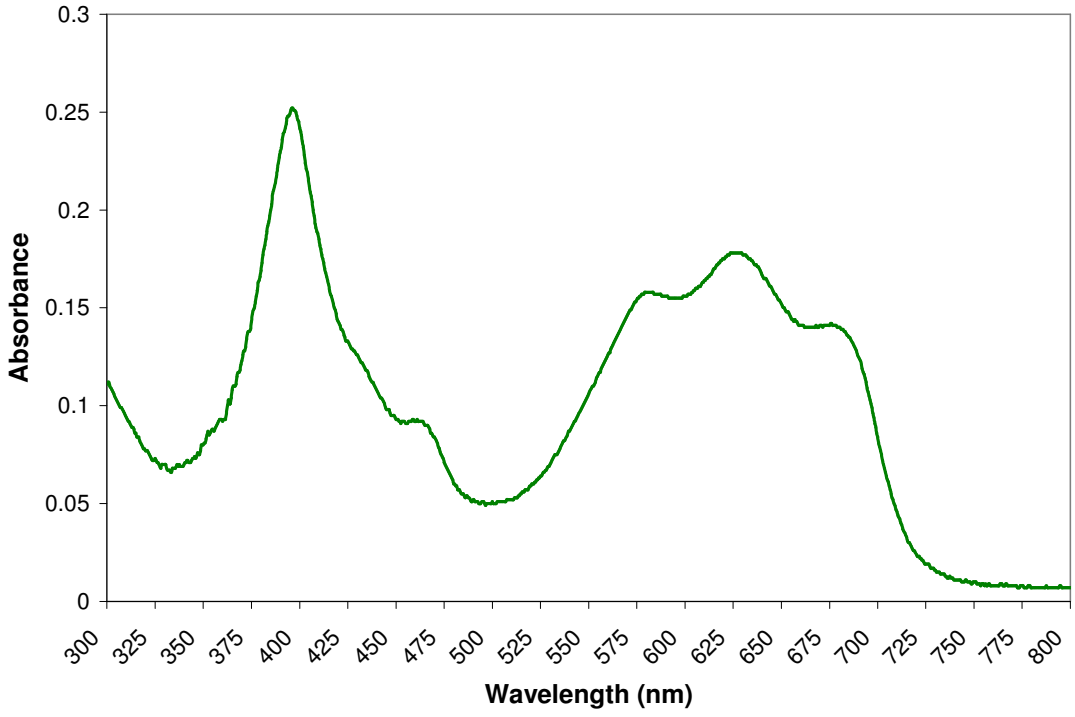

Figure 1.9. UV-vis spectrum of $(smif)CrN(TMS)_2$ (**4-Cr**) in benzene: 396 nm (ε ~ 27,000 M^{-1} cm^{-1}), 424 nm (sh, ε ~ 12,500 M^{-1} cm^{-1}), 461 nm (ε ~ 9,500 M^{-1} cm^{-1}), 581 nm (ε ~ 17,000 M^{-1} cm^{-1}), 627 nm (ε ~ 19,000 M^{-1} cm^{-1}), 675 nm (ε ~ 15,000 M^{-1} cm^{-1}).

Proposed Mechanism for the Formation of (smif)CrN(TMS)$_2$ (4-Cr).

Treating Cr{N(TMS)$_2$}$_2$(THF)$_2$ with **BrArpy$_2$N** surprisingly generated (smif)CrN(TMS)$_2$ in 52 % isolated yield, thus suggesting that the mechanism should avoid steps which may be detrimental, i.e. changing chromium oxidation states, to the eventual formation of the Cr(II) species, **4-Cr**. The mechanism must also account for the formation of HN(TMS)$_2$ and 2-bromo-4-*tert*-butyltoluene,[24] which were observed as byproducts by ^{1}H NMR spectroscopy. The proposed mechanism, shown in Scheme 1.5, begins by coordinating **BrArpy$_2$N** to Cr{N(TMS)$_2$}$_2$(THF)$_2$ upon the loss of 2 equivalents of THF, thereby generating the 5-coordinate {κ-N$_{py}$,N$_{py}$,N$_{am}$-(2-pyridylmethyl)$_2$N(CH$_2$(4-^{t}Bu-phenyl-2-Br))}Cr{N(TMS)$_2$}$_2$ complex. This adduct would undergo β-abstraction of the methylene group by the internal base, N(TMS)$_2$, with concomitant loss of HN(TMS)$_2$. Additionally, de-aromatization of a pyridine ring would produce an anionic chelate and form the proposed square planar Cr(II) compound. From this compound, α-migration of the benzyl group occurs while the pyridine ring is re-aromatized to generate a neutral chelate, **smifH**. This produces the 5-coordinate Cr(II) complex, (smifH)Cr(Bn){N(TMS)$_2$}. β-abstraction of the other methylene hydrogen by the benzyl group makes 2-bromo-4-*tert*-butyltoluene and **4-Cr**. Note that the proposed mechanism utilizes Cr(II) throughout the entire process as changes to other oxidation states, i.e. Cr(III) or Cr(IV), may prevent the ultimate formation of **4-Cr**. Even though this is a unique organic transformation mediated by a Cr(II) center, Westerhausen et al. also observed a similar degradation leading to the formation (smif)$_2$Zn by treating ZnMe$_2$ with di-(2-picolyl)amine, which presumably remained Zn(II) throughout the entire reaction.[36]

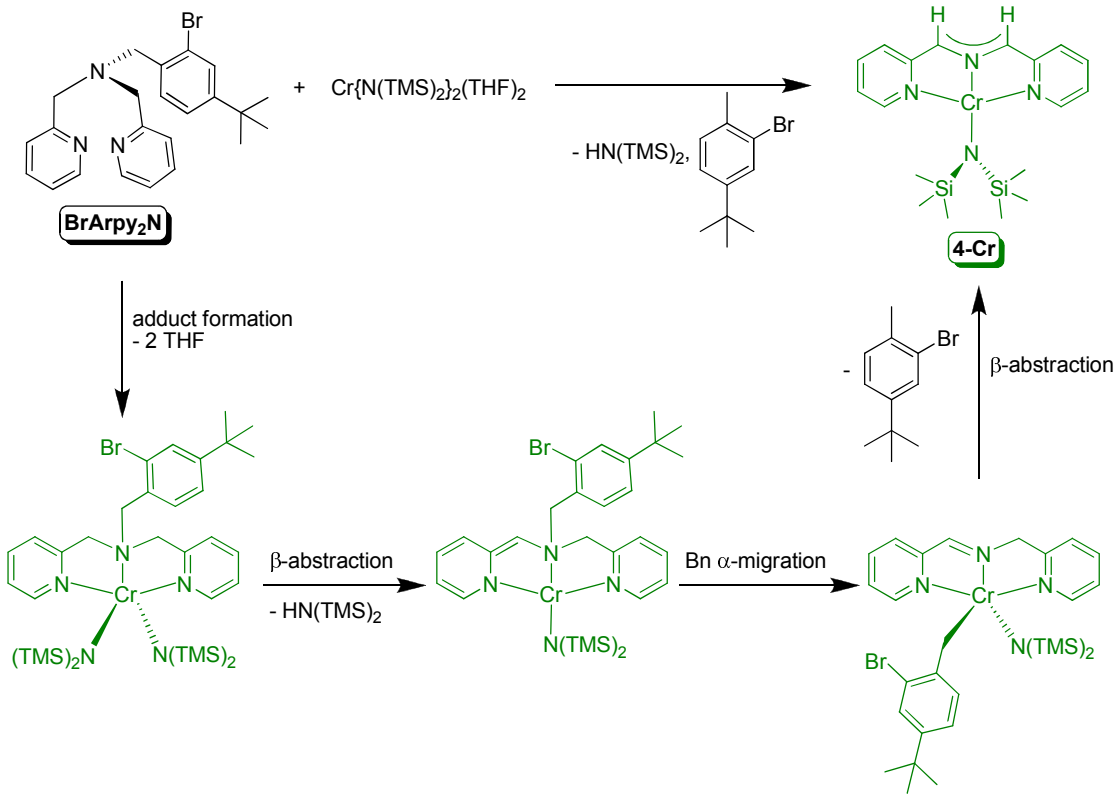

Scheme 1.5. Proposed mechanism for the synthesis of (smif)CrN(TMS)$_2$ from Cr{N(TMS)$_2$}$_2$(THF)$_2$ and **BrArpy$_2$N**.

Conclusions

The use of metal-aryl bonds to invoke strong fields within 1st-row transition metal complexes was unsuccessful with the tetradentate ligands used in this study. Heterolytic CH bond activation attempts failed, even with electrophilic M(II) sources. Oxidative addition afforded two orange, diamagnetic Ni(II) complexes as expected for square planar and trigonal bipyramidal Ni(II). Only very weak field ligands and different coordination geometries, such as tetrahedral or octahedral, would generate paramagnetic Ni(II) products. Iron(II) complexes, on the other hand, have the ability to exhibit a variety of spin states, i.e. low spin (S = 0), intermediate spin (S = 1), and high spin (S = 2), which may be controlled by the field strength of the ligand.

Unfortunately, the presence of one metal-aryl bond in **2-Fe** was unable to even produce an intermediate spin complex, as SQUID magnetometry data revealed that **2-Fe** is a high spin system. A strong field carbon-based ligand may require the presence of two metal-aryl bonds, but precautions must be taken to avoid aryl-aryl coupling of the ligand as was observed for the Ni(II) complexes.

These investigations also led to the discovery of the anionic ligand, smif, which was generated through an unusual C-N bond cleavage of a tertiary amine by a Cr(II) complex. The smif ligand enables the stabilization of low symmetry complexes and affords intense optical properties worth pursuing for materials applications.

Experimental

General Considerations. All manipulations were performed using either glovebox or high vacuum line techniques. Hydrocarbon solvents containing 1-2 mL of added tetraglyme, and ethereal solvents were distilled under nitrogen from purple sodium benzophenone ketyl and vacuum transferred from same prior to use. Benzene-d_6 and toluene-d_8 were dried over sodium, vacuum transferred and stored under N_2. THF-d_8 was dried over sodium benzophenone ketyl. Methylene chloride-d_2 was dried over CaH_2, vacuum transferred and stored over activated 4 Å molecular sieves. $Ni(COD)_2$,[25] $CrCl_2(THF)$,[33] $Fe\{N(TMS)_2\}_2(THF)$,[31] 2-bromo-4-*tert*-butylbenzyl bromide,[24] and 1,3-(2-pyridyl)-2-azapropene (smifH),[35] were prepared according to literature procedures. All other chemicals were commercially available and used as received. All glassware was oven dried.

NMR spectra were obtained using INOVA 400 and INOVA 500 spectrometers. Chemical shifts are reported relative to benzene-d_6 (^1H δ 7.16; $^{13}C\{^1H\}$ δ 128.39), toluene-d_8 (^1H δ 2.09; $^{13}C\{^1H\}$ δ 20.4), THF-d_8 (^1H δ 3.58; $^{13}C\{^1H\}$ δ 67.57), and methylene chloride-d_2 (^1H δ 5.32; $^{13}C\{^1H\}$ δ 54.00). Infrared spectra

were recorded on a Nicolet Avatar 370 DTGX spectrophotometer interfaced to an IBM PC (OMNIC software). UV-Vis spectra were obtained on a Shimadzu UV-2102 interfaced to an IBM PC (UV Probe software). GC-MS spectra were obtained on a JEOL GCMate 2 mass spectrometer coupled to an Agilent 689 N GC with EI ionization under standard conditions. Solution magnetic measurements were conducted via Evans' method in toluene-d_8.[37] Solid state magnetic measurements were performed using a Johnson Matthey magnetic susceptibility balance calibrated with $HgCo(SCN)_4$. Elemental analyses were performed by Robertson Microlit Laboratories, Madison, New Jersey and the services at the University of Erlangen-Nuremberg, Germany.

Synthesis. 1. *N*,*N*-bis(4-*tert*-butylbenzyl)-1-(pyridine-2-yl)methanamine (HAr$_2$pyN). To a 0 ºC biphasic solution of 2-(aminomethyl)pyridine (1.500 g, 13.87 mmol) in 10 mL H_2O and 4-*tert*-butylbenzyl bromide (6.302 g, 27.74 mmol) in 70 mL CH_2Cl_2 was slowly added a solution of NaOH (1.110g, 27.75 mmol) in 10 mL H_2O. The biphasic reaction mixture was slowly warmed to 23 ºC, while stirring vigorously, and monitored by pH. When the reaction mixture was neutral, the product was extracted from the aqueous layer with CH_2Cl_2 (4 x 15mL). Organic layers were combined, dried over $MgSO_4$, and filtered. Rotary evaporation of the filtrate yielded a red-orange oil. After the addition of hexanes, a brown impurity was filtered. The hexanes filtrate was concentrated, cooled, and yielded yellow crystals of **HAr$_2$pyN**. (4.198g, 76 %). ^{1}H NMR (C_6D_6, 400 MHz): δ 1.25 (s, C(C*H*$_3$)$_3$,18 H), 3.64 (s, C*H*$_2$, 4 H), 3.93 (s, C*H*$_2$, 2 H), 6.63 (t, py-C^4*H*,1 H, J = 4.8 Hz), 7.14 (t, py-C^5*H*, 1 H, J = 4.8 Hz), 7.31 (d, C^{2,6}*H*, 4 H, J = 8 Hz), 7.43 (d, C^{3,5}*H*, 4 H, J = 8 Hz), 7.55 (d, py-C^3*H*, 1 H, J = 8 Hz), 8.48 (d, py-C^6*H*, 1 H, J = 5 Hz). ^{13}C{^{1}H} NMR (C_6D_6, 100 MHz): δ 31.89 (C(*C*H$_3$)$_3$), 34.81 (*C*(CH$_3$)$_3$), 58.41 (*C*H$_2$), 60.21 (*C*H$_2$), 122.05 (py-*C*^{5}H),

122.97 (py-C^3H), 125.82 (C^3H), 129.19 (C^2H), 136.22 (py-C^4H), 137.24 (C^1), 149.62 (py-C^6H), 150.07 (C^4), 161.29 (py-C^2).

2. *N*-(4-*tert*-butylbenzyl)-1-(pyridine-2-yl)-*N*-(pyridine-2-ylmethyl)methanamine ($HArpy_2N$). To a 0 ºC biphasic solution of di-(2-picolyl)amine (5.000 g, 25.10 mmol) in 100 mL CH_2Cl_2 and 4-*tert*-butylbenzyl bromide (5.700 g, 25.10 mmol) in 40 mL H_2O was slowly added a solution of NaOH (1.004 g, 25.10 mmol) in 10 mL H_2O. The canary yellow biphasic reaction mixture was slowly warmed to 23 ºC, while stirring vigorously, and monitored by pH. When the reaction mixture was neutral, the product was extracted from the aqueous layer with CH_2Cl_2 (4 x 15mL). Organic layers were combined, dried over $MgSO_4$, and filtered. Rotary evaporation of the filtrate yielded an orange-yellow oil. After the addition of hexanes, a brown impurity was filtered. The hexanes filtrate was concentrated, cooled, and yielded yellow crystals of **$HArpy_2N$** (6.499 g, 75 %). ^{1}H NMR (C_6D_6, 400 MHz): δ 1.23 (s, C(CH_1)$_3$, 9 H), 3.69 (s, CH_2, 2 H), 3.97 (s, CH_2, 4 H), 6.63 (t, py-C^4*H*, 2 H, J = 5.6 Hz), 7.13 (t, py-C^5*H*, 2 H, J = 7.6 Hz), 7.29 (d, C^{2,6}*H*, 2 H, J = 8 Hz), 7.42 (d, C^{3,5}*H*, 2 H, J = 8 Hz), 7.50 (d, py-C^3*H*, 2 H, J = 7.9 Hz), 8.48 (d, py-C^6*H*, 2 H, J = 4.6 Hz). ^{13}C{^{1}H} NMR (C_6D_6, 100 MHz): δ 31.86 (C(CH$_3$)$_3$), 34.80 (C(CH$_3$)$_3$), 58.56 (CH$_2$), 60.48 (CH$_2$), 122.10 (py-C^5H), 123.11 (py-C^3H), 125.81 (C^3H), 129.27 (C^2H), 136.21 (py-C^4H), 137.06 (C^1), 149.75 (py-C^6H), 150.09 (C^4), 160.91 (py-C^2).

3. *N*,*N*-bis(2-bromo-4-*tert*-butylbenzyl)-1-(pyridine-2-yl)methanamine ($BrAr_2pyN$). To a 0 ºC biphasic solution of 2-(aminomethyl)pyridine (1.000 g, 9.25 mmol) in 10 mL H_2O and 2-bromo-4-*tert*-butylbenzyl bromide (5.660 g, 18.50 mmol) in 60 mL CH_2Cl_2 was slowly added a solution of NaOH (0.740 g, 18.50 mmol) in 10 mL H_2O. The biphasic reaction mixture was slowly warmed to 23 ºC, while stirring vigorously, and turned red within 2 h. The organic layer became orange upon

complete conversion to product. The product was extracted from the aqueous layer with CH_2Cl_2 (3 x 15mL). Organic layers were combined, dried over Na_2SO_4, and filtered. Rotary evaporation of the filtrate yielded an orange oil. After the addition of hexanes, a brown impurity was filtered. The hexanes filtrate was concentrated and cooled to form orange-yellow crystals of **$BrAr_2pyN$** (16.16 g, 62 %). ^1H NMR (C_6D_6, 400 MHz): δ 1.06 (s, $C(CH_3)_3$, 18 H), 3.96 (s, CH_2, 6 H), 6.59 (t, py-C^4H, 1 H, J = 5.8 Hz), 7.06 (t, py-C^5H, 1 H, J = 7.6 Hz), 7.10 (d, C^4H, 2H, J = 8 Hz), 7.33 (d, py-C^3H, 1 H, J = 8 Hz), 7.62 (s, C^6H, 2 H), 7.76 (d, C^3H, 2 H, J = 8 Hz), 8.48 (d, py-C^6H, 1 H, J = 5.6 Hz). $^{13}C\{^1H\}$ NMR (C_6D_6, 100 MHz): δ 31.46 ($C(CH_3)_3$), 34.73 ($C(CH_3)_3$), 58.53 (CH_2), 60.60 (CH_2), 122.17 (py-C^5H), 123.19 (py-C^3H), 125.08 (C^1), 125.15 (C^4H), 130.43 (C^6H), 130.78 (C^3H), 136.18 (py-C^4H), 136.35 (C^2), 149.86 (py-C^6H), 152.23 (C^5), 160.26 (py-C^2). MS: m/z (%) 464, 466, 468 (58), 331, 333 (36), 225, 227 (50), 93 (100), M^+ not observed.

4. *N*-(2-bromo-4-*tert*-butylbenzyl)-1-(pyridine-2-yl)-*N*-(pyridine-2-ylmethyl)methanamine ($BrArpy_2N$). To a 0 ºC biphasic solution of di-(2-picolyl)amine (10.000 g, 50.19 mmol) in 100 mL CH_2Cl_2 and 2-bromo-4-*tert*-butylbenzylbromide (15.36 g, 50.19 mmol) in 50 mL H_2O was slowly added a solution of NaOH (2.01 g, 50.25 mmol) in 20 mL H_2O. The orange biphasic reaction mixture was slowly warmed to 23 ºC, while stirring vigorously, and monitored by pH. When the reaction mixture was neutral, the product was extracted from the aqueous layer with CH_2Cl_2. Organic layers were combined, dried over $MgSO_4$, and filtered. Rotary evaporation of the filtrate yielded tan-yellow solid. After hot filtration of the solid in hexanes, tan-yellow crystals were isolated from the filtrate as pure **$BrArpy_2N$** (15.713 g, 74 %). ^1H NMR (C_6D_6, 400 MHz): δ 1.06 (s, $C(CH_3)_3$, 9 H), 3.98 (s, CH_2, 6 H), 6.60 (t, py-C^4H, 2 H, J = 8 Hz), 7.10 (t, py-C^5H, C^4H, 3 H, J = 8 Hz), 7.45 (d, py-C^3H, 2 H, J = 7.8 Hz), 7.63 (s, C^6H, 1 H), 7.78 (d, C^3H, 1 H, J = 8 Hz), 8.47 (d, py-C^6H, 2

H, J = 4.6 Hz). $^{13}C\{^{1}H\}$ NMR (C_6D_6, 100 MHz): δ 31.47 ($C(CH_3)_3$), 34.73 ($C(CH_3)_3$), 58.62 (CH_2), 60.52 (CH_2), 122.16 (py-C^5H), 123.37 (py-C^3H), 125.07 (C^1), 125.25 (C^4H), 130.43 (C^6H), 131.18 (C^3H), 136.20 (py-C^4H), 136.50 (C^2), 149.79 (py-C^6H), 152.21 (C^5), 160.43 (py-C^2).

5. {κ-C,N,N^{py}-(2-pyridylmethyl)N(CH$_2$(4-^{t}Bu-phenyl-2-yl))(CH$_2$(4-^{t}Bu-phenyl-2-Br))}NiBr (1-Ni). To a 100 mL round bottom flask charged with $Ni(COD)_2$ (1.000 g, 3.64 mmol) and **BrAr$_2$pyN** (2.030 g, 3.64 mmol) was vacuum transferred 60 mL THF at -78 ºC. After slowly warming to 23 ºC, the reaction mixture was stirred for 1 h and filtered. The filtrate was concentrated, cooled to -78 ºC, and filtered to yield 2.150 g **1-Ni** as a crystalline orange solid (96 %). ^1H NMR (C_6D_6, 400 MHz): δ 0.88 (s, $C(CH_3)_3$, 9 H), 1.47 (s, $C(CH_3)_3$, 9 H), 3.38 (d, CH_2, 1 H, J = 14.4 Hz), 3.43 (d, CH_2, 1 H, J = 16 Hz), 3.49 (d, CH_2, 1 H, J = 13.2 Hz), 4.15 (d, CH_2, 2 H, J = 13.2 Hz), 5.18 (d, CH_2, 1 H, J = 14 Hz), 6.03 (t, py-C^4H, 1 H, J = 6 Hz), 6.23 (d, 1 H, J = 7.6 Hz), 6.49 (t, py-C^5H, 1 H, J = 7.6 Hz), 6.69 (d, C^4H, 1 H, J = 7.6 Hz), 6.97 (s, C^6H, 1 H), 7.04 (t, $C^{3,4}H$, 2 H, J = 7.6 Hz), 8.58 (s, C^6H, 1 H), 8.82 (d, py-C^6H, 1 H, J = 4.8 Hz), 10.13 (d, C^3H, 1 H, J = 8 Hz). $^{13}C\{^{1}H\}$ NMR (C_6D_6, 100 MHz): δ 31.04 ($C(CH_3)_3$), 32.40 ($C(CH_3)_3$), 34.72 ($C(CH_3)_3$), 35.40 ($C(CH_3)_3$), 63.67 (CH_2), 64.93 (CH_2), 70.92 (CH_2), 119.45 (C^6H), 120.95 (C^1), 121.90 (py-C^5H), 122.33 (py-C^3H), 125.35 (C^6H), 125.99 (C^4H), 129.20 (C^3H), 131.46 (C^3H), 136.12 (C^4H), 136.59 (C^2), 140.30 (py-C^4H). 141.96 (C^2), 147.91(C^5), 148.71(C^5), 150.42 (py-C^6H), 153.84 (py-C^2), 160.90 (C^1). Anal. Calcd. $H_{28}C_{34}N_2Br_2Ni$: C, 54.50; H, 5.55; N, 4.54. Found: C, 54.65, 54.71; H, 5.64, 5.64; N, 4.03, 4.07.

6. 2,10-di-*tert*-butyl-6-(pyridine-2-ylmethyl)-6,7-dihydro-5*H*-dibenzo[c,e]azepine (Coupled BrAr$_2$pyN). To a 50 mL round bottom flask charged with **1-Ni** (0.350 g, 0.57 mmol) and 0.95 % sodium amalgam (0.026 g Na, 1.13 mmol) was vacuum transferred 25 mL THF at -78 ºC. Upon warming to 23 ºC and stirring for

30 min, the orange reaction mixture turned orange-brown. After stirring at 23 ºC for 7 h, volatiles were removed *in vacuo* leaving a brown solid (0.164 g, 73 %). ^{1}H NMR (C_6D_6, 400 MHz): δ 1.30 (s, C(CH_3)$_3$, 18 H), 3.51 (s, CH_2, 4 H), 3.98 (s, CH_2, 2 H), 6.71 (t, py-C^4*H*, 1 H, J = 5.5 Hz), 7.19 (t, py-C^5*H*, 1 H, J = 7.3 Hz), 7.30 (s, C^{5,6}*H*, 4 H), 7.60 (d, py-C^3*H*, 1 H, J = 7.8 Hz), 7.71 (s, C^3*H*, 2 H), 8.57 (d, py-C^6*H*, 1 H, J = 4 Hz). ^{13}C{^{1}H} NMR (C_6D_6, 125 MHz): δ 31.03 (C(*C*H$_3$)$_3$), 35.07 (*C*(CH$_3$)$_3$), 55.55 (*C*H$_2$), 61.85 (*C*H$_2$), 122.22 (py-*C*^{5}H), 123.65 (py-*C*^{3}H), 125.16 (*C*^{5}H), 125.28 (*C*^{3}H), 130.55 (*C*^{6}H), 133.21 (*C*^{1}), 136.41 (py-*C*^{4}H), 142.32 (*C*^{2}), 149.75 (py-*C*^{6}H), 151.27 (*C*^{4}), 161.30 (py-*C*^{2}). MS: m/z (%) 306 (100), 93 (30), 57 (15), M$^+$ not observed.

7. {κ-C,N,N$^{py}_2$-(2-pyridylmethyl)$_2$N(CH$_2$(4-^{t}Bu-phenyl-2-yl))}NiBr (2-Ni). To a 100 mL round bottom flask charged with Ni(COD)$_2$ (0.324 g, 1.18 mmol) and **BrArpy$_2$N** (0.500 g, 1.18 mmol) was vacuum transferred 50 mL benzene. The red-orange reaction mixture was stirred at 23 ºC for 24 h while orange needles precipitated from solution. The reaction was filtered to yield microcrystalline orange needles of **2-Ni** (0.380 g, 67 %). ^{1}H NMR (THF-d_8, 400 MHz): δ 1.27 (s, C(CH_3)$_3$, 9 H), 4.39 (d, CH_2, 2 H, J = 13.8 Hz), 4.45 (s, CH_2, 2 H), 4.87 (d, CH_2, 2 H, J = 13.9 Hz), 6.76 (d, C^4*H*, 1 H, J = 7.7 Hz), 6.82 (d, C^3*H*, 1 H, J = 7.3 Hz), 7.07 (t, py-C^4*H*, 2 H, J = 6.6 Hz), 7.63 (t, py-C^5*H*, 2 H, J = 7.8 Hz), 7.86 (d, py-C^3*H*, 2 H, J = 7.5 Hz), 8.34 (s, C^6*H*, 1 H), 8.57 (d, py-C^6*H*, 2 H, J = 4.7 Hz). ^{13}C{^{1}H} NMR (THF-d_8, 100 MHz): δ 32.34 (C(*C*H$_3$)$_3$), 64.17 (*C*H$_2$), 69.75 (*C*H$_2$), 121.34 (*C*^{3}H), 122.16 (py-*C*^{5}H), 124.02 (py-*C*^{3}H), 125.26 (*C*^{5}), 138.01 (py-*C*^{4}H), 141.01(*C*^{4}H), 150.40 (py-*C*^{6}H), 158.63 (*C*^{1}). Anal. Calcd. $H_{26}C_{23}N_3BrNi$: C, 57.19; H, 5.42; N, 8.70. Found: C, 56.43, 56.26; H, 5.26, 5.20; N, 8.45, 8.33.

8. *N*,*N*'-(5,5'-di-*tert*-butylbiphenyl-2,2'-diyl)bis(methylene)bis(1-pyridin-2-yl)-*N*-(pyridine-2-ylmethyl)methanamine) (Coupled BrArpy$_2$N). Thermolysis of **2-Ni** in pentane at 85 ºC for 2 d led to the formation of coupled ligand and presumably

$NiBr_2$ and Ni^0. ^1H NMR (C_6D_6, 400 MHz): δ 1.22 (s, $C(CH_3)_3$, 9 H), 3.70 (s, CH_2, 2 H), 3.97 (s, CH_2, 2 H), 6.62 (t, py-C^4H, 2 H, J = 5.8 Hz), 7.11 (t, py-C^5H, 2 H, J = 7.3 Hz), 7.36 (s, C^3H, 1 H), 7.43 (d, $C^{5,6}H$, 2 H, J = 8.1 Hz), 7.51 (d, py-C^3H, 2 H, J = 7.7 Hz), 8.52 (d, py-C^6H, 2 H, J = 4 Hz). $^{13}C\{^1H\}$ NMR (C_6D_6, 125 MHz): δ 31.87 ($C(CH_3)_3$), 35.00 ($C(CH_3)_3$), 58.54 (CH_2), 60.44 (CH_2), 122.07 (py-C^5H), 122.15 (py-C^3H), 123.29 (C^5H), 124.76 (C^3H), 125.80 (C^6H), 136.23 (py-C^4H), 137.18 (C^1), 149.69 (C^2), 149.76 (py-C^6H), 149.90 (C^4), 157.93 (py-C^2).

9. {κ-C,N,N^{py}_2-(2-pyridylmethyl)$_2$N(CH$_2$(4-^{t}Bu-phenyl-2-yl))}FeBr (2-Fe). **A)** To a 25 mL round bottom flask charged with $Fe\{N(SiMe_3)_2\}_2(THF)$ (0.250 g, 0.56 mmol) and **BrArpy$_2$N** (0.473 g, 1.11 mmol) was vacuum transferred 10 mL Et_2O at -78 °C. The dark green reaction mixture was slowly warmed to 23 °C. The reaction stirred for 14 h prior to removing all volatiles and triturating with pentane. The green solid was taken up in benzene and filtered through a Celite plug. Red, rod-shaped crystals of **2-Fe** were obtained in 16 % yield (0.043 g). **B)** To a 100 mL round bottom flask containing **3-Fe** (0.900 g, 1.41 mmol) and 0.95 % sodium amalgam (0.066 g Na, 2.88 mmol) was vacuum transferred 50 mL THF at -78 °C. The reaction mixture became red after it was stirred at 23 °C for 2 h. Volatiles were removed *in vacuo* yielding an orange-red solid. The solid was dissolved in THF and filtered through Celite. The filtrates were concentrated to yield **2-Fe** as an orange powder (0.617 g, 91 %). ^1H NMR (THF-d_8, 400 MHz): δ -37.15 ($\upsilon_{1/2} \approx 26$ Hz, 1 H), -11.47 ($\upsilon_{1/2} \approx 29$ Hz, 1 H), 0.45 ($\upsilon_{1/2} \approx 15$ Hz, 1 H), 5.75 ($\upsilon_{1/2} \approx 49$ Hz, 1 H), 6.35 ($\upsilon_{1/2} \approx 40$ Hz, 1 H), 10.96 ($\upsilon_{1/2} \approx 22$ Hz, $C(CH_3)_3$, 9 H), 33.52 ($\upsilon_{1/2} \approx 462$ Hz, 1 H), 41.68 ($\upsilon_{1/2} \approx 45$ Hz, 1 H), 51.45 ($\upsilon_{1/2} \approx 71$ Hz, 1 H), 51.61 ($\upsilon_{1/2} \approx 44$ Hz, 1 H), 57.56 ($\upsilon_{1/2} \approx 67$ Hz, 1 H), 63.61 ($\upsilon_{1/2} \approx 174$ Hz, 1 H), 67.96 ($\upsilon_{1/2} \approx 215$ Hz, 1 H), 81.49 ($\upsilon_{1/2} \approx 351$ Hz, 1 H), 86.69 ($\upsilon_{1/2} \approx 397$ Hz, 1 H), 103.50 ($\upsilon_{1/2} \approx 52$ Hz, 1 H), 117.53 ($\upsilon_{1/2} \approx 536$ Hz, 1 H), 128.64 ($\upsilon_{1/2} \approx$

464 Hz, 1 H). Anal. Calcd. $H_{26}C_{23}N_3BrFe$: C, 57.52; H, 5.46; N, 8.75. Found: C, 58.17, 58.03; H, 5.61, 5.46; N, 8.42, 8.42. μ_{eff} (SQUID, 293K) = 5.28 μ_B.

10. {κ-N,N$^{py}_2$-(2-pyridylmethyl)$_2$N(CH$_2$(4-^{t}Bu-phenyl-2-Br))}FeBr$_2$ (3-Fe). To a 25 mL round bottom flask containing $FeBr_2$ (0.127 g, 0.59 mmol) and **BrArpy$_2$N** (0.250 g, 0.59 mmol) was vacuum transferred 10 mL THF at -78 °C. The yellow suspension was warmed to 23 °C and darkened to orange-yellow after 1 h. The reaction mixture was stirred for 6 h and the volatiles were removed. The yellow solid was taken up in Et_2O, filtered and washed to yield **3-Fe** (0.365 g, 97 %) . ^{1}H NMR (CD_2Cl_2, 400 MHz): δ 0.84 ($\upsilon_{1/2} \approx 9$ Hz, C(C*H*$_3$)$_3$,9 H), 1.36 ($\upsilon_{1/2} \approx 37$ Hz, C*H*$_2$,2 H), 5.54 ($\upsilon_{1/2} \approx 39$ Hz, C*H*, 1 H), 6.21 ($\upsilon_{1/2} \approx 24$ Hz, C*H*, 1 H), 23.96 ($\upsilon_{1/2} \approx 425$ Hz, C*H*, 1 H), 27.18 ($\upsilon_{1/2} \approx 432$ Hz, py-C*H*, 2 H), 50.48 ($\upsilon_{1/2} \approx 51$ Hz, C*H*$_2$, 2 H), 55.80 ($\upsilon_{1/2} \approx 44$ Hz, C*H*$_2$, 2 H), 102.43 ($\upsilon_{1/2} \approx 417$ Hz, py-C*H*, 2 H), 105.92 ($\upsilon_{1/2} \approx 231$ Hz, py-C*H*, 2 H), 116.06 ($\upsilon_{1/2} \approx 461$ Hz, py-C*H*, 2 H). Anal. Calcd. $H_{26}C_{23}N_3Br_3Fe$: C, 43.16; H, 4.09; N, 6.57. Found: C, 43.18, 42.95 H, 4.23, 4.05; N, 6.43, 6.37. μ_{eff} (Gouy balance, 295K) = 4.5 μ_B.

11. Cr{N(TMS)$_2$}$_2$(THF)$_2$. A modified literature synthesis was used.[34] To a 250 mL round bottom flask charged with $CrCl_2$(THF) (5.325 g, 27.31 mmol) and sodium hexamethydisilazide (10.000 g, 54.53 mmol) was vacuum transferred 150 mL THF at -78 °C. The reaction mixture immediately became deep indigo and was slowly warmed to 23 °C. After stirring at 23 °C for 12 h, the reaction was filtered, yielding a lavender filtrate and a green filter cake that was washed with THF. The filtrates were concentrated, cooled to -78 °C, and filtered to yield 10.050 g of Cr{N(TMS)$_2$}$_2$(THF)$_2$ as a crystalline lavender solid (71 %).

12. {κ-N,N$^{py}_2$-(1,3-dipyridyl-2-azaallyl}CrN(TMS)$_2$ ((smif)CrN(TMS)$_2$, 4-Cr). A) To a 25 mL round bottom flask containing Cr{N(SiMe$_3$)$_2$}$_2$(THF)$_2$ (0.250 g, 0.48 mmol) and **BrArpy$_2$N** (0.206 g, 0.48 mmol) was vacuum transferred 15 mL Et_2O

at -78 °C. The reaction mixture immediately turned green and was slowly warmed to 23 °C. After stirring at 23 °C for 1 d, the volatiles were removed *in vacuo*. The green solid was filtered in pentane to yield (smif)CrN($SiMe_3$)$_2$ as a green solid (0.103 g, 52 %). **B)** A solution of smifH (0.153 g, 0.78 mmol) in 10 mL Et_2O was added dropwise to a stirred solution of Cr{N($SiMe_3$)$_2$}$_2$(THF)$_2$ (0.400 g, 0.77 mmol) in Et_2O (10 mL) at 23 °C. The solution became emerald green. The reaction was degassed and allowed to stir for 12 h at 23 °C while green crystals precipitated from solution. The suspension was concentrated, filtered, and washed with cold Et_2O to isolate 0.237 g **4-Cr** as green crystals (74 %). ^{1}H NMR (C_6D_6, 400 MHz): δ -78.71 ($\upsilon_{1/2} \approx$ 2000 Hz, py-C*H*,1 H), -74.23 ($\upsilon_{1/2} \approx$ 300 Hz, C*H*, 1 H), -37.81 ($\upsilon_{1/2} \approx$ 520 Hz, py-C*H*, 1 H), -18.60 ($\upsilon_{1/2} \approx$ 580Hz, py-C*H*,1 H), 23.28 ($\upsilon_{1/2} \approx$ 500 Hz, py-C*H*, 1 H), 57.60 ($\upsilon_{1/2} \approx$ 5800 Hz, Si(C*H*$_3$)$_3$, 9 H). UV-vis (benzene) = 396 nm (ε ~ 27,000 M^{-1} cm^{-1}), 424 nm (sh, ε ~ 12,500 M^{-1} cm^{-1}), 461 nm (ε ~ 9,500 M^{-1} cm^{-1}), 581 nm (ε ~ 17,000 M^{-1} cm^{-1}), 627 nm (ε ~ 19,000 M^{-1} cm^{-1}), 675 nm (ε ~ 15,000 M^{-1} cm^{-1}). Anal. Calcd. $H_{28}C_{18}N_4Si_2Cr$: C, 52.91; H, 6.91; N, 13.71. Found: C, 51.90; H, 6.78; N, 14.02. μ_{eff} (SQUID, 293K) = 4.7 μ_B.

Magnetic Susceptibility Measurements. Magnetic susceptibility measurements of crystalline powdered samples (10-30 mg) were performed on a Quantum Design MPMS-5 SQUID magnetometer at 10 kOe between 5 and 300 K for all samples. All sample preparations and manipulations were performed under an inert atmosphere to due to the air sensitivity of the samples. The samples were either measured in a flame sealed NMR tube or a custom machine sealed Teflon capsule. The diamagnetic contribution from the sample container was subtracted from the experimental data. Pascal's constants[38] were used to subtract diamagnetic contributions, yielding paramagnetic susceptibilities.

Single Crystal X-Ray Diffraction Studies. Upon isolation, the crystals were covered in polyisobutenes and placed under a 173 K N_2 stream on the goniometer head of a Siemens P4 SMART CCD area detector (graphite-monochromated MoK_α radiation, $\lambda = 0.71073$ Å). The structures were solved by direct methods (SHELXS). All non-hydrogen atoms were refined anisotropically unless stated, and hydrogen atoms were treated as idealized contributions (Riding model).

13. 2-Fe. A red rod (0.20 x 0.03 x 0.03 mm) was obtained from toluene. A total of 15,951 reflections were collected with 3,192 determined to be symmetry independent ($R_{int} = 0.1178$), and 1,896 were greater than $2\sigma(I)$. A semi-empirical absorption correction from equivalents was applied, and the refinement utilized $w^{-1} = \sigma^2(F_o^2) + (0.0499p)^2 + 0.0000p$, where $p = ((F_o^2 + 2F_c^2)/3)$.

14. 4-Cr. A dark green hexagonal block (0.40 x 0.30 x 0.20 mm) was obtained from pentane. A total of 7,678 reflections were collected with 7,678 determined to be symmetry independent ($R_{int} = 0.0000$), and 5,121 were greater than $2\sigma(I)$. A semi-empirical absorption correction from equivalents was applied, and the refinement utilized $w^{-1} = \sigma^2(F_o^2) + (0.0400p)^2 + 0.0000p$, where $p = ((F_o^2 + 2F_c^2)/3)$.

REFERENCES

1 Samojłowicz, C.; Bieniek, M.; Grela, K. *Chem. Rev.* **2009**, *109*, 3708-3742.

2 Alcaide, B.; Almendros, P.; Luna, A. *Chem. Rev.* **2009**, *109*, 3817-3858.

3 Vougioukalakis, G. C.; Grubbs, R. H. *Chem. Rev.* **2010**, *110*, 1746-1787.

4 Miyaura, N.; Yamada, K.; Suzuki, A. *Tetrahedron Lett.* **1979**, *20*, 3437-3440.

5 Barder, T. E.; Walker, S. D.; Martinelli, J. R.; Buchwald, S. L. *J. Am. Chem. Soc.* **2005**, *127*, 4685-4696.

6 Beletskaya, I. P.; Cheprakov, A. V. *Chem. Rev.* **2000**, *100*, 3009-3066.

7 Ozawa, F.; Kubo, A.; Hayashi, T. *Selectivity in Catalysis.* **1993**, *517*, 75-85.

8 Hagiwara, H.; Sugawara, Y.; Hoshi, T.; Suzuki, T. *Chem. Commun.* **2005**, 2942-2944.

9 Chincilla, R.; Nájera, C. *Chem. Rev.* **2007**, *107*, 874-922.

10 Louie, J.; Hartwig, J. F. *Tetrahedron Lett.* **1995**, *36*, 3609-3612.

11 Guram, A. S.; Rennels, R. A.; Buchwald, S. L. *Angew. Chem. Int. Ed. Engl.* **1995**, *34*, 1348-1350.

12 Christensen, H.; Kiil, S.; Dam-Johansen, K.; Nielsen, O.; Sommer, M. B. *Org. Process Res. Dev.* **2006**, *10*, 762-769.

13 Sherry, B. D.; Fürstner, A. *Acc. Chem. Res.* **2008**, *41*, 1500-1511.

14 Buchwald, S. L.; Bolm, C. *Angew. Chem. Int. Ed.* **2009**, *48*, 5586-5587.

15 De Angelis, F.; Jin, N.; Car, R.; Groves, J. T. *Inorg. Chem.* **2006**, *45*, 4268-4276.

16 Bower, B. K.; Tennent, H. G. *J. Am. Chem. Soc.* **1972**, *94*, 2512-2513.

17 Dimitrov, V.; Linden, A. *Angew. Chem. Int. Ed.* **2003**, *42*, 2631-2633.

18 Carnes, M.; Buccella, D.; Chen, J. Y.-C.; Ramirez, A. P.; Turro, N. J.; Nuckolls, C.; Steigerwald, M. *Angew. Chem. Int. Ed.* **2009**, *48*, 290-294.

19 Figgis, B. N.; Hitchman, M. A. *Ligand Field Theory and Its Applications*; Wiley-VCH: New York, 2000.

20 Albrecht, M. *Chem. Rev.* **2010**, *110*, 576-623.

21 Volpe, E. C.; Chadeayne, A. R.; Wolczanski, P. T.; Lobkovsky, E. B. *J. Organomet. Chem.* **2007**, *692*, 4774-4783.

22 Collman, J. P.; Hegedus, L. S.; Norton, J. R.; Finke, R. G. *Principles and Applications of Organotransition Metal Chemistry*, University Science Books: Mill Valley, CA, 1987.

23 Crabtree, R. H. *The Organometallic Chemistr of Transition Metals*, 4th Ed.; John Wiley & Sons: New York, 2005.

24 Mallory, F. B.; Butler, K. E.; Berube, A.; Luzik, E. D.; Mallory, C. W.; Brondyke, E. J.; Hiremath, R.; Ngo, P.; Carroll, P. J. *Tetrahedron* **2001**, *57*, 3715-3724.

25 Schunn, R. A. *Inorg. Synth.* **1974**, *15*, 5-9.

26 Hassan, J.; Sévignon, M.; Gozzi, C.; Schulz, E.; Lemaire, M. *Chem. Rev.* **2002**, *102*, 1359-1469.

27 Terao, J.; Kambe, N. *Acc. Chem. Res.* **2008**, *41*, 1545-1554.

28 Kavaliunas, A. V.; Taylor, A.; Rieke, R. D. *Organometallics* **1983**, *2*, 377-383.

29 Rathke, J. W.; Muetterties, E. L. *J. Am. Chem. Soc.* **1975**, *97*, 3272-3273.

30 DiMauro, P. T.; Wolczanski, P. T. *Organometallics* **1987**, *6*, 1947-1954.

31 (a) Olmstead, M. M.; Power, P. P.; Shoner, S. C. *Inorg. Chem.* **1991**, *30*, 2547-2551. (b) Andersen, R. A.; Faegri, K.; Green, J. C.; Haaland, A.; Lappert, M. F.; Leung, W. P.; Rypdal, K. *Inorg. Chem.* **1988**, *27*, 1782-1786.

32 Bradley, D. C.; Copperwaithe, R. G. *Inorg. Synth.* **1978**, *18*, 112-120.

33 Kern, R. J. *J. Inorg. Nucl. Chem.* **1962**, *24*, 1105-1109.

34 Bradley, D.C.; Hursthouse, M. B.; Newing, C. W.; Welch, A. J. *J. Chem. Soc., Chem. Commun.* **1972**, 567-568.

35 Incarvito, C.; Lam, M.; Rhatigan, B.; Rheingold, A. L.; Qin, C. J.; Gavrilova, A. L.; Bosnich, B. *J. Chem. Soc., Dalton Trans.* **2001**, 3478-3488.

36 Westerhausen, M.; Kneifel, A. N. *Inorg. Chem. Comm.* **2004**, *7*, 763-766.

37 (a) Evans, D. F. *J. Chem. Soc.* **1959**, 2003-2005. (b) Schubert, E. M. *J. Chem. Educ.* **1992**, *69*, 62.

38 Carlin, R. L. *Magnetochemistry*; Springer-Verlag: Berlin; New York, 1986.

CHAPTER 2

Synthesis, Characterization, and Redox Reactivity of $(smif)_2M$ Complexes (M = V, Cr, Mn, Fe, Co, Ni, Zn)*

Introduction

A variety of nitrogen-based tridentate chelating ligands have been explored over the years. Ligation of two tridentate chelates may result in either a *facial* or *meridional* coordination geometry about the metal center (Figure 2.1). Typically, the ligand geometry dictates the mode of coordination.

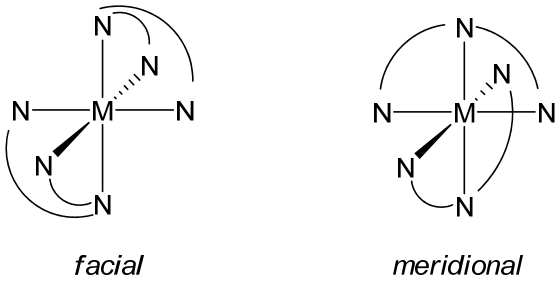

Figure 2.1. Coordination geometry for ligation of two tridentate N-based chelates.

Facial ligand coordination arises from non-planar molecules. One of the most common tridentate chelates is the scorpionate ligand, i.e. tris(pyrazolyl)hydroborate. This ligand and its various derivatives have been coordinated to a variety of metal centers, i.e. Mn,[1,2] Fe,[1,2] Co,[1,2,3] Ni,[1,2] Cu,[1,2] and Zn.[1,2] These scorpionate complexes are restricted to facial coordination when binding in a tridentate fashion due to the tetrahedral geometry about boron (Figure 2.2). Coordination of di-(2-picolyl)amine (**Hdpma**), as a neutral ligand, also results in *facial* coordination (Figure 2.2). Several cationic complexes have been prepared with Mn,[4] Fe,[5,6,7,8] Co,[7] Ni,[5,9] Cu,[10] and Zn.[4]

* Reproduced with permission from: Frazier, B. A.; Wolczanski, P. T.; Lobkovsky, E. B.; Cundari, T. R. *J. Am. Chem. Soc.* **2009**, *131*, 3428-3429. Copyright 2009 American Chemical Society.

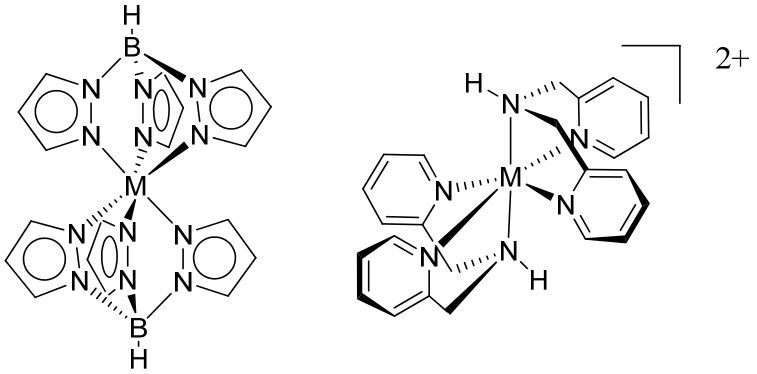

Figure 2.2. Examples of *fac* coordination metal complexes.

Planar organic molecules give rise to *meridional* coordination geometry and typically D_{2d} symmetry. Early work with N-based chelates focused on 2,2';6',2''-terpyridine, more commonly called terpy. Coordination of two molecules of terpy or its various derivatives around a metal center generally resulted in cationic species;[11-17] however, neutral examples exist for titanium[18] and vanadium[19] in which the metal center has a formal oxidation state of zero (Figure 2.3). Terpy metal complexes are of interest as they exhibit interesting optical and redox properties.[12,15]

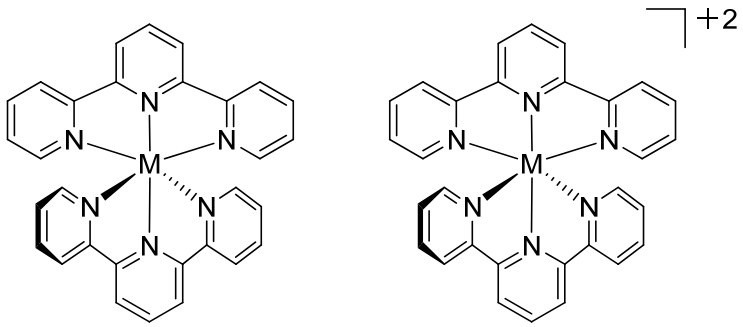

Figure 2.3. Terpy complexes.

Variations on terpy ligands exist, which are shown in Figure 2.4. Metal coordination complexes for these dipyridylimines[20-22] and pyridine diimines[20,22,24]

have also been well studied because these tridentate ligands are easier to prepare than terpy. These complexes are typically cationic; however, the (2-py)CH=NNH(2-py) ligand can be easily deprotonated, which results in the de-aromatization of the pyridine ring yielding an anionic chelate and a neutral metal complex as observed for iron and nickel.[22] Interestingly, only a couple of anionic N-based chelates exist that give rise to D_{2d} symmetry.

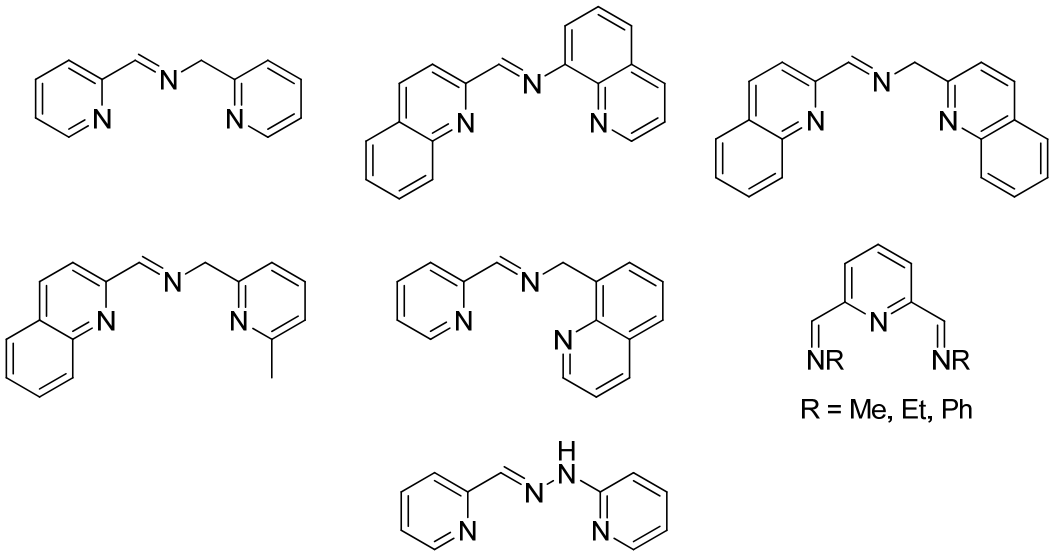

Figure 2.4. Examples of other tridentate N-based ligands.

Ligation of two bis(2-pyridylcarbonyl)aminate (bpca) ligands around a metal(II) center results in D_{2d} symmetry and a neutral complex (Figure 2.5). $(bpca)_2M$ complexes exist for Mn,[25] Fe,[26] Ni,[27] Cu,[27] and Zn.[27] Several M(III) species have been prepared, such that M = Cr,[28] Fe,[26,28] and Co.[28] These complexes possess interesting physical properties and are used as molecular building blocks for multi-nuclear chains due to their tridentate and bidentate modes for chelation. As shown in Figure 2.6, additional derivatives of bpca have also been ligated to metal centers.[29-32]

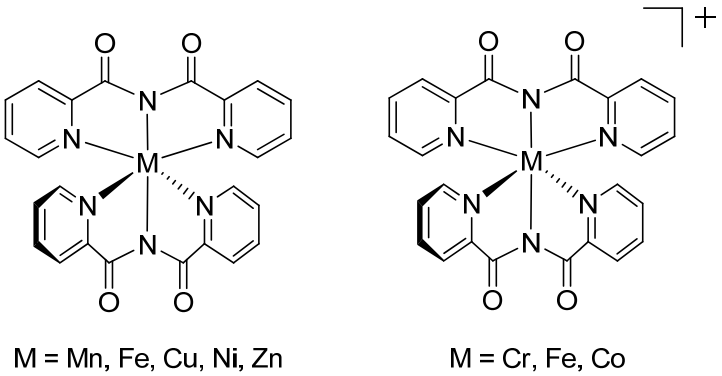

Figure 2.5. Examples of $(bpca)_2M$ complexes and $[(bpca)_2M]^+$ complexes.

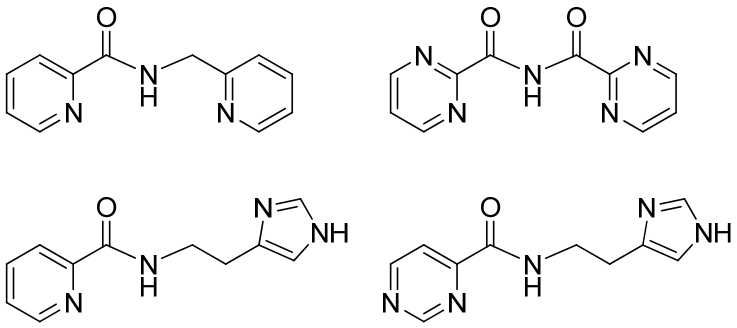

Figure 2.6. Variants of the bpca ligand.

The smif ligand, (2-py)CHNCH(2-py), which was described at the end of Chapter 1, was originally discovered in 2004 (Figure 2.7).[33] This mono-anionic tridentate N-based chelate was the degradation product resulting from heating a mixture of $ZnMe_2$ and di-(2-picolyl)amine.[33] Since the formation of $(smif)_2Zn$ was not the desired result, neither the complex nor the anionic ligand were further studied.

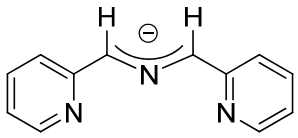

Figure 2.7. smif ligand ((2-py)CHNCH(2-py)).

As discussed in Chapter 1, the smif ligand exhibits unique optical properties and possesses the ability to stabilize complexes of low symmetry. Our research efforts focused on generating a homologous series of $(smif)_2M$ within the 1st-row in order to examine physical and optical properties while attempting to isolate complexes with formal electron counts ranging from 15 to 20.

Results and Discussion

Synthesis of ligands. Condensation of 2-pyridinecarboxaldehyde with 2-(aminomethyl)pyridine afforded 1,3-di-(2-pyridyl)-2-azapropene, **smifH**, in quantitative yield (eq 2.1).[34] The pale yellow liquid was moderately temperature, air, and moisture sensitive. ^{1}H NMR spectroscopy revealed the presence of only one isomer in solution.

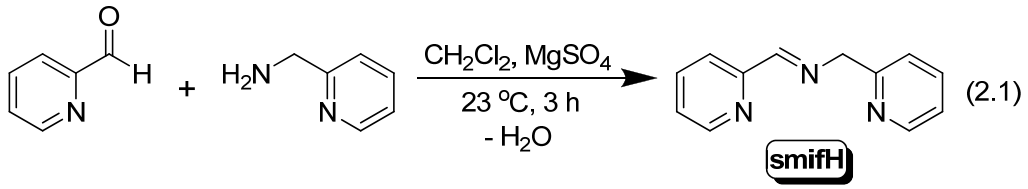

Deprotonation of the fairly acidic (pKa ~ 24) benzylic methylene group on **smifH** generated the delocalized, anionic 1,3-di-(2-pyridyl)-2-azaallyl ligand, smif. As shown in eq 2.2, treatment of lithium hexamethydisilazide (LiHMDS) with a solution of **smifH** in THF produced a deep magenta solution from which lithium 1,3-di-(2-pyridyl)-2-azapropenide (Li(smif), (**5-Li**)) was isolated as a metallic gold foamy solid in excellent yield (90 %). An identical synthesis utilizing sodium hexamethyldisilazide[35] (NaHMDS) afforded Na(smif) (**5-Na**) in 96 % yield, also as a foamy metallic gold solid. In solution, these compounds (**5-Li** and **5-Na**) displayed rather intense colors that were noticeably solvent-dependent; benzene solutions generated a deep royal purple color whereas THF yielded a deep magenta solution.

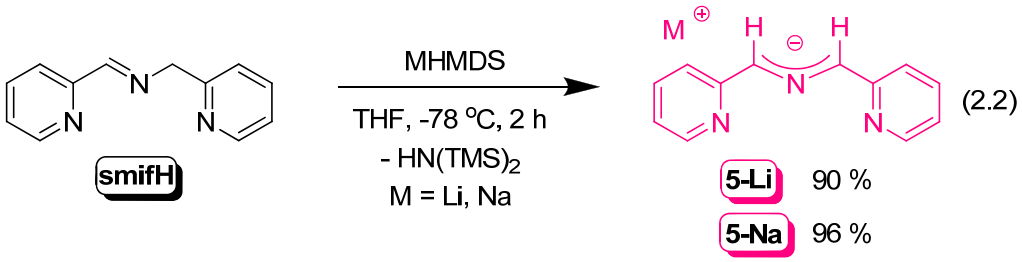

(2.2)

Synthesis of (smif)$_2$M Complexes [M = V, Cr, Mn, Fe, Co, Ni, Zn]. Efforts toward synthesizing (smif)$_2$M complexes featured a variety of 1st-row M(II) sources. The syntheses were accomplished via two major routes: utilization of an internal base and salt metathesis.

A. Deprotonation by an Internal Base. Initial efforts focused on deprotonating the acidic benzylic protons of **smifH** by using 1st-row transition metal complexes containing internal bases, e.g. amides. As shown in eq 2.3, exposing Fe{N(TMS)$_2$}$_2$(THF)[36] in Et$_2$O to two equivalents of **smifH** resulted in the formation of the 18 e$^-$ complex, (smif)$_2$Fe (**6-Fe**), with concomitant loss of HN(TMS)$_2$, therefore indicating that the hexamethyldisilazide groups acted as effective internal bases. Metallic purple-black crystals of **6-Fe** were isolated from an intensely colored, deep forest green solution in excellent yield (80 %). The ^{1}H NMR spectrum for **6-Fe** was diamagnetic and is consistent with a low spin (S = 0) ground state (GS). This suggested the smif ligand possessed strong field character. Only one smif ligand environment was observed via NMR spectroscopy, indicating D_{2d} symmetry that was confirmed by x-ray crystallographic studies.

Analogously, the synthesis of (smif)$_2$Cr (**6-Cr**) was achieved by treating Cr{N(TMS)$_2$}$_2$(THF)$_2$[37,38] in Et$_2$O with two equivalents of **smifH** (eq 2.3). The resulting dark forest green solution afforded dark forest green crystals of **6-Cr**, a 16 e$^-$ complex, in 79 % yield. The ^{1}H NMR spectrum was consistent with a paramagnetic

complex. D_{2d} symmetry was revealed by the presence of one smif ligand environment, in its ^{1}H NMR spectrum and an x-ray crystal structure.

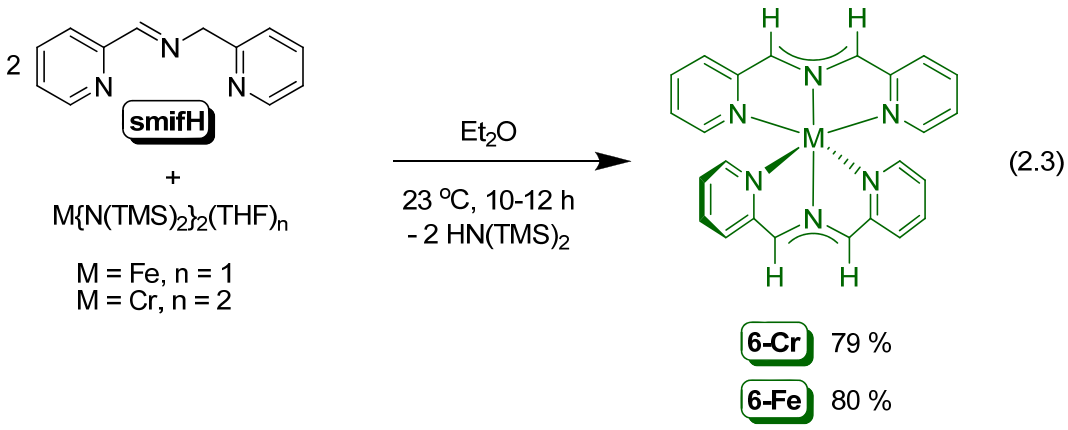

(2.3)

B. Salt Metathesis. Several 1st-row transition metal bis-amide complexes, i.e. $[Mn\{N(TMS)_2\}_2]_2$,[39] $Cr\{N(TMS)_2\}_2(THF)_2$,[37,38] $Fe\{N(TMS)_2\}_2(THF)$,[36] $[Co\{N(TMS)_2\}_2]_2$,[40] and $[Ni(NPh_2)_2]_2$,[41] are ideal starting materials because they are quite soluble and require simple work-up procedures. The byproducts, $HN(TMS)_2$ and $HNPh_2$, are readily washed away from the desired metal complexes. Since the starting amides require extra synthetic steps for their preparation and purification, a simple one-pot synthesis for preparing $(smif)_2M$ complexes was desired.

As depicted in Scheme 2.1, treatment of $MnCl_2$, $FeBr_2(THF)_2$,[42] $CoCl_2$, and $(DME)NiCl_2$[43] in THF with two equivalents of **5**-Li, generated *in situ*, yielded the corresponding $(smif)_2M$ complexes [M = Mn (**6-Mn**); Fe (**6-Fe**); Co (**6-Co**); Ni (**6-Ni**)], which were all crystallographically characterized. Intense purple solutions produced metallic gold crystals of **6-Mn** in 72 % yield. This 17 e$^-$ complex showed two broad paramagnetically shifted peaks in its ^{1}H NMR spectrum. **6-Fe** was obtained as metallic purple-black crystals in 52 %. Metallic gold crystals of **6-Co**, formally a 19 e$^-$ compound, were isolated from a deep purple-magenta solution in an excellent yield, 87 %. The ^{1}H NMR spectrum for **6-Co** was consistent with a paramagnetic compound

and revealed D_{2d} symmetry with the observation of only one smif environment. The 20 e^- compound, **6-Ni**, was collected as metallic gold crystals from a deep magenta solution in 67 % yield. **6-Ni** also possessed D_{2d} symmetry according to its ^{1}H NMR spectrum, which was consistent with a paramagnetic complex.

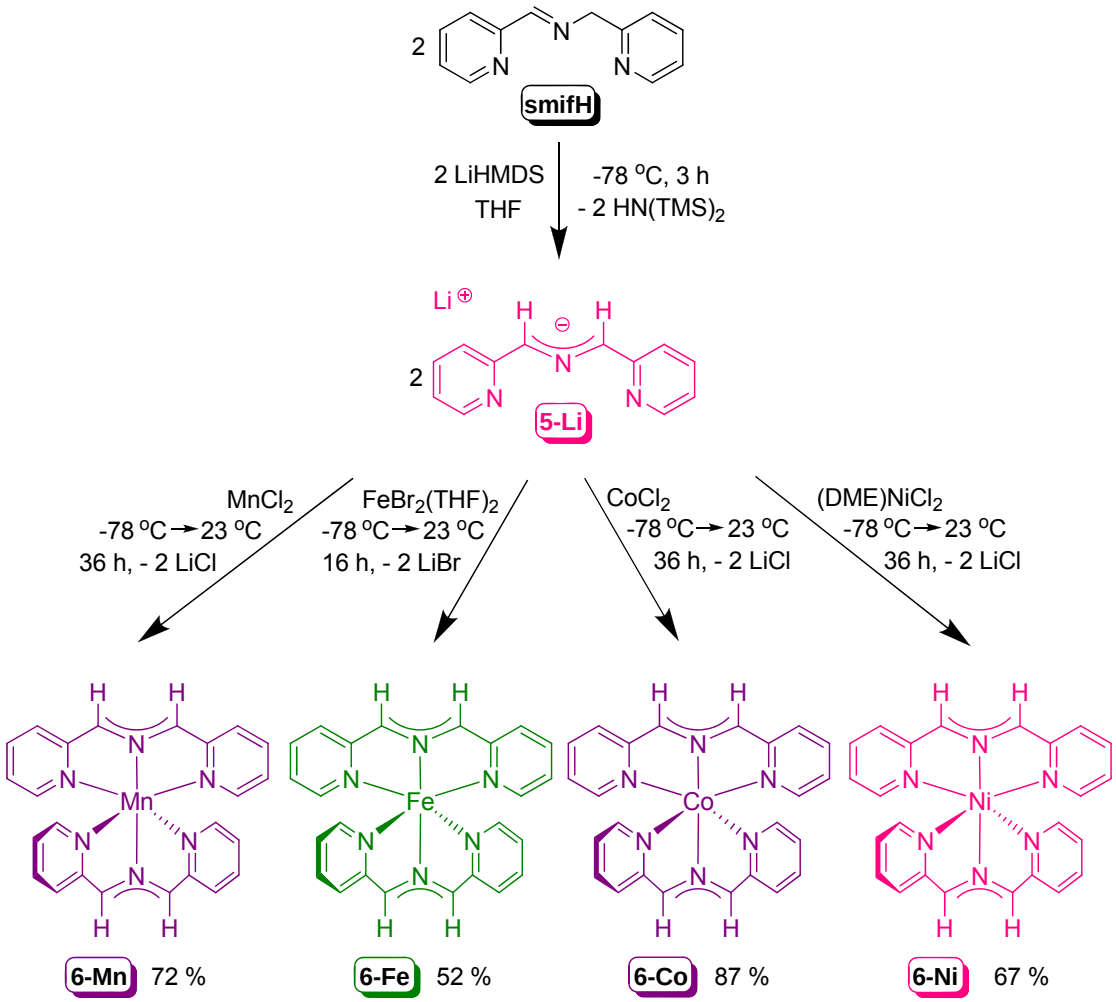

Scheme 2.1. Syntheses of $(smif)_2M$ complexes, where M = Mn, Fe, Co, and Ni, via salt metathesis.

Additionally, the salt metathesis of $ZnCl_2$ in THF with two equivalents of **5**-Li, generated *in situ*, produced an intense cherry red solution from which metallic gold crystals of $(smif)_2Zn$[33] (**6-Zn**) were isolated in 47 % yield (Scheme 2.2). Westerhausen

et al. observed the formation of **6-Zn** via a degradation associated with $ZnMe_2$ and di-(2-picolyl)amine.[33] Unfortunately, efforts to prepare $(smif)_2Cu$ from $CuBr_2$ led to an intractable mixture with physical properties that were vastly different than all other prepared $(smif)_2M$ complexes.

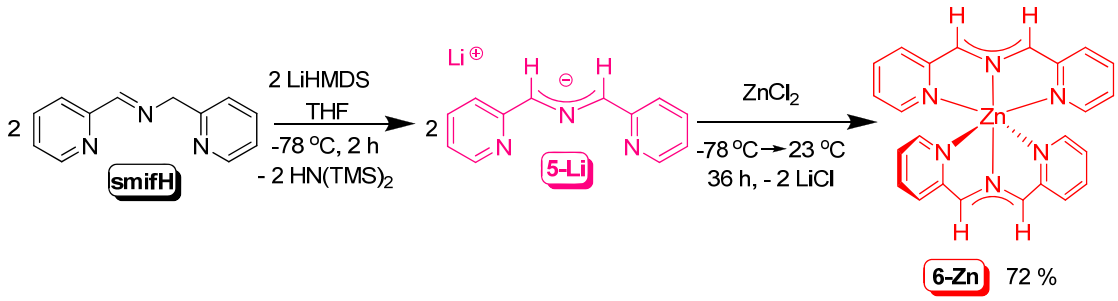

Scheme 2.2. Synthesis of $(smif)_2Zn$ via salt metathesis.

C. Salt Metathesis Under Reducing Conditions. Since vanadium(II) starting materials are not readily available, all attempts to synthesize $(smif)_2V$ required *in situ* reductions from higher valent vanadium sources. Initially, $VCl\{N(TMS)_2\}_2(THF)$[44] was a desirable starting material as the amides should deprotonate coordinated **smifH** ligands, thereby generating $[(smif)_2V]Cl$, which placed under reducing conditions should generate the desired $(smif)_2V$ complex. However, treatment of $VCl\{N(TMS)_2\}_2(THF)$ with either one or two equivalents of **smifH** in C_6D_6 generated an orange brown solution with a minute amount of red crystals, and revealed similar ^1H NMR spectra containing nine paramagnetic peaks. All scale-up attempts aimed toward isolating and characterizing the red crystals failed; therefore, an alternative route was sought. $(smif)_2V$ (**6-V**) was obtained in 81 % yield by treating $VCl_3(THF)_3$[45] in THF with two equivalents of **5**-Li, generated *in situ*, in the presence of one equivalent of sodium amalgam (Scheme 2.3). The deep cherry red solution afforded metallic gold crystals of **6-V**, formally a 15 e^- compound, which were NMR silent. The structure of **6-V** was confirmed via x-ray crystallographic studies.

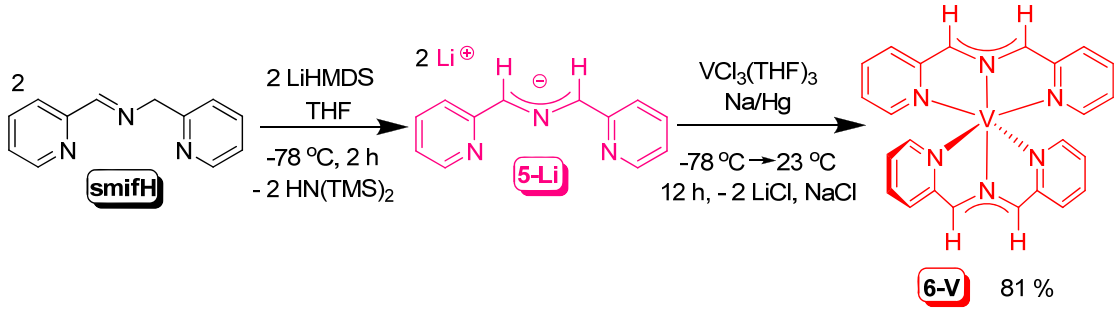

Scheme 2.3. Synthesis of $(smif)_2V$ via salt metathesis under reducing conditions.

Redox Chemistry and Electrochemical Studies of $(smif)_2M$ complexes [M = V, Cr, Mn, Fe, Co, and Ni]. The redox chemistry of $(smif)_2M$ complexes was investigated both electrochemically and synthetically. Collaborative research efforts enabled electrochemical studies on several $(smif)_2M$ complexes and Li(smif), **5**-Li, in hopes of understanding synthetic redox chemistry that was observed. All cyclic voltammograms (CV) were obtained using a 0.1 M $^tBu_4NPF_6$, TBAP, solution in THF at a Pt electrode, and stated reduction or oxidation potentials were referenced relative to Ag. The results are summarized in Table 2.1. Initial studies began by examining the electrochemistry of **5**-Li to help identify processes observed for $(smif)_2M$ complexes. Two reversible ligand reductions were observed for **5**-Li with potentials at -1.59 V and -1.94 V, denoted L when observed in metal complexes. An irreversible ligand oxidation occurred at 0.48 V, which resulted in the presence of a new irreversible reduction at -0.79 V.

The electrochemistry for $(smif)_2M^n$ complexes [n = 0, M = Cr, Mn, Fe, Co, Ni; n = +1, M = Co (**7-Co**)] was examined next. The CV for **6-Cr** showed four reversible processes with potentials at 0.13 V ($Cr^{II/III}$), -0.48 V ($Cr^{II/I}$), -1.55 V (L), and -1.87 V (L), thereby indicating the possibility to form both the anionic and cationic complexes of **6-Cr**. Two irreversible reductions, i.e. -1.03 V and -0.078 V, appeared as the result of other electrochemical processes at -1.87 V and 1.55 V, respectively. While two

reversible reductions were observed for **6-Mn** at -1.40 V and -1.60 V, an irreversible oxidation potential at 0.59 V for **6-Mn** led to the formation of three irreversible reductions with potentials at -0.034 V, -0.190 V, and -0.509 V. The CV for **6-Fe** revealed two reversible processes at 0.28 V ($Fe^{II/III}$) and -1.68 V (L) implying that **6-Fe** could be oxidized under the right conditions. Similar to that observed for **6-Cr**, the CV, shown in Figure 2.8, for **6-Co** displayed four reversible processes with potentials at 0.048 V ($Co^{II/III}$), -0.56 V, -1.00 V ($Co^{II/I}$), and -1.53 V (L), suggesting the possibility of generating both the cation and anion. The reversible reduction at -0.56 V was a result of the reduction at -1.53 V. An irreversible process was observed at 0.61 V. The CV corresponding to $[(smif)_2Co](OTf)$, **7-Co**, displayed five reversible processes at 1.14 V, -0.38 V ($Co^{III/II}$), -1.00 V ($Co^{II/I}$), -1.45 V ($Co^{I/0}$ or L), and -1.97 V (L), which were shifted towards cathodic potentials. Ideally, **6-Co** and **7-Co** should portray identical CVs. The last compound examined was **6-Ni**, which displayed only one reversible process with a potential at -1.54 V (L). These electrochemical studies suggested that every compound, except **6-Ni**, had the potential to be oxidized, and all complexes would undergo either a metal- or ligand-based reduction.

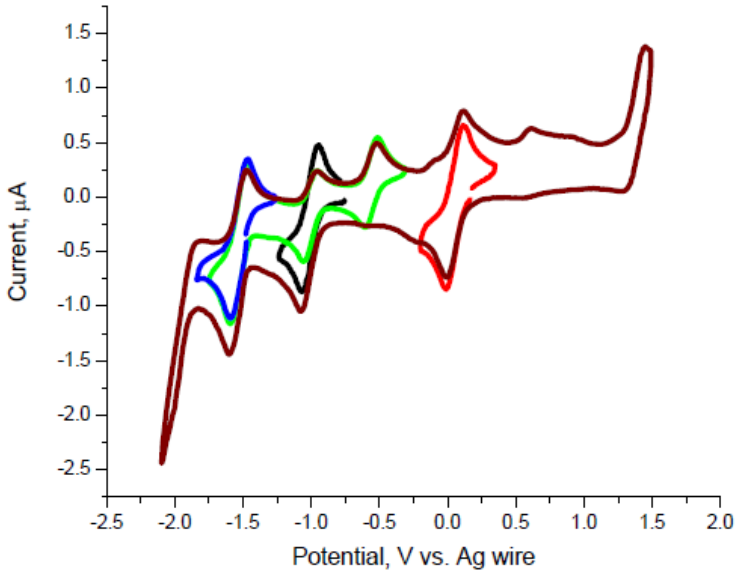

Figure 2.8. Cyclic voltammogram for **6-Co** obtained in THF.

Table 2.1. Redox potentials for Li(smif) and $(smif)_2M^n$ complexes [n = 0, M = Cr, Mn, Fe, Co, Ni; n = +1, M = Co] with respect to Ag wire.

	Li(smif)	**$(smif)_2Cr$**		**$(smif)_2Mn$**		**$(smif)_2Fe$**		**$(smif)_2Co$**		**$[(smif)_2Co](OTf)$**		**$(smif)_2Ni$**	
	0.48*	1.55*		0.59*		1.00*		1.42*		1.14		0.61*	
	-0.79*[a]	0.13	$Cr^{II/III}$	-0.34*[d]		0.28	$Fe^{II/III}$	0.61*		1.00*		-0.22*[h]	
	-1.59	-0.078*[b]		-0.190*[d]		-0.95*[e]		0.048	$Co^{II/III}$	0.94*[g]		-0.29[i]	
***E* °' (V)**	-1.94	-0.48	$Cr^{II/I}$	-0.509*[d]		-1.68	L	-0.56[f]		0.36*[g]		-0.78*[h]	
		-1.03*[c]		-1.40	L			-1.00	$Co^{II/I}$	-0.38	$Co^{III/II}$	-1.54	L
		-1.55	L	-1.60	L			-1.53	L	-1.00	$Co^{II/I}$	-1.90[j]	
		-1.87	L							-1.45	L		
										-1.97	L		

*Irreversible processes.

[a] Result of oxidation at 0.48 V. [b] Result of oxidation at 1.55 V. [c] Result of reduction at -1.87 V. [d] Result of oxidation at 0.59 V. [e] Result of oxidation at 1.00 V. [f] Result of of reduction at -1.53 V. [g] Result of oxidation at 1.00 V. [h] Result of reduction at -1.90 V. [i] Coupled to oxidation at 0.61 V. [j] Appears to be coupled to reduction at -1.54 V.

Synthetic redox chemistry began with oxidation attempts for all compounds. Treatment of **6-Mn**, **6-Cr**, or **6-Co** with silver triflate (AgOTf) in ethereal solvents afforded the corresponding oxidized compounds, $[(smif)_2M](OTf)$ [M = Mn (**7-Mn**); Cr (**7-Cr**); Co (**7-Co**)], with loss of Ag^0. **7-Mn** was isolated in 78 % yield from a very deep purple solution as metallic red-bronze crystals (eq 2.4) and was NMR silent.

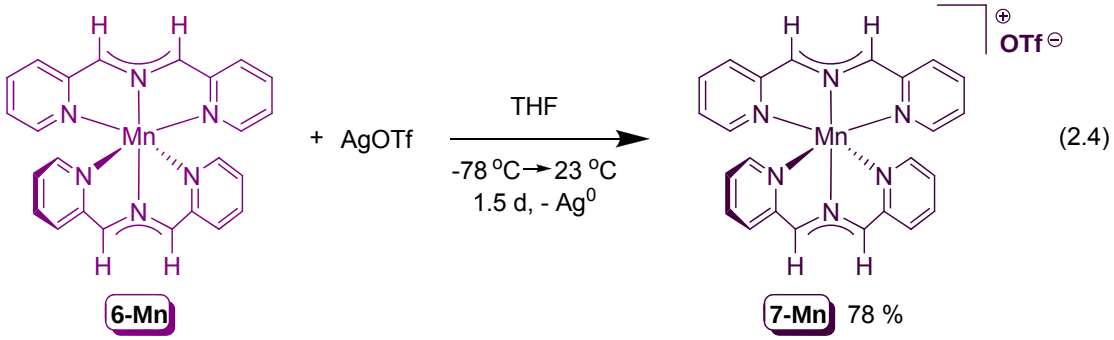

(2.4)

Metallic red crystals of **7-Cr** were obtained from a dark green solution in 75 % yield (eq. 2.5). The ^{1}H NMR spectrum possessed two broad paramagnetic peaks.

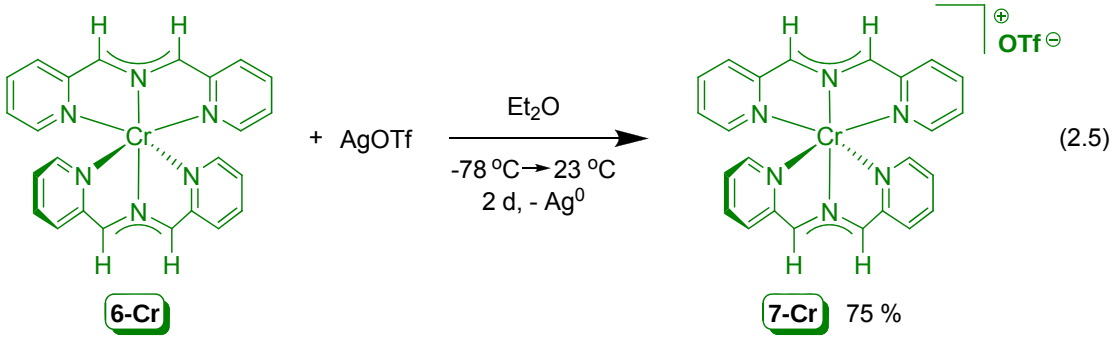

(2.5)

A deep cobalt blue solution produced metallic red crystals of **7-Co** in 81 % yield (eq. 2.6). A D_{2d} symmetric compound was revealed in its ^{1}H NMR spectrum obtained in THF-d_8, which was consistent with an S = 0 GS for **7-Co**.

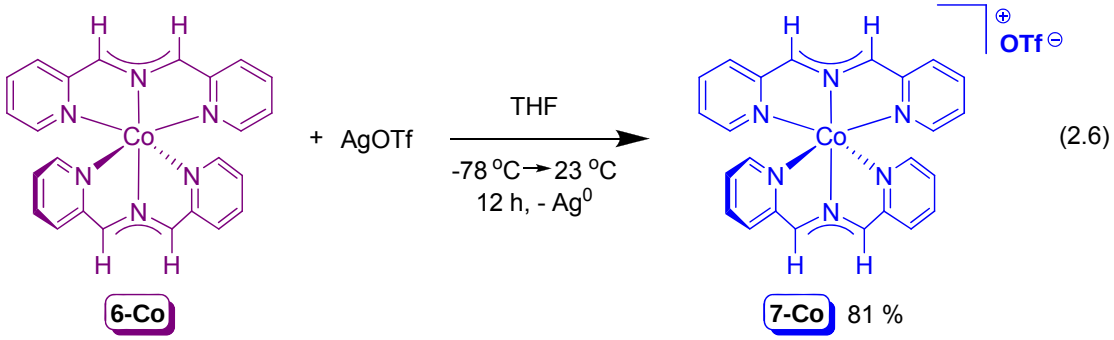

(2.6)

Metal oxidation was not observed for **6-Fe** even though the $Fe^{II/III}$ couple was observed electrochemically. The addition of AgOTf to **6-Fe** in THF yielded a forest green solution from which a dark magenta-purple solid was isolated. Unfortunately, the solid was not the expected paramagnetic Fe(III) species, $[(smif)_2Fe](OTf)$, as ^1H NMR spectroscopy revealed the presence of a mixture of diamagnetic complexes (Scheme 2.4). 1-D and 2-D NMR spectroscopic studies in CD_3CN assisted in elucidating the presence of four (smifH)Fe(II) complexes marked by the downfield chemical shifts (δ 10.22, 10.25, 10.33, 10.40 ppm) corresponding to the imine C*H*. Two compounds were identified, $[(smifH)_2Fe](OTf)_2$ (**8-Fe(OTf)$_2$**, δ 10.22 ppm) and [(smifH)(smif)Fe](OTf) (**9-Fe(OTf)**, δ 10.25 ppm), based upon their independent syntheses. Previous work by Lions and Martin[20] showed that **8-Fe(X)$_2$**, a dark magenta-purple solid, was formed by exposing FeX_2 sources with two equivalents of **smifH** (Scheme 2.5). Two variants of **8-Fe(X)$_2$** were prepared such that X = Br (**8-Fe(Br)$_2$**) and OTf (**8-Fe(OTf)$_2$**). Alternatively, treatment of **6-Fe** in THF with two equivalents of $HBF_4{\cdot}OEt_2$ afforded $[(smifH)_2Fe][BF_4]_2$ (**8-Fe(BF$_4$)$_2$**) in 87 % yield. Identical ^1H NMR spectra were obtained regardless of the counterion present. Treatment of **8-Fe(BF$_4$)$_2$** with **6-Fe** in CD_3CN led to the formation of **9-Fe(BF$_4$)** (eq 2.7), presumably from a comproportionation via proton transfer, thus verifying the NMR assignments for the mixture. The presence of (smifH)Fe(II) complexes suggests

that oxidation occurred in the ligand, presumably generating a radical that abstracted a hydrogen atom, possibly from a solvent molecule, and produced the neutral **smifH** chelate.

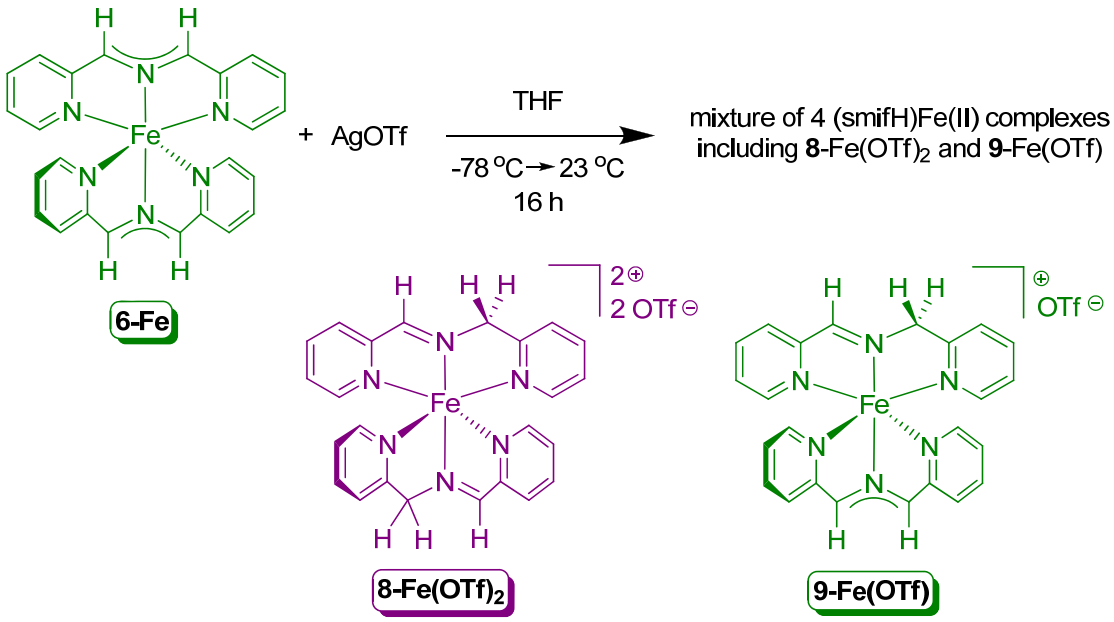

Scheme 2.4. Oxidation of $(smif)_2Fe$ led to a mixture of (smifH)Fe(II) complexes.

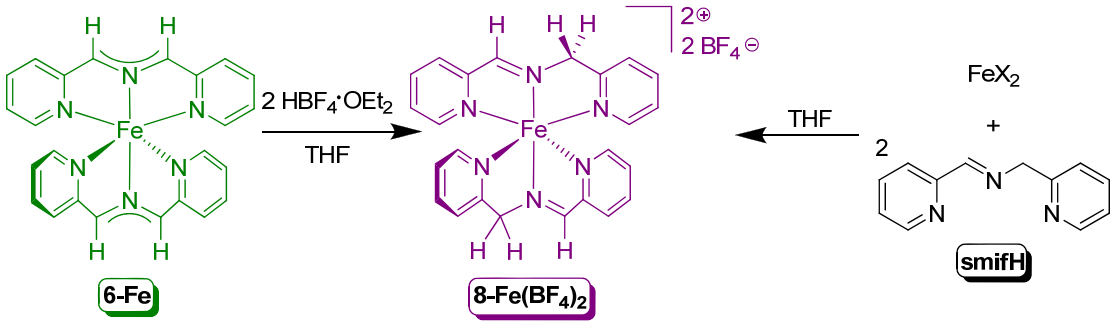

Scheme 2.5. Synthetic routes to $[(smifH)_2Fe]X_2$.

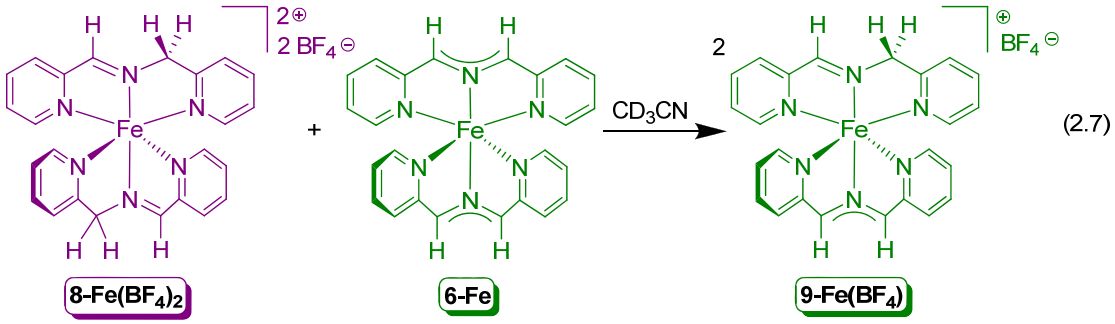

(2.7)

Unfortunately, tractable oxidization products were not observed for **6-V** or **6-Ni** as their treatment with an equivalent of silver triflate (AgOTf) in THF yielded insoluble brown-black solids.

Efforts to synthesize anionic $(smif)_2M$ complexes via 1 e^- reduction chemistry were explored as the electrochemistry showed promising possibilities to effect both metal- and ligand-based reductions. However, all reduction attempts failed even under varied reaction conditions with reducing agents, such as sodium amalgam, sodium naphthalenide, and cobaltocene.

Characterization of $(smif)_2M^n$ Complexes: X-ray Crystal Structures of 6-V, 6-Cr, 7-Cr, 6-Mn, 6-Fe, 6-Co, 7-Co, 6-Ni. Single crystal, x-ray diffraction quality, thin metallic gold plates of **6-V**, **6-Mn**, and **6-Co** were isolated from toluene. Dark forest green plates of **6-Cr** were also collected from toluene. Thin metallic red plates of the cationic complexes, **7-Cr** and **7-Co**, were obtained from THF. Benzene yielded thin metallic purple and metallic gold plates of **6-Fe** and **6-Ni**, respectively. Select crystallographic and refinement data for **6-V**, **6-Cr**, **7-Cr**, **6-Mn**, **6-Fe**, **6-Co**, **7-Co**, and **6-Ni** are listed in Table 2.2. Pertinent distances and angles are listed in Table 2.3. The solid state structure of **6-Fe**, shown in Figure 2.9, displays two tridentate smif ligands occupying an octahedral coordination geometry giving rise to a D_{2d} symmetric molecule, which has been observed with other tridentate N-donor ligands such as terpy,[11-19] bpca,[25-28] and bpca derivatives.[29-32] All crystal structures possess

$N_{aza}MN_{aza}$', specifically ∠N2-M-N5, angles within the range from a nearly perfect axis, 179.11(6) ° in **6-Fe**, to a significantly distorted one, 166.49(7) ° observed in **6-Mn**. Every smif chelate displays $N_{py}MN_{py}$ angles between 146.7(5) ° and 167.68(9) °, for **6-Mn** and **7-Co**, respectively. Smaller $N_{py}MN_{py}$ angles result in narrow bite angles, i.e. $\angle N_{aza}MN_{py}$, for the chelate. In general, the constraints of the ligand are indicative of its proximity to the metal center, such that chelates with smaller bite angles have longer M-N_{aza} and M-N_{py} bond distances. Similar to $(bpca)_2M$ complexes,[25-28] distinctions between metal-nitrogen bond distances are observed. M-N_{aza} bond distances are always shorter than M-N_{py} distances resulting from the geometry of the smif ligand. Additionally, the N_{aza}-C bond lengths, ~1.33 Å, on the smif backbone are consistent with a delocalized anion as observed in $(smif)CrN(TMS)_2$. They are longer than the 1.29 Å expected for an imine N=C (sp^2-sp^2) and shorter than expected for an amide N-C (sp^2-sp^3) bond, i.e. 1.36 Å.

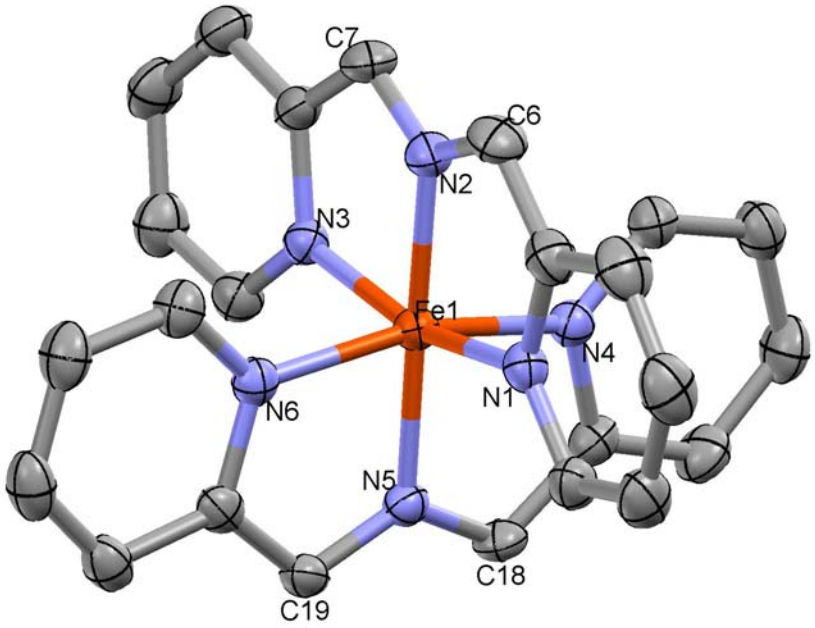

Figure 2.9. Molecular structure of $(smif)_2Fe$ (**6-Fe**). Thermal ellipsoids are at 50 % probability level.

The crystal structures for the homologous $(smif)_2M$ series exhibit a few key distortions, i.e. C_{2v}, D_2, C_s, C_2, and C_1, away from true D_{2d} symmetry (Figure 2.10). A C_{2v} distortion simply arises when one smif ligand is pulled away from the metal center, thus lengthening the M-N_{aza} and M-N_{py} bond distances with respect to the other ligand. Canting one smif ligand off of the perpendicular axis, such that the $N_{aza}MN_{aza}$' angle deviates from a perfect 180 °, results in a C_s distortion. Rotating one smif ligand about the $N_{aza}MN_{aza}$' axis, i.e. twisting the propeller of a D_{2d} symmetric compound, yields a D_2 distortion. Recognizing this distortion involves either using a visualization program, such as Mercury, to carefully look for twisting or by closely inspecting the angles generated between pyridine rings on opposite ligands. One set of angles, i.e. ∠N1-M-N4 and ∠N3-M-N6, may decrease with concomitant widening of the opposite pair, i.e. ∠N1-M-N6 and ∠N3-M-N4. In complexes that possess other distortions, discerning propeller twists via the aforementioned angles becomes complicated, as the observed angles may solely be a result of the other distortions and not a true D_2 twist. A C_2 distortion arises in molecules exhibiting a D_2 twist while "sliding" one smif ligand toward the opposite ligand (C_s). This distortion becomes evident when comparing the angles generated between the azaallyl nitrogen of one smif ligand and the pyridine nitrogens for the other, i.e. ∠$N_{aza}MN_{py}$'. For instance, a C_2 distortion arises if ∠N2-M-N4 equals ∠N5-M-N1 and ∠N2-M-N6 equals ∠N5-M-N3, but the two sets do not equal each other. If the molecule displays one equivalent set, i.e. ∠N5-M-N1 and ∠N5-M-N3, and one inequivalent set, i.e. ∠N2-M-N6 and ∠N2-M-N4, in addition to the sets being inequivalent, a C_s distortion is present. When all the $N_{aza}MN_{py}$' angles are different, the distortion is considered C_1. $(smif)_2M$ complexes are categorized and described according to the closest distortion symmetry they exhibit (Table 2.3).

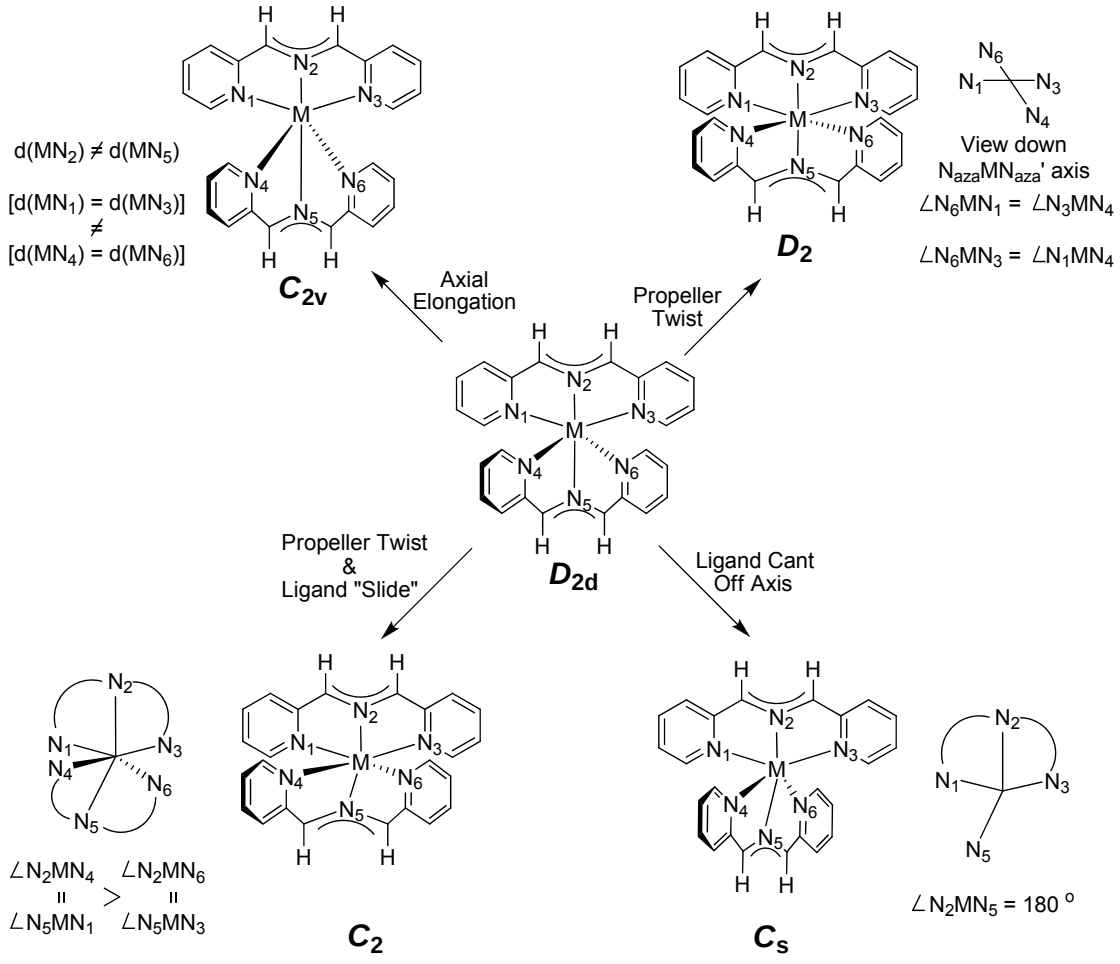

Figure 2.10. Distortions away from D_{2d} symmetry observed in crystal structures of $(smif)_2M$ complexes.

Table 2.2. X-ray crystallographic data for $(smif)_2M$ complexes [M = V (**6-V**); Cr (**6-Cr**); Mn (**6-Mn**); Fe (**6-Fe**); Co (**6-Co**); Ni (**6-Ni**)] and $[(smif)_2M](OTf)$ complexes[M = Cr (**7-Cr**); Co (**7-Co**)].

	6 - V	**6 - Cr**	**7 - Cr**	**6 - Mn**	**6 - Fe**	**6 - Co**	**7 - Co**	**6 - Ni**
Formula	$C_{24}H_{20}N_6V$[a,b]	$C_{24}H_{20}N_6Cr$[a,c]	$C_{29}H_{28}N_6O_4SF_3Cr$[d]	$C_{24}H_{20}N_6Mn$[a,c]	$C_{24}H_{20}N_6Fe$	$C_{24}H_{20}N_6Co$[a]	$C_{29}H_{28}N_6O_4SF_3Co$[e]	$C_{25.50}H_{21.50}N_6Ni$[f]
Formula weight	443.40	444.46	665.63	447.4	448.31	451.39	672.56	470.7
Crystal system	Triclinic	Triclinic	Triclinic	Triclinic	Monoclinic	Triclinic	Monoclinic	Triclinic
Space group	*P* $\bar{1}$	*P* $\bar{1}$	*P* $\bar{1}$	*P* $\bar{1}$	$P2_1/n$	*P* $\bar{1}$	*C* 2/c	*P* $\bar{1}$
Z	4	4	2	4	4	4	8	4
a (Å)	8.940(6)	8.9763(6)	8.7769(4)	8.9189(11)	8.7442(4)	9.028(6)	30.8068(12)	9.0129(8)
b (Å)	14.245(9)	14.4378(10)	12.5575(6)	14.4448(19)	27.4138(14)	14.398(9)	14.4243(5)	14.4774(12)
c (Å)	17.526(9)	16.9883(11)	15.6932(7)	17.849(2)	9.2149(4)	16.882(9)	18.5224(7)	17.0517(14)
α (°)	94.41(5)	94.086(4)	86.978(3)	94.240(6)	90	93.92(5)	90	94.368(3)
β (°)	98.06(5)	97.642(4)	76.027(3)	98.287(6)	113.809(2)	98.35(5)	126.141(2)	97.829(3)
γ (°)	96.16(4)	97.152(4)	80.361(3)	93.988(5)	90	97.35(4)	90	97.521(3)
V (Å^3)	2188(2)	2156.5(3)	1654.63(13)	2261.8(5)	2020.93(16)	2145(2)	6646.9(4)	2175.2(3)
ρ_{calc} g/cm^3	1.346	1.369	1.336	1.314	1.473	1.398	1.344	1.437
μ (mm^{-1})	0.477	0.554	0.467	0.606	0.771	0.824	0.637	0.918
temp (K)	100(2)	173(2)	173(2)	296(2)	173(2)	100(2)	173(2)	213(2)
λ (Å)	0.97890	0.71073	0.71073	0.71073	0.71073	0.97890	0.71073	0.71073
final R indices [$I > 2\sigma(I)$][g,h]	$R_1 = 0.0482$	$R_1 = 0.0484$	$R_1 = 0.0482$	$R_1 = 0.0433$	$R_1 = 0.0424$	$R_1 = 0.0474$	$R_1 = 0.0551$	$R_1 = 0.0436$
	$wR_2 = 0.1444$	$wR_2 = 0.1008$	$wR_2 = 0.1135$	$wR_2 = 0.0910$	$wR_2 = 0.0932$	$wR_2 = 0.1325$	$wR_2 = 0.1424$	$wR_2 = 0.0795$
R indices (all data)[g,h]	$R_1 = 0.0500$	$R_1 = 0.0816$	$R_1 = 0.0677$	$R_1 = 0.0754$	$R_1 = 0.0586$	$R_1 = 0.0488$	$R_1 = 0.0782$	$R_1 = 0.0882$
	$wR_2 = 0.1469$	$wR_2 = 0.1109$	$wR_2 = 0.1208$	$wR_2 = 0.0997$	$wR_2 = 0.1001$	$wR_2 = 0.1349$	$wR_2 = 0.1543$	$wR_2 = 0.0934$
GOF[i]	1.071	1.034	1.075	1.024	1.041	1.030	1.055	1.004

[a] The asymmetric unit contains two formula units. [b] 1/2 molecule toluene per asymmetric unit SQEEZEd. [c] Toluene molecule SQEEZEd. [d] The asymmetric unit contains one molecule of **7-Cr** and one molecule of THF. One molecule of THF was SQEEZEd. [e] The asymmetric unit contains one molecule of **7-Co** and one molecule of THF. One molecule of THF was SQEEZEd.
[f] The asymmetric unit contains two molecules of **6-Ni** and 1/2 molecule of C_6H_6. [g] $R_1 = \Sigma||F_o| - |F_c||/\Sigma|F_o|$. [h] $wR_2 = [\Sigma w(|F_o| - |F_c|)^2/\Sigma wF_o^2]^{1/2}$.
[i] GOF (all data) = $[\Sigma w(|F_o| - |F_c|)^2/(n - p)]^{1/2}$, n = number of independent reflections, p = number of parameters.

Table 2.3. Selected interatomic distances and angles for $(smif)_2M$ complexes [M = V (**6-V**); Cr (**6-Cr**); Mn (**6-Mn**); Fe (**6-Fe**); Co (**6-Co**); Ni (**6-Ni**)] and [$(smif)_2M$](OTf) complexes[M = Cr (**7-Cr**); Co (**7-Co**)].

Compound	d(M-N_{aza})	d(M-N_{py})	d(N_{aza}-C)	∠N_{aza}-M-$N_{aza'}$	∠N_{py}-M-N_{py}	∠N_{aza}-M-N_{py}	∠N_{aza}-M-$N_{py'}$	∠N_{py}-M-$N_{py'}$	Overall Symmetry	Closest Distortion Symmetry
6 - V	2.058(18) Å*	2.118(7) Å*	1.347(11) Å*	172.08(36)°*	154.24(48)°*	77.25(22)°*	95.08(10)° -110.10(10)°	92.8(13)°*	C_1	C_1[a], C_1[a]
6 - Cr	1.9481(19), 1.992(2) Å 2.026(2), 1.932(2) Å	2.034(12) Å*	1.341(11) Å*	175.81(18)° 176.45(8)°	158.32(8)°* 158.17(8)°*	79.19(3)°*	97.10(8)° - 104.79(8)°	89.36(8)° - 94.90(8)°	C_1	C_1[a] C_{2v}[b]
7 - Cr	1.994(3) Å*	2.035(2) Å	1.334(2) Å*	176.72(9)°	160.79(10)°*	80.42(8)°*	97.02(9)° - 102.13(9)°	89.81(9)° - 92.25(9)°	C_1	C_2[c]
6 - Mn	2.207(2), 2.186(3) Å 2.215(2), 2.220(3) Å	2.236(7) Å*	1.325(5) Å*	169.22(10)° 166.51(9)°	148.6(8)°* 146.7(5)°*	74.0(4)°*	95.99(9)° - 115.16(9)°	92.97(9)° - 97.26(9)°	C_1	C_1[a] C_2[c]
6 - Fe	1.9012(14) Å*	1.9634(12) Å*	1.333(3) Å*	179.11(6)°	164.53(11)°*	82.30(24)°*	97.7(5)°*	91.0(12)°*	D_{2d}	D_{2d}
6 - Co	1.946(3) Å 1.888(3) Å	2.193(3), 2.175(3) Å 1.980(3), 1.962(3) Å	1.341(2) Å*	177.30(11)°	158.43(11)° 164.32(12)°	79.24(34)°* 82.20(13)°*	95.12(12)° - 101.22(12)°	91.5(14)°*	C_1	C_s[d]
	1.945(3) Å 1.939(3) Å	2.094(3), 2.116(3) Å 2.049(3), 2.056(3) Å	1.333(9) Å*	177.76(12)°	159.78(12)° 160.87(12)°	80.3(6)°*	97.51(12)° - 102.12(13)°	91.7(24)°*	C_1	C_2[c]
7 - Co	1.8768(11) Å*	1.9252(19) Å*	1.331(9) Å*	179.05(10)°	167.68(9)°*	83.9(2)°*	96.1(7)°*	90.7(19)°*	D_{2d}	D_{2d}
6 - Ni	2.019(5) Å*	2.093(9) Å*	1.325(4) Å*	176.07(12)°*	158.1(4)°*	79.1(3)°*	96.66(11)° - 104.63(11)°	92.1(16)°*	C_1	C_1[a], C_2[c]

* Values averaged.

[a] C_1: ∠N2-M-N4 ≠ ∠N2-M-N6 ≠ ∠N5-M-N1 ≠ ∠N5-M-N3. [b] C_{2v}: d(M-N2) ≠ d(M-N5); [d(M-N1) = d(M-N3)] ≠ [d(M-N4) = d(M-N6)]. [c] C_2: [∠N2-M-N4 = ∠N5-M-N1] > [∠N2-M-N6 = ∠N5-M-N3].

[d] C_s: ∠N2-M-N4 ≠ ∠N2-M-N6; ∠N5-M-N1 = ∠N5-M-N3.

Two $(smif)_2M$ complexes are considered D_{2d} symmetric, $(smif)_2Fe$ (**6-Fe**) and $[(smif)_2Co](OTf)$ (**7-Co**), and their crystal structures reveal only one molecule per asymmetric unit. **6-Fe** and **7-Co** clearly lack the presence of any distortion previously mentioned. Their $N_{aza}MN_{aza}$' angles are very close to 180 °, i.e. 179.11(6) ° and 179.05(10) °, for **6-Fe** and **7-Co**, respectively. Essentially identical $N_{aza}MN_{py}$' angles are observed, i.e. 97.50(6) ° and 97.87(6) ° for **6-Fe** as well as 96.22(8) ° and 96.06(8) ° for **7-Co**, showing that the ligand is centered with respect to the other. The crystal structures reveal the largest $N_{py}MN_{py}$ angles of 164.53(11) ° (ave) for **6-Fe** and 167.68(9) ° (ave) for **7-Co**, thereby resulting in chelates with bite angles averaging 82.30(24) ° (**6-Fe**) and 83.9(2) ° (**7-Co**), which are larger than those observed in the remaining compounds. Consequently, these compounds exhibit the shortest bond distances as a result of possessing the largest ligand field stabilization energy (-24 Dq + 2P, for a low spin d^6 configuration) when compared to the remainder of the series. The average Fe-N_{aza} bond length of 1.9012(14) Å is shorter than the iron-amide distances of 1.918(7) Å and 1.928(7) Å in the $(bpca)_2Fe$,[26] suggesting the smif ligand possesses a stronger field than the bpca ligand. Interestingly, **6-Fe** possesses Fe-N_{py} distances averaging 1.9634(12) Å, which are significantly longer than those observed in $(bpca)_2Fe$ ranging from 1.929(8) Å to 1.957(7) Å.[26] In comparison, **7-Co** possesses cobalt-nitrogen distances that are slightly contracted, which is expected for a cationic complex with the same d^n count. The cobalt-azaallyl nitrogen distances average a value of 1.8768(11) Å, whereas the cobalt-pyridine nitrogen bond lengths are 1.9252(19) Å on average. A twisted propeller was not observed in either complex; **6-Fe** possessed $N_{py}MN_{py}$' angles averaging 91.0(12) °, and the corresponding angles viewed in **7-Co** averaged 90.7(19) °.

The remaining complexes in the series all display C_1 symmetry overall. Each molecule possesses a C_s distortion, such that one ligand cants away from the

$N_{aza}MN_{aza}$' axis. Therefore, the $N_{aza}MN_{aza}$' angles are less than 180 °. Combinations of other distortions are exhibited by the complexes. These slightly more pronounced distortions dictate the assignment of the closest distortion symmetry, which primarily results from a comparison of the $N_{aza}MN_{py}$' angles (Table 2.3).

$(smif)_2Ni$ displays the mildest deviations away from D_{2d} symmetry giving rise to its C_1 symmetry. The crystal structure of **6-Ni** has two molecules in the asymmetric unit, and both show a slight C_s distortion with $N_{aza}NiN_{aza}$' angles of 176.00(12) ° (Ni1) and 176.11(12) ° (Ni2). Molecule 1 exhibits C_1 symmetry; it possess four different $N_{aza}NiN_{py}$' angles, i.e. ∠N2-Ni1-N4 = 99.83(11) °, ∠N2-Ni1-N6 = 101.94(11) °, ∠N5-Ni1-N1 = 96.63(12) °, and ∠N5-Ni1-N3 = 104.61(12) °. On the other hand, molecule 2 displays C_2 symmetry. It has two sets of angles that are equal, but not to each other: ∠N8-Ni2-N10 = 98.07(12) °, ∠N8-Ni2-N12 = 104.03(12) °, ∠N11-Ni2-N7 = 98.69(11) °, and ∠N11-Ni2-N9 = 103.48(12) °. In comparison to **6-Fe** and **7-Co**, **6-Ni** displays smaller chelate angles. The average $N_{py}NiN_{py}$ angle is 158.1(4) °, and the $N_{aza}NiN_{py}$ bite angles average a value of 79.1(3) ° between the two molecules. Nickel-nitrogen bond distances, i.e. $d(Ni\text{-}N_{aza})_{ave}$ = 2.019(5) Å and $d(Ni\text{-}N_{py})_{ave}$ = 2.093(9) Å, are elongated with respect to **6-Fe** and **7-Co**. This result is not surprising because a smaller ligand field stabilization energy (-12 Dq) is associated with the d^8 Ni(II) center due to population of the σ* orbitals; therefore, the bond order decreases with concomitant lengthening of bonds.

The asymmetric unit of $[(smif)_2Cr](OTf)$, **7-Cr**, contains one molecule that nominally displays C_1 symmetry. A mild C_s distortion is apparent in the $N_{aza}CrN_{aza}$' angle of 176.72(9) °, as one smif ligand cants away from the axis. Based upon the observation of two equivalent sets of $N_{aza}CrN_{py}$' angles, **7-Cr** is best described as a C_2 symmetric complex. One set possesses ~ 97 ° angles (∠N2-Cr1-N4 = 97.69(9) ° and ∠N5-Cr1-N1 = 97.02(9) °), whereas the second set spans ~ 102 ° (∠N2-Cr1-N6 =

101.50(9) ° and ∠N5-Cr1-N3 = 102.13(9) °). Angles associated with the chelate are similar to those observed in **6-Fe**, **7-Co**, and **6-Ni**: $\angle N_{py}CrN_{py}$ = 160.79(10) ° (ave) and $\angle N_{aza}CrN_{py}$ = 80.42(8) ° (ave). Chromium-nitrogen bond distances in **7-Cr** are similar to those observed in **6-Ni**, as would be anticipated for complexes possessing similar covalent radii. The charge on **7-Cr** compensates for the small difference observed between the covalent radius of nickel and chromium. The average Cr-N_{aza} distance is 1.994(3) Å, and the Cr-N_{py} bond lengths average 2.035(2) Å.

The asymmetric unit for $(smif)_2Cr$ has two molecules that display slight ligand canting as their $N_{aza}CrN_{aza}$' angles deviate from 180 °, i.e. ∠N2-Cr1-N5 = 175.81(8) ° and ∠N8-Cr2-N10 = 176.45(8) °. A slight C_{2v} distortion appears in the Cr-N_{aza} bond lengths (d(Cr1-N2) = 1.9481(19) Å and d(Cr1-N5) = 1.992(2) Å) in molecule 1 and produces four different $N_{aza}Cr1N_{py}$' angles, such that ∠N2-Cr1-N4 = 97.10(8) °, ∠N2-Cr1-N6 = 104.79(8) °, ∠N5-Cr1-N1 = 99.01(8) °, and ∠N5-Cr1-N3 = 102.36(8) °; therefore, molecule 1 is best described as a C_1 symmetric species. Molecule 2 displays a more pronounced C_{2v} distortion in its Cr-N_{aza} bond distances, i.e. d(Cr2-N8) = 2.026(2) Å, and d(Cr2-N11) = 1.932(2) Å, and is subsequently described as a C_{2v} symmetric complex. In contrast to molecule 1, the $N_{aza}Cr2N_{py}$' angles still exhibit C_2 symmetry with two equivalent sets: ∠N8-Cr2-N10 = 103.37(8) °, ∠N8-Cr2-N12 = 97.55(8) °, ∠N11-Cr2-N7 = 103.29(8) °, and ∠N11-Cr2-N9 = 99.34(8) °. Chromium-pyridine bond lengths average 2.034(12) Å. The bond distances are slightly shorter than those observed in **6-Ni**, as would be expected for a system with approximately the same stabilization energy without populating the σ* orbitals. The smif chelates display bite angles of 79.19(3) ° (ave), consistent with larger $N_{py}CrN_{py}$ angles, i.e. 158.17(8) ° (Cr1, ave) and 158.32(8) ° (Cr2, ave).

$(smif)_2V$ has two molecules in its asymmetric unit, which are best described by C_1 symmetry. The azaallyl nitrogens span an angle of 172.08(36) ° (ave) around

vanadium, indicative of a significant C_s distortion. Molecule 1 displays a slight C_{2v} distortion in the V-N_{aza} bond lengths [d(V1-N2) = 2.032(3) Å and d(V1-N5) = 2.062(3) Å], which generates four very different $N_{aza}V1N_{py}$' angles, such that ∠N2-V1-N4 = 100.42(10) °, ∠N2-V1-N6 = 105.31(10) °, ∠N5-V1-N1 = 95.08(10) °, and ∠N5-V1-N3 = 110.10(10) °; therefore, molecule 1 is considered C_1 symmetric. Similarly, molecule 2 exhibits C_1 symmetry because of the four strikingly different $N_{aza}Cr1N_{py}$' angles: ∠N8-V2-N10 = 110.04(10) °, ∠N8-V2-N12 = 95.63(10) °, ∠N11-V2-N7 = 99.00(10) °, and ∠N11-V2-N9 = 107.24(10) °. Vanadium-azaallyl nitrogen distances are 2.058(18) Å (ave) with concomitantly long V-N_{py} lengths 2.118(7) Å (ave). In comparison to the metal-nitrogen distances observed in **6-Cr** and **7-Cr**, the elongation seen in **6-V** may be attributed to a slightly larger covalent radius for vanadium, as the field stabilizations are approximately equal. **6-V** exhibits the second smallest $N_{py}VN_{py}$ bond angle averaging a value of 154.24(48) ° and subsequently small bite angles averaging 77.25(22) °.

Two distinct molecules appear in the asymmetric unit representing $(smif)_2Co$. A C_s distortion arises in each molecule as one smif ligand cants away from the other; therefore, the $N_{aza}CoN_{aza}$' angles are smaller than 180 °, i.e. 177.30(11) ° (Co1) and 177.76(12) ° (Co2). With respect to the other complexes in the series, **6-Co** has the only asymmetric unit with a molecule (Co1) exhibiting mostly C_s symmetry. This molecule has one equivalent and one inequivalent set of angles, i.e. ∠N2-Co1-N4 = 100.51(12) °, ∠N2-Co1-N6 = 95.12(12) °, ∠N5-Co1-N1 = 100.34(11) °, and ∠N5-Co1-N3 = 101.22(12) °. Surprisingly, the C_{2v} distortion present does not distort the $N_{aza}Co1N_{py}$' angles as observed in **6-Cr** and **6-V**. Instead, all remaining parameters display the deviations. Two different $N_{py}CoN_{py}$ angles (158.43(11) ° and 160.87(12) °) exist and give rise to the corresponding bite angles of 79.24(34) ° (ave) and 82.20(13)° (ave), which are markedly different. Both smif ligands exhibit shorter Co-N_{aza}

distances (d(Co1-N2) = 1.946(3) Å, d(Co1-N5) = 1.888(3) Å) than Co-N_{py} bond lengths (d(Co1-N1) = 2.193(3) Å, d(Co1-N3) = 2.175(3) Å, d(Co1-N4) = 1.980(3) Å, and d(Co1-N6) = 1.962(3) Å). However, the smif ligand, comprised of N4, N5, and N6, is significantly (~ 0.06 Å) closer to cobalt, indicative of a C_{2v} distortion. The second molecule in the asymmetric unit possesses C_2 symmetry with its two equivalent sets of $N_{aza}Co2N_{py}$' angles: ∠N8-Co2-N10 = 97.51(12) °, ∠N8-Co2-N12 = 101.40(12) °, ∠N11-Co2-N7 = 98.06(12) °, and ∠N11-Co2-N9 = 102.12(13) °. One smif is marginally closer than the other, i.e d(Co2-N2) = 1.945(3) Å, d(Co2-N5) = 1.939(3) Å, which is projected in the Co-N_{py} distances: d(Co2-N7) = 2.094(3) Å, d(Co2-N9) = 2.116(3) Å, d(Co2-N10) = 2.049(3) Å, and d(Co2-N12) = 2.056(3) Å. Even with deviations from D_{2d} symmetry, the bond distances lie between those observed for **6-Fe**, **7-Co**, and **6-Ni**. These results were anticipated as the ligand field stabilization energy for a low spin Co(II) center lies between the two aforementioned sets (-18 Dq + P, for a low spin d^7 complex) due to population of a σ* orbital. The observation of two statistically different molecules within the asymmetric can be rationalized either on the basis of a Jahn-Teller distortion or a mixture of two different electronic structures. An elongation in the distances for one smif ligand in molecule 1 may result from the population of the d_{z^2} orbital, whereas the remaining unpaired electron in molecule 2 may reside in the $d_{x^2-y^2}$ orbital. Alternatively, the two molecules may display an equilibrium between a Co(II) species and a Co(III) species with the unpaired electron residing in a smif-π* orbital. The observed differences between molecules in the asymmetric unit were separately confirmed by single crystal x-ray data collected on a different crystal and may assist in explaining the observed magnetism of **6-Co**.

The last complex in the series, $(smif)_2Mn$, displays the greatest distortions away from D_{2d} symmetry. Significant canting exists in the two molecules of the

asymmetric unit: $\angle N_{aza}$-Mn1-N_{aza}' = 169.20(8) ° and $\angle N_{aza}$-Mn2-N_{aza}' = 166.49(7) °. Similar to **6-Ni** and **6-Cr**, molecule 1 is ascribed as having C_1 symmetry, as none of the four $N_{aza}Mn1N_{py}$' angles are equivalent: ∠N2-Mn1-N4 = 114.90(7) °, ∠N2-Mn1-N6 = 96.00(7) °, ∠N5-Mn1-N1 = 101.27(8) °, and ∠N5-Mn1-N3 = 110.72(8) °. This molecule possesses a small $N_{py}Mn1N_{py}$ angle averaging 148.6(8) ° with concomitantly narrow bite angles that average 74.0(4) °. On the other hand, molecule 2 exhibits two equivalent sets of $N_{aza}Mn1N_{py}$' angles, which are ∠N8-Mn2-N10 = 98.40(7) °, ∠N8-Mn2-N12 = 115.15(7) °, ∠N11-Mn2-N7 = 116.93(7) °, and ∠N11-Mn2-N9 = 95.96(7) °. Molecule 2 is best described as a C_2 symmetric species. The pyridine nitrogens span an angle of 146.7(5) ° on average. Metal-nitrogen bond lengths in **6-Mn** are the longest in the series. The crystal structure of **6-Mn** reveals average Mn-N_{py} lengths of 2.236(7) Å with slightly C_{2v} distorted Mn-N_{aza} distances: d(Mn1-N2) = 2.2084(18) Å, d(Mn1-N5) = 2.186(2) Å, d(Mn2-N8) = 2.215(2) Å, and d(Mn2-N11) = 2.220(2) Å. These distances are similar to those observed in $(bpca)_2Mn$[25] and are consistent with a high spin, Mn(II) center due to population of the σ* orbitals.

In general, D_{2d} symmetry was observed for the diamagnetic complexes, **6-Fe** and **7-Co**. Deviations from D_{2d} symmetry arose in all paramagnetic complexes, ranging from mild C_s, and C_2 distortions in **6-Ni** to combinations of more pronounced C_s, C_2, and C_{2v} distortions in the remaining complexes, i.e. **6-V**, **6-Cr**, **6-Mn**, **7-Cr**, and **6-Co**. Ligand field stabilization energies, orbital populations, and covalent radii may assist in understanding the distortions and varying bond lengths within the series.

Magnetism of $(smif)_2M^n$ Complexes [n = 0, M = V, Cr, Mn, Co, Ni; n = +1, M = Cr, Mn]. The synthesis of a homologous series of complexes and presence of paramagnetic ^{1}H NMR spectra prompted studies into the magnetochemistry. The effective magnetic moments, μ_{eff}, were determined in toluene-*d*8 solutions via Evans'

method[46] and/or in the solid state via Gouy balance measurements. Temperature dependence studies of the molar susceptibility were also performed (Figure 2.11), and ground states (GS) and effective magnetic moments are listed in Table 2.5.

$(smif)_2Fe$ is a low spin Fe(II) complex, and low spin electronic configurations were initially anticipated for all compounds within the series. Movement to the left of **6-Fe** should result in an S = 1/2 GS for **6-Mn** if the complex is low spin. SQUID magnetometry data revealed a μ_{eff} of 5.7 μ_B at 293 K. The effective magnetic moment is consistent with a high spin Mn(II), S = 5/2 GS. A minimal amount of zero field splitting (ZFS) was observed below 20 K, and solution magnetic studies yielded a slightly higher μ_{eff} of 6.0 μ_B at 293 K. The oxidation of **6-Mn** to **7-Mn** resulted in the formation of a high spin Mn(III) complex, and SQUID magnetometry data revealed a μ_{eff} of 5.4 μ_B at 293 K. The value is higher than the expected spin-only value of 4.90 μ_B for an S = 2 GS. Gouy balance measurements for **7-Mn** yielded a μ_{eff} of 5.0 μ_B at 295 K, which is more consistent with an S = 2 GS.

Both solution studies and SQUID magnetometry data for **6-Cr** showed a μ_{eff} of 2.7 μ_B at 293 K, consistent with the expected S = 1 GS for Cr(II). The slight increase in magnetic moment values observed around 0 K in Figure 2.4, is field-dependent. Oxidation of **6-Cr** to produce **7-Cr** resulted in an S = 3/2 GS, as was established by the μ_{eff} of 3.5 μ_B at 293 K obtained from SQUID magnetometry data for **7-Cr**. The decrease in magnetic moment values below 30 K may be attributed to a small amount of ZFS. Gouy balance measurements revealed a slightly lower μ_{eff} of 3.6 μ_B at 295 K for **7-Cr**.

Magnetic studies on **6-V** also showed an S = 3/2 GS for V(II) as SQUID magnetometry data revealed a μ_{eff} of 3.4 μ_B at 293 K. The magnetic moment values decrease below 50 K, presumably resulting from ZFS. A slightly lower magnetic

moment of 3.2 μ_B was observed for **6-V** in solution and in the solid state at 293 K and 295 K, respectively.

Assuming the field strength of the smif ligand is constant throughout the series, moving one column to the right of **6-Fe** may result in an S = 1/2 GS for a low spin, Co(II) center in **6-Co**. A high spin Co(II) complex would possess an S = 3/2 GS if the field strength changes. Magnetic studies for **6-Co** utilized all three methods mentioned. Initial solution studies revealed a μ_{eff} of 2.8 μ_B at 293 K, averaged over six trials. This value is consistent with an "S = 1" GS, and Gouy balance measurements confirmed the magnetic moment with a value of 2.8 μ_B at 294 K. SQUID magnetometry data exhibited a spin-crossover for **6-Co**, which has been observed for other Co(II) systems.[47-50] The magnetic moment at 10 K is 1.7 μ_B, consistent with an S = 1/2 GS, and μ_{eff} rises to 3.2 μ_B at 300 K. At 293 K, the effective magnetic moment has a value of 2.8 μ_B, suggesting a 1:1 mixture of an S =1/2 GS and S = 3/2 GS. This may be evident in the crystal structure of **6-Co**, whose unit cell contains two distinctly different molecules. As expected, **6-Ni** exhibits an S = 1 GS. SQUID magnetometry data revealed a μ_{eff} of 2.8 μ_B at 293 K confirming the solution μ_{eff} of 2.7 μ_B at 293 K.

Table 2.4. Data from fitting SQUID magnetometry data using julX. Fit parameters were g_{av}, D, E/D, and χ_{TIP}.

Compound	g_{av}	D (cm^{-1})	E/D	χ_{TIP} (emu)
6-V	1.758	-35.00	0.000	0
6-Cr	1.892	0.007	0.000	-300 x 10^{-6}
7-Cr	1.795	3.112	0.002	-400 x 10^{-6}
6-Mn	1.930	1.50	0.000	-600 x 10^{-6}
7-Mn	2.214	-17.14	0.000	100 x 10^{-6}
6-Ni	1.984	3.81	0.005	-340 x 10^{-6}

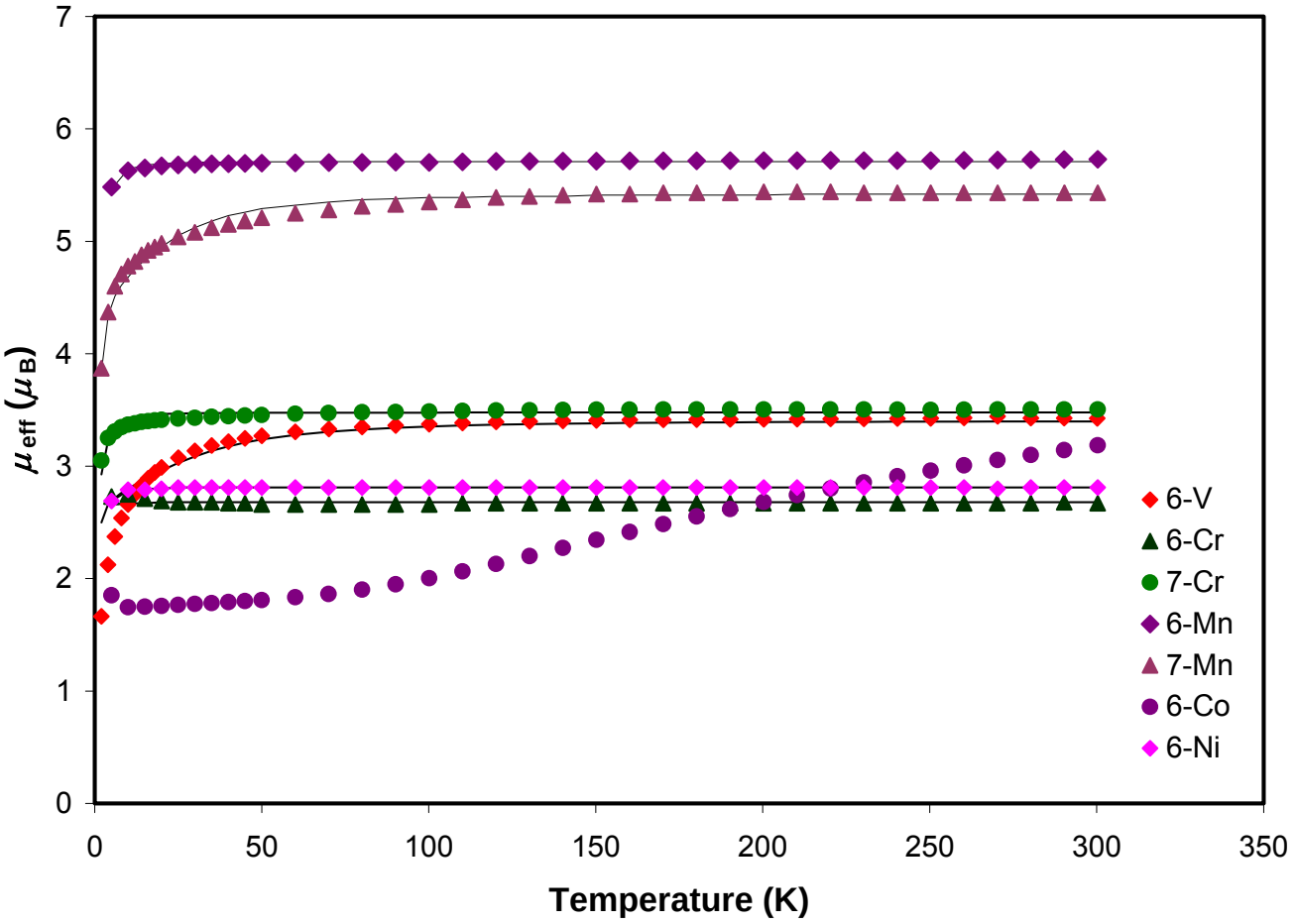

Figure 2.11. SQUID data for $(smif)_2M$ complexes [M = V (**6-V**); Cr (**6-Cr**); Mn (**6-Mn**); Co (**6-Co**); Ni (**6-Ni**)] and $[(smif)_2M](OTf)$ complexes [M = Cr (**7-Cr**); Mn (**7-Mn**)]: Magnetic moment (μ_{eff} in μ_B) as a function of T (K).

UV-vis Spectra of of Li(smif) and $(smif)_2M^n$ Complexes [n = 0, M = V, Cr, Mn, Fe, Co, Ni, Zn; n = +1, M = Cr, Mn, Co]. All smif containing complexes generate colors of unusual intensity in solution separating them from terpy,[51,52] bpca,[25-27] and other N-based tridentate chelates.[53] Distinguishing features with corresponding extinction coefficients are listed in Table 2.5. Li(smif), **5**-Li, yields a deep royal purple solution in benzene. The UV-vis spectrum, shown in Figure 2.12, shows two major features, i.e. 420 nm ($\varepsilon \sim 7{,}000\ M^{-1}\ cm^{-1}$) and 583 nm ($\varepsilon \sim 18{,}000\ M^{-1}\ cm^{-1}$), which may be attributed to intraligand (IL) transitions between azaallyl $CN_{aza}C^{nb}$ orbitals to pyridine π^* orbitals based upon calculations for related smif containing complexes.

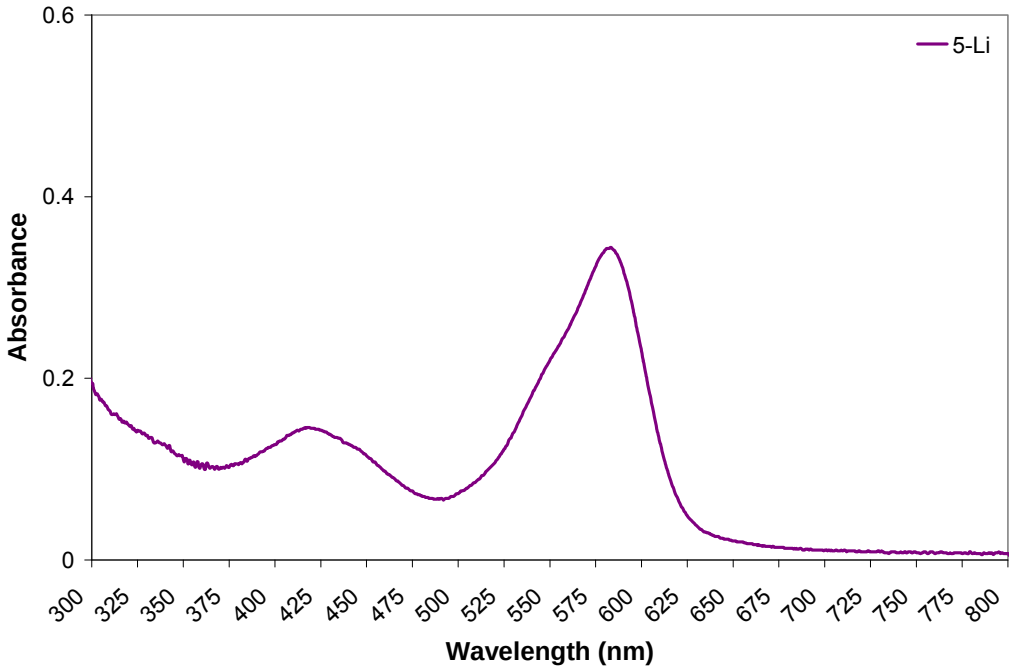

Figure 2.12. UV-vis spectrum of Li(smif) (**5**-Li) in benzene.

$(smif)_2Fe$ (**6-Fe**) produces a deep forest green solution in benzene, and strong absorptions are observed in the blue and red regions. Three main features appear in the

UV-vis spectrum (Figure 2.13). The strongest absorption occurs in the high energy regime, 441 nm (ε ~ 42,000 M^{-1} cm^{-1}). Intense absorptions are also observed at lower energy with extinction coefficients ~ 17,000 M^{-1} cm^{-1} (510 nm, ε ~ 19,000 M^{-1} cm^{-1}; 597 nm, ε ~ 16,000 M^{-1} cm^{-1}). In contrast, the UV-vis spectrum of $[(smifH)_2Fe](ClO_4)_2$ reveals absorptions at 586 nm (ε ~ 11,000 M^{-1} cm^{-1}) and 483 nm (ε ~ 6,250 M^{-1} cm^{-1}).[52] A time-dependent density functional theory (TDDFT) calculated UV-vis spectrum for **6-Fe** is blue shifted by ~ 0.25 eV from the UV-vis spectrum obtained in pentane (Figure 2.14). The features observed in **6-Fe** and other related smif complexes all possess at least two major features that are primarily attributed to the IL transitions between the azaallyl $CN_{aza}C^{nb}$ orbitals and the pyridine π* orbitals. Additionally, minor contributions from underlying metal-to-ligand charge transfers (MLCT) are also attributed to these bands as the calculations show that the azaallyl $CN_{aza}C^{nb}$ orbital is energetically close to the metal 3d orbitals.

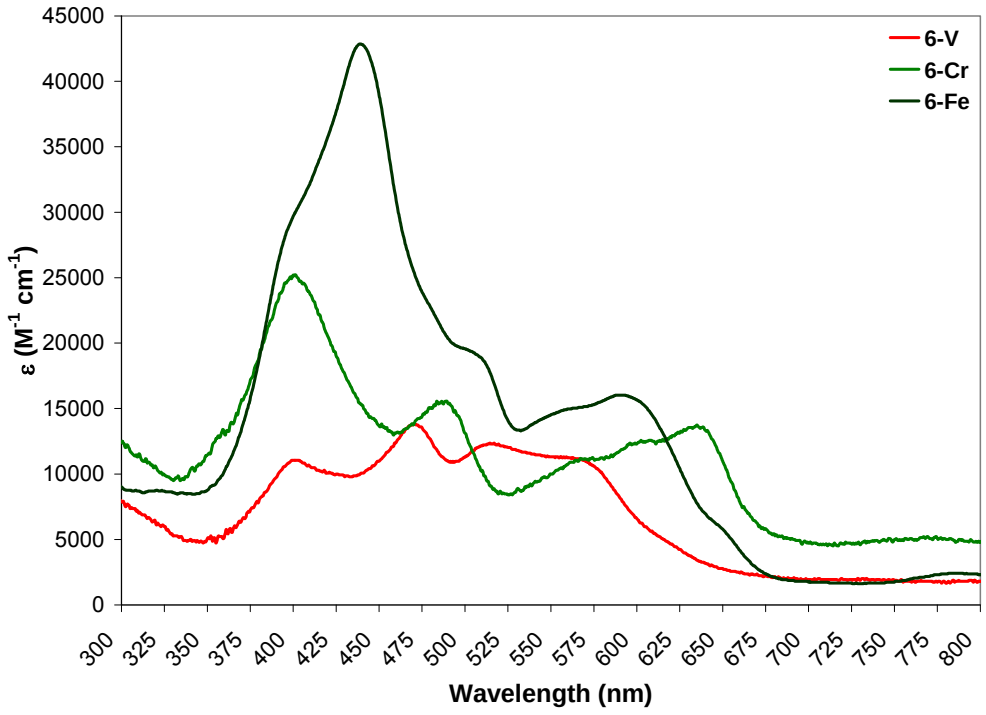

Figure 2.13. UV-vis spectra of $(smif)_2M$ complexes [M = V (**6-V**); Cr (**6-Cr**); Fe (**6-Fe**)] in benzene.

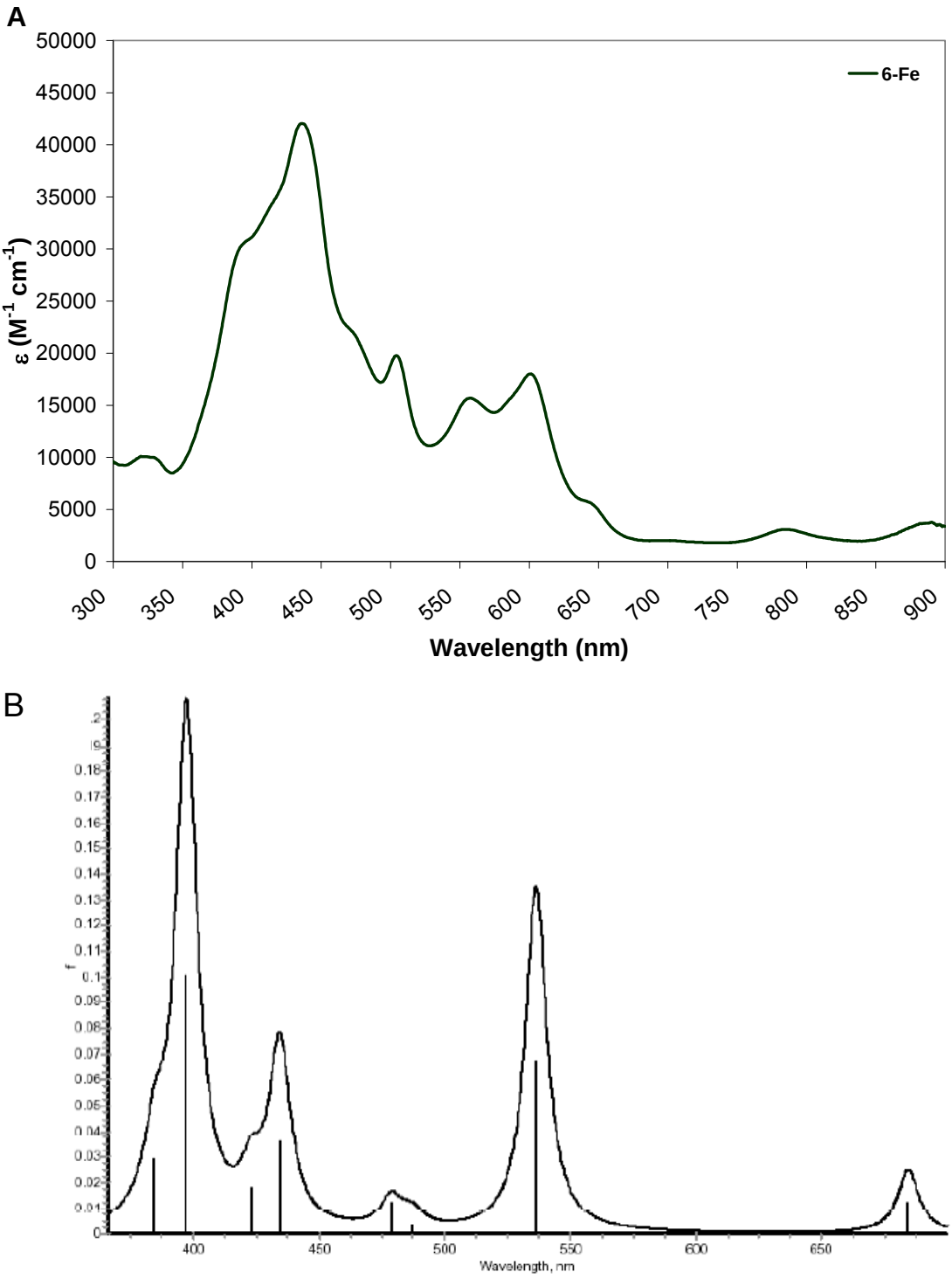

Figure 2.14. A. UV-vis spectrum of $(smif)_2Fe$ in pentane. **B**. TDDFT calculated UV-vis spectrum for **6-Fe**.

Deep forest green solutions of $(smif)_2Cr$ (**6-Cr**) are obtained in benzene. The UV-vis spectrum for **6-Cr**, shown in Figure 2.13, displays three major features corresponding to the strong absorptions observed in the blue and red regions. High energy absorptions at 401 nm and 490 nm possess extinction coefficients of 25,000 M^{-1} cm^{-1} and 15,000 M^{-1} cm^{-1}, respectively. An intense, low energy feature appears at 637 nm ($\varepsilon \sim 14{,}000$ M^{-1} cm^{-1}). The dark cherry red benzene solution of $(smif)_2V$ (**6-V**) absorbs everywhere except in the red region of its UV-vis spectrum (Figure 2.13). Strong features exist at 401 nm ($\varepsilon \sim 10{,}000$ M^{-1} cm^{-1}), 471 nm ($\varepsilon \sim 12{,}000$ M^{-1} cm^{-1}), and 514 nm ($\varepsilon \sim 11{,}000$ M^{-1} cm^{-1}).

Strong absorptions in the green region of the UV-vis spectrum permit the transmission of the various shades of intense red-purple solutions observed for $(smif)_2Mn$, $(smif)_2Co$, $(smif)_2Ni$, and $(smif)_2Zn$ (Figure 2.15). All compounds possess two major features which may be attributed to IL bands and underlying MLCT bands. The largest extinction coefficient, $\varepsilon \sim 60{,}000$ M^{-1} cm^{-1}, in the homologous series is observed in the UV-vis spectrum of **6-Mn** at 590 nm in addition to a high energy absorption at 403 nm possessing an ε of $\sim 23{,}000$ M^{-1} cm^{-1}. Intense features in the UV-vis spectrum of **6-Co** exist at 563 nm ($\varepsilon \sim 29{,}000$ M^{-1} cm^{-1}) and 401 nm ($\varepsilon \sim 20{,}000$ M^{-1} cm^{-1}). **6-Ni** exhibits strong absorption bands at 574 nm and 399 nm with extinction coefficients of $\sim 50{,}000$ M^{-1} cm^{-1} and $\sim 18{,}000$ M^{-1} cm^{-1}, respectively. The strongest absorption for **6-Zn** occurs in the low energy regime at 569 nm with an extinction coefficient of $\sim 24{,}000$ M^{-1} cm^{-1}, whereas a high energy band possessing an $\varepsilon \sim 8{,}900$ M^{-1} cm^{-1} appears at 398 nm.

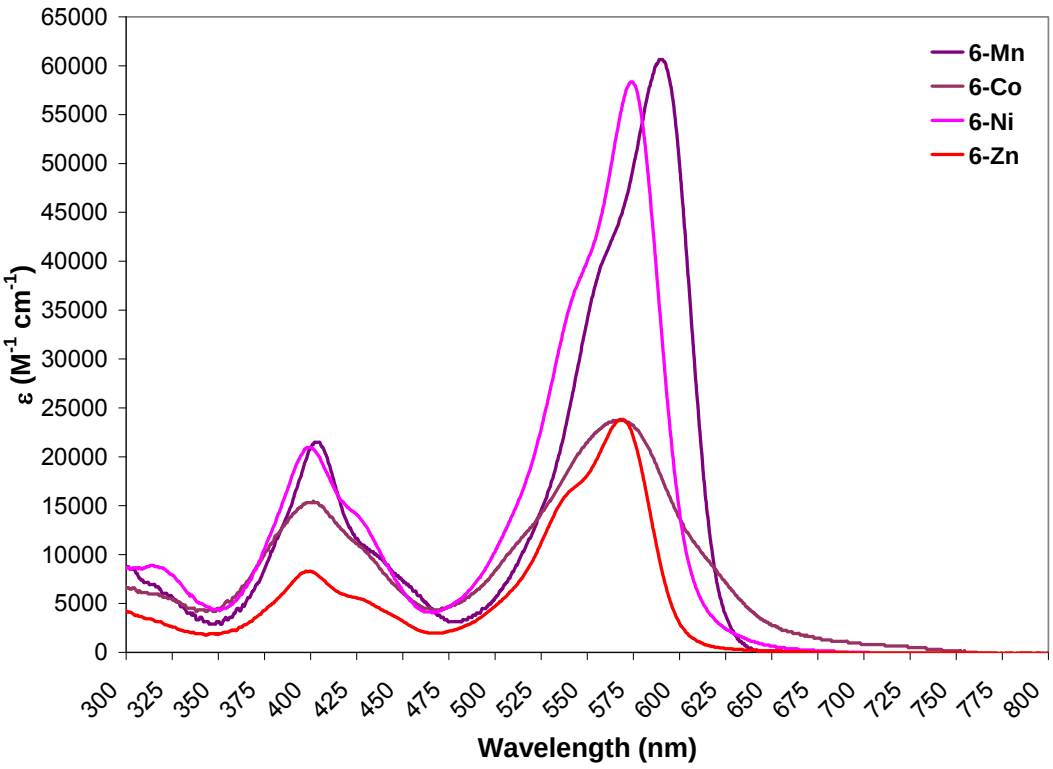

Figure 2.15. UV-vis spectra of $(smif)_2M$ complexes, where M = Mn (**6-Mn**), Co (**6-Co**), Ni (**6-Ni**), and Zn (**6-Zn**), in benzene.

As shown in Figure 2.16, the UV-vis spectra for all oxidized species exhibit three major features: one low energy band slightly blue shifted from that observed for the neutral species and two very high energy bands displaying the same intensity. $[(smif)_2Cr](OTf)$ (**7-Cr**) generates a dark green solution in THF, and the UV-vis spectrum possesses strong absorptions in the blue and red regions. The strongest absorption occurs in the low energy regime, 627 nm with an $\varepsilon \sim 22{,}000\ M^{-1}\ cm^{-1}$. Intense high energy absorptions are also observed for **7-Cr** with extinction coefficients of $\sim 13{,}000\ M^{-1}\ cm^{-1}$ at 385 nm and 492 nm. The deep purple solution of **7-Mn** exhibits intense features at 571 nm ($\varepsilon \sim 26{,}000\ M^{-1}\ cm^{-1}$), 398 nm ($\varepsilon \sim 10{,}000\ M^{-1}\ cm^{-1}$), and 259 nm ($\varepsilon \sim 16{,}000\ M^{-1}\ cm^{-1}$). High energy bands with extinction coefficients of $\sim 12{,}000\ M^{-1}\ cm^{-1}$ (321 nm, $\varepsilon \sim 11{,}000\ M^{-1}\ cm^{-1}$; 383 nm, $\varepsilon \sim 13{,}000$

M^{-1} cm^{-1}) exist for $[(smif)_2Co](OTf)$, which generates a deep cobalt blue color in THF solution. **7-Co** also possesses a strong low energy absorption at 586 nm with an extinction coefficient of ~ 23,000 M^{-1} cm^{-1}.

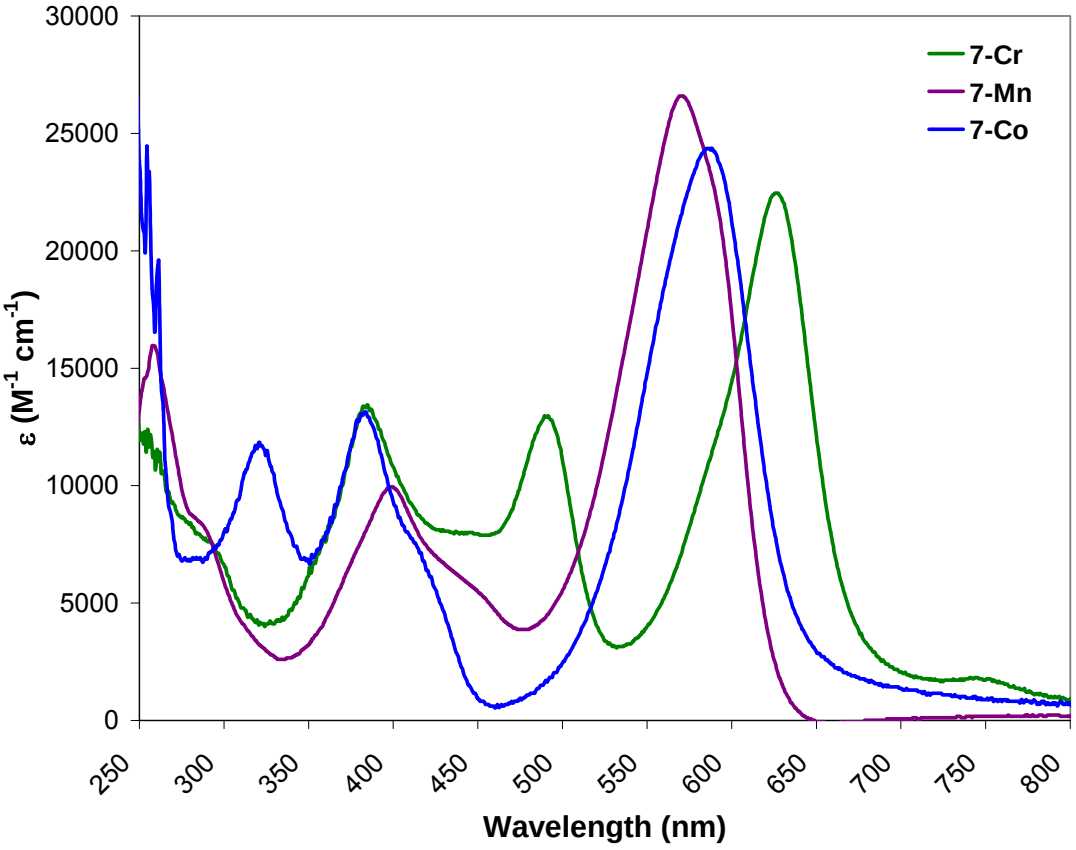

Figure 2.16. UV-vis spectra obtained in THF of $[(smif)_2M](OTf)$ complexes, where M = Cr (**7-Cr**), Mn (**7-Mn**), and Co (**7-Co**).

All $(smif)_2M$ complexes exhibit similar features within the lower energy absorptions in their UV-vis spectra. Based upon the distinctions observed in the pentane UV-vis spectrum of **6-Fe**, shown in Figure 2.14, the bands subsequently listed were acquired from UV-vis spectra obtained in pentane. For **6-V**, these features occur at 471 nm (21,230 cm^{-1}), 514 nm (19,460 cm^{-1}), and 573 nm (17,450 cm^{-1}), and they are separated by 1,770 cm^{-1} and 2,010 cm^{-1}. **6-Cr** shows 1,040 cm^{-1} and 830 cm^{-1}

separations between the features appearing at 17,570 cm^{-1} (569 nm), 16,530 cm^{-1} (605 nm), and 15,700 cm^{-1} (637 nm), whereas an energy difference of 970 cm^{-1} exists for the two features observed in **6-Mn** at 558 nm (17,920 cm^{-1}) and 590 nm (16,950 cm^{-1}). The aforementioned pronounced features exhibited by **6-Fe** appear at 17,860 cm^{-1} (560 nm), 16,580 cm^{-1} (603 nm), and 15,580 cm^{-1} (642 nm) yielding separations of 1,280 cm^{-1} and 1,000 cm^{-1}. Separations of 1,470 cm^{-1} and 1,180 cm^{-1} resulting from the features at 520 nm (19,230 cm^{-1}), 563 nm (17,760 cm^{-1}), and 603 nm (16,580 cm^{-1}) occur in the UV-vis spectrum of **6-Co**. Only two features appear for **6-Ni** and **6-Zn** yielding separations of 1,030 cm^{-1} and 1,020 cm^{-1}, respectively. **6-Ni** exhibits absorptions at 18,450 cm^{-1} (542 nm) and 17, 420 cm^{-1} (574 nm), whereas features for **6-Zn** appear at 538 nm (18,590 cm^{-1}) and 569 nm (17,570 cm^{-1}). All of these bands observed in the low energy regime may be attributed to a progression associated with vibronic coupling to a single electronic IL transition. The observed sharp absorptions between 1,130 cm^{-1} and 1,140 cm^{-1} in the IR spectra of all the aforementioned compounds may potentially serve as indication of the type of vibration likely to couple in the excited state. In the IR spectrum, this previously mentioned absorption may be attributed to a bending vibration of the smif backbone $CN_{aza}C$ that is capable of coupling to the electronic IL transition. Unfortunately, distinguishing these features was rather difficult for the cationic species due to the broadness of the overlapping absorptions.

Table 2.5. Magnetism and UV-vis spectral data for Li(smif) (**5**-Li), $(smif)_2M$ complexes [M = V (**6-V**); Cr (**6-Cr**); Mn (**6-Mn**); Fe (**6-Fe**); Co (**6-Co**); Ni (**6-Ni**); Zn (**6-Zn**)] and $[(smif)_2M](OTf)$ complexes [M = Cr (**7-Cr**); Mn (**7-Mn**); Co (**7-Co**)].

Compound	GS	μ_{eff} (SQUID)	λ_{max} (nm)	ε (M^{-1} cm^{-1})
6-V	3/2	3.4	401	10,000
			471	12,000
			514	11,000
			573	9,000
6-Cr	1	2.7	401	25,000
			490	15,000
			569	12,000
			605	14,000
			637	14,000
7-Cr	3/2	3.5	385	13,000
			492	13,000
			627	22,000
6-Mn	5/2	5.7	403	23,000
			590	60,000
7-Mn	2	5.4	259	16,000
			398	10,000
			571	26,000
6-Fe	0	0	399(sh)	29,000
			441	42,000
			510	19,000
			597	16,000
6-Co	1/2	1.7 (10 K)	401	20,000
		3.2 (300 K)	563	29,000
7-Co	0	0	321	11,000
			383	13,000
			586	23,000
6-Ni	1	2.8	399	18,000
			574	50,000
6-Zn	0	0	398	8,900
			569	24,000
5-Li	0	0	420	7,000
			583	18,000

EPR Studies on $(smif)_2M^n$ Complexes [n = 0, M = V, Cr, Mn, Co, Ni; n = +1, M = Cr]. Several $(smif)_2M$ complexes have unpaired electrons warranting the use of electron paramagnetic resonance (EPR) spectroscopy for further characterization. At 5.5 K, a toluene glass of **6-V** yields a broad EPR spectrum, consistent with an S = 3/2 GS (Figure 2.17). Three g values are observed: 1.92, 2.5, and 5.7. The vanadium hyperfine observed at g = 2.0 is consistent with a VO^{2+} impurity, and an unidentified 8-line peak occurs at a g value of 5.7, which also appears to possess vanadium hyperfine. That 8-line peak, however, was not modeled in the simulation.

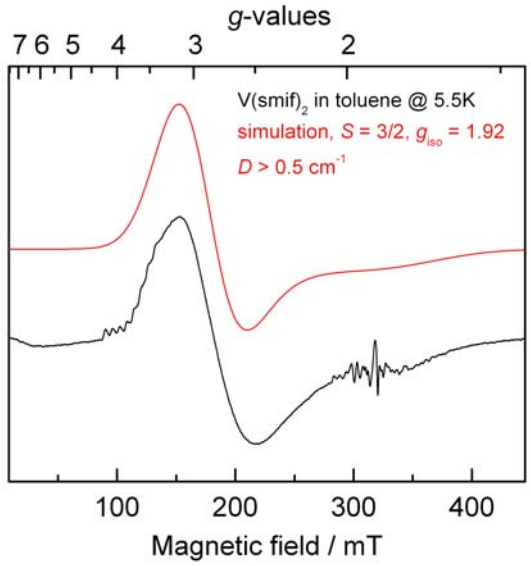

Figure 2.17. EPR spectrum of $(smif)_2V$ in toluene at 5.5 K containing the experimental spectrum (black) with an overlay of the simulated spectrum (red).

Unexpectedly, **6-Cr**, an S = 1 complex, yielded a rhombic EPR spectrum in toluene. As shown in Figure 2.18, the spectrum, which is consistent with an S = 1 species, possesses three g values of 1.980, 1.980, 2.000, and the line widths are 20, 30, and 40 Gauss. The best fit of the data yielded a D value of 0.004 and an E/D ~ 1/3. The spectrum does not arise from an impurity in an otherwise EPR silent sample, as

may be expected for an S = 1 compound, as spin quantification with $CuSO_4$ permitted the counting of 65% spins implying the spectrum was in fact **6-Cr**.

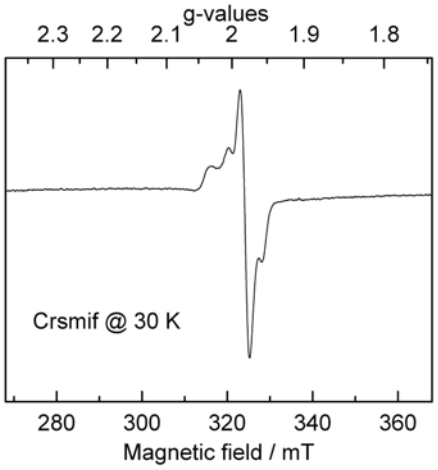

Figure 2.18. EPR spectrum of $(smif)_2Cr$ in toluene at 30 K.

Similar to **6-V**, **7-Cr** yields a very broad EPR spectrum in CH_3CN at 6 K with a g value of 2.05, consistent with an S = 3/2 species (Figure 2.19). A broad EPR spectrum of **6-Mn** was obtained, consistent with an S = 5/2 species.

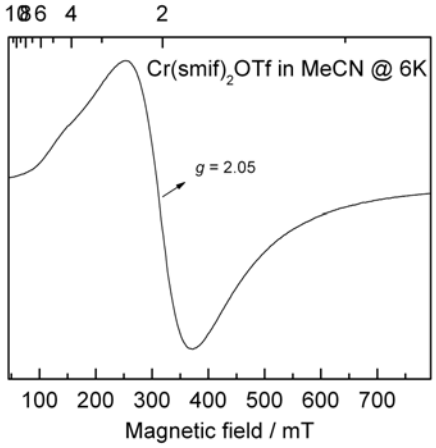

Figure 2.19. EPR spectrum of $[(smif)_2Cr](OTf)$ in CH_3CN at 6 K.

A rhombic EPR spectrum exists for **6-Co** at 30 K in toluene, consistent with an S = 1/2 species (Figure 2.20). The g values of 2.01, 2.135, and 2.21 possess hyperfine coupling of 44 Gauss, 66 Gauss, and 64 Gauss, respectively. An EPR spectrum consistent with the S = 3/2 species was not observed at any temperature, presumably due to relaxation at temperatures where observable amounts of S = 3/2 species would be present. **6-Ni** was EPR silent, as expected for an S = 1 species.

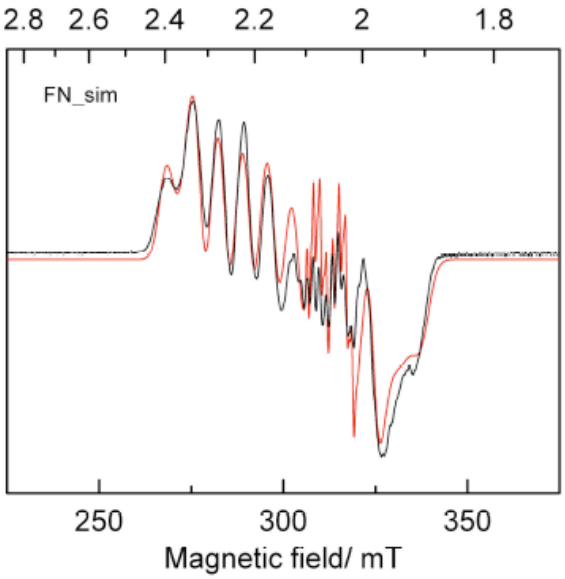

Figure 2.20. EPR spectrum of $(smif)_2Co$ in toluene at 30 K containing the experimental spectrum (black) with an overlay of the simulated spectrum (red).

XAS Spectroscopy. Identifying the oxidation state for a compound is typically simple. For example, $(smif)_2Fe$ is a diamagnetic species comprised of two anionic ligands, consistent with the assignment of a low spin, S = 0, Fe(II) metal center. Complications may arise in pinpointing the oxidation state of species, e.g. $(smif)_2Co$, and warrant the use of x-ray absorption spectroscopy (XAS) to gain a better grasp on the effective nuclear charge of the metal center. A comparison study between the neutral and oxidized complexes for chromium and cobalt lends itself toward assigning oxidation states for all species involved. If a metal-based oxidation occurs, the

effective nuclear charge observed for the neutral and cationic species will be different. On the contrary, a ligand-based oxidation will not alter the effective nuclear charge between the neutral and cationic species, thus the charges will remain the same. As shown in Figure 2.21, the XAS data for **6-Cr** and **7-Cr** display the same effective nuclear charge for both species in the Cr K-edge spectra, thereby suggesting a primarily ligand-based oxidation. Close inspection of the Cr K pre-edge implies a very similar ligand field splitting for both species. A comparison of Cr K-edge spectra for **6-Cr** and **7-Cr** with *trans*-$[CrCl_2(H_2O)_4]Cl$, a Cr(III) reference, suggests an assignment of Cr(III) is correct.

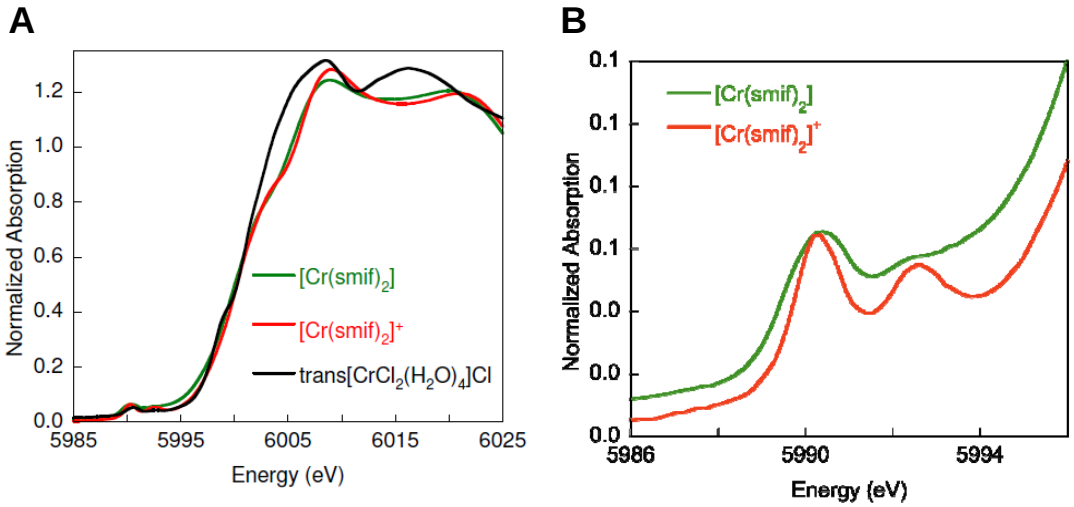

Figure 2.21. Normalized Cr K-edge XAS spectra obtained for $(smif)_2Cr$ (green) and $[(smif)_2Cr](OTf)$ (red). Comparison of **6-Cr** and **7-Cr** with *trans*-$[CrCl_2(H_2O)_4]Cl$, a Cr(III) reference (**A**) and expanded Cr K pre-edge (**B**).

Alternatively, a primarily metal-based oxidation occurs for the transformation from **6-Co** to **7-Co** as indicated by the XAS data, which shows a significant change, i.e. ~ 2 eV, in the effective nuclear charge upon oxidation (Figure 2.22). The Co K pre-edge suggests an increase in the ligand field upon oxidation. An assignment of

Co(II) for **6-Co** and Co(III) for **7-Co** seems appropriate based upon a comparison of their Co K-edge spectra with a Co(III) reference, i.e. $[Co(en)_3]^{3+}$.

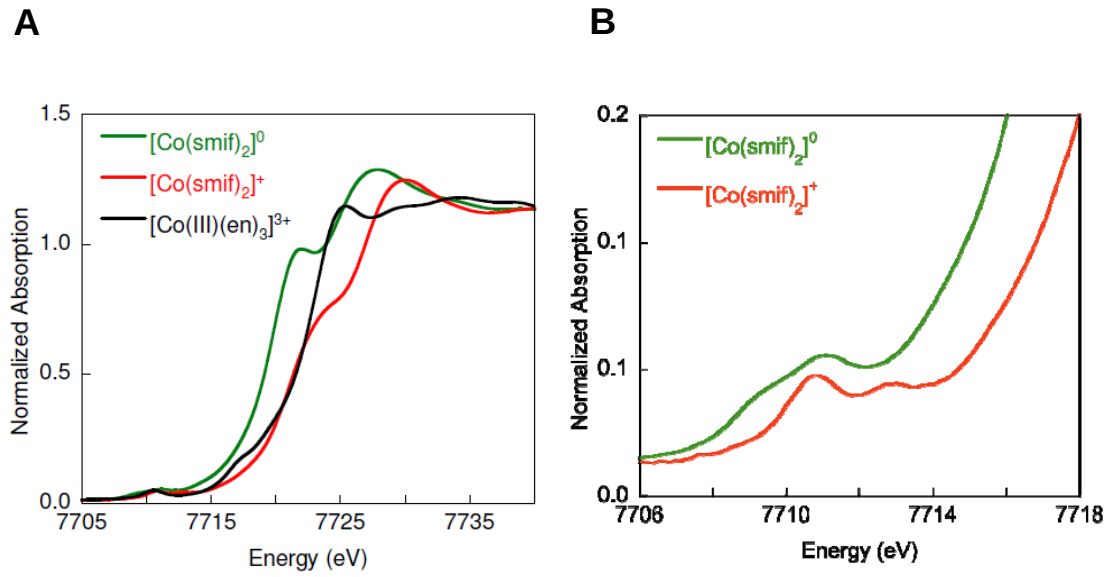

Figure 2.22. Normalized Co K-edge XAS spectra obtained for $(smif)_2Co$ (green) and $[(smif)_2Co](OTf)$ (red). Comparison of **6-Co** and **7-Co** with $[Co(en)_3]^{3+}$, a Co(III) reference (**A**) and expanded Cr K pre-edge (**B**).

Mössbauer Spectroscopy of $(smif)_2Fe$ (6-Fe). A better grasp on the oxidation state, covalency, and overall charge distribution of an iron complex may be obtained via Mössbauer spectroscopy. The Mössbauer spectrum previously reported for $[(smifH)_2Fe](ClO_4)_2$ possesses an isomer shift (δ) of 0.188 mm/s with quadrupole splitting (ΔE_Q) of -0.925 mm/s.[54] Similarly, the Mössbauer spectrum of $(smif)_2Fe$, shown in Figure 2.23, reveals an δ of 0.30(1) mm/s with a ΔE_Q value of 0.62(1) mm/s and line widths (Γ_{FWHM}) of 0.25(1) mm/s at 80 K. Small ΔE_Q values suggest the presence of a moderately symmetric electric field about the iron center, and δ values closer to zero are consistent with low spin Fe(II) centers,[55-58] thereby suggesting **6-Fe** possesses a covalent, low spin Fe(II) center.

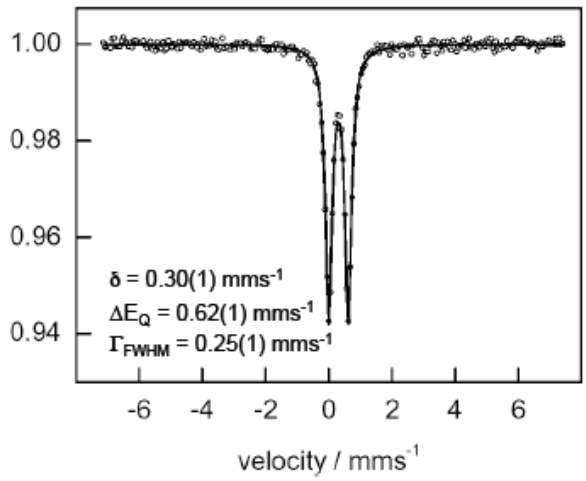

Figure 2.23. Mössbauer spectrum of $(smif)_2Fe$ at 80 K.

DFT Calculations on $(smif)_2M$ Complexes [M = V, Cr, Mn, Fe, Co, Ni].

Density functional theory[59-63] (DFT) calculations permit a better understanding of the electronic structures, magnetism, geometries, and optical features observed for a given complex. Initial DFT investigations on $(smif)_2Fe$ show a low spin Fe(II) center containing predominantly metal-based fully occupied "t_{2g}" orbitals [d_{xy} (b_1) plus d_{xz} and d_{yz} (e set) in D_{2d} symmetry] and empty "e_g" orbitals [$d_{x^2-y^2}$ (b_2) and d_{z^2} (a_1)], as shown in Figure 2.24. All remaining orbitals are primarily ligand-based. The "t_{2g}" set is energetically higher than an occupied smif π orbital set, yet the "t_{2g}" set does not contain the highest occupied molecular orbitals (HOMO). Fully occupied nonbonding carbon-based (C^{nb}) azaallyl backbone orbitals of a_2 and b_1 symmetry rise above these "t_{2g}" orbitals, and are of appropriate symmetry to permit intraligand (IL) transitions to the smif π* lowest unoccupied molecular orbitals (LUMO). Optical features observed in the UV-vis spectra are attributed to these IL transitions between C^{nb} and smif-π* orbitals. Time-dependent DFT (TDDFT) calculations on **6-Fe** permits the proposed identification of d-d transitions at ~ 18,000 cm^{-1} and 25,000 cm^{-1} in the UV-vis spectrum, and the calculated splittings between the "e_g" and "t_{2g}" orbitals (described

above) in O_h symmetry are less than 1,600 cm^{-1}. A Tanabe-Sugano fit shows $\Delta_o \sim$ 18,000 cm^{-1} and $B \approx 470$ cm^{-1}. These parameters corroborate the covalency observed in the Mössbauer parameters.

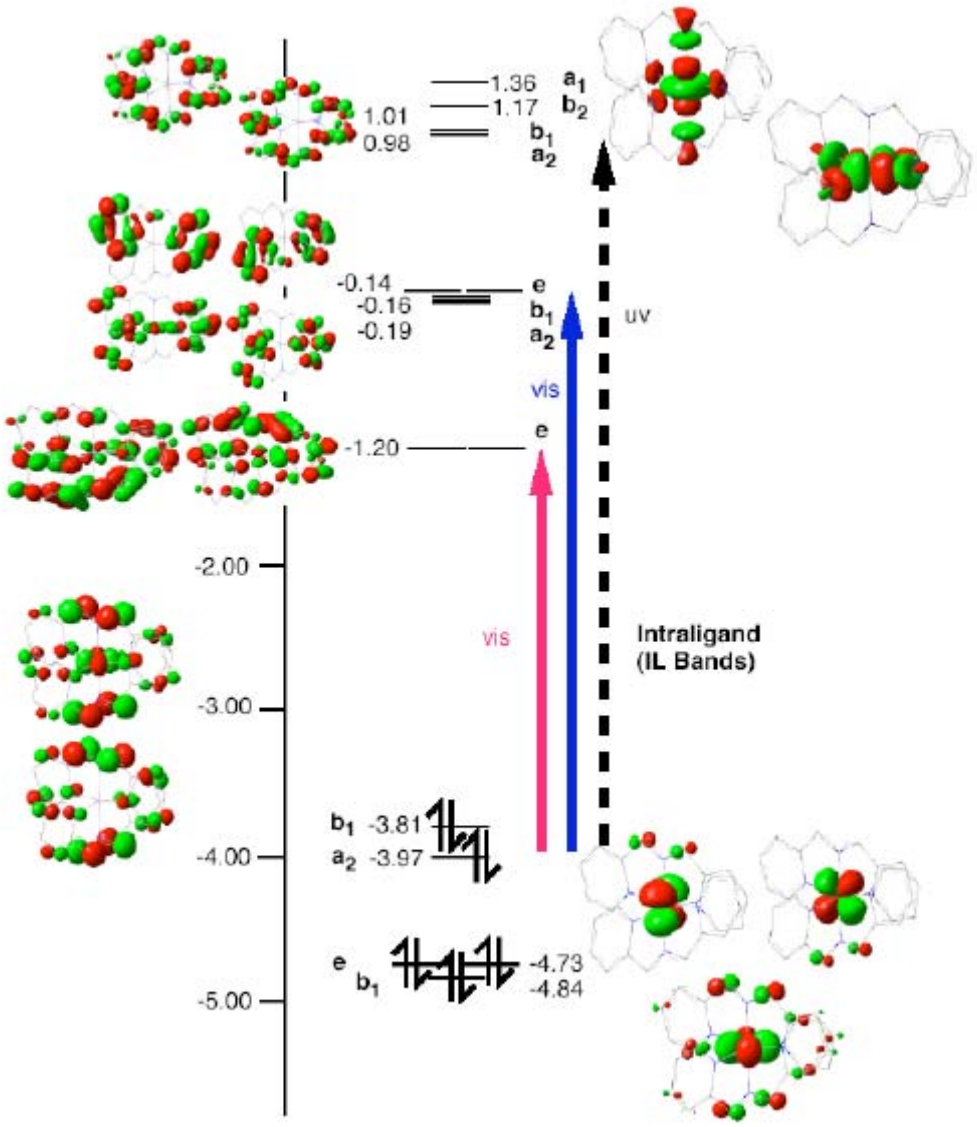

Figure 2.24. DFT calculations on $(smif)_2Fe$.

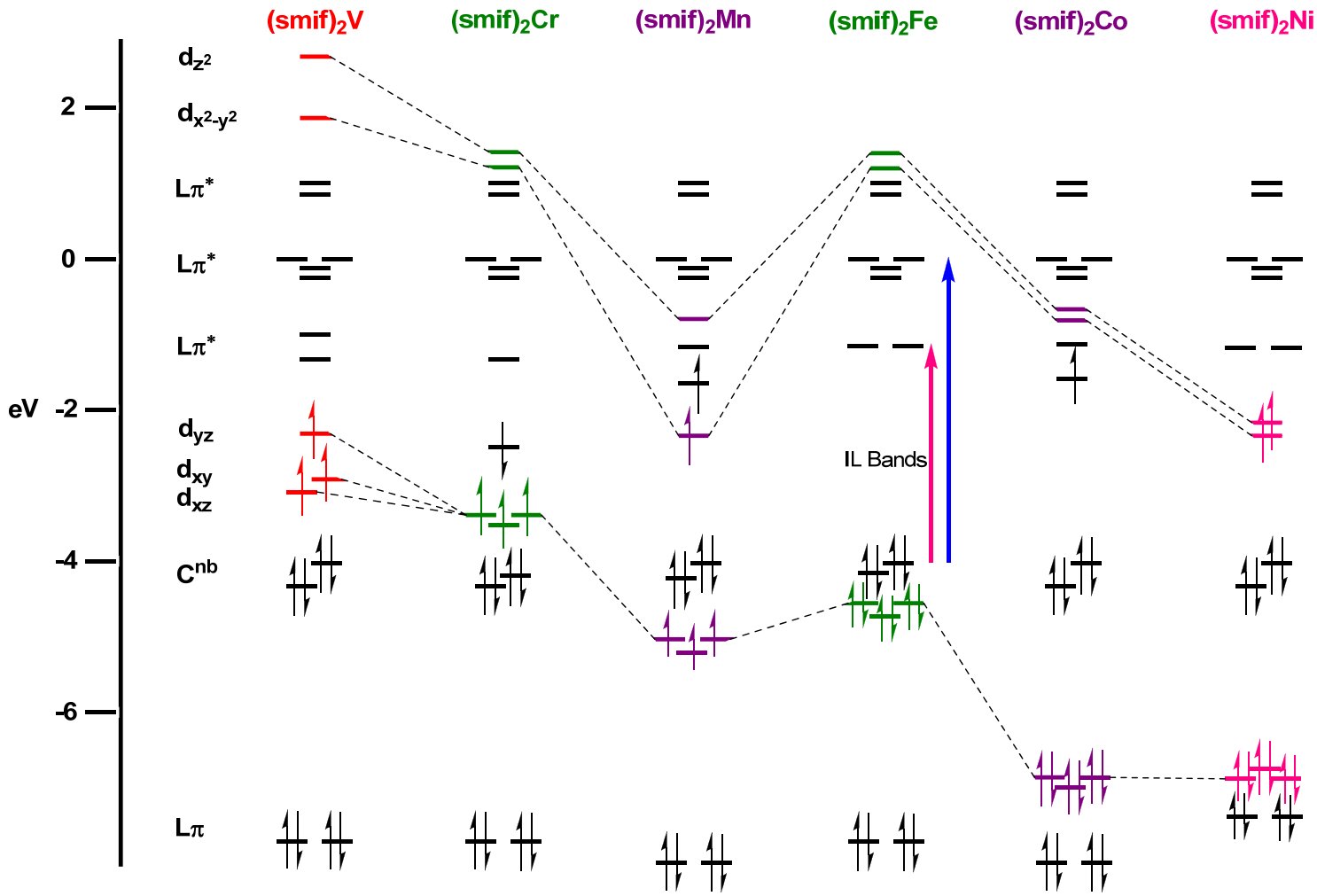

Figure 2.25. Truncated molecular orbital diagrams for (smif)2M, where M = V, Cr, Mn, Fe, Co, and Ni, were generated from DFT calculations. Orbital energies of open-shell systems were derived from averaging the α and β spins.

DFT calculations on the remaining smif complexes, i.e. **6-V**, **6-Cr**, **6-Mn**, **6-Co**, and **6-Ni**, show that the azaallyl backbone C^{nb} orbitals possess essentially the same energy, - 4.0 eV, for all compounds within the series (Figure 2.25). They retain the appropriate symmetry to allow for the IL transitions (C^{nb} to smif-π*) observed in the UV-vis spectra, and smif-π and smif-π* orbitals also remain around the same energy throughout. As expected, energies for "t_{2g}" and "e_g" orbitals decrease as Z_{eff} increases for the metal center.

In the case of **6-Ni**, DFT calculations agree with experimental data, and an appropriate electronic description may be Ni(II), $(t_{2g})^6(C^{nb})^4(e_g)^2$. A triplet GS is predicted, consistent with the S = 1 species exhibiting both a μ_{eff} of 2.8 μ_B and EPR silence. Placement of the unpaired electrons in the "e_g" orbitals, which have dropped below the smif-π* orbitals, seems reasonable as the crystal structure reveals only slightly distorted molecules within the asymmetric unit. A ligand-localized unpaired electron may result in greater distortions from D_{2d} symmetry.

Discrepancies between experimental data and DFT calculations arise in the study of **6-Co**. Calculations favor a doublet GS, consistent with the S = 1/2 species observed in the EPR spectrum and SQUID magnetometry data at 10 K yielding a μ_{eff} of 1.7 μ_B. Nevertheless, a quartet state must be energetically close based on the observation of μ_{eff} of 3.2 μ_B at 300 K, indicative of an intermediate spin system between an S = 1/2 GS and S = 3/2 GS. DFT calculations predict the unpaired electron resides in a smif-π* orbital implying that **6-Co** is best described as Co(III). However, Co K-edge XAS data suggests that a singly occupied "e_g" orbital should be energetically lower than the smif-π* orbitals, as the data reveals a change in effective nuclear charge upon the oxidation of **6-Co** resulting in **7-Co**, indicative of a predominantly metal based oxidation. A more appropriate description for **6-Co** is Co(II), $(t_{2g})^6(C^{nb})^4(e_g)^1$, whereas **7-Co** would best be described as Co(III), $(t_{2g})^6(C^{nb})^4$.

DFT calculations favor a sextet GS for **6-Mn** corroborating with the magnetic moment of 5.8 μ_B observed at 293 K. Various levels of sophisticated theory have a difficult time finding an appropriate model for **6-Mn**. Based solely upon DFT calculations, it seems appropriate to described **6-Mn** as Mn(III), $(t_{2g})^3(C^{nb})^4(e_g)^1(L\pi^*)^1$. However, multireference calculations report a standard Mn(II) S = 5/2 GS, where all unpaired electrons lie in metal based orbitals.

Experimental data and DFT calculations agree on an S = 1 GS for **6-Cr**, matching the μ_{eff} of 2.8 μ_B observed at 293 K. Cr K-edge XAS data indicate the effective nuclear charge for **6-Cr** and **7-Cr** is best described as Cr(III), which is also depicted in the DFT calculations. The unpaired electron highest in energy resides in a smif-π^* orbital and is antiferromagnetically coupled to an electron in the "t_{2g}" set resulting in the observed S = 1 GS. The distortions away from D_{2d} symmetry observed in the crystal structure may result from the presence of an electron in ligand π^* system. Therefore, **6-Cr** may be appropriately described as Cr(III), $(C^{nb})^4(t_{2g})^3(L\pi^*)^1$ and **7-Cr** would best be depicted as $(C^{nb})^4(t_{2g})^3$ with a Cr(III) metal center.

Calculations corroborate with experimental data for **6-V**. DFT calculations predict an S = 3/2 GS. Both the EPR spectrum and magnetism data, i.e. μ_{eff} of 3.6 μ_B at 293 K, for **6-V** suggest an S = 3/2 GS. The highest occupied orbital, assigned as d_{yz}, is an orbital comprised of 50 % metal character and 50% ligand character.

Conclusions

A new homologous series of 1st-row $(smif)_2M$ complexes, where M = V, Cr, Mn, Fe, Co, and Ni, was synthesized. Explorations in redox chemistry led to the synthesis of three $[(smif)_2M](OTf)$ complexes for M = Cr, Mn, and Co. To gain a better understanding of the smif ligand, complete physical inorganic characterization techniques were employed: single crystal x-ray crystallography, UV-vis spectroscopy,

SQUID magnetometry, electrochemistry, EPR, XAS, Mossbauer, and DFT calculations. These investigations suggest that smif, a monoanionic tridentate N-based ligand, is an intermediate field strength ligand possessing the ability to stabilize complexes formally ranging from 15 e^- (**6-V**) to 20 e^- (**6-Ni**). Intense optical properties suggest that smif complexes may lead to applications in photovoltaics.

Experimental

General Considerations. All manipulations were performed using either glovebox or high vacuum line techniques. Hydrocarbon solvents containing 1-2 mL of added tetraglyme, and ethereal solvents were distilled under nitrogen from purple sodium benzophenone ketyl and vacuum transferred from same prior to use. Benzene-d_6 and toluene-d_8 were dried over sodium, vacuum transferred and stored under N_2. THF-d_8 was dried over sodium benzophenone ketyl. $VCl_3(THF)_3$,[45] $CrCl_2(THF)$,[37] $Cr\{N(TMS)_2\}(THF)_2$,[38] $FeBr_2(THF)_2$,[42] $Fe\{N(TMS)_2\}_2(THF)$,[36] $NiCl_2(DME)$,[43] sodium bis(trimethylsilyl)amide,[35] and 1,3-(2-pyridyl)-2-azapropene (**smifH**)[34] were prepared according to literature procedures. Lithium bis(trimethylsilyl)amide was purchased from Aldrich and recrystallized from hexanes prior to use. All other chemicals were commercially available and used as received. All glassware was oven dried.

NMR spectra were obtained using an INOVA 400 spectrometer. Chemical shifts are reported relative to benzene-d_6 (^{1}H δ 7.16; ^{13}C{^{1}H} δ 128.39), toluene-d_8 (^{1}H δ 2.09; ^{13}C{^{1}H} δ 20.4), and THF-d_8 (^{1}H δ 3.58; ^{13}C{^{1}H} δ 67.57). Infrared spectra were recorded on a Nicolet Avatar 370 DTGX spectrophotometer interfaced to an IBM PC (OMNIC software). UV-Vis spectra were obtained on a Shimadzu UV-2102 interfaced to an IBM PC (UV Probe software). Solution magnetic measurements were conducted via Evans' method in toluene-d_8.[46] Solid state magnetic measurements

were performed using a Johnson Matthey magnetic susceptibility balance calibrated with $HgCo(SCN)_4$. Elemental analyses were performed by the services at the University of Erlangen-Nuremberg, Germany.

Synthesis. 1. Li(smif) (5-Li). To a solution of lithium bis(trimethylsilyl)amide (1.273 g, 7.60 mmol) in 50 mL THF was slowly added a solution of **smifH** (1.500 g, 7.60 mmol) in 50 mL THF at -78 °C under argon. The solution immediately turned magenta and was stirred at -78 °C for 2 h prior to warming to 23 °C. After stirring at 23 °C for 2 h, the volatiles were removed *in vacuo*. The solid was triturated with Et_2O and filtered. **5-Li** was isolated as a metallic gold solid (1.389 g, 90 %). ^{1}H NMR (C_6D_6, 400 MHz): δ 5.98 (t, py-C^5*H*, 1 H, J = 8 Hz), 6.50 (d, py-C^3*H*, 1 H, J = 8 Hz), 6.84 (t, py-C^4*H*, 1 H, J = 8 Hz), 7.16 (s, C*H*, 1 H), 7.66 (d, py-C^6*H*, 1 H, J = 4 Hz). ^{13}C{^{1}H} NMR (C_6D_6, 100 MHz): δ 113.20 (*C*H), 117.95 (py-*C*^{3}H), 118.65 (py-*C*^{5}H), 136.18 (py-*C*^{4}H), 148.90 (py-*C*^{6}H), 159.44 (py-*C*^{2}). UV-vis (benzene) = 420 nm (ε ~ 7,000 M^{-1} cm^{-1}), 583 nm (ε ~ 18,000 M^{-1} cm^{-1}).

2. Na(smif) (5-Na). To a solution of sodium bis(trimethylsilyl)amide (1.395 g, 7.60 mmol) in 50 mL THF was slowly added a solution of **smifH** (1.500 g, 7.60 mmol) in 50 mL THF at -78 °C under argon. The solution immediately turned magenta and was stirred at -78 °C for 2 h before warming to 23 °C. After stirring at 23 °C for 2 h, the volatiles were removed *in vacuo*. The solid was triturated with Et_2O (3 x 15 mL) prior to filtering. **5-Na** was isolated as a metallic gold solid (1.602 g, 96 %). ^{1}H NMR (C_6D_6, 400 MHz): δ 6.19 (t, py-C^5*H*, 1 H, J = 5.6 Hz), 6.55 (d, py-C^3*H*, 1 H, J = 8 Hz), 6.97 (t, py-C^4*H*, 1 H, J = 7.2 Hz), 7.04 (s, C*H*, 1 H), 7.72 (d, py-C^6*H*, 1 H, J = 4 Hz). ^{13}C{^{1}H} NMR (C_6D_6, 100 MHz): δ 112.19 (*C*H), 115.70 (py-*C*^{3}H), 119.05 (py-*C*^{5}H), 135.62 (py-*C*^{4}H), 149.81 (py-*C*^{6}H), 160.23 (py-*C*^{2}).

3. $(smif)_2V$ (6-V). To a 50 mL 3-neck flask charged with lithium bis(trimethylsilyl)amide (0.170 g, 1.02 mmol) and 0.95 % sodium amalgam (0.012 g

Na, 0.53 mmol) was vacuum transferred 10 mL THF at -78 °C. A solution of **smifH** (0.200 g, 1.01 mmol) in THF (8 mL) was slowly added to the 3-neck flask via a dropping funnel under argon. The solution immediately turned magenta and stirred at -78 °C for 3 h prior to the addition of $VCl_3(THF)_3$ (0.189 g, 0.51 mmol). The reaction mixture, which turned cherry red after slowly warming to 23°C and stirring for 12 h, was degassed and filtered. The volatiles were removed *in vacuo*, and the microcrystalline gold solid was triturated and filtered in Et_2O to yield 0.185 g of **6-V** (81 %). UV-vis (benzene) = 401 nm (ε ~ 10,000 M^{-1} cm^{-1}), 471 nm (ε ~ 12,000 M^{-1} cm^{-1}), 514 nm (ε ~ 11,000 M^{-1} cm^{-1}), 573 nm (ε ~ 10,000 M^{-1} cm^{-1}). Anal. Calcd. $H_{20}C_{24}N_6V$: C, 65.01; H, 4.55; N, 18.95. Found: C, 65.01; H, 4.55; N, 18.95. μ_{eff} (SQUID, 293 K) = 3.4 μ_B.

4. $(smif)_2Cr$ (6-Cr). To a solution of $Cr\{N(SiMe_3)_2\}_2(THF)_2$ (0.425 g, 0.82 mmol) in 8 mL Et_2O was slowly added a solution of **smifH** (0.325 g, 1.65 mmol) in 10 mL Et_2O at 23 °C. The solution immediately became dark emerald green. The reaction was degassed, warmed to 23 °C, and stirred for 12 h while dark green crystals precipitated from solution. The reaction was concentrated, and the green suspension was filtered to yield 0.288 g of crystalline **6-Cr** (79 %). ^1H NMR (C_6D_6, 400 MHz): δ -103.60 ($\upsilon_{1/2}$ ≈ 1700 Hz, py-C*H*, 1 H), -22.67 ($\upsilon_{1/2}$ ≈ 1900 Hz, py-C*H*, 1 H), -19.83 ($\upsilon_{1/2}$ ≈ 200 Hz, py-C*H*, 1 H), 19.35 ($\upsilon_{1/2}$ ≈ 130 Hz, C*H*, 1 H), 22.08 ($\upsilon_{1/2}$ ≈ 100 Hz, py-C*H*, 1 H). UV-vis (benzene) = 401 nm (ε ~ 29,000 M^{-1} cm^{-1}), 490 nm (ε ~ 19,000 M^{-1} cm^{-1}), 569 nm (ε ~ 14,000 M^{-1} cm^{-1}), 605 nm (ε ~ 16,000 M^{-1} cm^{-1}), 637 nm (ε ~ 18,000 M^{-1} cm^{-1}). Anal. Calcd. $H_{20}C_{24}N_6Cr$: C, 64.86; H, 4.54; N, 18.91. Found: C, 64.86; H, 4.54; N, 18.91. μ_{eff} (SQUID, 293 K) = 2.7 μ_B.

5. $(smif)_2Mn$ (6-Mn). To a solution of lithium bis(trimethylsilyl)amide (0.425 g, 2.54 mmol) in 15mL THF at -78 °C was added dropwise a solution of **smifH** (0.500 g, 2.53 mmol) in 10 mL THF under argon. The solution immediately turned

magenta and stirred at -78 °C for 2 h prior to the addition of $MnCl_2$ (0.160 g, 1.27 mmol). The reaction mixture became deep purple after stirring at 23 °C for 36 h. The volatiles were removed *in vacuo*, and the solid was dissolved and filtered in toluene. Toluene was removed, and the solid was triturated and filtered in Et_2O to isolate metallic gold crystals of **6-Mn** (0.410 g, 72 %). ^{1}H NMR (C_6D_6, 400 MHz): δ -13.52 ($\upsilon_{1/2} \approx 1200$ Hz, py-C*H*, 1 H), 48.08 ($\upsilon_{1/2} \approx 4100$ Hz, py-C*H*, 1 H). UV-vis (benzene) = 403 nm ($\varepsilon \sim 23{,}000$ M^{-1} cm^{-1}), 590 nm ($\varepsilon \sim 60{,}000$ M^{-1} cm^{-1}). Anal. Calcd. $H_{20}C_{24}N_6Mn$: C, 64.43; H, 4.51; N, 18.78. Found: C, 64.21; H, 4.40; N, 18.52. μ_{eff} (SQUID, 293 K) = 5.7 μ_B.

6. (smif)$_2$Fe (6-Fe). A) To a solution of $Fe\{N(SiMe_3)_2\}_2(THF)$ (0.284 g, 0.63 mmol) in 15 mL Et_2O was slowly added a solution of **smifH** (0.250 g, 1.27 mmol) in Et_2O (15 mL) at 23 °C. The solution immediately changed from pale green to deep forest green. The reaction was degassed and warmed to 23 °C. Black-metallic purple crystals began to precipitate from solution after stirring for 30 min. The reaction mixture was stirred for an addition 9.5 h. The volatiles were removed, and the solid was triturated and filtered in Et_2O to yield black-metallic purple crystals of **6-Fe** (0.229 g, 80 %). **B)** A solution of **smifH** (5.00 g, 25.35 mmol) in 100 mL THF was added dropwise to a solution of lithium bis(trimethylsilyl)amide (4.242 g, 25.35 mmol) in 50 mL THF at -78 °C under argon. The solution turned magenta and was stirred at -78 °C for 3 h prior to the addition of $FeBr_2(THF)_2$ (4.561 g, 12.67 mmol). After stirring at 23 °C for 16 h, a purple crystalline solid precipitated from the forest green solution. The volatiles were removed *in vacuo*, and the residue was dissolved in toluene and filtered. Toluene was removed, and the solid was triturated with Et_2O and filtered to yield black-metallic purple crystals of **6-Fe** (2.980 g, 52 %). ^{1}H NMR (C_6D_6, 400 MHz): δ 5.73 (t, py-C^5*H*, 1 H, J = 5.9 Hz), 6.11 (d, py-C^3*H*, 1 H, J = 7.9 Hz), 6.38 (t, py-C^4*H*, 1 H, J = 7.8 Hz), 7.59 (s, *CH, 1* H), 7.66 (d, py-C^6*H*, 1 H, J = 5.2

Hz). $^{13}C\{^1H\}$ NMR (C_6D_6, 100 MHz): δ 112.19 (*C*H), 115.64 (py-*C*^{3}H), 118.34 (py-*C*^{5}H), 134.68 (py-*C*^{4}H), 151.81 (py-*C*^{6}H), 165.65 (py-*C*^{2}). UV-vis (benzene) = 399 nm (sh, ε ~ 29,000 M^{-1} cm^{-1}), 441 nm (ε ~ 42,000 M^{-1} cm^{-1}), 510 nm (ε ~ 19,000 M^{-1} cm^{-1}), 597 nm (ε ~ 16,000 M^{-1} cm^{-1}). Mössbauer parameters (80 K): δ = 0.30(1) mms^{-1}, ΔE_Q = 0.62(1) mms^{-1}, Γ_{FWHM} = 0.25(1) mms^{-1}. Anal. Calcd. $H_{20}C_{24}N_6Fe$: C, 64.30; H, 4.50; N, 18.75. Found: C, 63.76; H, 4.64; N, 17.69.

7. (smif)$_2$Co (6-Co). To a solution of lithium bis(trimethylsilyl)amide (0.425 g, 2.54 mmol) in 15 mL THF at -78 °C was added dropwise a solution of **smifH** (0.500 g, 2.53 mmol) in 10 mL THF under argon. The reaction solution immediately turned magenta and was stirred at -78 °C for an additional 2 h prior to the addition of $CoCl_2$ (0.165 g, 1.27 mmol). After stirring at 23 °C for 36 h, the solution had darkened to a deep purple-magenta. The volatiles were removed, and the residue was dissolved and filtered in toluene. Toluene was removed *in vacuo*, and the solid was triturated with Et_2O and filtered to yield metallic gold crystals of **6-Co** (0.501 g, 87 %). ^1H NMR (C_6D_6, 400 MHz): δ 10.06 ($\upsilon_{1/2}$ ≈ 50 Hz, C*H*, 1 H), 37.63 ($\upsilon_{1/2}$ ≈ 70 Hz, py-C*H*, 1 H), 39.90 ($\upsilon_{1/2}$ ≈ 80 Hz, py-C*H*, 1 H), 85.19 ($\upsilon_{1/2}$ ≈ 140 Hz, py-C*H*, 1 H), 108.94 ($\upsilon_{1/2}$ ≈ 480 Hz, py-C*H*, 1 H). UV-vis (benzene) = 401 nm (ε ~ 20,000 M^{-1} cm^{-1}), 563 nm (ε ~ 29,000 M^{-1} cm^{-1}). Anal. Calcd. (for (smif)$_2$Co·(C_7H_8)$_{0.5}$) $H_{24}C_{27.5}N_6Co$: C, 66.40; H, 4.86; N, 16.89. Found: C, 65.92, 64.99; H, 4.68, 4.47; N, 17.23, 16.92. μ_{eff} (SQUID, 10 K) = 1.7 μ_B and μ_{eff} (SQUID, 293 K) = 2.8 μ_B.

8. (smif)$_2$Ni (6-Ni). A solution of lithium bis(trimethylsilyl)amide (0.425 g, 2.54 mmol) in 15 mL THF under argon at -78 °C was slowly treated with a solution of **smifH** (0.500 g, 2.53 mmol) in THF (10 mL). The solution instantly turned magenta and was stirred at -78 °C for 2 h prior to the addition of $NiCl_2$(dme) (0.278 g, 1.27 mmol). After stirring at 23 °C for 36 h, the volatiles were removed *in vacuo* from the magenta reaction mixture. The solid was dissolved and filtered in toluene. Toluene

was removed, and the solid was triturated and filtered in Et_2O to yield metallic gold crystals of **6-Ni** (0.385 g, 67 %). ^{1}H NMR (C_6D_6, 400 MHz): δ 9.40 ($\upsilon_{1/2} \approx 170$ Hz, C*H*, 1 H), 51.75 ($\upsilon_{1/2} \approx 400$ Hz, py-C*H*, 1 H), 57.01 ($\upsilon_{1/2} \approx 470$ Hz, py-C*H*, 1 H), 140.85 ($\upsilon_{1/2} \approx 3300$ Hz, py-C*H*, 1 H), 248.32 ($\upsilon_{1/2} \approx 6200$ Hz, py-C*H*, 1 H). UV-vis (benzene) = 399 nm (ε ~ 18,000 M^{-1} cm^{-1}), 574 nm (ε ~ 50,000 M^{-1} cm^{-1}). Anal. Calcd. (for $(smif)_2Ni\cdot(C_6H_6)_{0.5}$) $H_{23}C_{27}N_6Ni$: C, 66.15; H, 4.73; N, 17.14. Found: C, 65.52; H, 4.61; N, 17.13. μ_{eff} (SQUID, 293K) = 2.8 μ_B.

9. $(smif)_2$Zn (6-Zn). To a solution of lithium bis(trimethylsilyl)amide (0.425 g, 2.54 mmol) in 10 mL THF was slowly added a solution of **smifH** (0.500 g, 2.53 mmol) in 10 mL THF at -78 °C under argon. The solution immediately turned magenta and was stirred at -78 °C for 2 h prior to the addition of $ZnCl_2$ (0.173 g, 1.27 mmol). After the reaction stirred at 23 °C for 16 h, the volatiles were removed *in vacuo*. The solid was filtered in toluene, triturated with Et_2O and filtered in cold Et_2O to isolate **6-Zn** as a metallic gold solid (0.275 g, 47 %). Spectral parameters correspond to the previously published compound.[33] UV-vis (benzene) = 398 nm (ε ~ 8,900 M^{-1} cm^{-1}), 569 nm (ε ~ 24,000 M^{-1} cm^{-1}).

10. [$(smif)_2$Cr](OTf) (7-Cr). To a 25 mL round bottom flask charged with **6-Cr** (0.300 g, 0.67 mmol) and AgOTf (0.173 g, 0.67 mmol) was vacuum transferred 8 mL Et_2O at -78 °C. The reaction mixture became jester green within 5 min. The flask warmed slowly to 23 °C and was stirred for 2 d while a dark green solid precipitated from the pale blue solution. The volatiles were removed *in vacuo*. Recrystallization of the dark green solid in THF at 80 °C under a blanket of argon for 16 h led to the formation of metallic red crystals of **7-Cr** (0.309 g, 75 %). ^{1}H NMR (C_6D_6, 400 MHz): δ -12.19 ($\upsilon_{1/2} \approx 600$ Hz, py-C*H*, 1 H), -3.95 ($\upsilon_{1/2} \approx 600$ Hz, py-C*H*, 1 H). UV-vis (THF) = 385 nm (ε ~ 13,000 M^{-1} cm^{-1}), 492 nm (ε ~ 13,000 M^{-1} cm^{-1}), 627 nm (ε ~ 22,000 M^{-1} cm^{-1}). μ_{eff} (Gouy balance, 295 K) = 3.56 μ_B. μ_{eff} (SQUID, 293 K) = 3.5 μ_B.

11. [(smif)$_2$Mn](OTf) (7-Mn). To a 100 mL round bottom flask charged with **6-Mn** (0.700 g, 1.56 mmol) and AgOTf (0.402 g, 1.56 mmol) was vacuum transferred 50 mL THF at -78 °C. The dark magenta-purple solution slowly warmed to 23 °C and darkened to a deeper purple. After stirring at 23 °C for 1.5 d, the volatiles were removed *in vacuo* resulting in a red-bronze metallic solid which was filtered in toluene and THF. Filtrates were concentrated, cooled to -78 °C, and filtered to yield metallic red-bronze microcrystals of **7-Mn**(0.728 g, 78 %). UV-vis (THF) = 217 nm (ε ~ 15,000 M^{-1} cm^{-1}), 259 nm (ε ~ 16,000 M^{-1} cm^{-1}), 398 nm (ε ~ 10,000 M^{-1} cm^{-1}), 571 nm (ε ~ 26,000 M^{-1} cm^{-1}). Anal. Calcd. $H_{20}C_{25}N_6O_3F_3SMn$: C, 50.34; H, 3.38; N, 16.66; S, 5.38. Found: C, 50.18; H, 5.50; N, 12.75; S, 5.56. μ_{eff} (Gouy balance, 295K) = 5.0 μ_B. μ_{eff} (SQUID, 295 K) = 5.4 μ_B.

12. [(smif)$_2$Co](OTf) (7-Co). To a 10 mL round bottom flask charged with 0.200 g (0.44 mmol) **6-Co** and 0.114 g (0.44 mmol) AgOTf was vacuum transferred 8 mL THF at -78 °C. The reaction mixture changed from deep purple to cobalt blue within 5 min and slowly warmed to 23 °C. After stirring at 23 °C for 12 h, a magenta solid precipitated from solution. The volatiles were removed *in vacuo*. Recrystallization of the magenta solid in THF at 80 °C under a blanket of argon for 16 h led to the formation of metallic red crystals of **7-Co** (0.215 g, 81 %). ^{1}H NMR (THF-d_8, 400 MHz): δ 6.55 (t, py-C^5*H*, 1 H, J = 6.4 Hz), 6.85 (d, py-C^3*H*, 1 H, J = 8 Hz), 7.24 (s, C*H*, *1* H), 7.28 (t, py-C^4*H*, 1 H, J = 7.2 Hz), 7.59 (d, py-C^6*H*, 1 H, J = 6.0 Hz). ^{13}C{^{1}H} NMR (THF-d_8, 100 MHz): δ 117.47 (*C*H), 118.23 (py-*C*^{3}H), 119.54 (py-*C*^{5}H), 120.36 (py-*C*^{4}H), 139.24 (py-*C*^{6}H), 148.56 (py-*C*^{2}). UV-vis (THF) = 321 nm (ε ~ 11,000 M^{-1} cm^{-1}), 383 nm (ε ~ 13,000 M^{-1} cm^{-1}), 586 nm (ε ~ 23,000 $M^{-1}cm^{-1}$).

13. [(smifH)$_2$Fe][BF$_4$]$_2$ (8-Fe(BF$_4$)$_2$). Tetrafluoroboronic acid diethyl ether complex (0.18 mL, 1.32 mmol) was slowly added via syringe under argon to a stirring solution of **6-Fe** (0.300 g, 0.67 mmol) in 15 mL THF at -78°C. Upon warming to

23°C, the color changed from forest green to magenta-purple. The reaction mixture stirred for 16 h, was degassed, and filtered. The volatiles were removed, and the solid was washed with Et_2O and dried *in vacuo*. **8-Fe(BF$_4$)$_2$** was obtained as a magenta-purple solid (0.364 g, 87 %). ^{1}H NMR (D_2O, 400 MHz): δ 6.64 (q, CH_2, 2 H, J = 22 Hz), 6.97 (t, py-C^5*H*, 1 H, J = 6.8 Hz), 7.13 (t, py^{im}-C^4*H*, 1 H, J = 6.8 Hz), 7.50 (d, py-C^3*H*, 1 H, J = 7.2 Hz), 7.59 (t, py-C^4*H*, 1 H, J = 7.6 Hz), 7.64 (d, py^{im}-C^3*H*, 1 H, J = 5.2 Hz), 7.79 (t, py^{im}-C^5*H*, 1 H, J = 7.6 Hz), 7.84 (d, py-C^6*H*, 1 H, J = 5.2 Hz), 8.14 (d, py^{im}-C^6*H*, 1 H, J = 8.0 Hz), 10.27 (s, im-C*H*, 1 H).

14. [(smifH)(smif)Fe][BF$_4$] (9-Fe(BF$_4$)). To a J-Young tube charged with **8-Fe(BF$_4$)$_2$** (0.010 g, 0.016 mmol) and **6-Fe** (0.007 g, 0.016 mmol) was vacuum transferred 0.5 mL of CD_3CN resulting in a dark black solution with solid consistent with **9-Fe(BF$_4$)**. ^{1}H NMR (CD_3CN, 600 MHz): δ 6.01 (t, py^{smif}-C^5*H*, 2 H, J = 6.5 Hz), 6.36 (s, 2 H, py-CH_2), 6.52 (d, 2 H, py^{smif}-C^3*H*, J = 8.6 Hz), 6.71 (d, 2 H, py^{smif}-C^6*H*, J = 5.6 Hz), 6.91 (t, 2 H, py^{smif}-C^4*H*, J = 7.1 Hz), 7.15 (t, 1 H, py^{im}-C^5*H*, J = 6.7 Hz), 7.28 (t, 1 H, py-C^5*H*, J = 6.7 Hz), 7.48 (d, 1 H, py^{im}-C^3*H*, J = 7.9 Hz), 7.64 (t, 1 H, py^{im}-C^4*H*, J = 7.4 Hz), 7.71 (s, 2 H, smif-C*H*), 7.74 (t, 1 H, py-C^4*H*, J = 8.0 Hz), 8.06 (d, 1 H, py-C^3*H*, J = 8.0 Hz), 8.15 (d, 1 H, py-C^6*H*, J = 5.6 Hz), 8.45 (d, 1 H, py^{im}-C^6*H*, J = 5.6 Hz), 10.25 (s, im-C*H*, 1 H).

Magnetic Susceptibility Measurements. Magnetic susceptibility measurements of crystalline powdered samples (10-30 mg) were performed on a Quantum Design MPMS-5 SQUID magnetometer at 10 kOe between 5 and 300 K for all samples. All sample preparations and manipulations were performed under an inert atmosphere to due to the air sensitivity of the samples. The samples were either measured in a flame sealed NMR tube or a custom machine sealed Teflon capsule. The diamagnetic contribution from the sample container was subtracted from the

experimental data. Pascal's constants[64] were used to subtract diamagnetic contributions, yielding paramagnetic susceptibilities.

Mössbauer Spectroscopy. ^{57}Fe Mössbauer spectra were recorded on a WissEl Mössbauer spectrometer (MRG-500) at 77 K in constant acceleration mode. ^{57}Co/Rh was used as the radiation source. WinNormos for Igor Pro software has been used for the quantitative evaluation of the spectral parameters (least-squares fitting to Lorentzian peaks). The minimum experimental line widths were 0.20 mms^{-1}
The temperature of the samples was controlled by an MBBC-HE0106 MÖSSBAUER He/N_2 cryostat within an accuracy of ±0.3 K. Isomer shifts were determined relative to α-iron at 298 K.

XAS Spectroscopy. XAS data were measured at the Stanford Synchrotron Radiation Lightsource using focused beam line 9-3, under ring conditions of 3 GeV and 60-100 mA. A Si(220) double-crystal monochromator was used for energy selection and a Rh-coated mirror (set to an energy cutoff of 9 keV) was utilized in combination with 30% detuning for rejection of higher harmonics. All samples were prepared as dilutions in BN and measured as transmission spectra. Sample were maintained at 10K using an Oxford continuous flow. To check for reproducibility, 2-3 scans were measured for all samples. The energy was calibrated from Cr and Co foil spectra, with the first inflection set to 5989.0 eV and 7709.5 eV, respectively. A step size of 0.11 eV was used over the edge region. Data were averaged, and a smooth background was removed from all spectra by fitting a polynomial to the pre-edge region and subtracting this polynomial from the entire spectrum. Normalization of the data was accomplished by fitting a flattened polynomial or straight line to the post-edge region and normalizing the edge jump to 1.0.

Computational Methods. B3LYP[59-63] geometry optimization utilized the Gaussian03[i] suite of programs; the 6-31G(d) basis set was employed. Tests with the

larger 6-311+G(d) basis set did not reveal significant differences in the optimized geometries. No symmetry constraints were employed in geometry optimization. Where applicable, geometry optimizations were started from both a pseudo-D_{2d} structure (akin to crystal structure of $(smif)_2Fe$ (**6-Fe**)) and/or a highly Jahn-Teller distorted starting geometry (e.g., $(smif)_2Co$ (**6-Co**)). Calculation of the energy Hessian was performed to confirm species as minima on their respective potential energy surfaces at this level of theory. All plausible spin multiplicities were investigated for the different $M(smif)_2$ complexes. Modeling of open-shell species with density functional theory employed unrestricted Kohn-Sham methods.

Single Crystal X-Ray Diffraction Studies. Upon isolation, the crystals were covered in polyisobutenes and placed under a 173 K N_2 stream on the goniometer head of a Siemens P4 SMART CCD area detector (graphite-monochromated MoK_α radiation, $\lambda = 0.71073$ Å). The structures were solved by direct methods (SHELXS). All non-hydrogen atoms were refined anisotropically unless stated, and hydrogen atoms were treated as idealized contributions (Riding model).

15. 6-V. A metallic gold needle (0.30 x 0.02 x 0.01 mm) was obtained from toluene at 23 °C. A total of 4,195 reflections were collected with 4,195 determined to be symmetry independent ($R_{int} = 0.0000$), and 3,918 were greater than $2\sigma(I)$. A semi-empirical absorption correction from equivalents was applied, and the refinement utilized $w^{-1} = \sigma^2(F_o^2) + (0.1134p)^2 + 1.3469p$, where $p = ((F_o^2 + 2F_c^2)/3)$.

16. 6-Cr. A dark green plate (0.40 x 0.15 x 0.02 mm) was obtained from the slow evaporation of toluene at 23 °C. A total of 36,536 reflections were collected with 7,312 determined to be symmetry independent ($R_{int} = 0.0760$), and 5,019 were greater than $2\sigma(I)$. A semi-empirical absorption correction from equivalents was applied, and the refinement utilized $w^{-1} = \sigma^2(F_o^2) + (0.0489p)^2 + 0.0000p$, where $p = ((F_o^2 + 2F_c^2)/3)$.

17. 7-Cr. A metallic red plate (0.30 x 0.10 x 0.03 mm) was obtained from a solution of tetrahydrofuran at -40 °C. A total of 23,529 reflections were collected with 5,637 determined to be symmetry independent (R_{int} = 0.0540), and 4,220 were greater than 2σ(I). A semi-empirical absorption correction from equivalents was applied, and the refinement utilized $w^{-1} = \sigma^2(F_o^2) + (0.0583p)^2 + 0.0687p$, where $p = ((F_o^2 + 2F_c^2)/3)$.

18. 6-Mn. A metallic gold plate (0.60 x 0.20 x 0.03 mm) was obtained from the slow evaporation of toluene at 23 °C. A total of 30,750 reflections were collected with 6,863 determined to be symmetry independent (R_{int} = 0.0622), and 4,492 were greater than 2σ(I). A semi-empirical absorption correction from equivalents was applied, and the refinement utilized $w^{-1} = \sigma^2(F_o^2) + (0.0447p)^2 + 0.0000p$, where $p = ((F_o^2 + 2F_c^2)/3)$.

19. 6-Fe. A black-metallic purple block (0.45 x 0.30 x 0.20 mm) was obtained from the slow evaporation of benzene at 23 °C. A total of 25,212 reflections were collected with 5,007 determined to be symmetry independent (R_{int} = 0.0497), and 3,994 were greater than 2σ(I). A semi-empirical absorption correction from equivalents was applied, and the refinement utilized $w^{-1} = \sigma^2(F_o^2) + (0.0422p)^2 + 0.9777p$, where $p = ((F_o^2 + 2F_c^2)/3)$.

20. 6-Co. A metallic gold thin plate (0.25 x 0.20 x 0.01 mm) was obtained after heating a solution of toluene at 80 °C for 8 h in a sealed tube under a blanket of argon and slowing cooling to room temperature. A total of 3,587 reflections were collected with 3,587 determined to be symmetry independent (R_{int} = 0.0000), and 3,406 were greater than 2σ(I). A semi-empirical absorption correction from equivalents was applied, and the refinement utilized $w^{-1} = \sigma^2(F_o^2) + (0.1045p)^2 + 1.8144p$, where $p = ((F_o^2 + 2F_c^2)/3)$.

21. 7-Co. A metallic red-orange rod (0.40 x 0.15 x 0.10 mm) was obtained after heating a solution of tetrahydrofuran at 80 °C for 16 h in a sealed tube under a blanket of argon and slowing cooling to room temperature. A total of 28,729 reflections were collected with 6,783 determined to be symmetry independent (R_{int} = 0.0622), and 4,835 were greater than 2σ(I). A semi-empirical absorption correction from equivalents was applied, and the refinement utilized $w^{-1} = \sigma^2(F_o^2) + (0.0846p)^2 + 0.0000p$, where $p = ((F_o^2 + 2F_c^2)/3)$.

22. 6-Ni. A metallic gold plate (0.60 x 0.20 x 0.03 mm) was obtained from the slow evaporation of benzene at 23 °C. A total of 25,347 reflections were collected with 5,631 determined to be symmetry independent (R_{int} = 0.0809), and 3,712 were greater than 2σ(I). A semi-empirical absorption correction from equivalents was applied, and the refinement utilized $w^{-1} = \sigma^2(F_o^2) + (0.0331p)^2 + 0.8315p$, where $p = ((F_o^2 + 2F_c^2)/3)$.

REFERENCES

1 (a) Trofimenko, S. *J. Am. Chem. Soc.* **1967**, *89*, 3170-3177. (b) Jesson, J. P.; Trofimenko, S.; Eaton, D. R. *J. Am. Chem. Soc.* **1967**, *89*, 3148-3158. (c) Trofimenko, S. *J. Am. Chem. Soc.* **1967**, *89*, 6288-6294.

2 (a) Trofimenko, S. *Acc. Chem. Res.* **1971**, *4*, 17-22. (b) Trofimenko, S. *Chem. Rev.* **1972**, *72*, 497-509.

3 Churchill, M. R.; Gold, K.; Maw, C. E. *Inorg. Chem.* **1970**, *9*, 1597-1604.

4 Glerup, J.; Goodson, P. A.; Hodgson, D. J.; Michelsen, K.; Nielsen, K. M.; Weihe, H. *Inorg. Chem.* **1992**, *31*, 4611-4616.

5 Nelson, S. M.; Rodgers, J. *J. Chem. Soc. A* **1968**, 272-276.

6 Butcher, R. J.; Addison, A. W. *Inorg. Chim. Acta* **1989**, *158*, 211-215.

7 Davies, C. J.; Solan, G. A.; Fawcett, J. *Polyhedron* **2004**, *23*, 3105-3114.

8 Malassa, A.; Gorls, H.; Buchholz, A.; Plass, W.; Westerhausen, M. *Z. Anorg. . Chem.* **2006**, *632*, 2355-2362.

9 Velusamy, M.; Palaniandavar, M.; Thomas, K. R. J. *Polyhedron* **1998**, *17*, 2179-2186.

10 Palaniandavar, M.; Butcher, R. J.; Addison, A. W. *Inorg. Chem.* **1996**, *35*, 467-471.

11 Dobson, J. C.; Taube, H. *Inorg. Chem.* **1968**, *7*, 254-261.

12 Hughes, M. C.; Macero, D. J. *Inorg. Chem.* **1976**, *15*, 2040-2044.

13 Hogg, R.; Wilkins, R. C. *J. Chem. Soc.* **1962**, 341-350.

14 Harris, C. M.; Patil, H. R. H.; Sinn, E. *Inorg. Chem.* **1969**, *8*, 101-104.

15 Braterman, P. S.; Song, J. I.; Peacock, R. D. *Inorg. Chem.* **1992**, *31*, 555-559.

16 (a) Kremer, S.; Henke, W.; Reinen, D. *Inorg. Chem.* **1982**, *21*, 3013-3022. (b) Schmidt, J. D.; Brey, W. S.; Stoufer, R. C. *Inorg. Chem.* **1967**, *6*, 268-271.

17 Henke, W.; Reinen, D. *Z. Anorg. Allg. Chem.* **1977**, *436*, 187-200.

18 Behrens, H.; Brandl, H. *Z. Naturforsch., B: Chem. Sci.*. **1967**, *22*, 1216.

19 Behrens, H.; Brandl, H.; Lutz, K. *Z. Naturforsch., B: Chem. Sci.* **1967**, *22*, 99-100.

20 Lions, F.; Martin, K. V. *J. Am. Chem. Soc.* **1957**, *79*, 2733-2738.

21 Goodwin, H. A.; Lions, F. *J. Am. Chem. Soc.* **1959**, *81*, 6415-6422.

22 Geldard, J. F.; Lions, F. *J. Am. Chem. Soc.* **1962**, *84*, 270-282.

23 Figgins, P. E.; Busch, D. H. *J. Am. Chem. Soc.* **1960**, *82*, 820-824.

24 Juhász, G.; Hayami, S.; Inoue, K.; Maeda, Y. *Chem. Lett.* **2003**, *32*, 882-883.

25 Marcos, D.; Folgado, J.-V.; Beltrán-Porter, D. *Polyhedron* **1990**, *9*, 2699-2704.

26 Wocadlo, S.; Massa, W.; Folgado, J.-V. *Inorg. Chim. Acta* **1993**, *207*, 199-206.

27 Marcos, D.; Martinez-Mañe, R.; Folgado, J.-V.; Beltrán-Porter, A.; Beltrán-Porter, D.; Fuertes, A. *Inorg. Chim. Acta* **1989**, *159*, 11-18.

28 Kajiwara, T.; Sensui, R.; Noguchi, T.; Kamiyama, A.; Ito, T. *Inorg. Chim. Acta* **2002**, *337*, 299-307.

29 Nonoyama, M.; Yamasaki, K. *Inorg. Chim. Acta* **1971**, *5*, 124-128.

30 Rowland, J. M.; Olmstead, M. M.; Mascharak, P. K. *Inorg. Chem.* **2002**, *41*, 2754-2760.

31 Hazra, S.; Naskar, S.; Mishra, D.; Gorelsky, S. I.; Figgie, H. M.; Sheldrick, W. S.; Chattopadhyay, S. K. *Dalton Trans.* **2007**, 4143-4148.

32 Hellyer, R. M.; Larsen, D. S.; Brooker, S. *Eur. J. Inorg. Chem.* **2009**, 1162-1171.

33 Westerhausen, M.; Kneifel, A. N. *Inorg. Chem. Comm.* **2004**, *7*, 763-766.

34 Incarvito, C.; Lam, M.; Rhatigan, B.; Rheingold, A. L.; Qin, C. J.; Gavrilova, A. L.; Bosnich, B. *J. Chem. Soc., Dalton Trans.* **2001**, 3478-3488.

35 Clark, D. L.; Sattelberger, A. P. *Inorg. Synth.* **1997**, *31*, 307-315.

36 (a) Olmstead, M. M.; Power, P. P.; Shoner, S. C. *Inorg. Chem.* **1991**, *30*, 2547-2551. (b) Andersen, R. A.; Faegri, K.; Green, J. C.; Haaland, A.; Lappert, M. F.; Leung, W. P.; Rypdal, K. *Inorg. Chem.* **1988**, *27*, 1782-1786.

37 Kern, R. J. *J. Inorg. Nucl. Chem.* **1962**, *24*, 1105-1109.

38 Bradley, D.C.; Hursthouse, M. B.; Newing, C. W.; Welch, A. J. *J. Chem. Soc., Chem. Commun.* **1972**, 567-568.

39 Bürger, H.; Wannagat, U. *Monatsh. Chem.* **1964**, *95*, 1099-1102.

40 Bürger, H.; Wannagat, U. *Monatsh. Chem.* **1963**, *94*, 1007-1012.

41 Hope, H.; Olmstead, M. M.; Murray, B. D.; Power, P. P. *J. Am. Chem. Soc.* **1985**, *107*, 713-715.

42 Ittel, S. D.; English, A. D.; Tolman, C. A.; Jesson, J. P. *Inorg. Chim. Acta.* **1979**, *33*, 101-106.

43 Ward, L. G. L. *Inorg. Synth.* **1971**, *13*, 154-165.

44 Berno, P.; Minhas, R.; Hao, S.; Gambarotta, S. *Organometallics* **1994**, *13*, 1052-1054.

45 (a) Liu, X.; Ellis, J. E.; Miller, T. D.; Ghalasi, P.; Miller, J. S. *Inorg. Synth.* **2004**, *34*, 96-103. (b) Manzer, L. E. *Inorg. Synth.* **1982**, *21*, 135-140.

46 (a) Evans, D. F. *J. Chem. Soc.* **1959**, 2003-2005. (b) Schubert, E. M. *J. Chem. Educ.* **1992**, *69*, 62.

47 Stoufer, R. C.; Smith, D. W.; Clevenger, E. A.; Norris, T. E. *Inorg. Chem.* **1967**, *5*, 1167-1171.

48 Schmidt, J. G.; Brey, W. S.; Stoufer, R. C. *Inorg. Chem.* **1967**, *5*, 268-271.

49 Kremer, S.; Henke, W.; Reinen, D. *Inorg. Chem.* **1982**, *21*, 3013-3022.

50 Krivokapic, I.; Zerara, M.; Daku, M. L.; Vargas, A.; Enachescu, C.; Ambrus, C.; Treganna-Piggott, P.; Amstutz, N.; Krausz, E.; Hauser, A. *Coord. Chem. Rev.* **2007**, *251*, 364–378.

51 Constable, E. C. *Adv. Inorg. Chem.* **1986**, *30*, 69-121.

52 Wadman, S. H.; van der Geer, E. P. L.; Havenith, R. W. A.; Gebbink, R. J. M.; van Klink, G. P. M.; van Koten, G. *J. Organomet. Chem.* **2008**, *693*, 3188-3190.

53 Holanda, M. I. D.; Krumholz, P.; Chum, H. L. *Inorg. Chem.* **1976**, *15*, 890-893.

54 Baggio-Saitovitch, E.; de Paoli, M. A. *Inorg. Chim. Acta* **1978**, *27*, 15-20.

55 a) Khusniyarov, M. M.; Weyhermüller, T.; Bill, E.; Wieghardt, K. *Angew. Chem. Int. Ed.* **2008**, *47*, 1228-1231. b) Khusniyarov, M. M.; Bill, E.; Weyhermüller, T.; Bothe, E.; Harms, K; Sundermeyer, J.; Wieghardt, K. *Chem. Eur. J.* **2008**, *14*, 7608-7622.

56 Blomquist, J.; Helgeson, U.; Moberg, L. C.; Larsson, R.; Miezis, A. *J. Inorg. Nucl. Chem.* **1977**, *39*, 1539-1542.

57 Epstein, L. M. *J. Chem. Phys.* **1964**, *40*, 435.

58 Volpe, E. C. Ph. D Dissertation, Cornell University, 2010.

59 Becke, A. D. *J. Chem. Phys*. **1993**, *98*, 5648 - 5652.

60 Lee, C. ; Yang, W. ; Parr, R. G. *Phys. Rev. B* **1988**, *37*, 785-789.

61 GAUSSIAN’03, Revision C.02, Gaussian, Inc., Carnegie Office Park, Building 6, Suite 230, Carnegie, PA 15106, Frisch, M. J.; Trucks, G. W.; Schlegel, H. B.; Scuseria, G. E.; Robb, M. A.; Cheeseman, J. R.; Montgomery,

J. A.,Jr.; Vreven, T.; Kudin, K. N.; Burant, J. C.; Millam, J. M.; Iyengar, S. S.; Tomasi, J.; Barone, V.; Mennucci, B.; Cossi, M.; Scalmani, G.; Rega, N.; Petersson, G. A.; Nakatsuji, H.; Hada, M.; Ehara, M.; Toyota, K.; Fukuda, R.; Hasegawa, J.; Ishida, M.; Nakajima, T.; Honda, Y.; Kitao, O.; Nakai, H.; Klene, M.; Li, X.; Knox, J. E.; Hratchian, H. P.; Cross, J. B.; Adamo, C.; Jaramillo, J.; Gomperts, R.; Stratmann, R. E.; Yazyev, O.; Austin, A. J.; Cammi, R.; Pomelli, C.; Ochterski, J. W.; Ayala, P. Y.; Morokuma, K.; Voth, G. A.; Salvador, P.; Dannenberg, J. J.; Zakrzewski, V. G.; Dapprich, S.; Daniels, A. D.; Strain, M. C.; Farkas, O.; Malick, D. K.; Rabuck, A. D.; Raghavachari, K.; Foresman, J. B.; Ortiz, J. V.; Cui, Q.; Baboul, A. G.; Clifford, S.; Cioslowski, J.; Stefanov, B. B.; Liu, G.; Liashenko, A.; Piskorz, P.; Komaromi, I.; Martin, R. L.; Fox, D. J.; Keith, T.; Al-Laham, M. A.; Peng, C. Y.; Nanayakkara, A.; Challacombe, M.; Gill, P. M. W.; Johnson, B.; Chen, W.; Wong, M. W.; Gonzalez, C.; Pople, J. A.

62 Nakano, H. *J. Chem. Phys.* **1993**, *99*, 7983 - 7992.

63 Schmidt, M.W.; Baldridge, K.K.; Boatz, J.A.; Elbert, S.T.; Gordon, M.S.; Jensen, J.J.; Koseki, S.; Matsunaga, N.; Nguyen, K.A.; Su, S.; Windus, T.L.; Dupuis, M.; Montgomery, J.A. *J. Comput. Chem.* **1993**, *14*, 1347 - 1363.

64 Carlin, R. L. *Magnetochemistry*; Springer-Verlag: Berlin; New York, 1986.

CHAPTER 3

Synthesis and Characterization of Titanium(II) smif Complexes

Introduction

Inorganic and organometallic titanium(II) complexes are a rare class of compounds. They are frequently invoked as intermediates in organic transformations, yet their isolation and characterization have proven challenging.[1,2,3,4] Divalent titanium complexes typically contain strong field ligands, such as cyclopentadienyl (Cp) or alkyl groups. These compounds often require additional sigma donor and/or π-acceptor ligands, e.g. CO, phosphines, or alkynes, capable of not only increasing π-back-bonding, but also stabilizing the metal center. Titanium(II) complexes can be divided into a few categories: Cp and Cp derivatives, other non-Cp sandwich compounds, coordination complexes, and compounds with nitrogen-based ligands.

Divalent titanium complexes containing the Cp ligand comprise the largest class. The diamagnetic mono-Cp titanium(II) complexes, such as $CpTiR(dmpe)_2$[5,6] where dmpe is 1,2-bis(dimethylphosphino)ethane and $(C_5Me_4SiMe_2NR)Ti(diene)$,[7] are of interest since they show catalytic activity for oligomerization of alkenes (Figure 3.1).

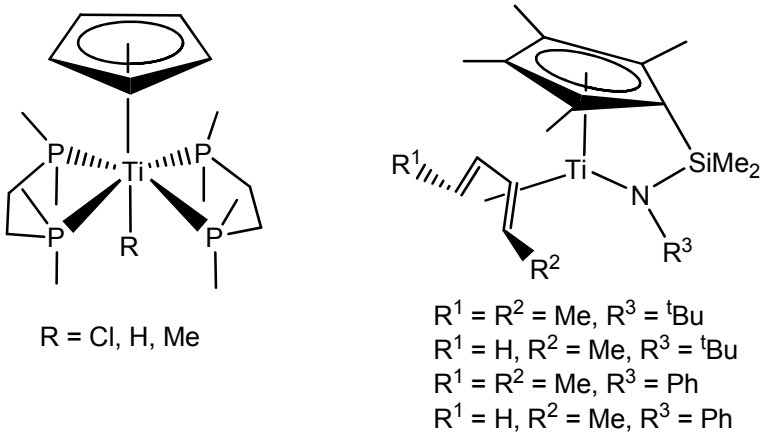

Figure 3.1. Examples of mono-Cp titanium(II) complexes.

All attempts to isolate titanocene, the ferrocene analog and simplest bis-Cp complex, are unsuccessful as the coordinatively unsaturated complex is too reactive. Only derivatives (Figure 3.2) generated by the coordination of additional π-acceptor ligands are structurally known for the parent compound.[8,9] Electronic and steric modification for Cp may be a plausible route to stabilize a titanocene sandwich. Currently, the only isolable bis-Cp titanium(II) sandwich complexes contain bulky substituents. They are prepared via the loss of a neutral ligand, such as an alkyne, as is the case for $\{\eta^5\text{-}C_5Me_4(SiMe_3)\}_2Ti$, or through the reduction of the titanium(III) precursor.[10] Reduction of *ansa*-titanocene dichlorides in the presence of coordinating π-acceptor ligands yields the corresponding *ansa*-titanocene complex.[11]

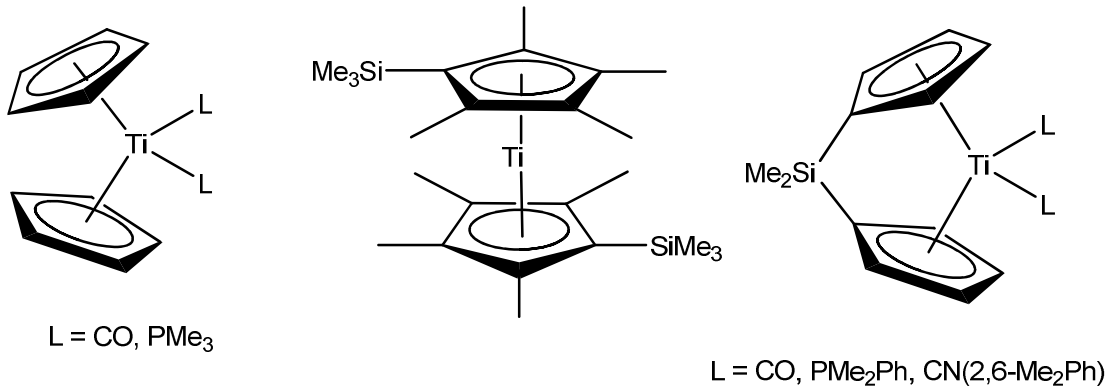

Figure 3.2. A few examples of bis-Cp titanium(II) complexes.

A variety of other metallocenes exist for titanium(II) (Figure 3.3). These include carbon-based sandwiches in which the coordinating ligand is cyclic, e.g. $(\eta^5\text{-}6,6\text{-}Me_2C_6H_5)_2Ti$,[12] as well as acyclic, e.g. $[\eta^5\text{-}1,5\text{-}(Me_3Si)_2C_5H_5]_2Ti$.[13] Another example of an organometallic titanium(II) species is a mixed metallocene containing both a Cp and a cyclic pentadienyl ligand,[14] and metallocenes may even contain heteroatoms and form complexes similar to the dark red, diamagnetic hexaphospha-

titanocene derivative.[15] In addition to the diverse examples of organometallic titanium(II) complexes, only a few inorganic species exist and are well characterized.

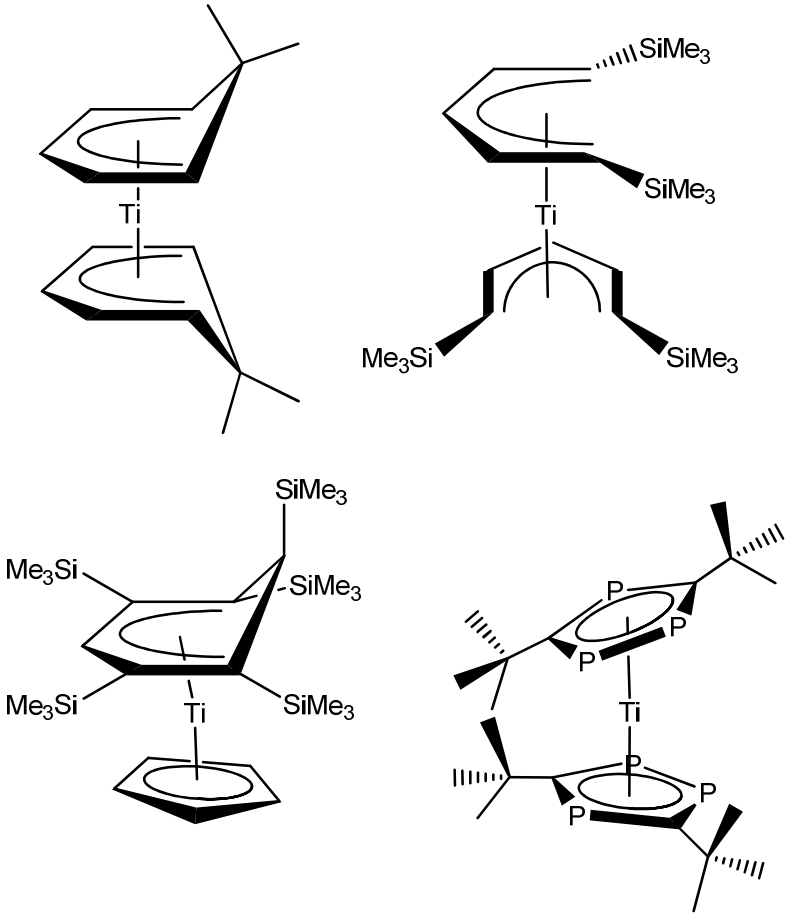

Figure 3.3. Examples of titanium(II) metallocene complexes.

Coordination complexes of titanium(II) halides comprise the earliest examples of stable divalent titanium compounds. The first titanium(II) examples reported are paramagnetic, are not structurally characterized, and contain the general formula of TiX_2L_2, where X is a halide and L is a coordinating solvent (e.g. pyridine, acetonitrile, or tetrahydrofuran), based on elemental analysis.[16,17] Even though the structures remain unknown, these complexes are postulated to exist as either dimers or polymers.

Titanium(II) halides also utilize simple bidentate chelates, such as tetramethylethylenediamine (TMEDA)[18] or dmpe,[19,20] and adopt an octahedral coordination geometry around the paramagnetic metal center (Figure 3.4). Treatment of *trans*-Ti(η^2-BH_4)$_2$(dmpe)$_2$,[21] a red-orange and paramagnetic complex, with two equivalents of MeLi affords the dark red, diamagnetic *trans*-$TiMe_2$(dpme)$_2$,[22] which readily undergoes ligand substitution with various butadienes yielding green, diamagnetic compounds possessing *cis* methyl groups (Figure 3.4).[23]

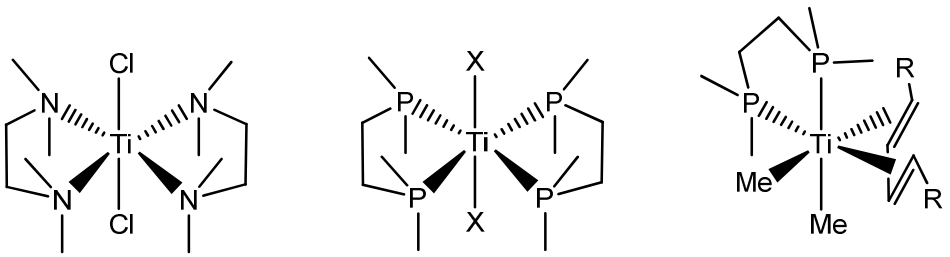

X = Cl, BH_4, Me, OPh

Figure 3.4. Inorganic coordination complexes of titanium(II).

The smallest number of titanium(II) complexes contains nitrogen-based ligands (Figure 3.5). One example is the paramagnetic homoleptic bis(trispyrazolylborate) titanium(II).[24] In addition to this complex, only a few titanium(II) porphyrin complexes exist, and all are stabilized with a variety of alkynes.[25,26] The rarity of divalent titanium stabilized with nitrogen-based ligands prompted our investigation to test the ability of the smif ligand to stabilize a titanium(II) metal center (See Figure 3.6).

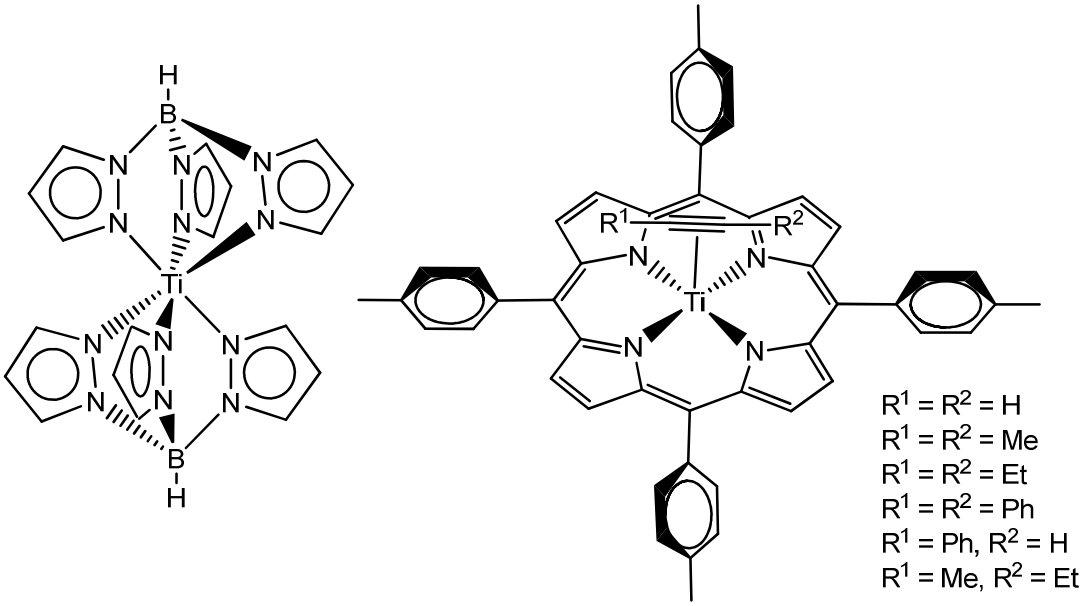

Figure 3.5. Examples of titanium(II) complexes with nitrogen-based ligands.

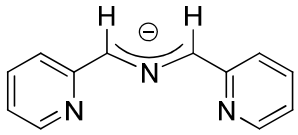

Figure 3.6. smif ligand ((2-py)CHNCH(2-py)).

Results and Discussion

Synthesis of titanium(II) smif compounds. Analogous to vanadium, titanium(II) halides are not readily available as starting materials. Thus, all attempts to synthesize $(smif)_2Ti$ utilized metathetical routes and *in situ* reductions from higher valent titanium halides. Treatment of $TiCl_3(THF)_3$[27] with two equivalents of Li(smif) (**5-Li**), generated *in situ*, yielded a deep purple solution containing a mixture of four diamagnetic titanium(II) complexes (Scheme 3.1): lithium[(k-C,N^{am},N^{im},$N^{py}{}_3$-1,2-bis(pyridin-2-yl)-2-(pyridin-2-ylmethyleneamino)ethyl)(pyridin-2-ylmethideyl)amido)Ti(smif)] (**10-Ti**), "$(smif)_2Ti$" (**11-Ti**), (smif)(((2-py)$CH)_2$N)Ti

(**12-Ti**), and (κ-N^{am},N^{py}_2-2,3,5,6-tetrakis(pyridin-2-yl)piperazin-1-yl)(smif)Ti (**13-Ti**). These compounds were identified through x-ray crystallography (**10-Ti**) and NMR spectroscopy.

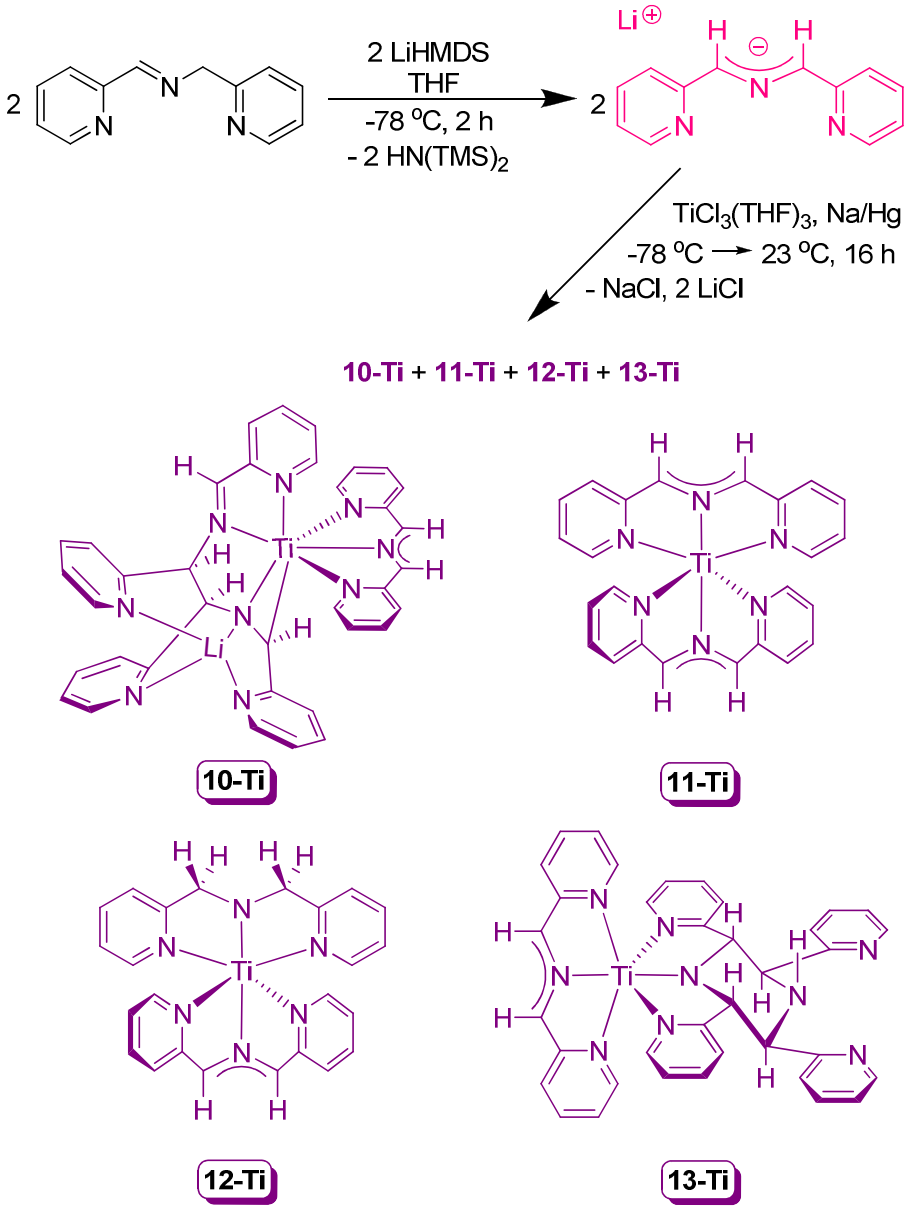

Scheme 3.1. Synthesis and structures of four (smif)Ti(II) complexes.

Several other attempts were made to isolate a pure sample of $(smif)_2Ti$. Reduction of $TiCl_4(THF)_2$[28] using a 0.95 % sodium amalgam preceding the addition of **5-Li** (two equivalents) generated a mixture of **11-Ti** and **13-Ti**. Unfortunately, the reduction of either $TiCl_3(THF)_3$ or $TiCl_4(THF)_2$ with Mg to generate $TiCl_2(THF)_2$[29] *in situ* prior to the addition of two equivalents of **5-Li** led to the formation of $(smif)_2Mg$ (**6-Mg**) along with **11-Ti** and **12-Ti**. **6-Mg** was independently prepared from the metathesis of $MgBr_2$ with two equivalents of **5-Li** in THF and isolated in 68 % yield as metallic gold crystals from a deep purple-magenta solution (eq. 3.1).

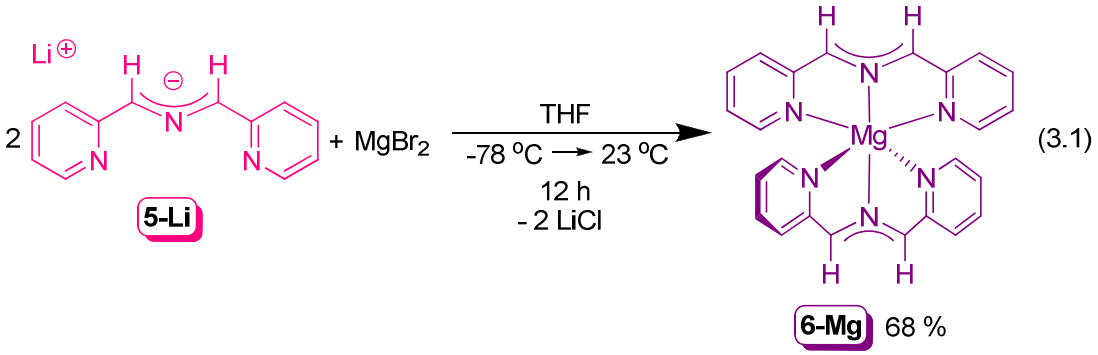

(3.1)

The use of *trans*-$TiCl_2(TMEDA)_2$[18] (**A**) was also explored as an alternative metathesis starting material. Regrettably, treatment of **A** with two equivalents of Na(smif) still yielded a mixture of **11-Ti** and **12-Ti** as well as new unidentified titanium complexes. In hopes of utilizing divalent transfer agents for transmetallation, **A** was treated with either **6-Mg** or **6-Zn**. Unfortunately at 23 °C, no reaction occurred with **6-Mg** and minimal transfer from **6-Zn** was observed. Elevation of reaction temperatures was prevented due to the instability of **A**.

Table 3.1. Product ratios for **10-Ti**, **11-Ti**, **12-Ti**, **13-Ti** obtained from synthetic attempts toward producing $(smif)_2Ti$ (**11-Ti**).

Trial	Titanium Source	smif source	Solvent	Reducing Agent	Temperature	Time	10-Ti	11-Ti	12-Ti	13-Ti
1	$TiCl_3(THF)_3$	**5-Li**	DME	1 Na/Hg	0°C - 23°C	16 h	3	1	0.75	0
2		**5-Li**		1 Na/Hg	0°C - 23°C	16 h	1	1	0	0
3		**5-Li**		1 Na/Hg	0°C - 23°C	16 h	1	0.5	0.5	0
4[a]		**5-Li**		1 Na/Hg	0°C - 23°C	16 h	2	1	1	0
5[b]		**5-Li**		1 Na/Hg	0°C - 23°C	2 d	0	1	0	1
6[c]		**5-Li**	THF	1 Na/Hg	-78°C - 23°C	14 h	0	0.5	2	0.25
7[c]		**5-Li**		1 Na/Hg	-78°C - 23°C	16 h	0	1	0	0.7
8		**5-Li**		1 Na/Hg	-78°C - 23°C	16 h	0	1	0.75	0.25
9		**5-Li**		1 Na/Hg	-78°C - 23°C	16 h	0	1	0	0
10		**5-Li**		1 Na/Hg	-78°C - 23°C	16 h	2	1	0	0
11		**5-Li**		1 Na/Hg	-78°C - 23°C	16 h	0	1	0	0
12[d]		**5-Li**		1 Na/Hg	-78°C - 23°C	16 h	0	1	0	0
13[e]		**5-Li**		1 Na/Hg	-78°C - 23°C	2.5 d	0	1	1	0
14		**5-Li**		2 Na/Hg	-78°C - 23°C	12 h	0	1	0.5	0
15		**5-Li**		**5-Li**	-78°C - 23°C	36 h	4	0	0	1
16[f]		**5-Li**		0.5 Mg	-78°C - 23°C	12 h	0	0.5	0.5	0
17	$TiCl_3$	**5-Li**	DME	1 Na/Hg	0°C - 23°C	18 h	0	1	0.5	0
18		**5-Li**		1 Na/Hg	0°C - 23°C	18 h	0	1	1	0
19		**5-Li**		2 Na/Hg	0°C - 23°C	18 h	0	1	0.25	0
20	$ClTi\{N(TMS)_2\}_2(THF)$	**smifH**	THF	1 Na/Hg	-78°C - 23°C	16 h	0	0	0	0
21[g]	$TiCl_4(THF)_2$	**5-Li**	THF	2 Mg	-78°C - 23°C	16 h	0	0	0	0
22		**5-Li**		2 Na/Hg	-78°C - 23°C	8 h	0	1	0	0
23		**5-Li**		2 Na/Hg	-78°C - 23°C	16 h	0	1	0	1
24[d]		**5-Li**		2 Na/Hg	-78°C - 23°C	16 h	0	3	0	1
25	$TiCl_2(TMEDA)_2$	**5-Na**	C_6D_6		23°C	17.5 h	0	1	3	0
26		**5-Na**			23°C	21.5 h	0	0.18	1	0
27[c]		**5-Na**			23°C	2.5 d	0	0	1	0
28		**6-Mg**			23°C	15 h	0	0	0	0
29		**6-Zn**			23°C	17.5 h	0	1	1	0
30		**5-Na**	d_8-THF		23°C	21.5 h	0	0.25	1	0
31		**5-Na**			23°C	3.75 d	0	2.5	0	6.5
32		**5-Na**	THF		-78°C - 23°C	18 h	0	1	0	0
33		**6-Mg**			-78°C - 23°C	2 d	0	0	0	0
34		**6-Zn**			-78°C - 23°C	2 d	0	0	0	0

[a] Also 27 eq **5-Li**. [b] Also 11 eq **5-Li**. [c] Other unidentified peaks. [d] Silylated glassware. [e] Also 32 eq 5-Li. [f] Also, 1 eq 6-Mg and 9 eq (smif)MgCl.

[g] Only (smif)MgCl present.

Characterization of D: X-ray crystal structure. Single crystal x-ray diffraction quality metallic gold-green blocks of **10-Ti** were isolated from a concentrated benzene solution at 23 °C. Selected crystallographic and refinement data are listed in Table 3.2. The solid state structure, shown in Figure 3.7, has a pseudo-octahedral arrangement of the two coordinating ligands around the metal center. In contrast to the homoleptic $(smif)_2M^n$ (n = 0, M = V, Cr, Fe, Co, and Ni; n = +1, M = Cr, Co) series possessing smif chelation bite angles between ~ 77 - 84 °, the smif ligand in **10-Ti** exhibits more acute bite angles, 73.41(4) ° and 72.63(4) ° (∠N1-Ti1-N2 and ∠N3-Ti1-N2, respectively) with concomitant lengthening of the titanium-aza nitrogen distance, 2.1956(12) Å, and titanium-pyridine nitrogen distances, i.e. d(Ti1-N1) = 2.1693(11) Å and d(Ti1-N3) = 2.1678(13) Å. The smif ligand 'backbone' shows distances consistent with a delocalized anion, i.e. d(N2-C6) = 1.3437(18) Å and d(N2-C7) = 1.3234(19) Å, as observed for the $(smif)_2M^n$ series. The second ligand is chelated through a reduced pyridine imine via the pyridine and imine nitrogens (d(Ti1-N4) = 2.1120(12) Å, d(Ti1-N5) = 2.0231(12) Å) as well as in an η^2 fashion, through N8 and C31, of a second reduced pyridine imine (d(Ti1-N8) = 1.9722(12) Å, d(Ti1-C31) = 2.3260(14) Å). This ligand displays distances more consistent with two reduced pyridine imine moieties: d(N5-C18) = 1.3789(18) Å, d(C18-C17) = 1.367(2) Å, d(N5-C19) = 1.4656(18) Å, d(N8-C31) = 1.3903(17) Å, d(C31-C32) = 1.424(2) Å, d(N8-C25) = 1.4528(18) Å. Additionally, the structure reveals the formation of a carbon-carbon bond (d(C19-C25) = 1.5472(19) Å) consistent with an sp^3-sp^3 assignment. The three additional pyridine rings associated with this coupled ligand are ligated in a monocapped trigonal prismatic coordination geometry to lithium: ∠N8-Li1-N6 = 93.07(11) °, ∠N8-Li1-N7 = 84.76(10) °, ∠N8-Li1-N9 = 85.79(10) °, ∠N6-Li1-N7 = 89.64(11) °, ∠N6-Li1-N9 = 153.60(14) °, ∠N7-Li1-N9 = 116.45(12) °.

Table 3.2. X-ray crystallographic data for **10-Ti**.

Formula	$C_{45}H_{39}N_9LiTi$[a]
Formula weight	760.69
Crystal system	Triclinic
Space group	$P\bar{1}$
Z	2
a (Å)	10.5641(5)
b (Å)	10.7536(5)
c (Å)	17.1299(9)
α (°)	88.685(2)
β (°)	78.420(2)
γ (°)	82.808(2)
V (Å^3)	1891.38(16)
ρ_{calc} g/cm^3	1.336
μ (mm^{-1})	0.273
temp, K	173(2)
λ, (Å)	0.71073
final R indices [I > 2σ(I)][b,c]	$R_1 = 0.0416$
	$wR_2 = 0.0987$
R indices (all data)[b,c]	$R_1 = 0.0625$
	$wR_2 = 0.1084$
GOF[d]	1.089

[a] The asymmetric unit contains one molecule of **10-Ti** and 1.5 molecules of C_6H_6.

[b] $R_1 = \Sigma||F_o| - |F_c||/\Sigma|F_o|$. [c] $wR_2 = [\Sigma w(|F_o| - |F_c|)^2/\Sigma wF_o^2]^{1/2}$.

[d] GOF (all data) = $[\Sigma w(|F_o| - |F_c|)^2/(n - p)]^{1/2}$, n = number of independent reflections, p = number of parameters.

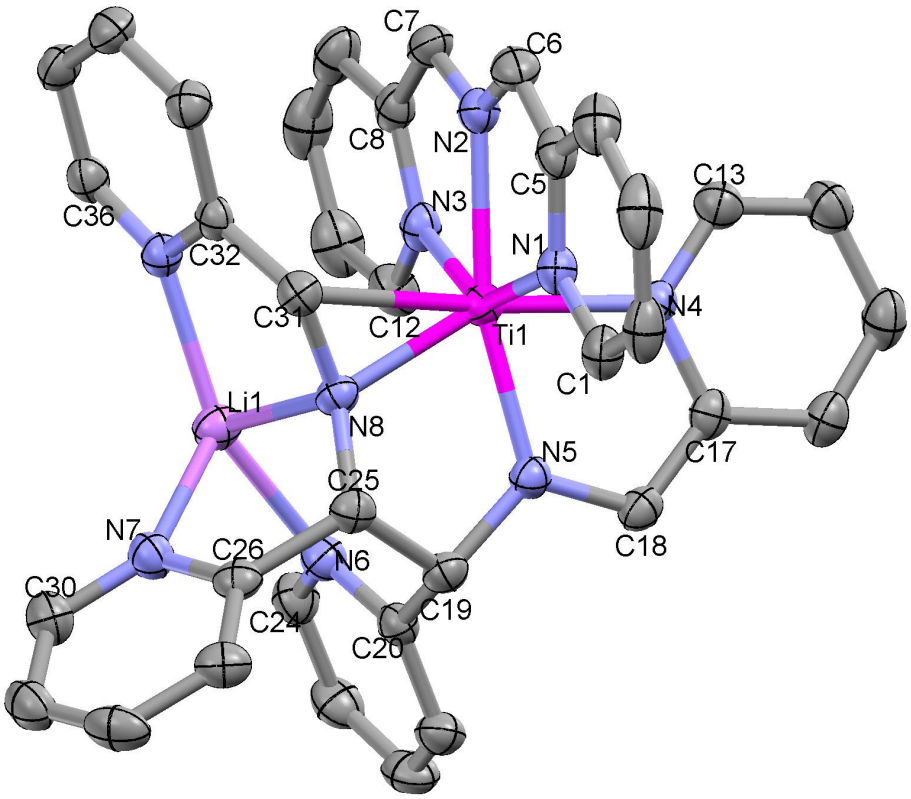

Figure 3.7. Molecular structure of **10-Ti**. Thermal ellipsoids are at 50 % probability level, and all hydrogens have been removed for clarity.

NMR spectroscopy. Correlating the diamagnetic ^{1}H NMR spectrum (Figure 3.8) with the crystal structure of C_1 symmetric **10-Ti**, which was comprised of 30 inequivalent protons, was more challenging than anticipated. Allowing crystals of **10-Ti** to re-dissolve in C_6D_6 for 30 min yielded a ^{1}H NMR spectrum consistent with 2:1 ratio of **10-Ti** and at least one other species, **11-Ti**. Heating the solution at 80 °C for 44 h generated a ^{1}H NMR spectrum containing 76 inequivalent protons. Three pyridine *ortho*-CH peaks appeared, shifted significantly downfield from the rest of the rings, and were indicative of three different titanium compounds (δ 13.61 **12-Ti**, 13.88 **11-Ti**, and 13.99 **13-Ti** ppm). Monitoring the mixture during thermolysis (80 °C for

over 16 d) enabled the identification of ^{1}H chemical shifts corresponding to **12-Ti,** as it was the last species to grow in. In order to elucidate the identity of the four compounds in solution, a series of two-dimensional (2-D) NMR spectroscopic experiments were employed.

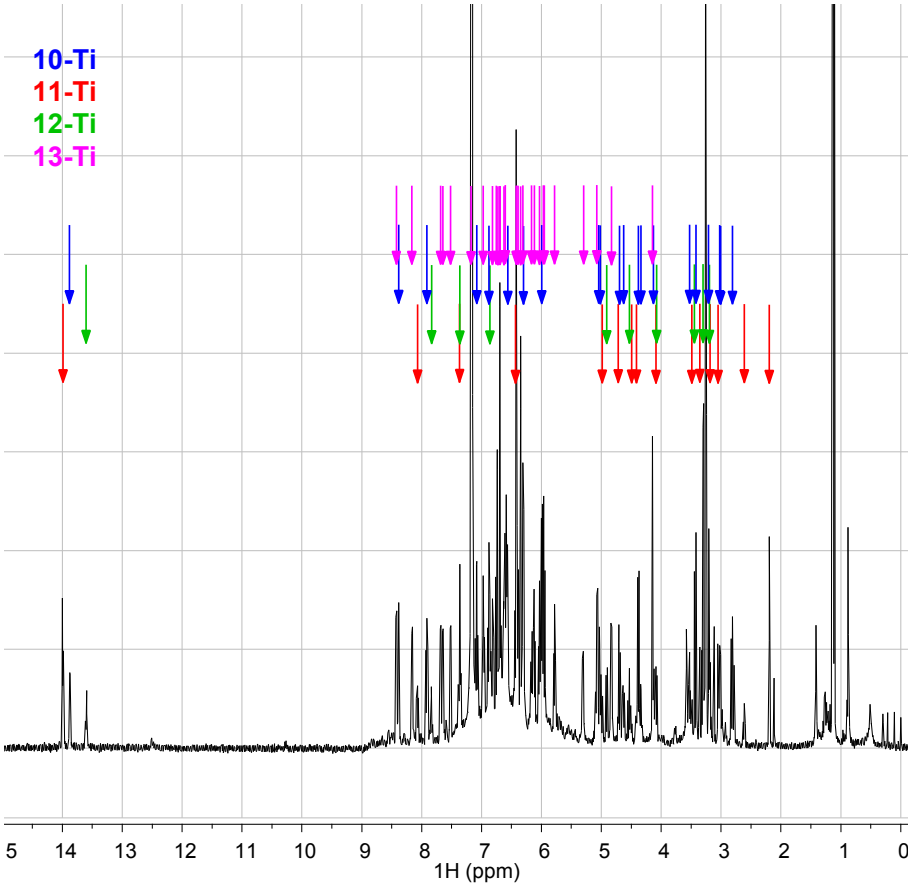

Figure 3.8. ^{1}H NMR spectrum of **10-Ti** (magenta), **11-Ti** (red), **12-Ti** (green), and **13-Ti** (blue) in C_6D_6.

Initial efforts to identify the species in solution focused on utilizing 2-D correlation spectroscopy (COSY), which facilitated the identification of protons that were spin coupled to one another, specifically adjacent protons on the pyridine rings. From these correlations, the gCOSY spectrum elucidated the possibility of 15 different

pyridine rings, and the proton with the most downfield chemical shift corresponded to the pyridine *ortho*-CH in most cases (Figure 3.9).

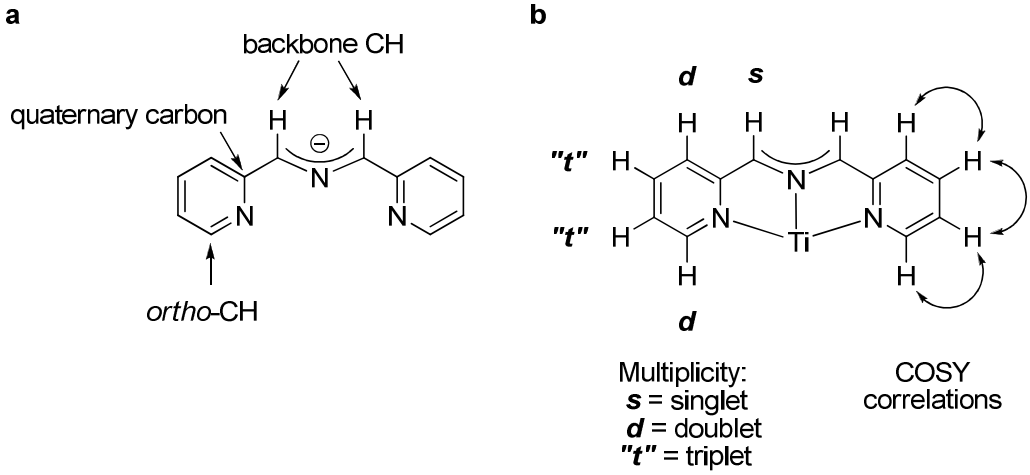

Figure 3.9. a. Pyridine ring and ligand nomenclature. b. ^{1}H NMR splitting pattern (left ring) and COSY correlations typically observed denoted with arrows (right ring).

Four pyridine rings (*ortho*-CH δ 13.99, 13.88, 7.65, 7.17 ppm) were completely assembled as a result of distinct proton chemical shifts and strong COSY correlations exhibited within the typical aromatic region. Strong cross peaks existed for at least five other pyridine rings (*ortho*-CH δ 8.42, 8.38, 8.15, 7.65, 7.51 ppm); however, overlapping signals observed around 6.30, 6.40, and 6.73 ppm hindered the precise assignment of ^{1}H chemical shifts. In contrast to the strong correlations observed for the aforementioned rings, all pyridine rings shifted upfield from the aromatic region displayed weaker COSY correlations. One of these pyridines, which was shifted significantly upfield (*ortho*-CH δ 4.12 ppm), was established through the weak COSY correlations observed between all four protons within the ring system. A unique set of cross peaks indicated that two triplets (δ 4.63, 3.52 ppm) were coupled to the same "doublet" (δ 5.03 ppm), whose chemical shift was consistent with a pyridine *ortho*-CH relative to the triplets, thus ambiguity complicated the ring assignment. Correlations between all proton sets within a ring were not observed for at least five other possible

rings. In addition to identifying pyridine rings, the COSY spectrum displayed a cross peak consistent with the interior CHs (δ 4.82, 5.30 ppm) on the coupled ligand in **10-Ti**. Unfortunately, due to overlapping cross peaks and weak correlations, all 15 rings were not solely assembled through gCOSY.

Adiabatic heteronuclear single quantum coherence (HSQCAD) 2-D spectroscopy displayed correlations between 75 protons and their adjacent carbons. Each correlation portrayed the multiplicity of the proton (Figure 3.10). Consequently, backbone CHs and pyridine ring protons were easily recognized. The diverse ^{13}C chemical shifts aided in differentiating between ^{1}H chemical shifts (δ 6.74, 6.73, 6.41, 6.40, 6.31, 6.30, 5.04, 5.02 ppm) in areas containing a cluster of overlapping ^{1}H NMR signals and COSY correlations, thus helping to elucidate six pyridine rings.

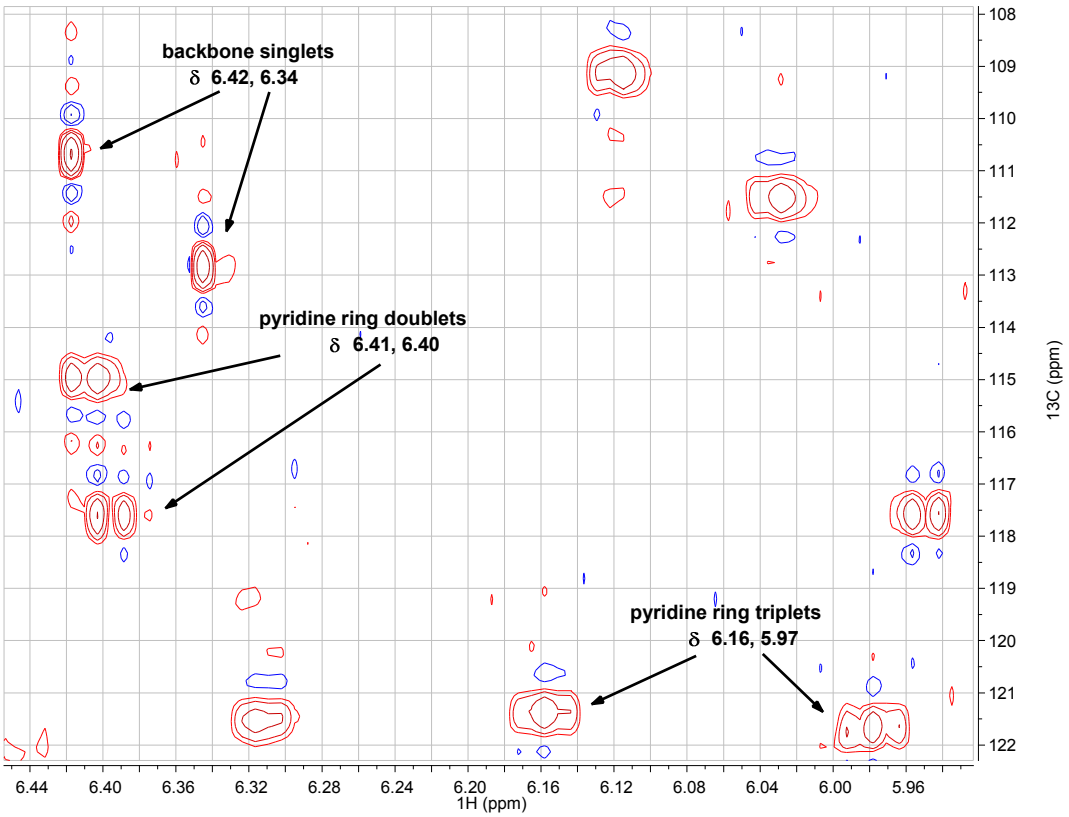

Figure 3.10. Examples of multiplicities observed in HSQCAD of **10-Ti**, **11-Ti**, **12-Ti**, and **13-Ti** in C_6D_6.

Additionally, HSQCAD revealed new ^{1}H-^{13}C correlations, which went undetected in the COSY presumably due to weak correlations. This accounted for eight pyridine ring signals as well as fifteen backbone CH signals, thereby indicating a total of fifteen pyridine rings. Ultimately, the presence of an NH peak, observed in **13-Ti**, was established through a lacking HSQCAD cross peak for the remaining proton (δ 3.01 ppm).

The quaternary carbons of all 15 pyridine rings were identified through the strong correlation observed with the pyridine ring's *ortho*-CH via the 2-D NMR experiment gHMBCAD (adiabatic heteronuclear multiple bond correlation). This spectroscopy also gave rise to a variety of other cross peaks useful for arranging protons around the pyridine rings as each ring portrayed the same correlation patterns and ^{13}C chemical shifts within a ring also portrayed a distinct pattern (Figure 3.11). Ligand fragments were established by correlations observed between pyridine rings and their adjacent backbone CH/CH_2 groups.

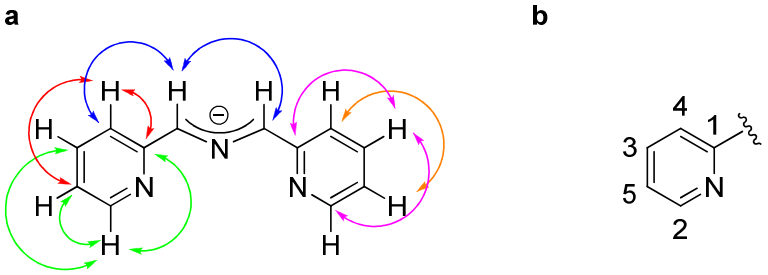

Figure 3.11. a. Typical correlations observed in gHMBCAD. **b**. Ordering of ^{13}C chemical shifts within a pyridine ring (highest shift 1, lowest shift 5).

These fragments were assembled to form eight different ligand environments via the cross peaks observed between a backbone proton and a carbon from the other fragment. Four symmetric and four asymmetric smif ligand environments were established. The spectroscopy verified **11-Ti** contained one symmetric ligand via the

self-correlation (δ 2.19 (^{1}H) with 74.93 (^{13}C) ppm). In the case of **12-Ti**, the gHMBCAD correlations (δ 3.43 (^{1}H) with 108.43 (^{13}C), 3.29 (^{1}H) with 61.83 (^{13}C) ppm) were indicative of two symmetric ligand environments. **13-Ti** also contained a symmetric ligand (δ 4.38 (^{1}H) with 73.85 (^{13}C) ppm). The gHMBCAD experiment aided in verifying pyridine ring assignments established through gCOSY.

In order to finish assigning the 15 pyridine rings, total correlation spectroscopy (TOCSY) was utilized since all protons within a specific spin system produced a series of cross peaks. The overall TOCSY spectrum appeared quite overwhelming initially (Figure 3.12).

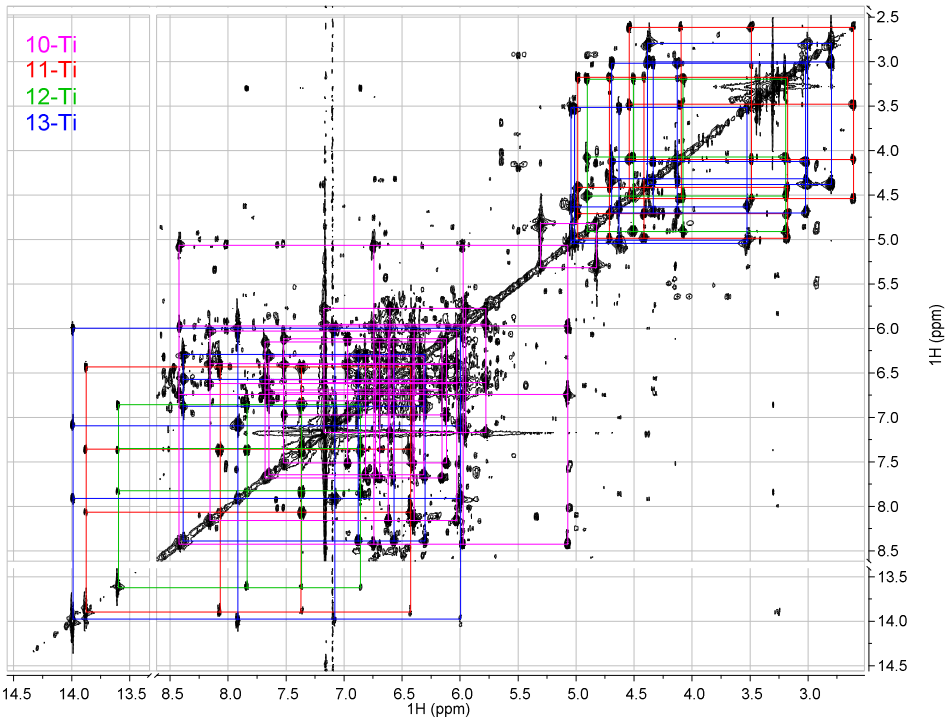

Figure 3.12. Complete TOCSY obtained for **10-Ti** (magenta), **11-Ti** (red), **12-Ti** (green), and **13-Ti** (blue) in C_6D_6.

Each pyridine ring contained its own spin system, and all protons corresponding to one ring appeared in a line, subsequently verifying assignments made based upon other 2-D spectra (see Figures 3.13, 3.14, 3.15, and 3.16).

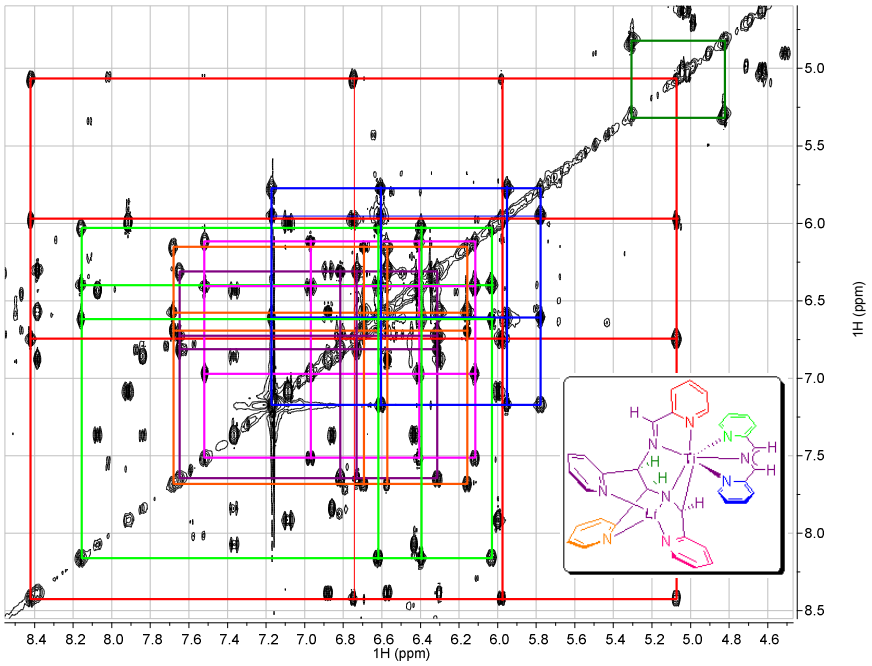

Figure 3.13. TOCSY depicting correlations for **10-Ti**.

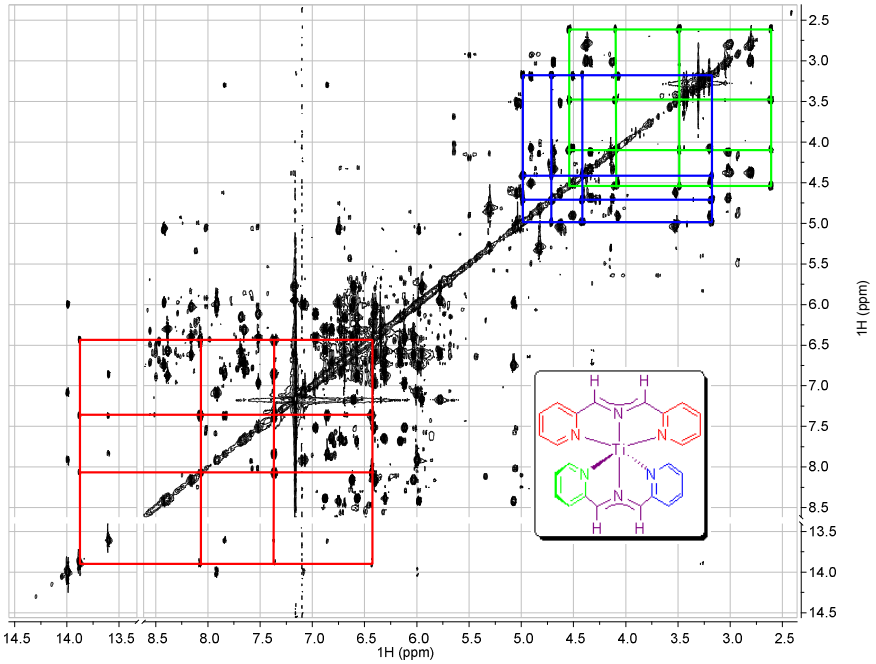

Figure 3.14. TOCSY highlighting correlations for **11-Ti**.

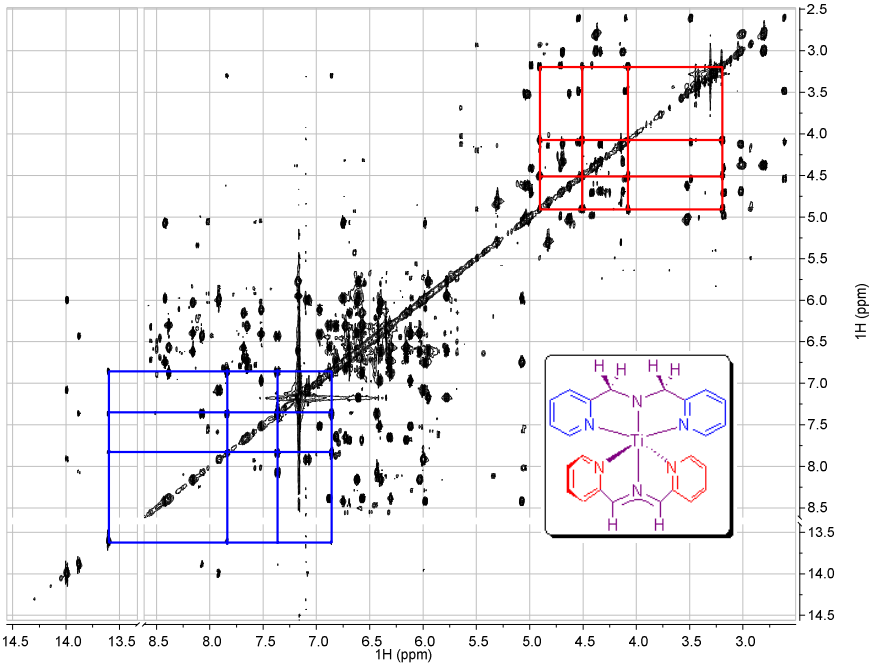

Figure 3.15. TOCSY showing correlations for **12-Ti**.

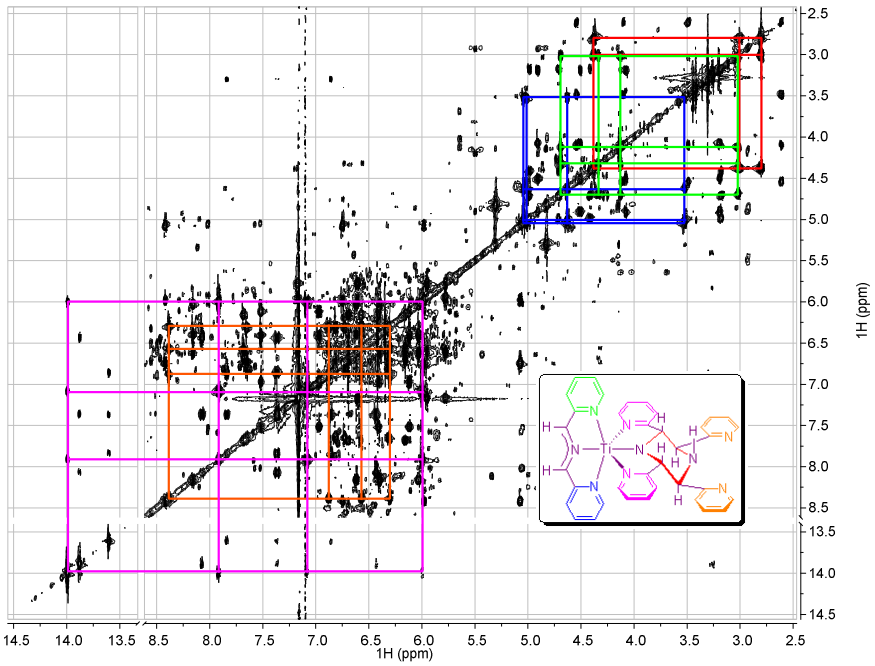

Figure 3.16. TOCSY emphasizing correlations for **13-Ti**.

Additionally, this experiment was particularly useful in differentiating pyridine rings that were hard to discern from the gCOSY and gHMBCAD due to overlapping cross peaks. The TOCSY spectrum for **13-Ti**, shown in Figure 3.16, corroborated the presence of five ring systems. Four rings were previously confirmed as pyridine rings, and the remaining ring corresponded to the substituted piperazine generated via ligand coupling. Interestingly, the TOCSY spectrum consistently displayed peaks connecting the backbone CH to the pyridine rings containing upfield chemical shifts.

Rotating-frame overhauser effect spectroscopy (ROESY) determined which ligand environments were associated with a specific titanium center. Furthermore, ROESY revealed the spatial orientation of the ligands surrounding titanium. In the case of **10-Ti**, ROESY cross peaks were seen for the four protons of coupled ligand's backbone (δ 4.15, 4.82, 5.30, 6.70 ppm) indicating they were all on the same side of the molecule. Strong correlations were observed between two of the aforementioned backbone CHs (δ 4.82, 5.30 ppm) and the pyridine *ortho*-CH (δ 8.15 ppm) on the smif ligand indicating the direction in which the smif ligand should lie. Weak correlations existed between the remaining backbone CHs (δ 4.15, 6.70 ppm) and the smif ligand's pyridine *ortho*-CH (δ 8.15 ppm). The other pyridine *ortho*-CH on the smif ligand (δ 7.17 ppm) only showed a correlation with the adjacent pyridine ring proton (δ 5.78 ppm). The smif ligand backbone CHs (δ 6.34, 6.42 ppm) exhibited cross peaks with the pyridine *ortho*-CH at δ 8.42 ppm. For **11-Ti**, the symmetric smif ligand backbone (δ 2.19 ppm) and the pyridine ortho-CHs (δ 3.49, 4.71 ppm) on the asymmetric smif ligand gave rise to cross peaks. No correlation was seen between the symmetric ligand's pyridine ortho-CH (δ 13.88 ppm) and the backbone CHs (δ 3.05, 3.35 ppm) for the asymmetric smif. The ROESY for **12-Ti** revealed that the two ligand environments were situated perpendicular to one another. The smif backbone CH (δ 3.43 ppm) and the di(2-pyridylmethyl)amine (dpma) pyridine *ortho*-CH (δ 13.61 ppm)

displayed a weak correlation while the backbone CH_2 groups (δ 3.29 ppm) on dpma and the pyridine ortho-CH (δ 4.08 ppm) on smif exhibited a strong correlation. For **13-Ti**, the orientation of the asymmetric smif ligand with respect to the coupled ligand was based on the ROESYs observed between the pyridine *ortho*-CH and the coupled ligand's backbone CHs. One pyridine *ortho*-CH (δ 5.02 ppm) correlated solely to a single backbone CH (δ 2.80 ppm), while the other *ortho*-CH (δ 4.12 ppm) gave rise to a cross peak with both the backbone CH (δ 4.38 ppm) and NH (δ 3.01 ppm). The asymmetric smif backbone CHs (δ 3.20, 3.41 ppm) both displayed correlations with the pyridine *ortho*-CH (δ 13.99 ppm) on the coupled ligand, indicative of a mirror plane within the ligand framework. Complete NMR spectroscopic assignments for compounds **10-Ti**, **11-Ti**, **12-Ti**, and **13-Ti** can be found in Figures 3.17, 3.18, 3.19, and 3.20, respectively.

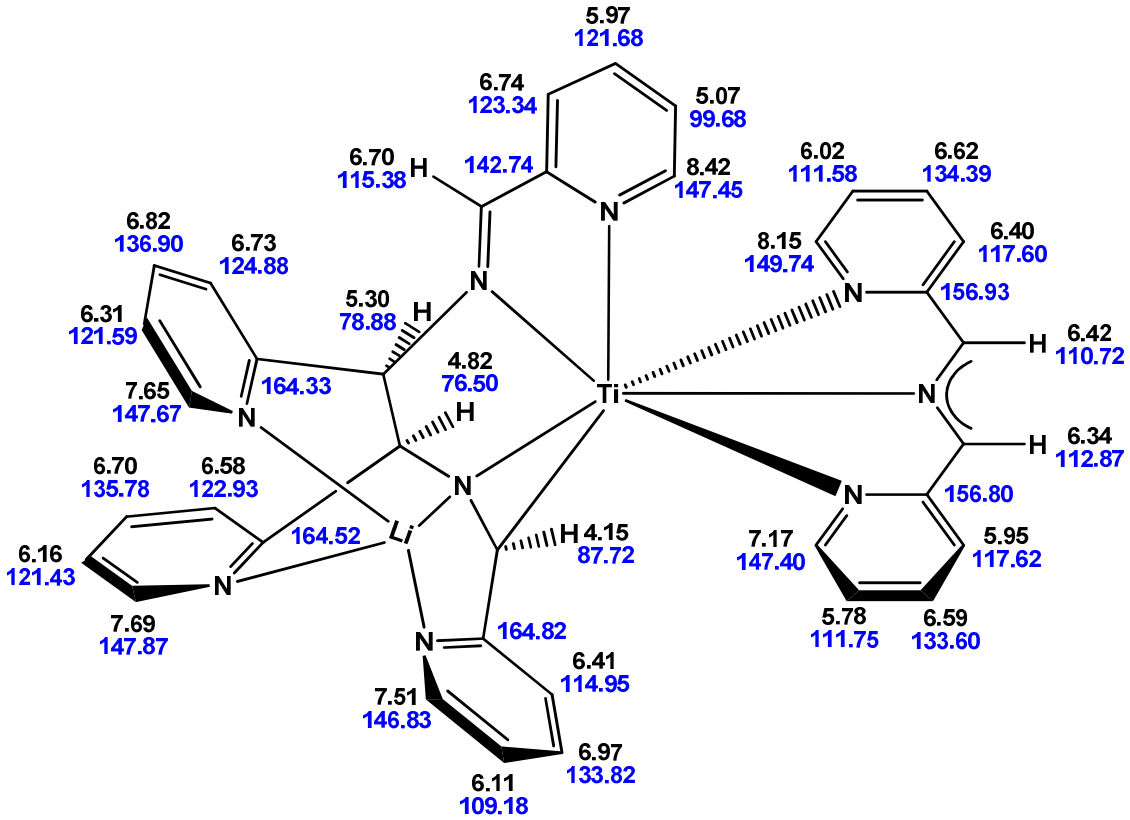

Figure 3.17. ^{1}H and $^{13}C\{^{1}H\}$ NMR Assignments for **10-Ti**.

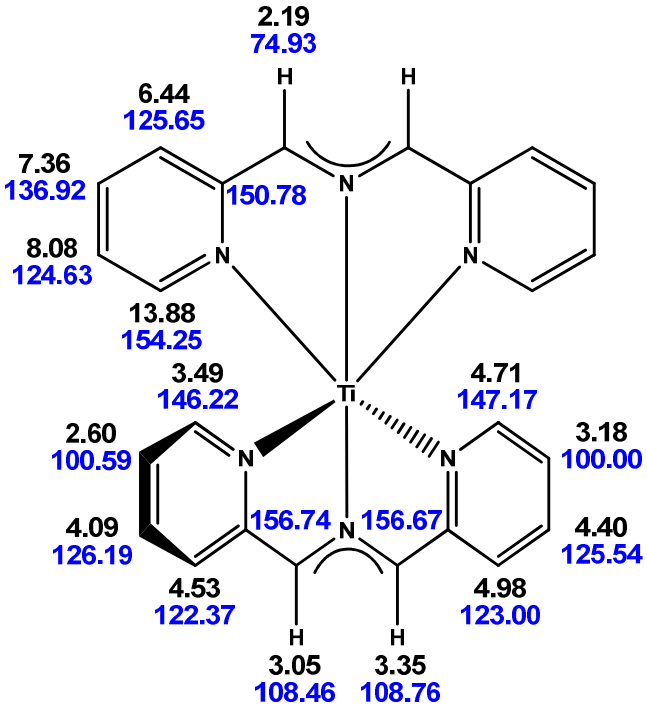

Figure 3.18. ^{1}H and $^{13}C\{^{1}H\}$ NMR Assignments for **11-Ti**.

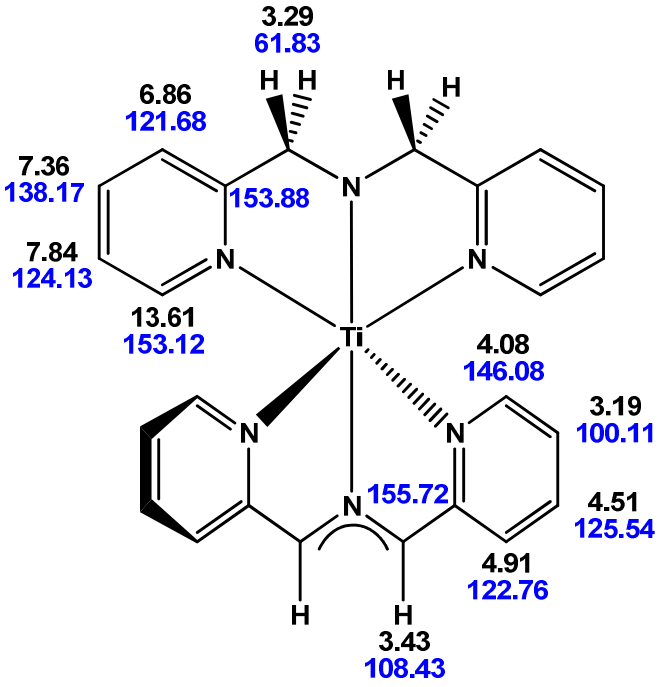

Figure 3.19. ^{1}H and $^{13}C\{^{1}H\}$ NMR Assignments for **12-Ti**.

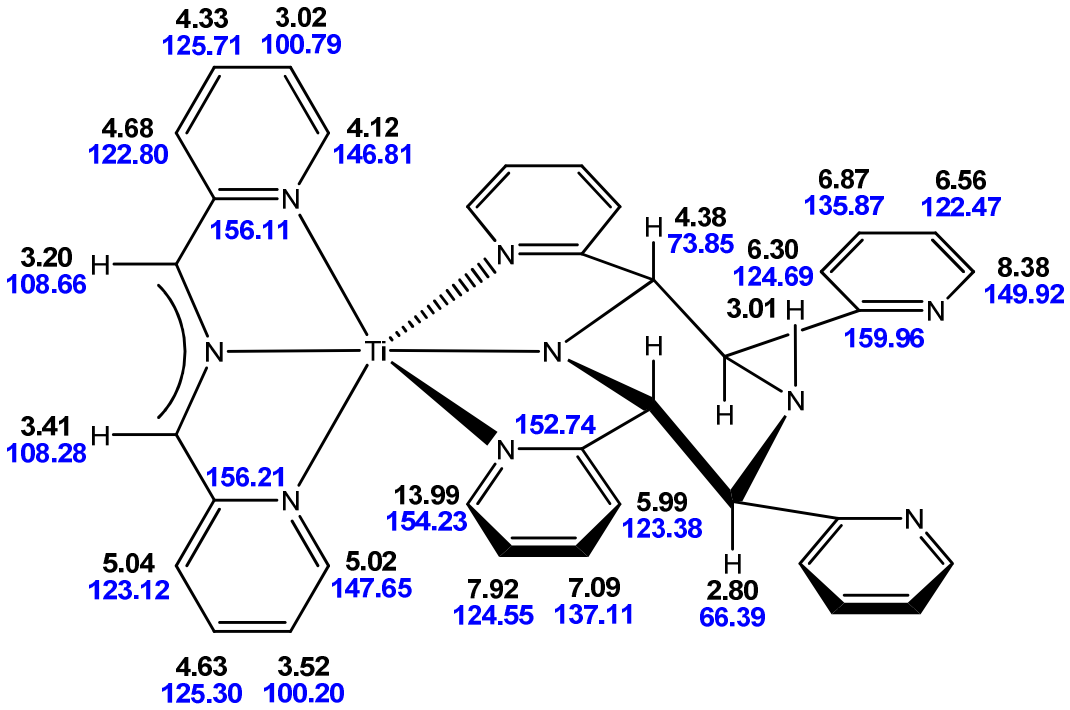

Figure 3.20. ^{1}H and ^{13}C{^{1}H} NMR Assignments for **13-Ti**.

Proposed Mechanism. The identification of the four titanium complexes, i.e. **10-Ti**, **11-Ti**, **12-Ti**, and **13-Ti**, from crystals of **10-Ti** by ^{1}H NMR spectroscopy suggests reversibility of C-C bond formations. Scheme 3.2 shows a plausible mechanism for the transformations between complexes. In the presence of **5-Li**, **11-Ti** may undergo two reversible C-C bond formations; one generates **10-Ti**, and the other produces **13-TiLi** via a reversible [3+3] cycloaddition. Protonation of **13-TiLi** yields **13-Ti**. Alternatively, **11-Ti** may dimerize via a reversible [3+3] cycloaddition to yield **[11-Ti]$_2$**. Subsequently, protonation of **[11-Ti]$_2$** may generate **13-Ti** and a "(smif)TiOH" complex, which may undergo further hydrolysis to yield **Hdpma** and TiO_2. In the presence of **Hdpma**, **[11-Ti]$_2$** may yield **12-Ti** and **13-Ti**.

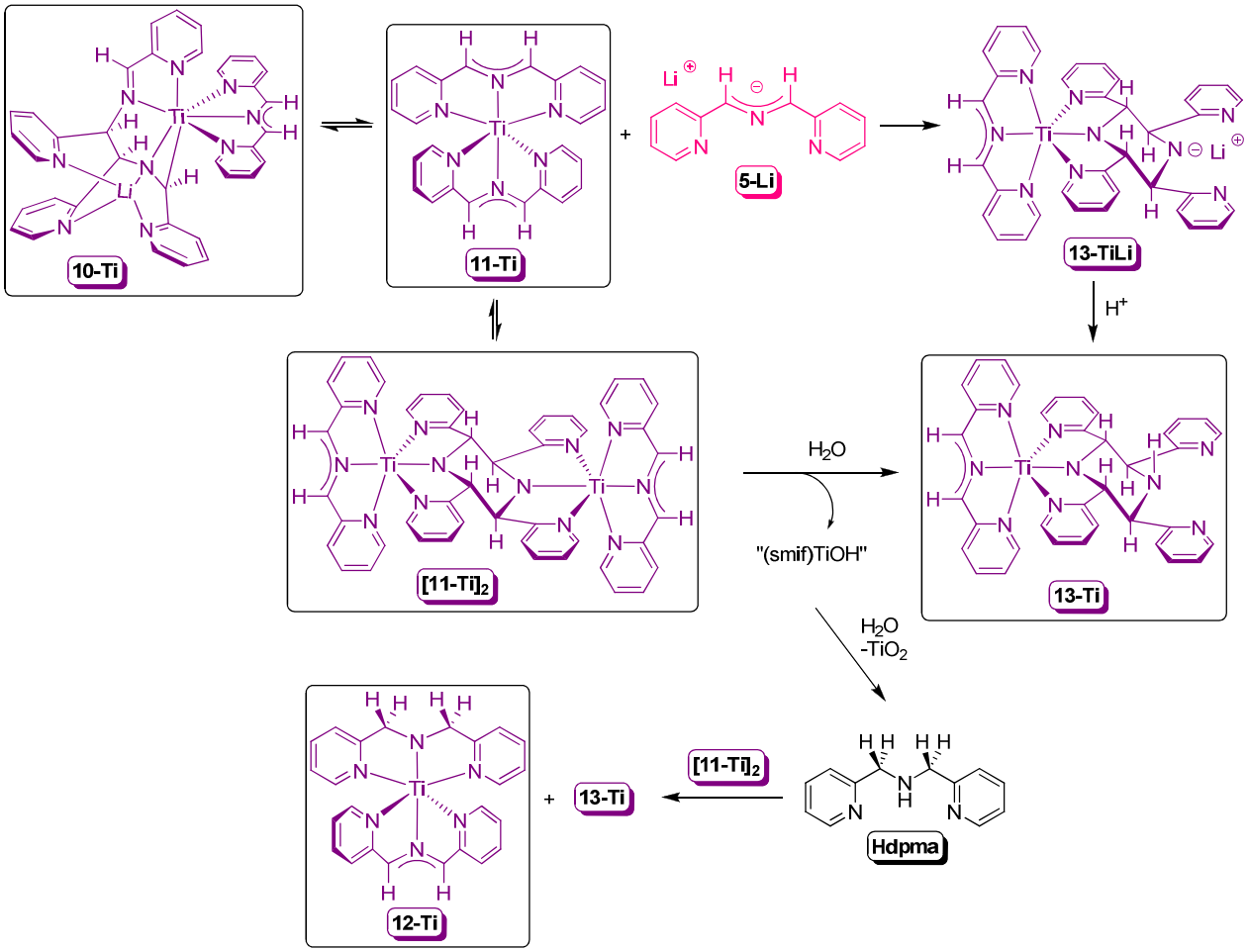

Scheme 3.2. Proposed mechanism for the formation of **10-Ti**, **11-Ti**, **12-Ti**, and **13-Ti**.

XAS Spectroscopy. X-ray absorption spectroscopy (XAS) was performed in order to gain a better grasp on the effective nuclear charge of the titanium center. The four titanium complexes are formally titanium(II) species, and XAS Ti K-edge data revealed the presence of a reduced titanium center (Figure 3.21). An assignment of Ti(III) seems appropriate for both **10-Ti** and **11-Ti** based upon a comparison of their Ti K pre-edge spectra with a Ti(III) reference, i.e. $TiCl_3(THF)_3$.

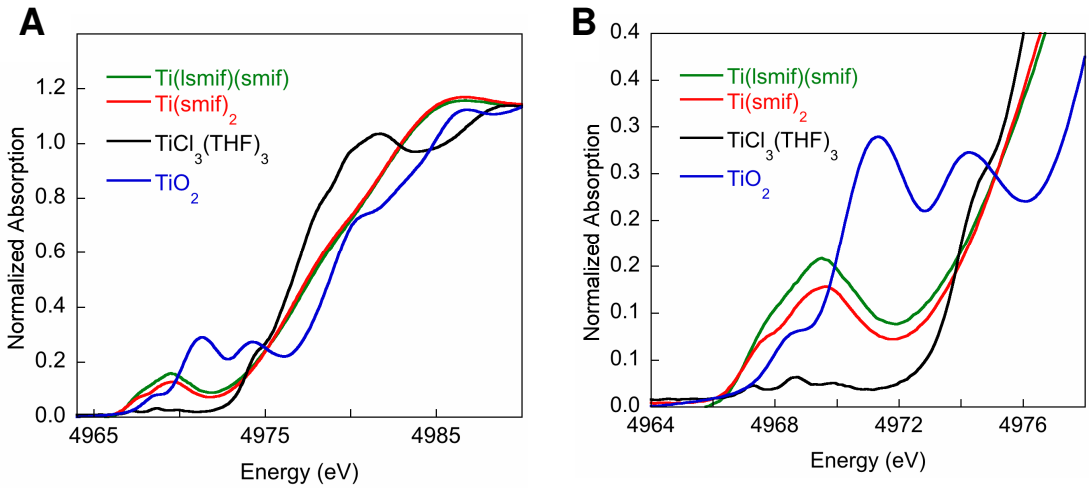

Figure 3.21. Normalized Ti K-edge XAS spectra obtained for **10-Ti** (denoted Ti(lsmif)(smif), green) and **11-Ti** (denoted $Ti(smif)_2$, red). Comparison of **10-Ti** and **11-Ti** with $TiCl_3(THF)_3$ and TiO_2, as references (**A**) and expanded Ti K pre-edge (**B**).

Conclusions

The smif ligand provided the necessary stabilization required for the formation of four new inorganic titanium(II) coordination complexes, albeit in various mixtures. Even though **10-Ti** was the only crystallographically characterized compound, NMR spectroscopy elucidated the identity of the three remaining species. XAS spectroscopy suggests this complex is best described as titanium(III). This would require at least a monoanionic smif ligand and the remaining three electrons may be distributed between smif and the rest of the ligand framework. The extensive 2-D spectroscopy in

conjunction with the ^{1}H NMR spectrum permitted the assignments and identification of four titanium(II) compounds. Unexpected for the assignment of **11-Ti** was the identification of three inequivalent pyridine rings. This seems consistent with a dimeric complex with a coupled smif ligand bridging between two (smif)Ti centers based upon the chemical shifts for the carbons in the smif backbone. XAS spectroscopy suggests a titanium(III) metal center. **11-Ti** may be described as $[(smif^{1.5-})_2Ti^{3+}]_2$, but this is a tentative assignment at best. The titanium(II) center in **12-Ti** has surprisingly been stabilized by a dipyridylamide and a smif ligand. The ability of smif to dimerize and undergo C–C coupling was observed in both complexes **10-Ti** and **13-Ti**. The fact that crystals of **10-Ti** in solution gave rise to the three other compounds suggests reversibility of the C–C bond formation.

Experimental

General Considerations. All manipulations were performed using either glovebox or high vacuum line techniques. Hydrocarbon solvents containing 1-2 mL of added tetraglyme, and ethereal solvents were distilled under nitrogen from purple sodium benzophenone ketyl and vacuum transferred from same prior to use. Benzene-d_6 was dried over sodium, vacuum transferred and stored under N_2. Li(smif) (**5-Li**) was prepared according to the procedures in the preceding chapter. $TiCl_3(THF)_3$[27] and 1,3-(2-pyridyl)-2-azapropene (smifH)[29] were prepared according to literature procedures. Lithium bis(trimethylsilyl)amide was purchased from Aldrich and recrystallized from hexanes prior to use. All other chemicals were commercially available and used as received. All glassware was oven dried.

NMR spectra were obtained using INOVA 400 and INOVA 600 spectrometers. Chemical shifts are reported relative to benzene-d_6 (^{1}H δ 7.16; ^{13}C{^{1}H} δ 128.39).

Synthesis. 1. (smif)$_2$Mg (6-Mg). To a 25 mL round bottom flask charged with $MgBr_2$ (0.091g, 0.49 mmol) and **5-Li** (0.200 g, 0.98 mmol) was vacuum transferred 10 mL THF at -78 °C resulting in a deep magenta solution which was slowly warmed to 23 °C. After the solution stirred for 12 h, the volatiles were removed *in vacuo*. The solid was triturated with Et_2O (3 x 5 mL) and filtered to yield $(smif)_2Mg$ as a microcrystalline gold solid (0.140 g, 68%). ^{1}H NMR (C_6D_6, 400 MHz): δ 5.82 (dd, py-C^5*H*, 1 H, J = 6.3, 1.0 Hz), 6.46 (d, py-C^3*H*, 1 H, J = 8.3 Hz), 6.72 (dd, py-C^4*H*, 1 H, J = 7.7, 1.8 Hz), 7.07 (s, C*H*, 1 H), 7.76 (d, py-C^6*H*, 1 H, J = 5.1 Hz). ^{13}C{^{1}H} NMR (C_6D_6, 100 MHz): δ 112.20 (*C*H), 114.14 (py-*C*^{3}H), 117.61 (py-*C*^{5}H), 137.04 (py-*C*^{4}H), 147.90 (py-*C*^{6}H), 158.46 (py-*C*^{2}).

Titanium smif compounds: To a 50 mL 3-neck flask charged with lithium bis(trimethylsilyl)amide (0.340 g, 2.04 mmol) and 0.95 % sodium amalgam (0.024 g Na, 1.06 mmol) was vacuum transferred 15 mL THF at -78 ℃. A solution of smifH (0.400 g, 2.02 mmol) in THF (20 mL) was slowly added to the 3-neck flask via a dropping funnel under argon. The solution immediately turned magenta and stirred at -78 ℃ for 2 h prior to the addition of $TiCl_3(THF)_3$ (0.376 g, 2.25 mmol). The reaction mixture turned dark purple after slowly warming to 23 ℃ and was stirred for 16 h. The volatiles were removed *in vacuo*, and the resulting dark black-purple solid was filtered in toluene yielding a mixture of 4 titanium compounds (0.290 g).

2. Lithium[(k-C,N^{am},N^{im},N$^{py}_3$-1,2-bis(pyridin-2-yl)-2-(pyridin-2-ylmethyleneamino)ethyl)(pyridin-2-ylmethideyl)amido)Ti(smif)] (10-Ti). ^{1}H NMR (C_6D_6, 600 MHz): δ 4.15 (s, backbone^C-C*H*, 1 H), 4.82 (d, backbone-C*H*, 1 H, J = 5.9 Hz), 5.07 (t, py^{im}-C^5*H*, 1 H, J = 6.3, 1.2 Hz), 5.30 (d, backbone-C*H*, 1 H, J = 6.0 Hz), 5.78 (t, py$^{asym'}$-C^5*H*, 1 H, J = 6.3 Hz), 5.95 (d, py$^{asym'}$-C^3*H*, 1 H, J = 8.5 Hz), 5.97 (t, py^{im}-C^4*H*, 1 H, J = 5.9, 1.2 Hz), 6.02 (t, py^{asym}-C^5*H*, 1 H, J = 6.3, 1.0 Hz), 6.11 (t, py$^{'''}$-C^5*H*, 1 H, J = 6.3, 1.1 Hz), 6.16 (t, py$^{''}$-C^5*H*, 1 H, J = 6.3, 1.1 Hz), 6.31 (t, py$^{'}$-C^5*H*, 1

H, J = 6.0 Hz), 6.34 (s, aza$^{asym'}$-C*H*, 1 H), 6.40 (d, py^{asym}-C^3*H*, 1 H, J = 7.7 Hz), 6.41 (d, py$^{'''}$-C^3*H*, 1 H, J = 9.0 Hz), 6.42 (s, aza^{sym}-C*H*, 1 H), 6.58 (d, py$^{''}$-C^3*H*, 1 H, J = 7.2 Hz), 6.59 (t, py$^{asym'}$-C^4*H*, 1 H, J = 8.0 Hz), 6.62 (dd, py^{asym}-C^4*H*, 1 H, J = 8.1, 1.4 Hz), 6.70 (t, py$^{''}$-C^4*H*, 1 H, J = 6.3, 1.8 Hz), 6.70 (s, im-C*H*, 1 H), 6.73 (d, py$^{'}$-C^3*H*, 1 H, J = 7.7 Hz), 6.74 (d, py^{im}-C^3*H*, 1 H, J = 9.0 Hz), 6.82 (t, py$^{'}$-C^4*H*, 1 H, J = 7.7, 1.8 Hz), 6.97 (t, py$^{'''}$-C^4*H*, 1 H, J = 7.7 Hz), 7.17 (d, py$^{asym'}$-C^6*H*, 1 H, J = 4.4 Hz), 7.51 (d, py$^{'''}$-C^6*H*, 1 H, J = 4.7 Hz), 7.65 (d, py$^{'}$-C^6*H*, 1 H, J = 4.7 Hz), 7.69 (d, py$^{''}$-C^6*H*, 1 H, J = 4.8 Hz), 8.15 (d, py^{asym}-C^6*H*, 1 H, J = 5.5 Hz), 8.42 (d, py^{im}-C^6*H*, 1 H, J = 6.6 Hz). ^{13}C{^{1}H} (C_6D_6, 150 MHz): δ 76.50 (backbone-*C*H), 78.88 (backbone-*C*H), 87.72 (backbone^C-*C*H), 99.68 (py^{im}-*C*^{5}H), 109.18 (py$^{'''}$-*C*^{5}H), 110.72 (aza^{sym}-*C*H), 111.58 (py^{asym}-*C*^{5}H), 111.75 (py$^{asym'}$-*C*^{5}H), 112.87 (aza$^{asym'}$-*C*H), 115.38 (im-*C*H), 114.95 (py$^{'''}$-*C*^{3}H), 117.60 (py^{asym}-*C*^{3}H), 117.62 (py$^{asym'}$-*C*^{3}H), 121.43 (py$^{''}$-*C*^{5}H), 121.59 (py$^{'}$-*C*^{5}H), 121.68 (py^{im}-*C*^{4}H), 122.93 (py$^{''}$-*C*^{3}H), 123.34 (py^{im}-*C*^{3}H), 124.88 (py$^{'}$-*C*^{3}H), 133.60 (py$^{asym'}$-*C*^{4}H), 133.82 (py$^{'''}$-*C*^{4}H), 134.39 (py^{asym}-*C*^{4}H), 135.78 (py$^{''}$-*C*^{4}H), 136.90 (py$^{'}$-*C*^{4}H), 142.74 (py^{im}-*C*^{2}), 146.83 (py$^{'''}$-*C*^{6}H), 147.40 (py$^{asym'}$-*C*^{6}H), 147.45 (py^{im}-*C*^{6}H), 147.67 (py$^{'}$-*C*^{6}H), 147.87 (py$^{''}$-*C*^{6}H), 149.74 (py^{asym}-*C*^{6}H), 156.80 (py$^{asym'}$-*C*^{2}), 156.93 (py^{asym}-*C*^{2}), 164.33 (py$^{'}$-*C*^{2}), 164.52 (py$^{''}$-*C*^{2}), 164.82 (py$^{'''}$-*C*^{2}).

3. (smif)$_2$Ti (11-Ti). ^{1}H NMR (C_6D_6, 600 MHz): δ 2.19 (s, aza^{sym}-C*H*, 2 H), 2.60 (td, py$^{asym'}$-C^5*H*, 1 H, J = 6.6, 1.1 Hz), 3.05 (s, aza$^{asym'}$-C*H*, 1 H), 3.18 (t, py^{asym}-C^4*H*, 1 H, J = 8.6 Hz), 3.35 (s, aza^{asym}-C*H*, 1 H), 3.49 (d, py$^{asym'}$-C^6*H*, 1 H, J = 7.3 Hz), 4.09 (t, py$^{asym'}$-C^4*H*, 1 H, J = 7.8 Hz), 4.40 (dd, py^{asym}-C^5*H*, 1 H, J = 9.3, 6.0 Hz), 4.53 (d, py$^{asym'}$-C^3*H*, 1 H, J = 9.3 Hz), 4.71 (d, py^{asym}-C^6*H*, 1 H, J = 7.0 Hz), 4.98 (d, py^{asym}-C^3*H*, 1 H, J = 9.7 Hz), 6.44 (d, py^{sym}-C^3*H*, 2 H, J = 8.1 Hz), 7.36 (t, py^{sym}-C^4*H*, 2 H, J = 8.6 Hz), 8.08 (t, py^{sym}-C^5*H*, 2 H, J = 6.6 Hz), 13.88 (d, py^{sym}-C^6*H*, 2 H, J = 4.6 Hz). ^{13}C{^{1}H} (C_6D_6, 150 MHz): δ 74.93 (aza^{sym}-*C*H), 100.00 (py^{asym}-*C*^{4}H), 100.59 (py$^{asym'}$-*C*^{5}H), 108.46 (aza$^{asym'}$-*C*H), 108.76 (aza^{asym}-*C*H), 122.37 (py$^{asym'}$-*C*^{3}H),

123.00 (py^{asym}-C^3H), 124.63 (py^{sym}-C^5H), 125.54 (py^{asym}-C^5H), 125.65 (py^{sym}-C^3H), 126.19 ($py^{asym'}$-C^4H), 136.92 (py^{sym}-C^4H), 146.22 ($py^{asym'}$-C^6H), 147.17 (py^{asym}-C^6H), 150.78 (py^{sym}-C^2), 154.25 (py^{sym}-C^6H), 156.67 (py^{asym}-C^2), 156.74 ($py^{asym'}$-C^2).

4. (smif)(dpma)Ti (12-Ti). ^{1}H NMR (C_6D_6, 600 MHz): δ 3.19 (t, py^{smif}-C^5H, 1 H, J = 8.6 Hz), 3.29 (s, dpma-CH_2, 2 H), 3.43 (s, aza-C*H*, 1 H), 4.08 (d, py^{smif}-C^6H, 1 H, J = 7.1 Hz), 4.51 (t, py^{smif}-C^4H, 1 H, J = 9.3, 6.0, 1.2 Hz), 4.91 (d, py^{smif}-C^3H, 1 H, J = 9.3 Hz), 6.86 (d, py^{dpma}-C^3H, 1 H, J = 9.4 Hz), 7.36 (t, py^{dpma}-C^4H, 1 H, J = 6.0 Hz), 7.84 (t, py^{dpma}-C^5H, 1 H, J = 6.6 Hz), 13.61 (d, py^{dpma}-C^6H, 1 H, J = 5.0 Hz). $^{13}C\{^1H\}$ (C_6D_6, 150 MHz): δ 61.83 (dpma-CH_2),100.11 (py^{smif}-C^5H), 108.43 (aza-*C*H), 121.68 (py^{dpma}-C^3H), 122.76 (py^{smif}-C^3H), 124.13 (py^{dpma}-C^5H), 125.54 (py^{smif}-C^4H), 138.17 (py^{dpma}-C^4H), 146.08 (py^{smif}-C^6H), 153.12 (py^{dpma}-C^6H), 153.88 (py^{dpma}-C^2), 155.72 (py^{smif}-C^2).

5. (κ-N^{am},N^{py}_2-2,3,5,6-tetrakis(pyridin-2-yl)piperazin-1-yl)(smif)Ti (13-Ti). ^{1}H NMR (C_6D_6, 600 MHz): δ 2.80 (t, backbone^{symUC}-C*H*, 2 H, J = 9.8 Hz), 3.01 (t, N*H*, 1 H, J = 9.8 Hz), 3.02 (t, py^{asym}-C^5H, 1 H, J = 7.6 Hz), 3.20 (s, aza^{asym}-C*H*, 1 H), 3.41 (s, $aza^{asym'}$-C*H*, 1 H), 3.52 (t, $py^{asym'}$-C^4H, 1 H, J = 6.5 Hz), 4.12 (d, py^{asym}-C^6H, 1 H, J = 6.8 Hz), 4.33 (dd, py^{asym}-C^4H, 1 H, J = 9.3, 6.0 Hz), 4.38 (d, backbone^{symC}-C*H*, 2 H, J = 8.7 Hz), 4.63 (dd, $py^{asym'}$-C^5H, 1 H, J = 9.0, 5.8 Hz), 4.68 (d, $py^{asym'}$-C^3H, 1 H, J = 9.1 Hz), 5.02 (d, $py^{asym'}$-C^6H, 1 H, J = 6.9 Hz), 5.04 (d, $py^{asym'}$-C^3H, 1 H, J = 9.0 Hz), 5.99 (d, py^{symC}-C^3H, 2 H, J = 5.8 Hz), 6.30 (d, py^{symUC}-C^3H, 2 H, J = 7.7 Hz), 6.56 (t, py^{symUC}-C^5H, 2 H, J = 6.8 Hz), 6.87 (t, py^{symUC}-C^4H, 2 H, J = 7.7 Hz), 7.09 (t, py^{symC}-C^4H, 2 H, J = 7.7, 1.4 Hz), 7.92 (t, py^{symC}-C^5H, 2 H, J = 6.3 Hz), 8.38 (d, py^{symUC}-C^6H, 2 H, J = 4.4 Hz), 13.99 (d, py^{symC}-C^6H, 2 H, J = 4.8 Hz). $^{13}C\{^1H\}$ (C_6D_6, 150 MHz): δ 66.39 (backbone^{symUC}-*C*H), 73.85 (backbone^{symC}-*C*H), 100.20 ($py^{asym'}$-C^4H), 100.79 (py^{asym}-C^5H), 108.28 ($aza^{asym'}$-*C*H), 108.66 (aza^{asym}-*C*H), 122.47 (py^{symUC}-C^5H), 122.80 ($py^{asym'}$-C^3H), 123.12 ($py^{asym'}$-C^3H), 123.38 (py^{symC}-C^3H),

124.55 (py^{symC}-C^5H), 124.69 (py^{symUC}-C^3H), 125.30 ($py^{asym'}$-C^5H), 125.71 (py^{asym}-C^4H), 135.87 (py^{symUC}-C^4H), 137.11 (py^{symC}-C^4H), 146.81 (py^{asym}-C^6H), 147.65 ($py^{asym'}$-C^6H), 149.92 (py^{symUC}-C^6H), 152.74 (py^{symC}-C^2), 154.23 (py^{symC}-C^6H), 156.11 (py^{asym}-C^2), 156.21 ($py^{asym'}$-C^2),159.96 (py^{symUC}-C^2).

XAS Spectroscopy. XAS data were measured at the Stanford Synchrotron Radiation Lightsource using focused beam line 9-3, under ring conditions of 3 GeV and 60-100 mA. A Si(220) double-crystal monochromator was used for energy selection and a Rh-coated mirror (set to an energy cutoff of 9 keV) was utilized in combination with 30% detuning for rejection of higher harmonics. All samples were prepared as dilutions in BN and measured as transmission spectra. Samples were maintained at 10K using an Oxford continuous flow. To check for reproducibility, 2-3 scans were measured for all samples. The energy was calibrated from Ti foil spectra, with the first inflection set to 4966.0 eV. A step size of 0.11 eV was used over the edge region. Data were averaged, and a smooth background was removed from all spectra by fitting a polynomial to the pre-edge region and subtracting this polynomial from the entire spectrum. Normalization of the data was accomplished by fitting a flattened polynomial or straight line to the post-edge region and normalizing the edge jump to 1.0 at 5000 eV.

Single Crystal X-Ray Diffraction Studies. Upon isolation, the crystals were covered in polyisobutenes and placed under a 173 K N_2 stream on the goniometer head of a Siemens P4 SMART CCD area detector (graphite-monochromated MoK_α radiation, λ = 0.71073 Å). The structures were solved by direct methods (SHELXS). All non-hydrogen atoms were refined anisotropically unless stated, and hydrogen atoms were treated as idealized contributions (Riding model).

6. 10-Ti. A metallic gold-green block (0.35 x 0.25 x 0.15 mm) was obtained from benzene at 23 °C. A total of 29,322 reflections were collected with 8,504

determined to be symmetry independent (R_{int} = 0.0356), and 6,256 were greater than 2σ(I). A semi-empirical absorption correction from equivalents was applied, and the refinement utilized $w^{-1} = \sigma^2(F_o^2) + (0.0461p)^2 + 0.3555p$, where $p = ((F_o^2 + 2F_c^2)/3)$.

REFERENCES

1 Sato, F.; Urabe, H.; Okamoto, S. *Chem. Rev.* **2000**, *100*, 2835-2886.

2 Kulinkovich, O. G.; de Meijere, A. *Chem. Rev.* **2000**, *100*, 2789-2834.

3 Wong, H. N. C. *Acc. Chem. Res.* **1989**, *22*, 145-152.

4 Hanamoto, T.; Yamada, K. *J. Org. Chem.* **2009**, *74*, 7559-7561.

5 You, Y.; Wilson, S. R.; Girolami, G. S. *Organometallics* **1994**, *13*, 4655-4657.

6 You, Y.; Girolami, G. S. *Organometallics* **2008**, *27*, 3172-3180.

7 Devore, D. D.; Timmers, F. J.; Hasha, D. L.; Rosen, R. K.; Marks, T. J.; Deck, P. A.; Stern, C. L. *Organometallics* **1995**, *14*, 3132-3134.

8 Sikora, D. J.; Macomber, D. W.; Rausch, M. D. *Adv. Organomet. Chem.* **1986**, *25*, 317-379.

9 Kool, L. B.; Rausch, M. D.; Alt, H. G.; Herberhold, M.; Thewalt, U.; Honold, B. *J. Organomet. Chem.* **1986**, *310*, 27-34.

10 Horáček, M.; Kupfer, V.; Thewalt, U.; Štěpnička, P.; Polášek, M.; Mach, K. *Organometallics* **1999**, *18*, 3572-3578.

11 Cuenca, T.: Gómez, R.; Gómez-Sal, P.; Royo, P. *J. Organomet. Chem.* **1993**, *454*, 105-111.

12 DiMauro, P. T.; Wolczanski, P. T. *Organometallics* **1987**, *6*, 1947-1954.

13 Gedridge, R. W.; Arif, A. M.; Ernst, R. D. *J. Organomet. Chem.* **1995**, *501*, 95-100.

14 Varga, V.; Polášek, M.; Hiller, J.; Thewalt, U.; Sedmera, P.; Mach, K. *Organometallics* **1996**, *15*, 1268-1274.

15 Cloke, F. G. N.; Hanks, J. R.; Hitchcock, P. B.; Nixon, J. F. *Chem. Commun.* **1999**, 1731-1732.

16 Fowles, G. W. A.; Lester, T. E. *Chem. Commun.* **1967**, *1*, 47-48.

17 Fowles, G. W. A.; Lester, T. E.; Walton, R. A. *J. Chem. Soc. A, Inorg. Phys. Theor.* **1968**, 1081-1085.

18 Edema, J. J. H.; Duchateau, R.; Gambarotta, S.; Hynes, R.; Gabe, E. *Inorg. Chem.* **1991**, *30*, 154-156.

19 Girolami, G. S.; Wilkinson, G.; Galas, A. M. R.; Thornton-Pett, M.; Hursthouse, M. B. *J. Chem. Soc., Dalton Trans.* **1985**, 1339-1348.

20 Morris, R. J.; Girolami, G. S. *Inorg. Chem.* **1990**, *29*, 4167-4169.
21 Jensen, J. A.; Girolami, G. S. *Inorg. Chem.* **1989**, *28*, 2107-2113.

22 Jensen, J. A.; Wilson, S. R.; Schultz, A. J.; Girolami, G. S. *J. Am. Chem. Soc.* **1987**, *109*, 8094-8096.

23 Spencer, M. D.; Wilson, S. R.; Girolami, G. S. *Organometallics* **1997**, *16*, 3055-3067.

24 Kayal, A.; Kuncheria, J.; Lee, S. C. *Chem. Commun.* **2001**, 2482-2483.

25 Woo. L. K.; Hays, J. A.; Jacobson, R. A.; Day, C. L. *Organometallics* **1991**, *10*, 2102-2104.

26 Woo, L. K.; Hays, J. A.; Young, V. G.; Day, C. L.; Caron, C.; D'Souza, F.; Kadish, K. M. *Inorg. Chem.* **1993**, *32*, 4186 - 4192.

27 Manzer, L. E. *Inorg. Synth.* **1982**, *21*, 135-140.

28 Liu, J.-Z.; Ernst, R. D. *J. Am. Chem. Soc.* **1982**, *104*, 3737-3739.

29 Incarvito, C.; Lam, M.; Rhatigan, B.; Rheingold, A. L.; Qin, C. J.; Gavrilova, A. L.; Bosnich, B. *J. Chem. Soc., Dalton Trans.* **2001**, 3478-3488.

CHAPTER 4

Reactivity of the Coordinated Dipyridylazaallyl Ligand on Iron*

Introduction

As previously mentioned in Chapter 1, the serendipitous formation of (smif)CrN(TMS)$_2$ (**4-Cr**) was an interesting discovery. The smif ligand not only exhibits unique optical properties, but it is also has the ability to stabilize complexes with low symmetry. In seeking to achieve the ultimate goal of the project by generating 1st-row transition metal catalysts, this ligand framework seemed promising. While the low symmetry of a mono-smif metal complex may lend itself toward catalysis, the azaallyl backbone has potential applications in the synthesis of new heterocycles, which may be beneficial in drug syntheses.

Hopes for catalysis stem from the Buchwald-Hartwig chemistry for synthesizing new C-N bonds from aryl halides and anilines.[1-3] Efforts in our laboratory would focus on generating the iron analog of **4-Cr** because this complex would be less toxic and less expensive. With respect to a potential catalytic cycle, one may envision treating a (smif)FeN(TMS)$_2$ complex with an aryl halide to generate the oxidative addition product, an iron(IV) species, which has the potential to be stabilized by the smif ligand. Reductive elimination of an arylated amine would generate a (smif)FeX species. This complex may be converted to a variety of different smif-iron-amide complexes depending upon which free amine was desired for coupling. One can envision the generation of secondary amines in addition to tertiary amines.

Heterocycles are an integral part of natural products and drug syntheses.[4] It is important to find new ways to generate these pieces as syntheses for natural products are often sensitive to reaction conditions. A common method used to synthesize

---

* Reproduced with permission from: Frazier, B. A.; Wolczanski, P. T.; Lobkovsky, E. B.; Cundari, T. R. *J. Am. Chem. Soc.* **2009**, *131*, 3428-3429.

heterocyclic five-membered rings has employed the use of azaallyl fragments. As shown in Figure 4.1, a few general types of azaallyl fragments have been prepared since the early 1900's and subsequent reactivity for the fragments has been probed.

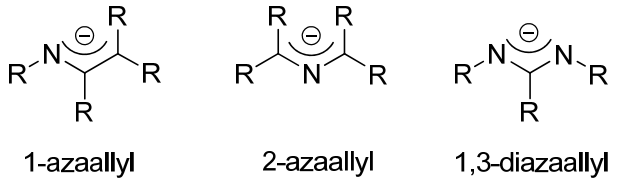

Figure 4.1. Anionic azaallyl fragments.

Treatment of the anionic 2-azaallyl complex with unsaturated organic substrates has led to the formation of new five-membered heterocyclic rings via [3+2] cycloadditions. These azaallyls have been subjected to alkenes,[5-14] imines,[5,6,15,16] nitriles,[5,6,17-20] carbonyl containing molecules,[5,6,15,16,20] and diazo compounds.[5,6,15,16] In a few cases, exposing an azaallyl complex to a diene has generated a ring size larger than five.[21-23] The smif ligand is a variant of the anionic 2-azaallyl fragment; therefore, similar reactivity from the smif backbone is anticipated.

Results and Discussion

Synthesis of ligands. As described in Chapter 2, condensation of 2-pyridinecarboxaldehyde with 2-(aminomethyl)pyridine yielded 1,3-di-(2-pyridyl)-2-azapropene, **smifH**, in quantitative yield (eq 4.1).[24]

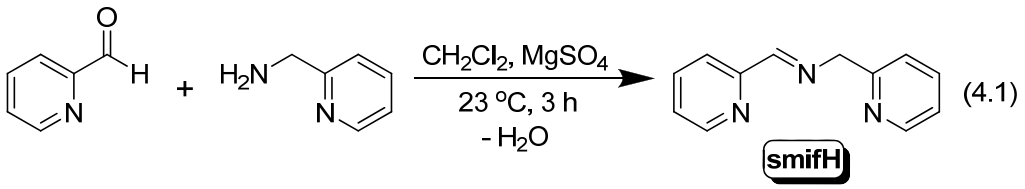

Ligand modifications for **smifH** proved synthetically challenging as altering pyridine rings is not a trivial task, and commercially available substituted 2-picolylamines, 2-pyridinecarboxaldehydes, or even 2-cyanopyridines are expensive. Condensation of 6-methyl-2-pyridinecarboxaldehyde with substituted 2-(aminomethyl)pyridines afforded new dipyridylimines (eq 4.2).[25] **^{o}MesmifH** was isolated as a pale yellow liquid in 97 % yield, and the pale yellow solid, **^{o}Me$_2$smifH**, was isolated in 92 % yield. ^{1}H NMR spectroscopy revealed the presence of only one isomer in solution. Substitution *ortho*

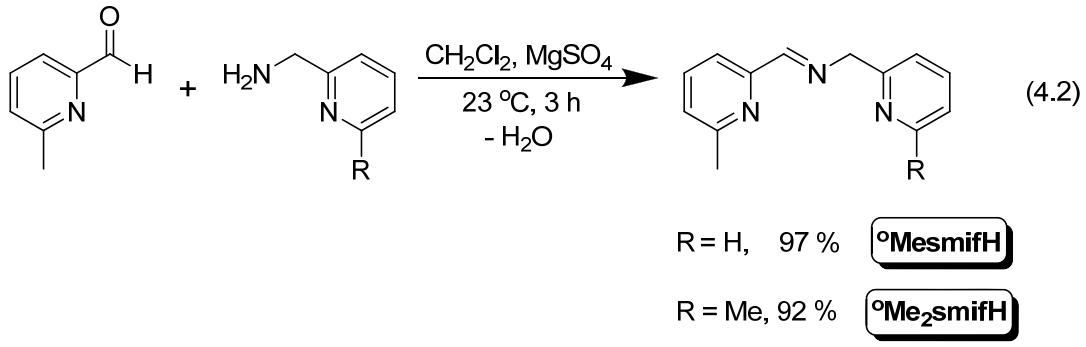

to the pyridine nitrogen was intended to prevent the formation of $(smif)_2M$ complexes, whereas backbone substitution was designed to prevent ligand reactivity. Deprotonation of the acidic benzylic protons on the appropriate **smifH** ligand in THF followed by the addition of two equivalents of CH_3I yielded ligands possessing methylated backbones (Scheme 4.1).

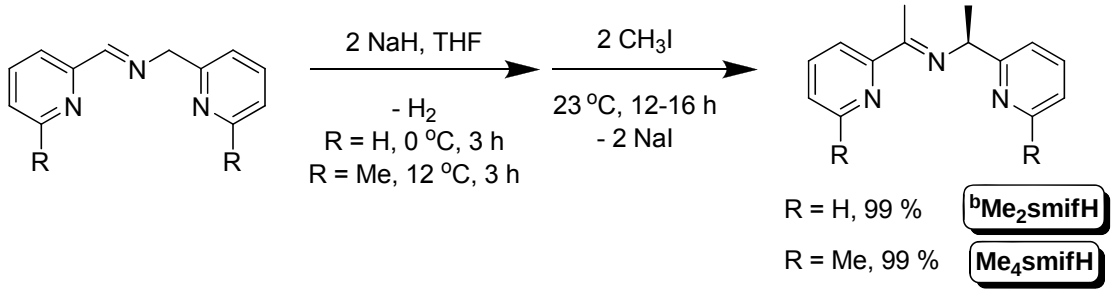

Scheme 4.1. Synthesis of backbone methylated **smifH** derivatives.

Di-(2-picolyl)amine, **Hdpma**, was another desired ligand as it would generate a monoanionic amide upon deprotonation, differing from an azaallyl ligand by 2 H^+ and 2 e^-. This organic molecule is commercially available, yet slightly expensive. Efforts to incorporate deuteration into the benzylic positions generating **D-$d_4$dpma** led to the discovery of an alternative and cheaper synthetic route. Previous work by Incarvito et al. showed that the reduction of **smifH** with sodium borohydride followed by an acidic work-up yielded **Hdpma** (eq 4.3).[24]

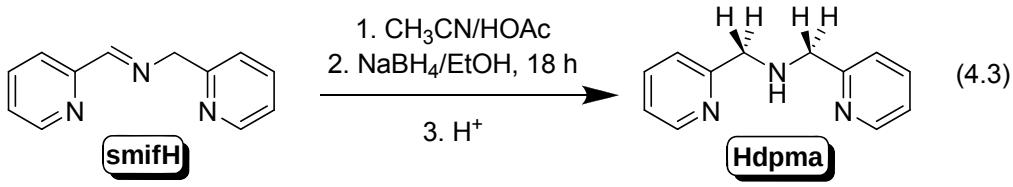

(4.3)

Interestingly, synthetic attempts to isolate deuterated (2-aminomethyl)pyridine, **D-$d_2$pma**, a **smifH** precursor, via a literature procedure[26] yielded a mixture of two compounds, i.e. **D-$d_2$pma** and **D-$d_4$dpma**, which were easily separated via distillation (eq 4.4). Optimization of reaction conditions showed that refluxing a suspension of 2-cyanopyridine and sodium borodeuteride in CH_3OD for 16 h yielded **D-$d_4$dpma** and **D-$d_2$pma** in 44% and 28 % yields, respectively.

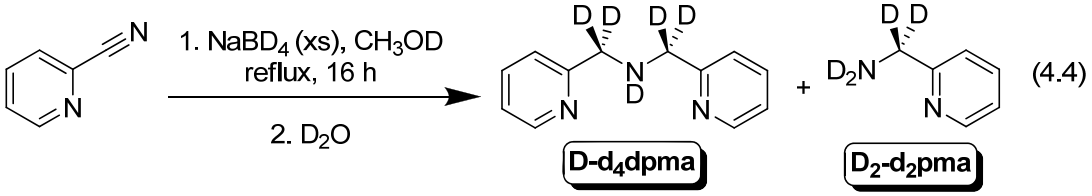

(4.4)

Synthesis of (smif)FeN(TMS)$_2$ and analogs. Efforts to generate potential Buchwald-Hartwig catalysts focused on synthesizing mono-smif iron analogues of (smif)CrN(TMS)$_2$ (**4-Cr**). Treatment of Fe{N(TMS)$_2$}$_2$(THF)[27] in Et_2O with one equivalent of **smifH** generated a deep emerald green solution, i.e. (smif)FeN(TMS)$_2$ (**14-Fe**), from which [{$(Me_3Si)_2$N}Fe]$_2$(μ-$N^{am}{}_2$,$N^{py}{}_4$-2,3,5,6-tetrakis(pyridin-2-

yl)piperazyl) (**[14-Fe]$_2$**) was isolated as orange crystals in 74 % yield (Scheme 4.2). ^{1}H NMR spectroscopy revealed a paramagnetic complex containing one smif environment and a N(TMS)$_2$ group. It is noteworthy to mention that optimization of reaction conditions, e.g. rate and order of addition for reagents, was important to avoid the formation of **6-Fe**. Single crystal, x-ray crystallographic studies revealed that **14-Fe** dimerizes in the solid state to form a bridging tetra-substituted piperazine bis-amide ligand, **[14-Fe]$_2$**. A K_{eq} value of ~ 4 x 10^{-4} M^{-1} ($\Delta G° \approx 5$ kcal/mol) for the dimerization from **14-Fe** ≡ **[14-Fe]$_2$** was established via ^{1}H NMR spectral analysis.[28]

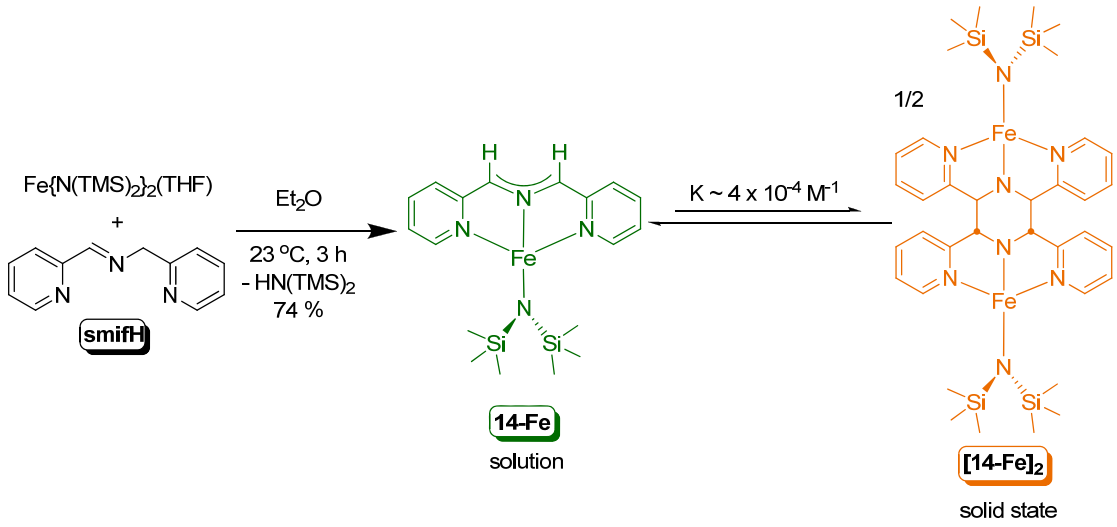

Scheme 4.2. Synthesis of (smif)FeN(TMS)$_2$ (**14-Fe**) and dimerization to **[14-Fe]$_2$.**

The dimerization of the smif backbone may be better understood by examining the electronic features associated with the $CN_{aza}C^{nb}$ orbital. As shown in Figure 4.2, the $CN_{aza}C^{nb}$ orbital can be utilized to write a simplified wave function, Ψ. Expansion of the orbital component of Ψ yields ionic and covalent portions, which may be indicative of heterolytic and diradical reactivity, respectively. Therefore, the dimerization event to yield **[14-Fe]$_2$** may be considered either an electrophile-nucleophile process or a diradical coupling event (Scheme 4.3).

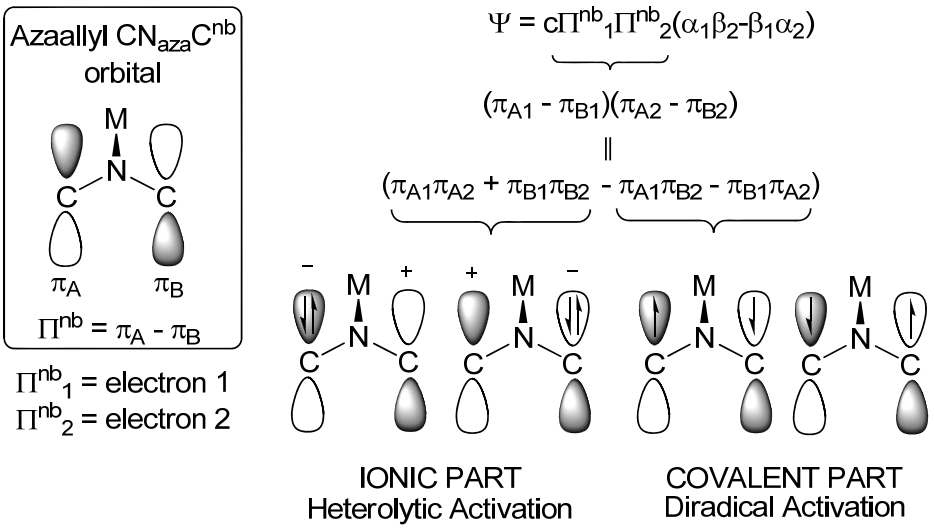

Figure 4.2. Electronic features of $CN_{aza}C^{nb}$ orbital providing rationale for potential reactivity.

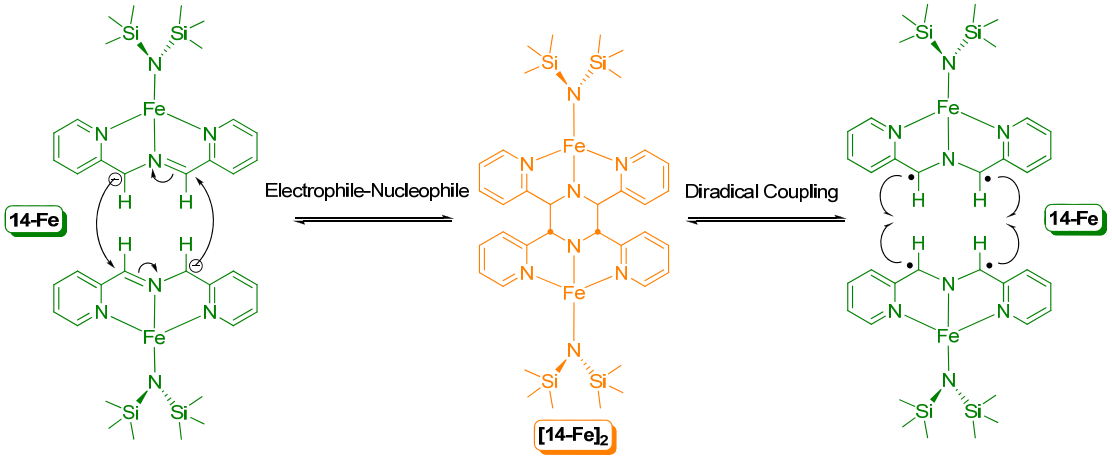

Scheme 4.3. Dimerization event to form **[14-Fe]$_2$** from **14-Fe** via an electrophile-nucleophile process (left) or diradical coupling event (right).

To better understand why orange crystals of **[14-Fe]$_2$** yielded a deep emerald green color in solution, a bis-amide analog incapable of C-C bond formation was prepared. Exposing $Fe\{N(TMS)_2\}_2(THF)$ in Et_2O with one equivalent of **Hdpma** afforded red needles of $(dpma)FeN(SiMe_3)_2$ (**15-Fe**) in 64 % yield (Scheme 4.4).

Cherry-red solutions of **15-Fe** did not exhibit unusual optical intensities (λ_{max} = 549 nm, ε ~ 1,500 M^{-1} cm^{-1}), thereby implying that solutions containing **[14-Fe]$_2$** as the piperazine amide would be relatively weakly colored. However, crystals of **[14-Fe]$_2$** dissolved in benzene produced solutions of great intensities (λ_{max} = 633 nm, e ~ 52,000 M^{-1} cm^{-1}) suggesting reversion to the monomeric form, **14-Fe**, in solution. The ^{1}H NMR spectrum of the paramagnetic complex, **15-Fe,** showed one N(TMS)$_2$ group and one dpma environment, and the compound is depicted as a monomeric square planar complex. However, **15-Fe** may exist as a dimeric complex as shown in Scheme 4.4.

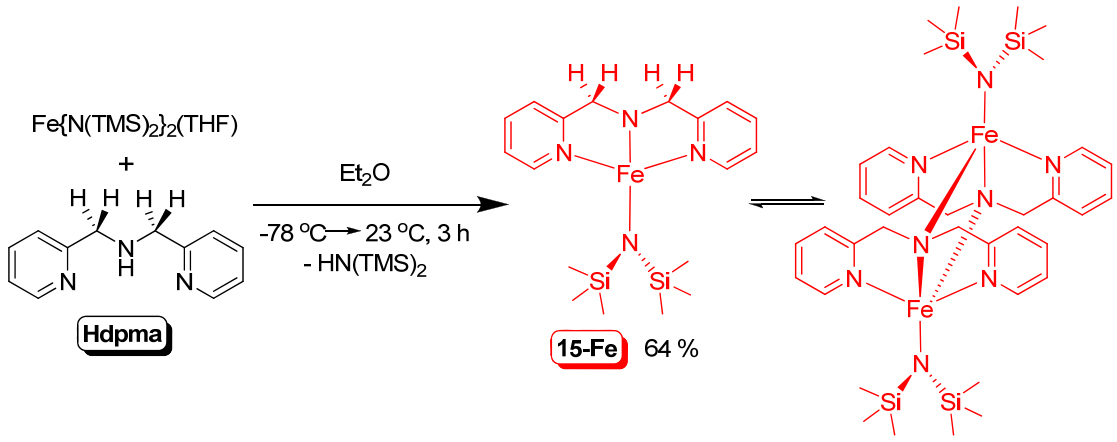

Scheme 4.4. Synthesis of (dpma)FeN(TMS)$_2$ (**17-Fe**).

Similar to the synthesis of **14-Fe**, reaction conditions were carefully controlled to produce **15-Fe** because a fast addition of **Hdpma** led to the formation of a new paramagnetic complex, (dpma)$_2$Fe (**16-Fe**), whose synthesis was optimized via the treatment of Fe{N(TMS)$_2$}$_2$(THF) in Et$_2$O with two equivalents of **Hdpma** (eq 4.5). **16-Fe** was isolated as dark blue-metallic purple crystals in 75 % yield from a dark blue solution and was crystallographically characterized. ^{1}H NMR spectroscopy revealed one set of dpma peaks with chemical shifts ranging from 8 to 165 ppm. It is important

to note that this complex differs from **6-Fe** by 4 H^+ and 4 e^-; therefore, **16-Fe** may be construed as a potential source of dihydrogen.

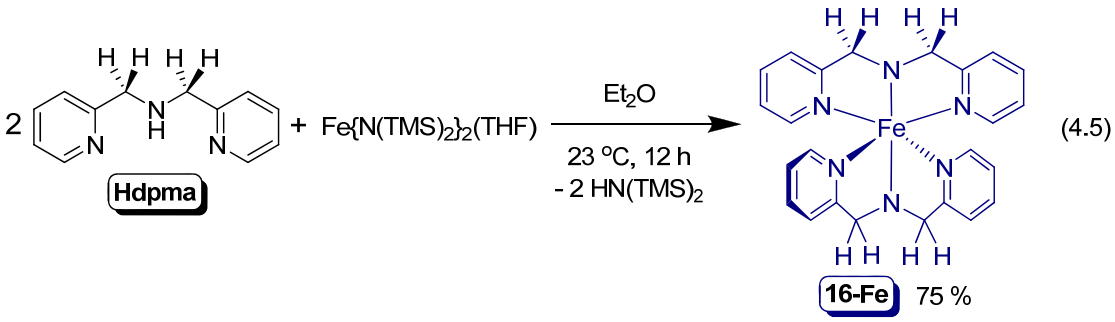

Characterization of (smif)FeN(TMS)$_2$ (14-Fe): X-ray Structure of [14-Fe]$_2$. X-ray quality, orange parallelpiped single crystals of **[14-Fe]$_2$** were isolated from pentane after recrystallization at 80 °C. Select crystallographic and refinement data for [**14-Fe]$_2$** are listed in Table 4.1. Pertinent bond distances and angles are listed in Table 4.2. The solid state structure of [**14-Fe]$_2$**, shown in Figure 4.3, depicts a square planar Fe(II) compound with an amide, N(TMS)$_2$, perpendicular to the plane produced by the dimerized smif ligand, or bridging tetra-substituted piperazine. Amide nitrogens in **[14-Fe]$_2$** span an angle of 178.53(4) ° (N2-Fe1-N4) around iron in contrast to the $N_{aza}CrN_{am}$ angle of 168.76(8) ° observed in the structure of (smif)CrN(TMS)$_2$ (**4-Cr**). Similar to all crystallographically characterized smif complexes, the pyridines of this tetra-substituted piperazine ligand span an angle of 154.48(4) ° around iron. The piperazine chelate has acute bite angles, i.e. ∠N2-Fe1-N1 = 77.20(4) ° and ∠N2-Fe1-N3 = 77.38(4) °. Consequently, the corresponding angles between the pyridine nitrogens and the amide nitrogen from N(TMS)$_2$ are obtuse: ∠N4-Fe1-N1 = 101.94(4) ° and ∠N4-Fe1-N3 = 103.43(4) °. Similar core angles are seen in the structure of **4-Cr**. The piperazine chelate possesses amide nitrogen-carbon distances of 1.4334(17) Å and 1.4356(16) Å, consistent with an sp^2(N)-sp^3(C) assignment, whereas smif complexes have N_{aza}-C distances ~ 1.33 Å, which are more indicative of a delocalized

anion. Additionally, the dimerization of **14-Fe** to **[14-Fe]$_2$** results in the reversible formation of an sp^3(C) -sp^3(C) bond with a distance of 1.5781(18) Å, slightly elongated from the expected value of 1.54 Å and perhaps indicative of its reversibility. Iron-nitrogen bond distances are normal and distinguish between the types of nitrogens. Pyridine nitrogen-iron bond lengths are 2.1950(11) Å and 2.1910(11) Å consistent with σ-donation from the pyridine, whereas the amide-iron distances are shorter, i.e. d(Fe1-N2) = 1.9432(10) Å and d(Fe1-N4) = 1.9538(10) Å.

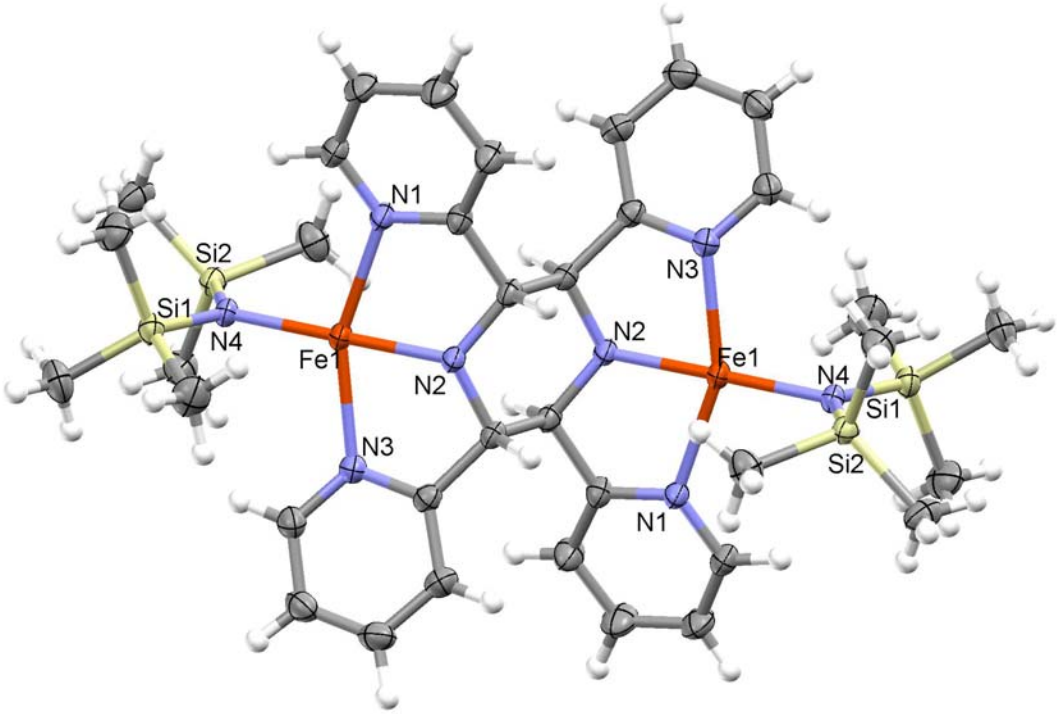

Figure 4.3. Molecular structure of [(smif)FeN(TMS)$_2$]$_2$ **[14-Fe]$_2$**. Thermal ellipsoids are at 50 % probability level.

Table 4.1. X-ray crystallographic data for [(smif)FeN(TMS)$_2$]$_2$ **[14-Fe]$_2$**, (dpma)$_2$Fe (**16-Fe**), [(Me$_4$smif)FeN(TMS)$_2$]$_2$ (**28-Fe**), [(2,5-di(pyridin-2-yl)-3,4-di-(*p*-tolyl-2,5-di hydropyrrol-1-ide))FeN(TMS)$_2$]$_2$ (**29-Fe**), and (2,6-^{i}Pr$_2$PhNCOsmif)$_2$Fe (**30-Fe**).

	[14-Fe]$_2$	**16-Fe**	**28-Fe**	**29-Fe**	**30-Fe-DIPP**
Formula	$C_{18}H_{28}N_4Si_2Fe$[a]	$C_{24}H_{24}N_6Fe$	$C_{44}H_{72}N_8Si_4Fe_2$[b]	$C_{68}H_{84}N_8Si_4Fe_2$[c]	$C_{54}H_{62}N_8O_3Fe$[d]
Formula weight	412.47	452.34	937.16	1237.49	926.97
Crystal system	Triclinic	Orthorhombic	Triclinic	Monoclinic	Orthorhombic
Space group	$P\bar{1}$	$P2_12_12_1$	$P\bar{1}$	$P2_1/c$	$Pcca$
Z	2	8	1	4	8
a (Å)	8.0558(5)	8.5577(4)	8.5974(6)	13.8897(7)	34.168(5)
b (Å)	10.8367(7)	16.6991(6)	12.1386(9)	35.0779(17)	17.174(3)
c (Å)	14.3114(9)	30.5536(12)	12.5960(9)	15.5291(8)	18.038(3)
α (°)	72.491(3)	90	87.456(5)	90	90
β (°)	85.244(4)	90	81.005(5)	90.361(2)	90
γ (°)	81.614(4)	90	69.286(4)	90	90
V (Å^3)	1177.73(13)	4366.3(3)	1214.34(15)	7566.0(7)	10585(3)
ρ_{calc} g/cm^3	1.163	1.376	1.282	1.086	1.163
μ (mm^{-1})	0.749	0.714	0.735	0.487	0.333
temp (K)	173(2)	173(2)	173(2)	173(2)	173(2)
λ (Å)	0.71073	0.71073	0.71073	0.71073	0.71073
final R indices [I > 2σ(I)][e,f]	R_1 = 0.0389	R_1 = 0.0388	R_1 = 0.0384	R_1 = 0.0431	R_1 = 0.0631
	wR_2 = 0.0963	wR_2 = 0.0708	wR_2 = 0.0794	wR_2 = 0.1050	wR_2 = 0.1402
R indices (all data)[e,f]	R_1 = 0.0533	R_1 = 0.0560	R_1 = 0.0586	R_1 = 0.0740	R_1 = 0.1287
	wR_2 = 0.1018	wR_2 = 0.0769	wR_2 = 0.0858	wR_2 = 0.1141	wR_2 = 0.1592
GOF[g]	1.048	1.035	1.014	1.016	1.002

[a] The asymmetric unit is twice the formula unit; Pentane was SQEEZEd. [b] The asymmetric unit is 1/2 the formula unit. [c] A molecule of Et_2O was SQEEZEd. [d] The asymmetric unit contains one molecule **30-Fe-DIPP** and one molecule of THF. A molecule of THF was SQEEZEd. [e] $R_1 = \Sigma||F_o| - |F_c||/\Sigma|F_o|$. [f] $wR_2 = [\Sigma w(|F_o| - |F_c|)^2/\Sigma wF_o^2]^{1/2}$. [g] GOF (all data) $= [\Sigma w(|F_o| - |F_c|)^2/(n - p)]^{1/2}$, n = number of independent reflections, p = number of parameters.

Table 4.2. Selected interatomic distances and angles for $[(smif)FeN(TMS)_2]_2$, **[14-Fe]$_2$**.

Bond Distances (Å)		Bond Angles (°)	
Fe1 - N1	2.1950(11)	N1 - Fe1 - N2	77.20(4)
Fe1 - N2	1.9432(10)	N1 - Fe1 - N3	154.48(4)
Fe1 - N3	2.1910(11)	N1 - Fe1 - N4	101.94(4)
Fe1 - N4	1.9538(10)	N2 - Fe1 - N3	77.38(4)
C6 - C7	1.5781(18)	N2 - Fe1 - N4	178.53(4)
N2 - C6	1.4334(17)	N3 - Fe1 - N4	103.43(4)
N2 - C7	1.4356(16)	Fe1 - N1 - C1	126.44(9)
		Fe1 - N1 - C5	112.76(8)
		Fe1 - N3 - C8	112.50(9)
		Fe1 - N3 - C12	126.93(9)
		Fe1 - N2 - C6	120.95(8)
		Fe1 - N2 - C7	120.66(8)
		Fe1 - N4 - Si1	118.22(6)
		Fe1 - N4 - Si2	114.75(6)
		C6 - N2 - C7	113.94(10)

Magnetism of $[(smif)FeN(TMS)_2]_2$ [14-Fe]$_2$ and $(dpma)FeN(TMS)_2$ (15-Fe). Temperature dependence studies of the molar susceptibility were conducted after the observation of a paramagnetic ^{1}H NMR spectrum for **14-Fe** (Figure 4.4). SQUID magnetometry data for **[14-Fe]$_2$** revealed a μ_{eff} of 7.34 μ_B at 293 K, consistent with the expected spin-only value of 6.93 μ_B for two high spin (S = 2) Fe(II) centers. The magnetic moment values decrease below 50 K, presumably due to a large amount of zero field splitting (ZFS). In comparison to **[14-Fe]$_2$**, an effective magnetic moment of 4.4 μ_B at 293 K was obtained from SQUID magnetometry data (Figure 4.4) for dimeric **[15-Fe]$_2$** as proposed in Scheme 4.4. This is consistent with an S = 2 GS with significant antiferromagnetic coupling between the metal centers. Similar behavior was observed for another bis-amide complex.

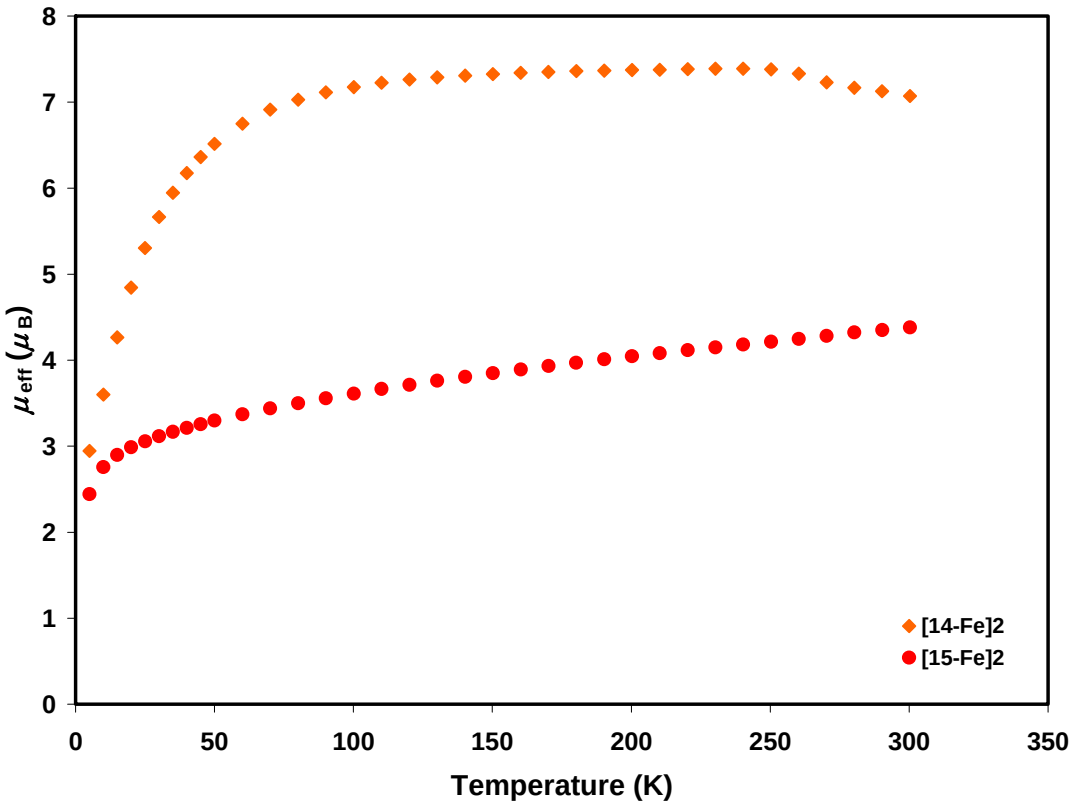

Figure 4.4. SQUID data for $[(smif)FeN(TMS)_2]_2$ **[14-Fe]$_2$** and $[(dpma)FeN(TMS)_2]_2$ **[15-Fe]$_2$**: Magnetic moment (μ_{eff} in μ_B) as a function of T (K).

UV-vis Spectra of (smif)FeN(TMS)$_2$ (14-Fe) and (dpma)FeN(TMS)$_2$ (15-Fe). In solution, **14-Fe** transmits an intense emerald green color, consistent with the strong absorptions observed in the red and blue regions of its UV-vis spectrum in pentane (Figure 4.5). Two main features occur at 399 nm and 633 nm with large extinction coefficients of ~ 37,000 M^{-1} cm^{-1} and ~ 52,000 M^{-1} cm^{-1}, respectively. These absorptions may be attributed to IL transitions between the $CN_{aza}C^{nb}$ orbitals to smif-π^* orbitals as seen in the UV-vis spectra of other smif complexes. Conversely, the UV-vis spectrum of **15-Fe** possesses one feature at 549 nm (ε ~ 1,500 M^{-1} cm^{-1}) in an otherwise mostly featureless spectrum (Figure 4.4).

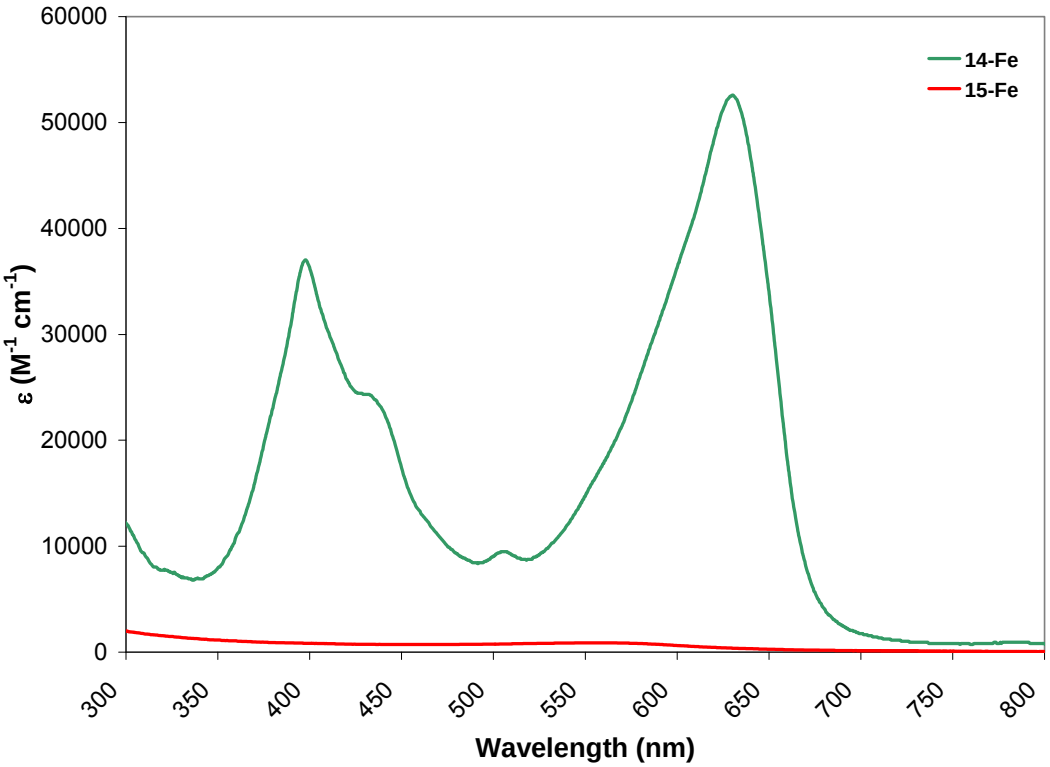

Figure 4.5. UV-vis spectra of (smif)FeN(TMS)$_2$ (**14-Fe**, emerald green) in pentane: 399 nm (ε ~ 37,000 M^{-1} cm^{-1}), 633 nm (ε ~ 52,000 M^{-1} cm^{-1}). UV-Vis spectrum of (dpma)FeN(TMS)$_2$ (**15-Fe**, red) in benzene: 549 nm (ε ~ 1,500 M^{-1} cm^{-1}).

Mössbauer Spectroscopy of [(smif)FeN(TMS)$_2$]$_2$ [14-Fe]$_2$. The Mössbauer spectrum of **[14-Fe]$_2$** is depicted in Figure 4.6, and pertinent parameters are listed in Table 4.3. The isomer shift for **[14-Fe]$_2$** is 0.86 mm/s, consistent with a high spin Fe(II) center. The quadrupole splitting value of 1.07 mm/s suggests asymmetry in the electric field, as expected with square planar geometry. Line widths are 0.46 mm/s.

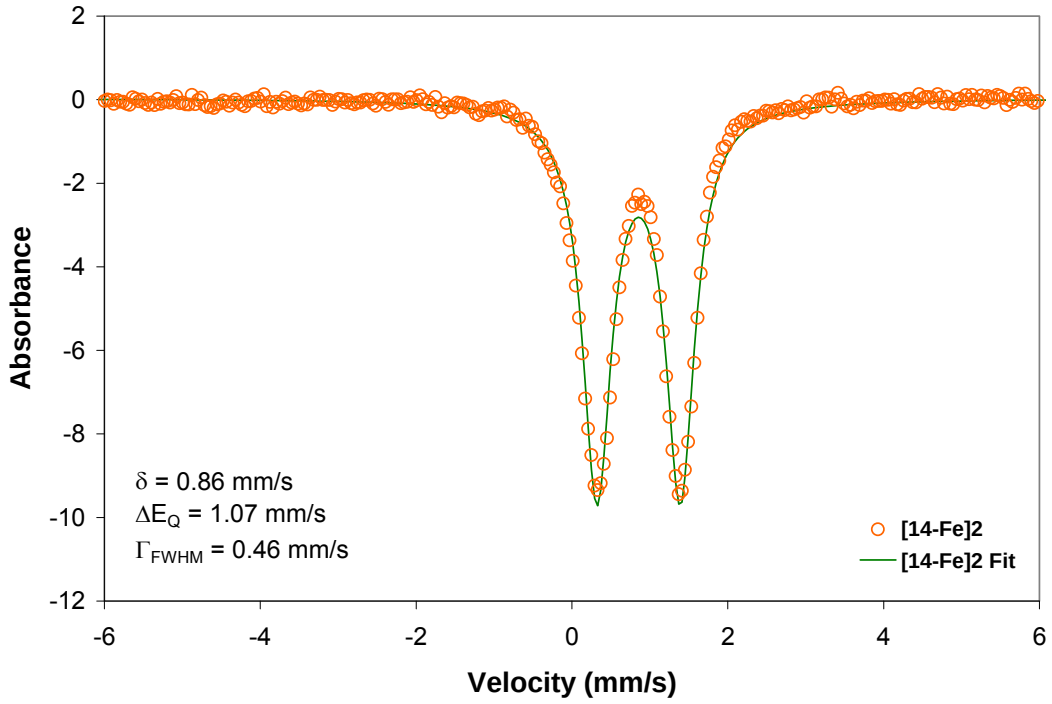

Figure 4.6. Mössbauer spectrum of $[(smif)FeN(TMS)_2]_2$ **[14-Fe]$_2$** at 80 K.

Table 4.3. Mössbauer parameters for $(smif)_2Fe$ (**6-Fe**), $[(smif)FeN(TMS)_2]_2$ (**[14-Fe]$_2$**), $(dpma)_2Fe$ (**16-Fe**), $(^oMesmif)_2Fe$ (**22-Fe**), and $(^oMe_2smif)_2Fe$ (**23-Fe**).

Compound	Temperature	δ (mm/s)	ΔE_Q (mm/s)	Γ_{FWHM} (mm/s)
6-Fe	80K	0.30(1)	0.62(1)	0.25(1)
[14-Fe]$_2$	80K	0.86	1.07	0.46
16-Fe	80K	0.94	0.86	0.39
22-Fe	80K 200K	0.38 0.34	0.99 1.00	0.31 0.28
23-Fe	15K[a] 15K[b] 80K[c] 80K[d]	1.05 1.01 1.04 1.02	2.24 0.77 2.18 0.65	0.36 0.49 0.39 0.50

[a] **23-Fe** (81 %). [b] Impurity (19 %). [c] **23-Fe** (82 %). [d] Impurity (18 %).

Characterization of $(dpma)_2Fe$ (16-Fe): X-ray Structure of 16-Fe. Single crystal, x-ray diffraction quality, dark blue-metallic purple plates of **16-Fe** were obtained from a 1:1 mixture of pentane and benzene. Select crystallographic and refinement data for **16-Fe** are listed in Table 4.1, and pertinent bond distances and angles are listed in Table 4.4. As shown in Figure 4.7, the solid state structure of **16-Fe** displays two tridentate ligands occupying an octahedral geometry about iron, thereby giving rise to the D_{2d} symmetry, which was also observed in the crystal structure of **6-Fe**. The asymmetric unit of **16-Fe** contains two molecules. **16-Fe** exhibits a slight C_s distortion from D_{2d} symmetry as the amide nitrogens span an angle of 175.9(16) °, and the corresponding angle in **6-Fe** is 179.11(6) °. The dipyridyl amide chelate possesses $N_{py}FeN_{py}$ angles averaging 150.9(16) ° resulting in acute bite angles, i.e. $\angle N_{am}FeN_{py}$ = 75.5(4) °, whereas the azaallyl chelate in **6-Fe** has $N_{py}FeN_{py}$ angles averaging 164.53(11) ° with concomitantly larger bite angles (82.30(24) °, ave). In comparison to **6-Fe**, the elongation of the iron-nitrogen bond lengths in **16-Fe** is consistent with a decrease in the ligand field stabilization energy relative to **6-Fe**; this suggests that dpma is a weaker field ligand than smif, and the σ* orbitals are populated in **16-Fe**. The iron-amide nitrogen distance in **16-Fe** of 2.001(13) Å (ave) is 0.10 Å larger than the average iron-azaallyl nitrogen distance of 1.9012(14) Å in **6-Fe**. A smaller difference was observed in the iron-pyridine nitrogen bond lengths, which increased from 1.9634(12) Å in **6-Fe** to 2.201(13) Å in **16-Fe**. The N_{am}-C bond lengths averaging 1.418(2) Å are consistent with an sp^2(N)-sp^3(C) assignment and are clearly different than the delocalized anion present in **6-Fe**, which possesses N_{aza}-C distances of ~ 1.33 Å.

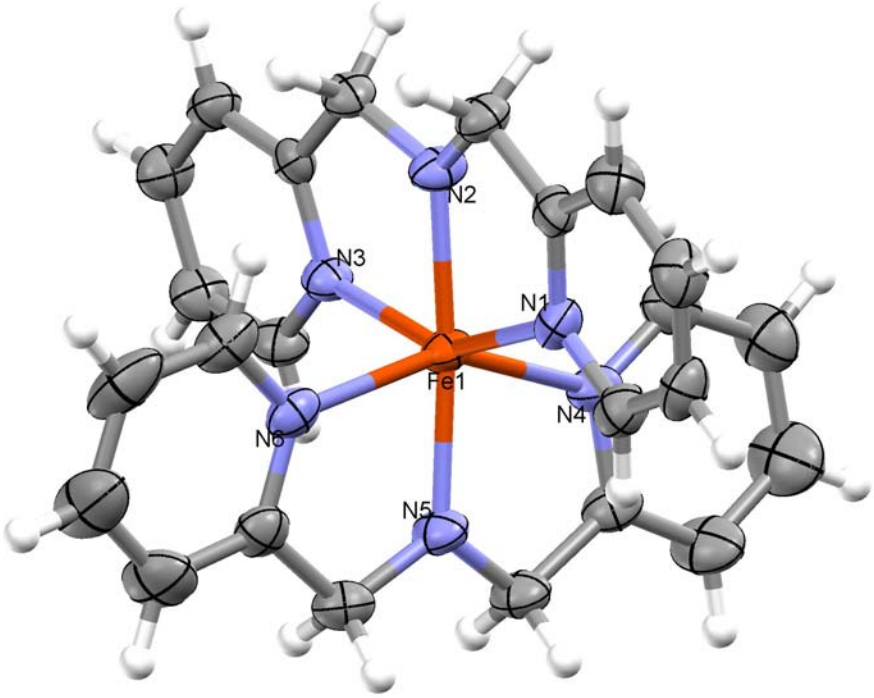

Figure 4.7. Molecular structure of $(dpma)_2Fe$ (**16-Fe**). Thermal ellipsoids are at 50 % probability level.

Table 4.4. Selected interatomic distances and angles for $(dpma)_2Fe$ (**16-Fe**).

Bond Distances (Å)		Bond Angles (°)	
Fe - N_{am}	2.001(13) ave	N_{am} - Fe - $N_{am'}$	175.9(16)
Fe - N_{py}	2.201(13) ave	N_{py} - Fe - N_{py}	150.9(16) ave
N_{am} - C	1.418(2) ave	N_{am} - Fe - N_{py}	75.5(4) ave
		N_{am} - Fe - $N_{py'}$	99.8(2) - 109.5(2)
		N_{py} - Fe - $N_{py'}$	86.90(7) - 101.00(7)

Magnetism of $(dpma)_2Fe$ (16-Fe). Initial studies on the magnetism of **16**-Fe were performed in solutions of C_6D_6, and effective magnetic moments were calculated using Evans' method.[29] Solution studies revealed a μ_{eff} of 5.0 μ_B at 293 K, consistent

with an S = 2 GS for a high spin Fe(II) center. Temperature dependence of the molar susceptibility was also investigated (Figure 4.8). SQUID magnetometry data confirmed an S = 2 GS for **16-Fe** with a value of 5.2 μ_B at 293 K, slightly higher than the solution value. Both μ_{eff} values are higher than the spin-only value of 4.90 μ_B expected for an S = 2 GS, which may be a result of spin-orbit coupling in addition to orbital angular momentum. A modest decrease in the magnetic moments occurs below 50 K and may be attributed to ZFS.

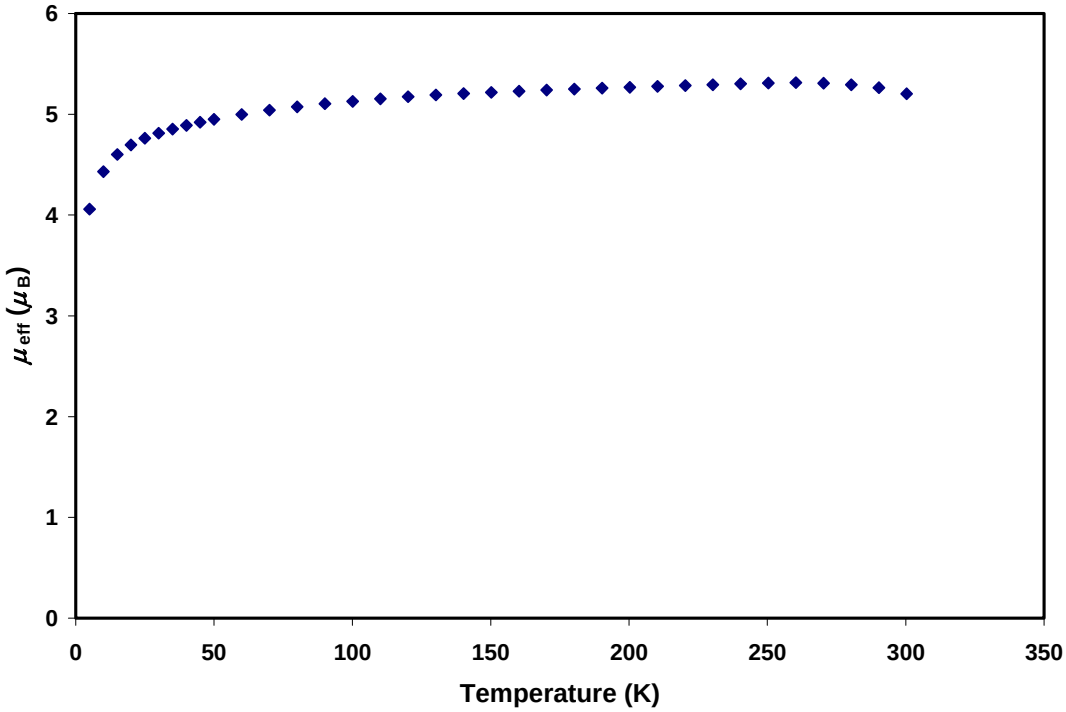

Figure 4.8. SQUID data for $(dpma)_2Fe$ (**16-Fe**): Magnetic moment (μ_{eff} in μ_B) as a function of T (K).

UV-vis Spectrum of $(dpma)_2Fe$ (16-Fe). Dark blue-metallic purple crystals of **16-Fe** generate a dark blue solution in pentane. In comparison to the UV-vis spectrum of **6-Fe** that possesses an extinction coefficient of 42,000 M^{-1} cm^{-1} for the strongest absorption, the UV-vis spectrum of **16-Fe**, shown in Figure 4.9, appears rather featureless. Only two distinguishable features occur at 360 nm and 708 nm with

relatively small extinction coefficents of ~ 5,000 M^{-1} cm^{-1} and ~ 3,700 M^{-1} cm^{-1}, respectively.

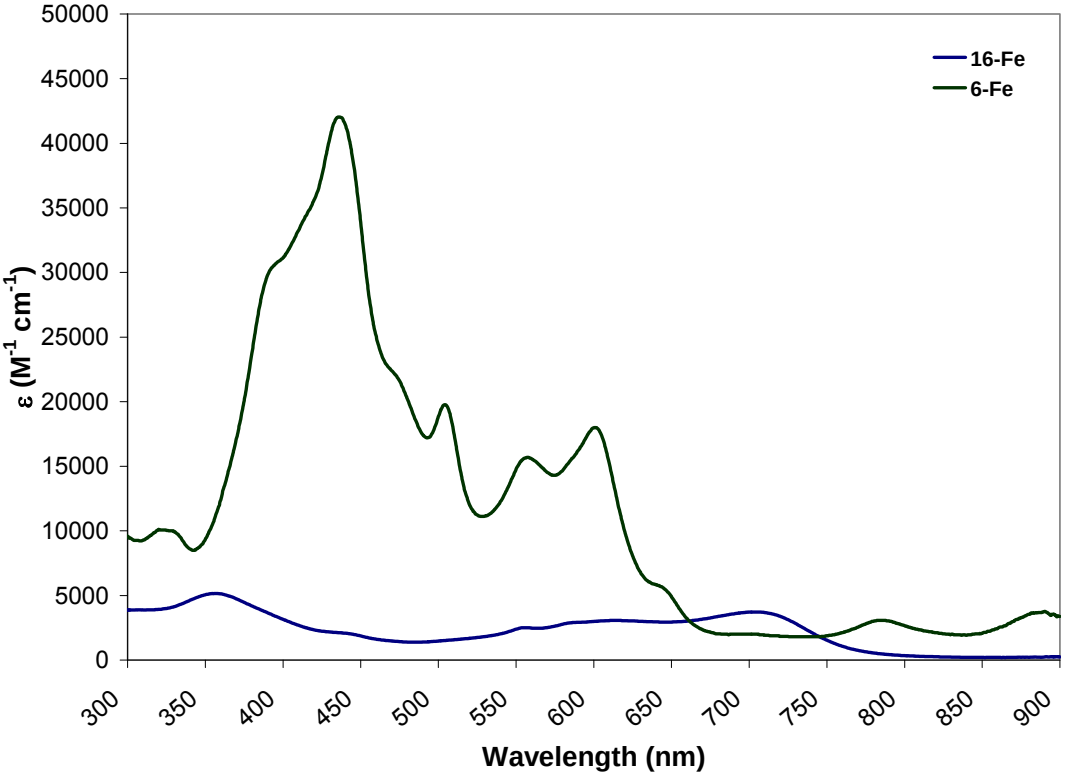

Figure 4.9. Overlay of UV-vis spectra for $(smif)_2Fe$ (**6-Fe**) and $(dpma)_2Fe$ (**16-Fe**). UV-vis spectrum of $(dpma)_2Fe$ (**16-Fe**, blue) in pentane: 360 nm (ε ~ 5,000 M^{-1} cm^{-1}), 708 nm (ε ~ 3,700 M^{-1} cm^{-1}).

Mössbauer Spectroscopy of $(dpma)_2Fe$ (16-Fe). Pertinent Mössbauer parameters for **16-Fe** are listed in Table 4.3. The spectrum of **16-Fe**, shown in Figure 4.10, reveals an isomer shift of 0.94 mm/s, indicative of a high spin Fe(II) center. A fairly symmetric electric field surrounds the iron as the ΔE_Q value is 0.86 mm/s. Line widths are 0.39 mm/s. These Mössbauer parameters are significantly different than those observed for **6-Fe**, the low spin Fe(II) complex, and are comparable to those observed for the other high spin Fe(II) complexes in our study.

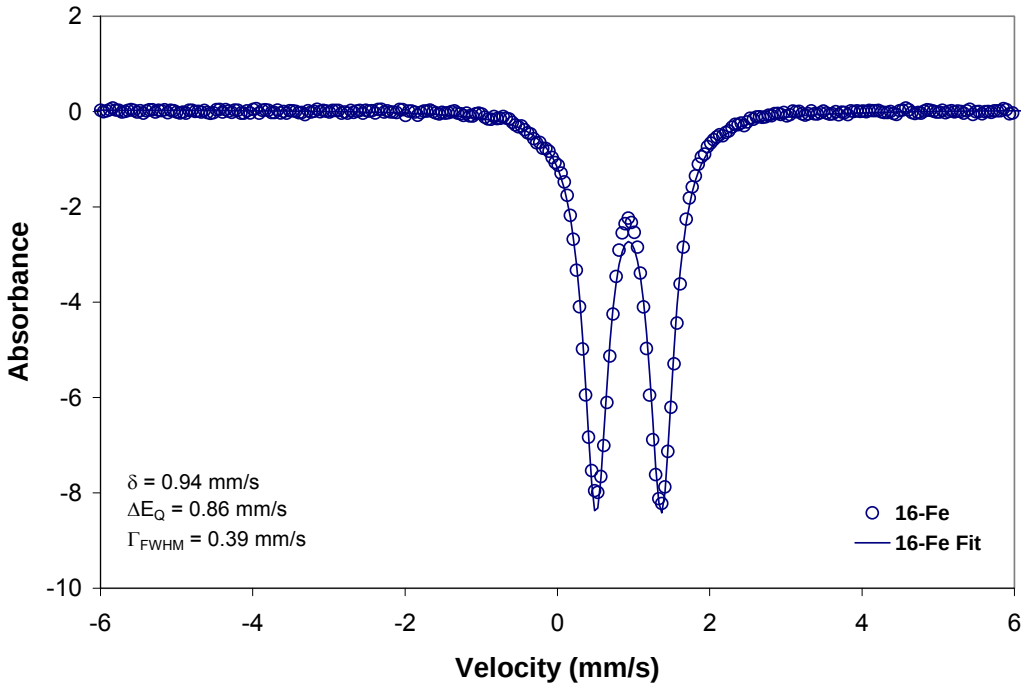

Figure 4.10. Mössbauer spectrum of $(dpma)_2Fe$ (**16-Fe**) at 80 K.

Hydrogenation Chemistry by $(dpma)_2Fe$ (16-Fe). With $(smif)_2Fe$ (**6-Fe**) and $(dpma)_2Fe$ (**16-Fe**) in hand, research efforts focused on finding a potential catalytic cycle between the two complexes as they differ by 4 H^+ and 4 e^-, which is ideal for proton coupled electron transfer processes. Unfortunately, all attempts to hydrogenate **6-Fe** to **16-Fe** via the addition of excess H_2, H_2 with Pd/C, 1,2-diphenylhydrazine, 1,3- and 1,4-cyclohexadiene were unsuccessful. Efforts to promote hydrogenation via photolysis in the presence of the cyclohexadienes also failed, suggesting stability of **6-Fe**. Density functional theory[30-34] calculations showed that the reverse process, i.e. the dehydrogenation of **16-Fe**, is favored by 12.5 kcal/mol (Figure 4.11).

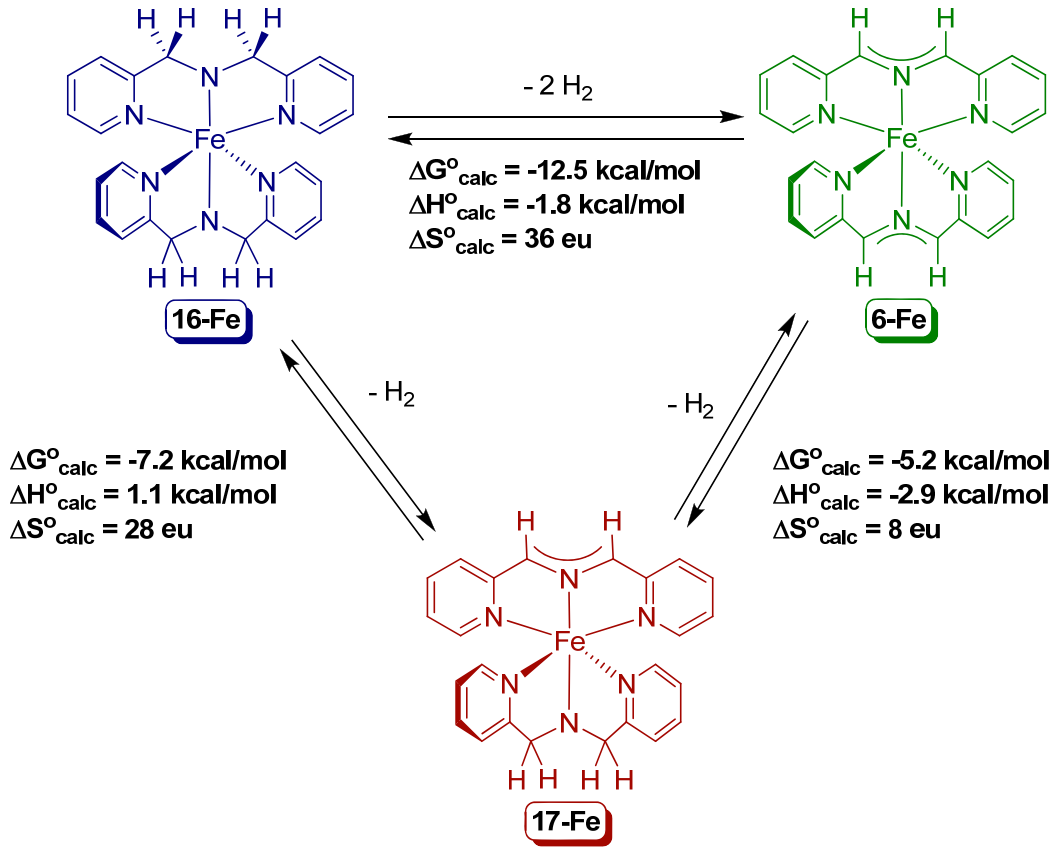

Figure 4.11. Calculated thermodynamic parameters for the conversions between $(dpma)_2Fe$ (**16-Fe**), (smif)(dpma)Fe (**17-Fe**), and $(smif)_2Fe$ (**6-Fe**).

Research efforts shifted toward investigating the dehydrogenation potential of **16-Fe** with a variety of unsaturated organic complexes, and the results of these sealed tube experiments are summarized in Scheme 4.5. ^{1}H NMR spectroscopy revealed the formation of **6-Fe** and **Hdpma** upon exposing **16-Fe** to benzophenone in addition to a series of new paramagnetically shifted peaks, whose identities were elucidated upon investigating potential side reactions. Several plausible paramagnetic species may exist: the partially dehydrogenated **16-Fe**, i.e. (smif)(dpma)Fe (**17-Fe**), as well as $(dpma)FeOCHPh_2$ (**18-Fe**) or $(smif)FeOCHPh_2$ (**19-Fe**) resulting from the reactivity of the hydrogenated benzophenone, i.e. diphenylmethanol, with **16-Fe** or **17-Fe**

displacing **Hdpma**. All potential side products were independently synthesized. The isolation of a pure sample of **17-Fe**, a dark red, paramagnetic solid, was complicated by contamination with **6-Fe** in varying ratios (Scheme 4.6). Exposure of **14-Fe** in Et_2O with an equivalent of **Hdpma** yielded **17-Fe** in a 16:1 ratio with **6-Fe**, whereas treating **15-Fe** with an equivalent of **smifH** afforded a 2:1 mixture of **17-Fe** and **6-Fe**, respectively. ^{1}H NMR spectroscopy revealed the presence of **17-Fe** during slower hydrogenation reactions. The presence of (dpma)FeOCHPh$_2$ (**18-Fe**), a plum colored solid, and absence of (smif)FeOCHPh$_2$ (**19-Fe**), a dark green compound, was also confirmed via their independent syntheses by treating the respective starting N(TMS)$_2$ complexes (**15-Fe** and **14-Fe**) with diphenylmethanol in ethereal solvents (Scheme 4.7). The remaining paramagnetic peaks may be attributable to the presence of an "Fe(OCHPh$_2$)$_2$" species.

Hydrogenation of unsaturated nitrogen containing organic molecules was also explored. ^{1}H NMR spectroscopy revealed the formation of dibenzylamine and **6-Fe** after heating a solution of **16-Fe** with benzylidene-1-phenylmethanamine (PhCH=NCH$_2$Ph) at 50 °C for 16 h. A significant amount of **Hdpma** was also present, presumably due to substitution of dibenzylamine to form an iron dibenzylamide. Treatment of **16-Fe** with 1,2-diphenyldiazene (PhN=NPh) instantly yielded a deep forest green solution, indicative of **6-Fe**, upon mixing. The reaction had finished producing **6-Fe** and 1,2-diphenylhydrazine before a ^{1}H NMR spectrum could be obtained. In addition to the expected products, a new smif containing complex was present in ~ 25-33 % relative to the observed **6-Fe** and was not characterized. Another immediate hydrogenation occurs to form N^1,N^4-dimesitylbenzene-1,4-diamine[35] from the corresponding quinone imine[36] derivative when exposed to **16-Fe**. The ^{1}H NMR spectrum showed only the presence of the diamine and **6-Fe**.

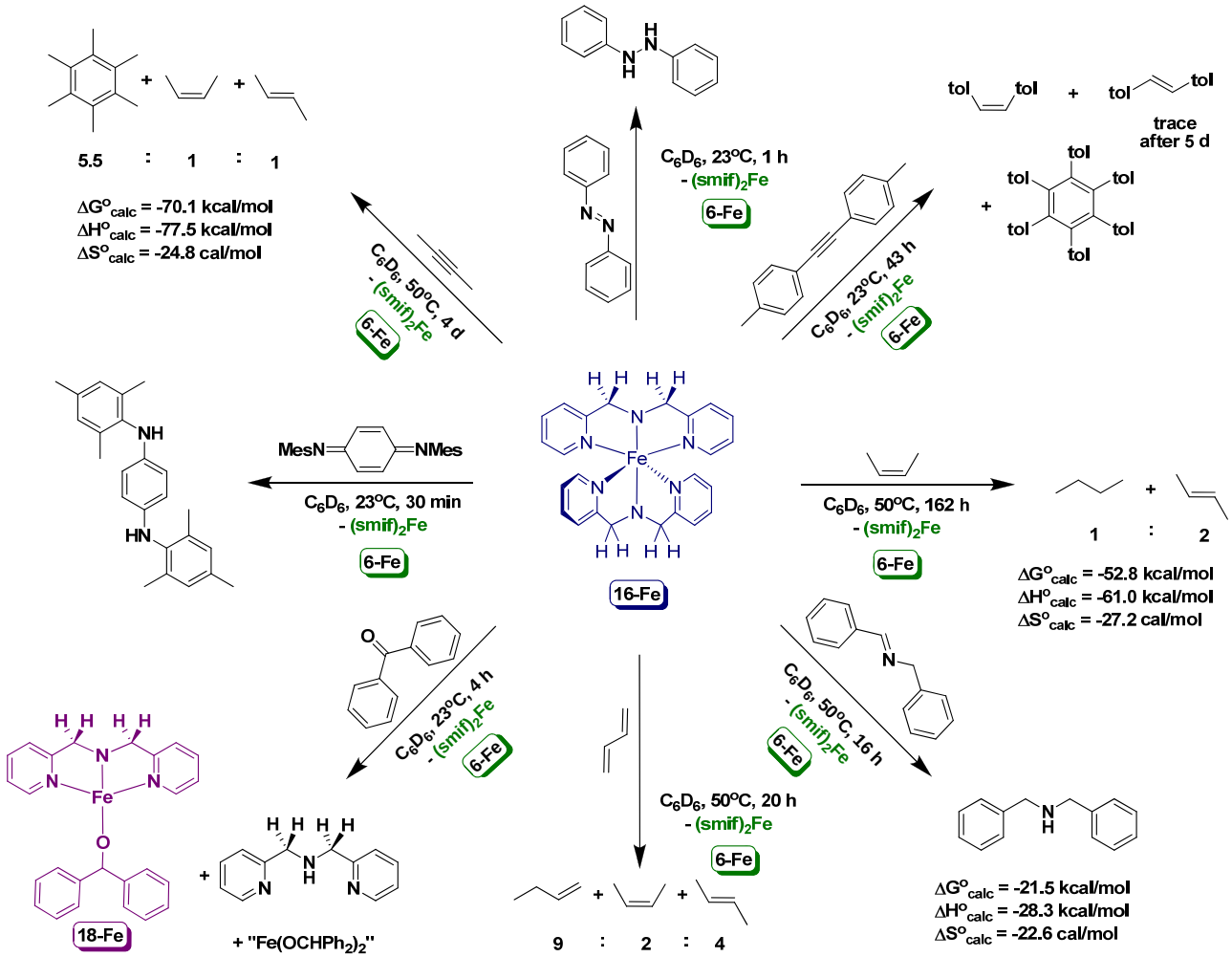

Scheme 4.5. Hydrogenation of unsaturated organic compounds via the dehydrogenation of $(dpma)_2Fe$ (**16-Fe**) to produce $(smif)_2Fe$ (**6-Fe**).

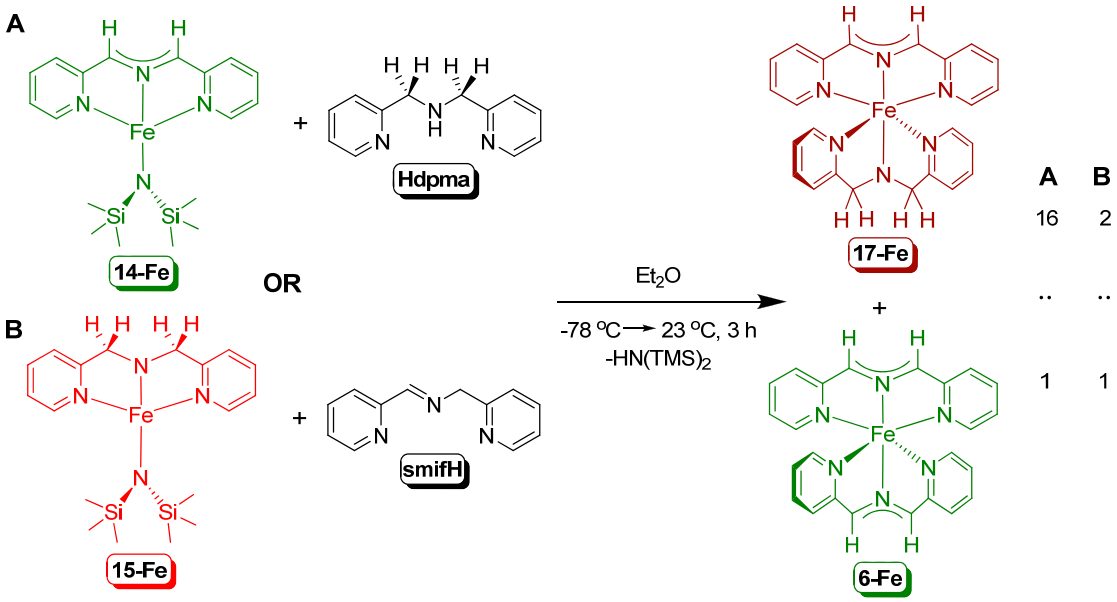

Scheme 4.6. Synthesis of (smif)(dpma)Fe (**17-Fe**).

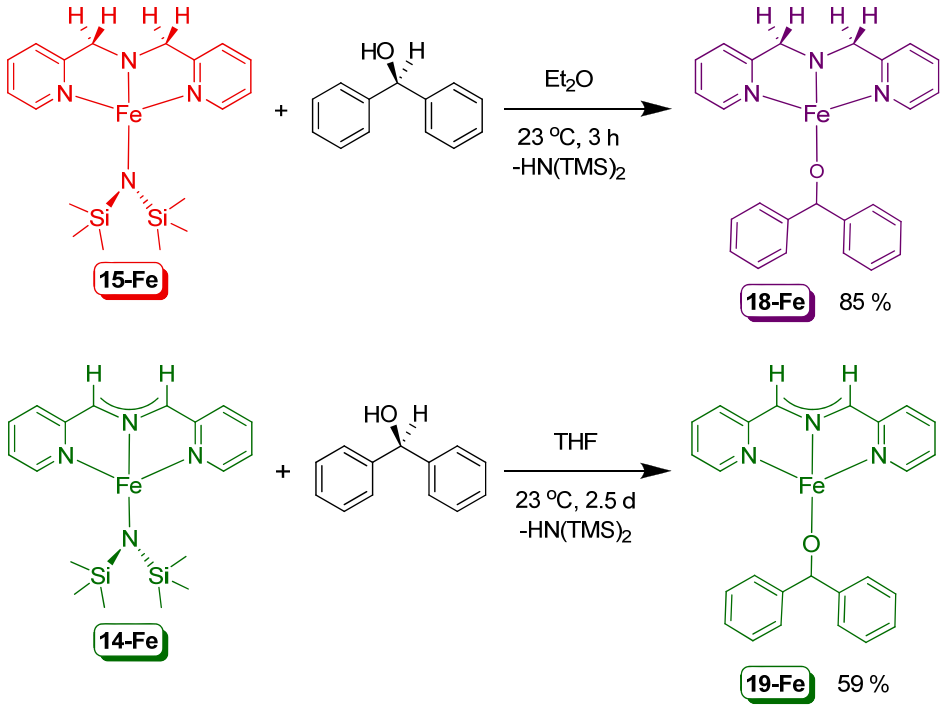

Scheme 4.7. Syntheis of (dpma)FeOCHPh$_2$ (**18-Fe**) and (smif)FeOCHPh$_2$ (**19-Fe**).

Slower hydrogenations were observed for carbon-based unsaturated organic substrates. Exposing **16-Fe** to *cis*-butene yielded a 1:2 mixture of *n*-butane and *trans*-2-butene after heating the solution for 162 h at 50 °C. Efforts toward probing a 1,2 versus a 1,4 hydrogenation reaction focused on using 1,3-butadiene. After 20 h at 50 °C, the predominant product was 1-butene; however, both *cis*- and *trans*-2-butene were also seen in the ^{1}H NMR spectrum. **16-Fe** also hydrogenates alkynes. Treatment of **16-Fe** with di-(*p*-tolyl)acetylene yielded a mixture of *cis*-di-(*p*-tolyl)ethylene[37] and hexa-(*p*-tolyl)benzene after 43 h at 23 °C. After 5 d , trace amounts of *trans*-di-(*p*-tolyl)ethylene[37] were observed. Heating a solution of **16-Fe** with 2-butyne, a substantially smaller alkyne, at 50 °C for 4 d yielded hexamethylbenzene in a 5.5 : 1 : 1 mixture with *cis*- and *trans*-2-butene. It is interesting to note that these iron complexes cyclotrimerize alkynes.

Several possible mechanisms for the hydrogenation of unsaturated organic substrates from **16-Fe** can be envisioned. Three proposed mechanisms for the hydrogenation of alkynes to alkenes are shown in Scheme 4.8. One mechanism suggests a concerted ligand-mediated transfer hydrogenation from **16-Fe** to an alkyne, which would result in the formation of a *cis*-alkene. A radical process can also be envisioned such that the treatment of **16-Fe** with an alkyne results in the formation of a vinyl radical and a dpma ligand based radical. Both radicals may subsequently react to yield **17-Fe** and the olefins, which will likely be a mixture of *cis*- and *trans*-alkenes. The last proposed mechanism invokes iron hydrides. **16-Fe** may undergo β-H elimination and bind an alkyne to form a (smifH)(dpma)Fe(H)(alkyne) complex, which may insert to form the (smifH)(dpma)Fe(vinyl) complex. The iron-vinyl may either undergo β-H abstraction to yield **17-Fe** and the alkene or β-H elimination to generate another iron hydride corresponding to the $(smifH)_2Fe(H)(vinyl)$ complex shown. Reductive elimination from the $(smifH)_2Fe(H)(vinyl)$ complex would produce

the desired alkene in addition to $(smifH)_2Fe$, which may undergo β-H elimination and insertion processes to convert it to **17-Fe**. If the resulting *cis*-olefin bound in place of an alkyne after the formation of the first iron hydride, isomerization from *cis* to *trans* may be observed.

Deuteration studies were performed in an attempt to understand the mechanism, and the results of tube reactions are listed in Table 4.5. The fully deuterated iron complex, $(d_4\text{-dpma})_2Fe$ (**16-Fe-d$_4$)**, was prepared by treating $Fe\{N(TMS)_2\}_2(THF)$ with two equivalents of **D-d$_4$dpma** and was isolated as dark blue-metallic purple crystals in 66 %. With the idea of ruling out radical mechanisms, **16-Fe-d$_4$** was treated with a variety of asymmetric alkynes in hopes of observing only *cis*-alkenes. Unfortunately, all alkynes led to the formation of other unidentified diamagnetic and paramagnetic complexes.

The best hydrogenation substrates, i.e. the quinone imine derivative and 1,2-diphenyldiazene, were subsequently tested. Treatment of **16-Fe-d$_4$** with the quinone imine derivative yielded the corresponding N^1,N^4-dimesitylbenzene-1,4-diamine with varying amounts of H incorporation on the amine hydrogen (25 - 32 %), whereas only 1-6 % H incorporation was observed in the backbone of **6-Fe**, suggesting an alternative proton source was present. 16 % H incorporation in the diamine was seen even after silylating the glassware. Exposing **16-Fe-d$_4$** to 1,2-diphenyldiazene produced **6-Fe-d$_2$**, the uncharacterized smif complex, and the deuterated 1,2-diphenylhydrazine with no H incorporation. This reaction seemed ideal for a potential k_H/k_D study. Unfortunately, complications arose when using mixtures of **16-Fe** and **16-Fe-d$_4$** to probe HH, HD, and DD incorporation. A definitive mechanism and a k_H/k_D were not elucidated for the observed hydrogenation from **16-Fe** from the deuteration studies.

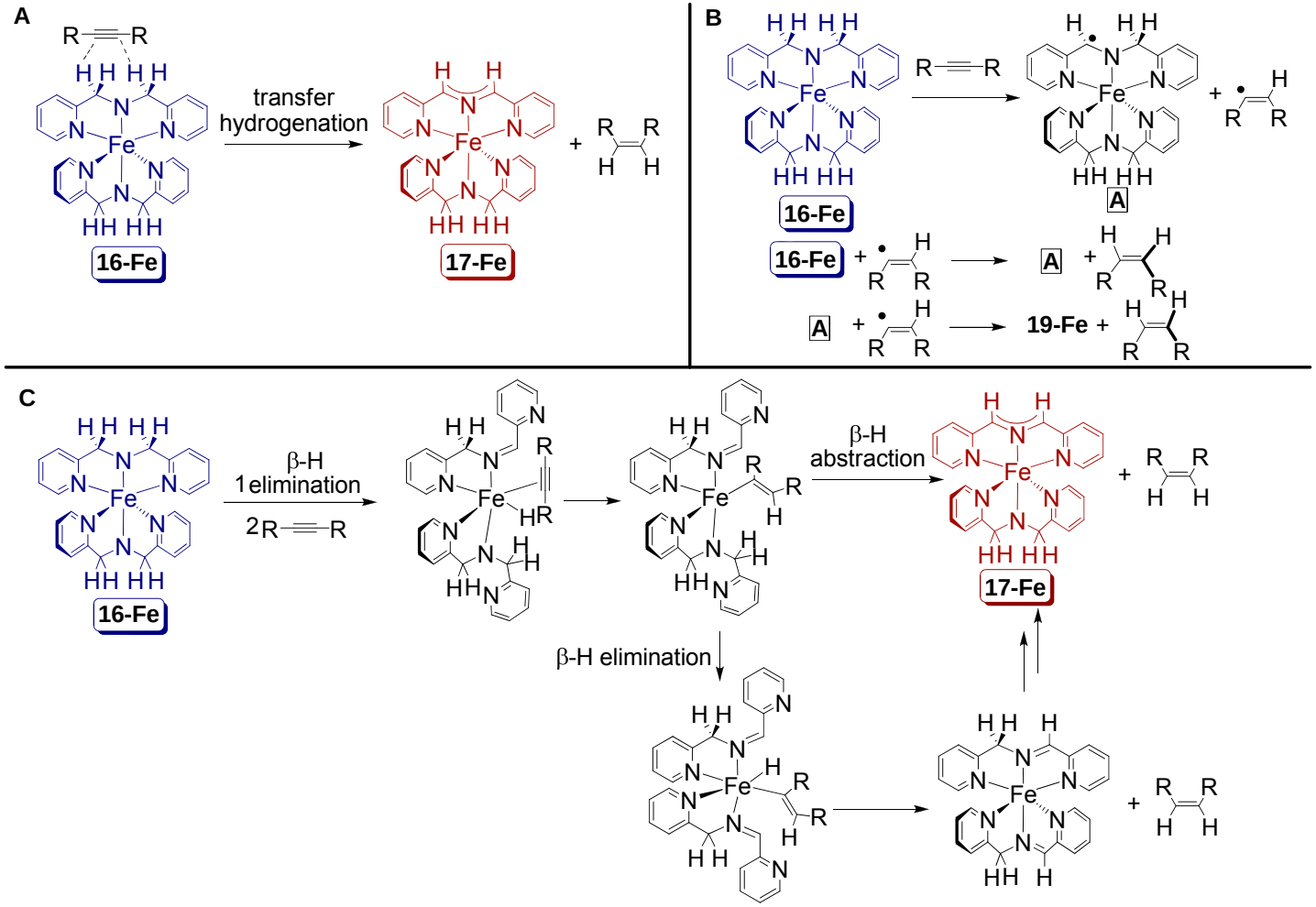

Scheme 4.8. Proposed hydrogenation mechanisms.

Table 4.5. Hydrogenation & deuteration study attempts to probe the mechanism of hydrogenation.

Substrate	**16-Fe-H4**	**16-Fe-d4**	T (°C)	t	**17-Fe**	Leftover **16-Fe**	**Hdpma**	**6-Fe**	[sub]	[sub] $(H/D)_2$	etc.
p-CF_3PhC=NBn	X		23	1.5 h	0	0	19	1	8.5	0	black solid
		X - SI	23	1.5 h	0	0	79	1	14	0	black solid
p-^{t}BuPhC=NBn	X		50	27 h	0	0	1	?	1	0.5	
		X - SI	50	49 h	0	0	1	1	14	92 % D	
PhC=NBn	X		50	37 h	0	0	1	0.75	1	1	
		X - SI	50	37 h	0	0	1	1.5	0.75	1.5	
Indene	X		23	20 min	0	0	0	0	0	0	$(Ind)_2Fe$?
		X - SI	23	20 min	0	0	0	0	0	0	$(Ind)_2Fe$?
p-^{t}BuPhC≡CPh	X		23	45 h	1	0	4	1	overlapping	overlapping	new para
		X	23	45 h	1	0	3.5	0.25	overlapping	overlapping	new para
		X - SI	23	3.5 h	0.14	1	0.68	0	3	0	new para
p-CF_3PhC≡CPh	X		23	14 h	0	0	1	0.25	overlapping	overlapping	new para
		X - SI	50	37 h	0	0	1	1.5	overlapping	overlapping	new para
PhC≡CMe	X		23	6.5 d	1	0	2.75	2	1	0.33	cyclotri-1,2,4
		X	50	7 h	1	0	4.5	0.75	2	X	cyclotri-1,2,4
		X - SI	23	45.5 h	0.5	0	2.8	0.2	2.8	X	cyclotri-1,2,4
EtC≡CMe	X		23	35 d	1	0	17.75	5	?	7	cyclotri-1,2,4
		X	23	35 d	1	0	9	4.25	?	?	cyclotri-1,2,4
MesN quinone	X		23	30 min	0	0	1	0.75	0	2.4	
derivative		X	23	5 min	0	0	1	1 (1 % H)	0	6.3 (32 % H)	
		X	23	15 min	0	0	1	1.5 (6 % H)	0	3.7 (25 % H)	
		X - SI	23	30 min	0	0	1	1.4 (2 % H)	0	6.2 (16 % H)	
PhN=NPh	X		23	1 h	0	0	1	0.25	0.5	2	
		X	23	0 min	0	0	1	0.25 (6 % H)	0	d_2	
			23	5 min	0	0	1	0.36 (6 % H)	0	d_2	
			23	15 min	0	0	1	0.25 (2 % H)	0	d_2	

X - SI = silylated glassware

Cyclotrimerization of Alkynes via Iron Amides. The ability of **16-Fe** to cyclotrimerize internal alkynes was a curious result. Cyclotrimerization of alkynes is well documented,[38-42] yet the challenge remains to find an appropriate regioselective catalyst. Initial investigations focused on probing the utility of available iron complexes, i.e. $Fe\{N(TMS)_2\}_2(THF)$, **6-Fe**, **14-Fe**, **15-Fe**, and **16-Fe**, as cyclotrimerization catalysts for 2-butyne (eq 4.6).

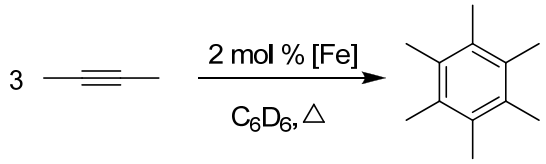

(4.6)

No cyclotrimerization reactivity was observed for **6-Fe**. Treatment of **15-Fe** and **16-Fe** led to the formation of hexamethylbenzene in addition to *cis*- and *trans*-2-butene. In this case, hydrogenation of the alkynes is detrimental since **15-Fe** and **16-Fe** convert to **6-Fe**. Promising results, shown in Table 4.6, arose from the use of catalytic amounts of **14-Fe** or $Fe\{N(TMS)_2\}_2(THF)$ in the presence of 2-butyne. For **14-Fe**, elevated temperatures were required to effect the cyclotrimerization to hexamethylbenzene, and turnover frequencies (TOF) increased from 1.1 h^{-1} to 8.9 h^{-1} upon increasing the concentration of catalyst present in solution from 2 mg/mL to 6 mg/mL, respectively. Unfortunately, catalysis death was observed via ^1H NMR spectroscopy; loss of **14-Fe** was accompanied by presence of $HN(TMS)_2$ and **6-Fe**. No evidence of disproportionation from **14-Fe** to $[Fe\{N(TMS)_2\}_2]_2$ was observed spectroscopically, and cyclotrimerization rates did not increase over time to suggest the presence of the $[Fe\{N(TMS)_2\}_2]_2$. Therefore, it seems likely that **14-Fe** was responsible for the cyclotrimerization catalysis. $Fe\{N(TMS)_2\}_2(THF)$ catalyzed the cyclotrimerization of 2-butyne at 23 °C. Similar to **14-Fe**, better TOFs (10.4 h^{-1}) were observed with higher catalyst concentrations. In an effort to rule out trace impurities in

the $Fe\{N(TMS)_2\}_2(THF)$, control reactions were performed. Both LiHMDS and $FeBr_2(THF)_2$[43] were unsuccessful at cyclotrimerizing internal alkynes, suggesting that $Fe\{N(TMS)_2\}_2(THF)$ was responsible for the catalysis. Clearly, $Fe\{N(TMS)_2\}_2(THF)$, the iron precursor to **14-Fe**, is the better cyclotrimerization catalyst as it works at 23 °C, whereas **14-Fe** does not.

Table 4.6. Catalytic cyclotrimerization results for the conversion of 2-butyne to hexamethylbenzene using $Fe\{N(TMS)_2\}_2(THF)$ or $(smif)FeN(TMS)_2$ (**14-Fe).**

Trial	Catalyst	Cat. Mol %	Cat. Conc.(mg/mL)	Temperature (°C)	TON	TOF (h^{-1})
1	$Fe\{N(TMS)_2\}_2(THF)$	1.6	2	75	60	4.4
2	$Fe\{N(TMS)_2\}_2(THF)$	2	2	90	50	3.7
3	$Fe\{N(TMS)_2\}_2(THF)$	2	4	90	50	10
4	$Fe\{N(TMS)_2\}_2(THF)$	2	6	90	52	10.4
5[a]	**14-Fe**	2	2	75	14	0.31
6[b]	**14-Fe**	2	2	90	12	1.1
7[c]	**14-Fe**	2	4	90	50	7.4
8[d]	**14-Fe**	1.6	6	90	60	8.9
9	$LiN(TMS)_2$	2	6	90	0	0
10	$FeBr_2(THF)_2$	2	6	90	0	0

[a] 20 % **14-Fe** remaining. [b] 23 % **14-Fe** remaining. [c] 29 % **14-Fe** remaining. [d] 24 % **14-Fe** remaining.

Synthesis of $(smif)FeN(TMS)_2$ Analogues with *ortho*-substitution. A variety of $(smif)FeN(TMS)_2$ analogues were prepared using aforementioned **smifH** derivatives with the hope of finding a potential catalyst and preventing the backbone reactivity observed with **14-Fe**. Treatment of $Fe\{N(TMS)_2\}_2(THF)$ in Et_2O with one equivalent of **^{o}MesmifH** produced an emerald-teal green solution, presumably (^{o}Mesmif)$FeN(TMS)_2$ (**20-Fe**)), from which yellow-orange crystals of $[(^o Mesmif)FeN(TMS)_2]_2$ **[20-Fe]$_2$** were isolated in 47 % yield (Scheme 4.9). ^{1}H NMR spectroscopy showed one ^{o}Mesmif environment and a $N(TMS)_2$ group. Based upon

the similar physical properties to **[14-Fe]$_2$**, it seems reasonable that **20-Fe** exists as a dimer in the solid state.

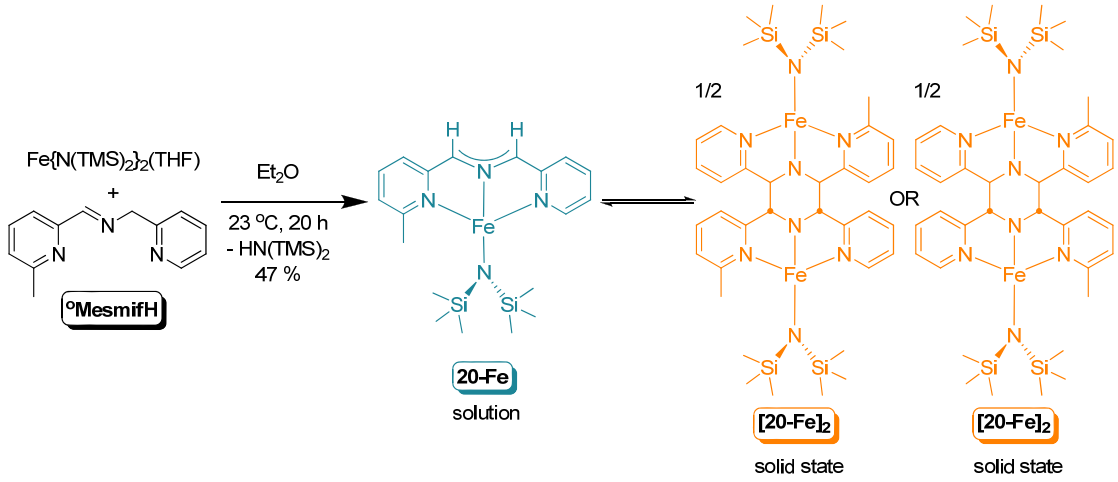

Scheme 4.9. Synthesis of (^{o}Mesmif)FeN(TMS)$_2$ (**20-Fe**).

Exposure of Fe{N(TMS)$_2$}$_2$(THF) in Et$_2$O with one equivalent of **^{o}Me$_2$smifH** afforded metallic gold crystals of (^{o}Me$_2$smif)FeN(TMS)$_2$ (**21-Fe**) in 39 % yield from an intensely colored teal solution (eq 4.7). The presence of one ^{o}Me$_2$smif environment and one N(TMS)$_2$ was revealed in the ^{1}H NMR spectrum of **21-Fe**.

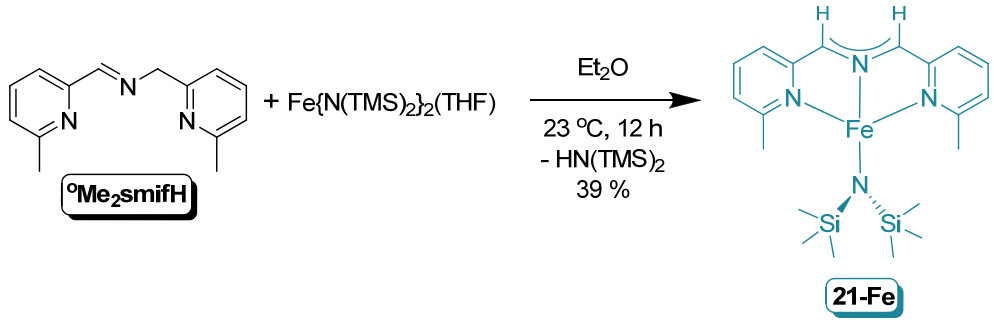

(4.7)

Unsubstituted smif backbones can easily dimerize to form substituted piperazines. These complexes are typically orange in the solid state, whereas several (smif)$_2$M complexes exist as metallic gold crystals. Therefore, it seems plausible that **21-Fe** is a monomer. SQUID magnetometry data revealed a μ_{eff} of 5.1 μ_B at 293 K, consistent

with a high spin Fe(II) center (Figure 4.12). A modest amount of ZFS is observed below 50 K.

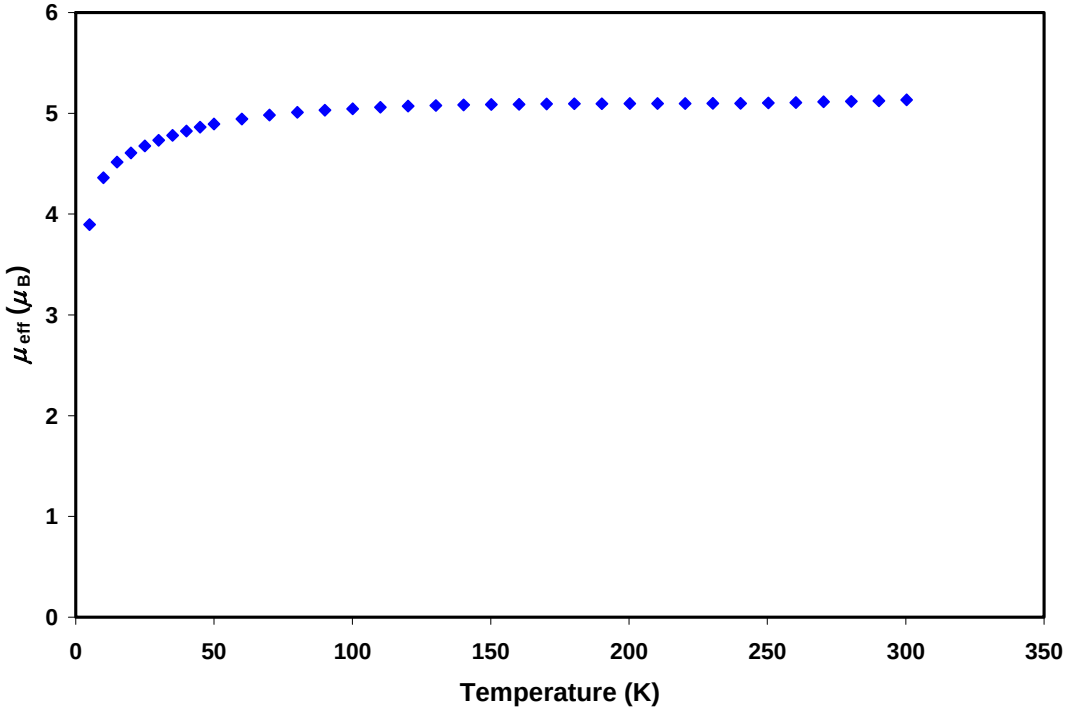

Figure 4.12. SQUID data for (^{o}Me$_2$smif)FeN(TMS)$_2$ (**21-Fe**): Magnetic moment (μ_{eff} in μ_B) as a function of T (K).

Synthesis of (smif)$_2$Fe Derivatives with *ortho*-substitution. In an effort toward prevent the formation of the fairly unreactive (smif)$_2$Fe, **6-Fe**, derivatives, which may be detrimental for catalysis, our research focused on increasing steric bulk on **smifH** in the form of *ortho*-CH_3 groups. Purple-mauve crystals precipitated from an ether solution containing Fe{N(TMS)$_2$}$_2$(THF) and two equivalents of **^{o}MesmifH**. ^{1}H NMR spectroscopy of the crystals revealed the presence of only one ^{o}Mesmif environment and no hexamethyldisilazide [N(TMS)$_2$] group, suggesting the formation of (^{o}Mesmif)$_2$Fe (**22-Fe**) (eq 4.8). The purple-mauve crystals of **22-Fe** were isolated in 59 % yield.

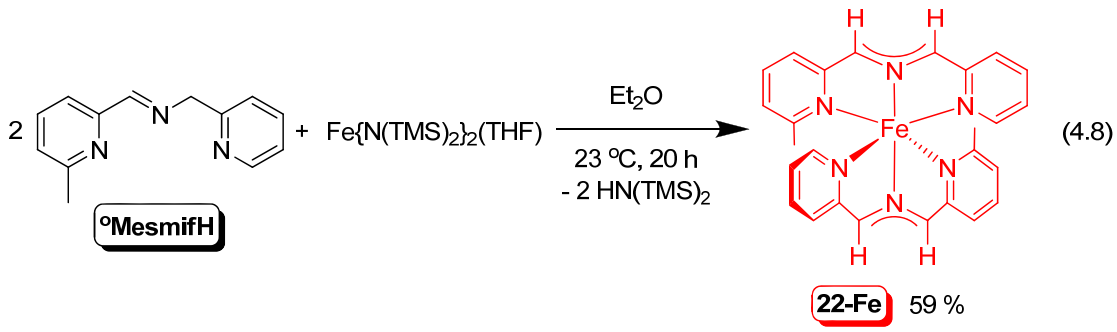

(4.8)

Exposing $Fe\{N(TMS)_2\}_2(THF)$ in Et_2O to two equivalents of **^{o}Me$_2$smifH** afforded metallic gold crystals from an intensely colored blue solution. The ^{1}H NMR spectrum did not contain an $N(TMS)_2$ group, but showed only one paramagnetically shifted $^{o}Me_2$smif environment indicative of $(^{o}Me_2smif)_2Fe$ (**23-Fe**), which was verified by a preliminary x-ray crystal structure (eq 4.9). **23-Fe** was isolated in 85 % yield.

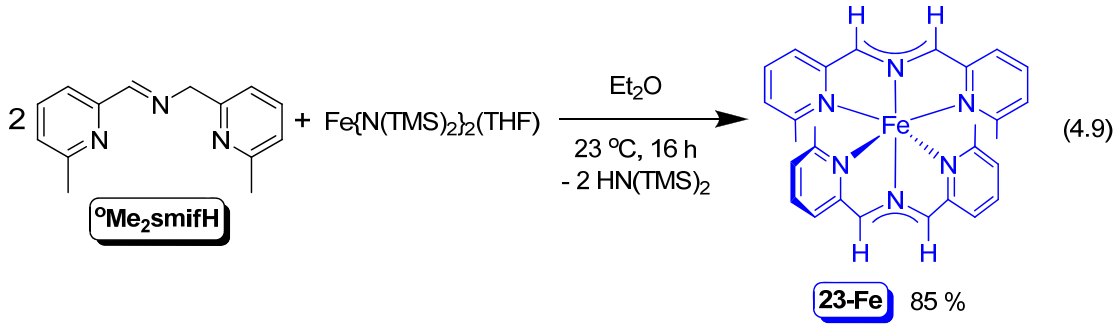

(4.9)

Three other $(smif)_2Fe$ derivatives, i.e. $(^{o}Mesmif)(smif)Fe$ (**24-Fe**), $(^{o}Me_2smif)(smif)Fe$ (**25-Fe**), and $(^{o}Mesmif)(^{o}Me_2smif)Fe$ (**26-Fe**), were prepared by treating the appropriated iron amide with the corresponding imine. All reactions yielded the mixed ligand complex in addition to both parent $(smif)_2Fe$ derivatives in varying ratios, and complexes were identified by ^{1}H NMR spectroscopy. **24-Fe** is a diamagnetic complex, whereas both **25-Fe** and **26-Fe** are paramagnetic. Clearly, the addition of *ortho*-CH_3 groups changes the field strength of smif.

Characterization of (^{o}Mesmif)$_2$Fe (22-Fe) and (^{o}Me$_2$smif)$_2$Fe (23-Fe):

Magnetism. Temperature dependence studies of the molar susceptibility commenced after the observation of paramagnetic complexes in the ^{1}H NMR spectra for **22-Fe** and **23-Fe** (Figure 4.13). The effective magnetic moments, μ_{eff}, were also determined via Gouy balance measurements. ^{1}H NMR spectroscopy revealed three broadened peaks between 11 and 14 ppm for **22-Fe**. SQUID magnetometry data for **22-Fe** revealed an effective magnetic moment of 1.2 μ_B at 293 K and is best interpreted as an S = 0 GS with temperature independent paramagnetism based upon the comparison of Mössbauer parameters for **22-Fe**, **23-Fe**, and **6-Fe**. Gouy balance measurements confirmed the μ_{eff} value of 1.5 μ_B at 296 K for **22-Fe**. Both Gouy balance and SQUID magnetometry data confirmed a high spin Fe(II), S = 2 GS for **23-Fe** with magnetic moments of 5.0 μ_B at 295 K and 5.5 μ_B at 293 K, respectively. Similar to **22-Fe**, magnetic moment values below 50 K significantly decrease and may be attributed to ZFS. The addition of *ortho*-CH_3 groups has changed from a low spin species in **6-Fe** to a high spin system as observed in **23-Fe**.

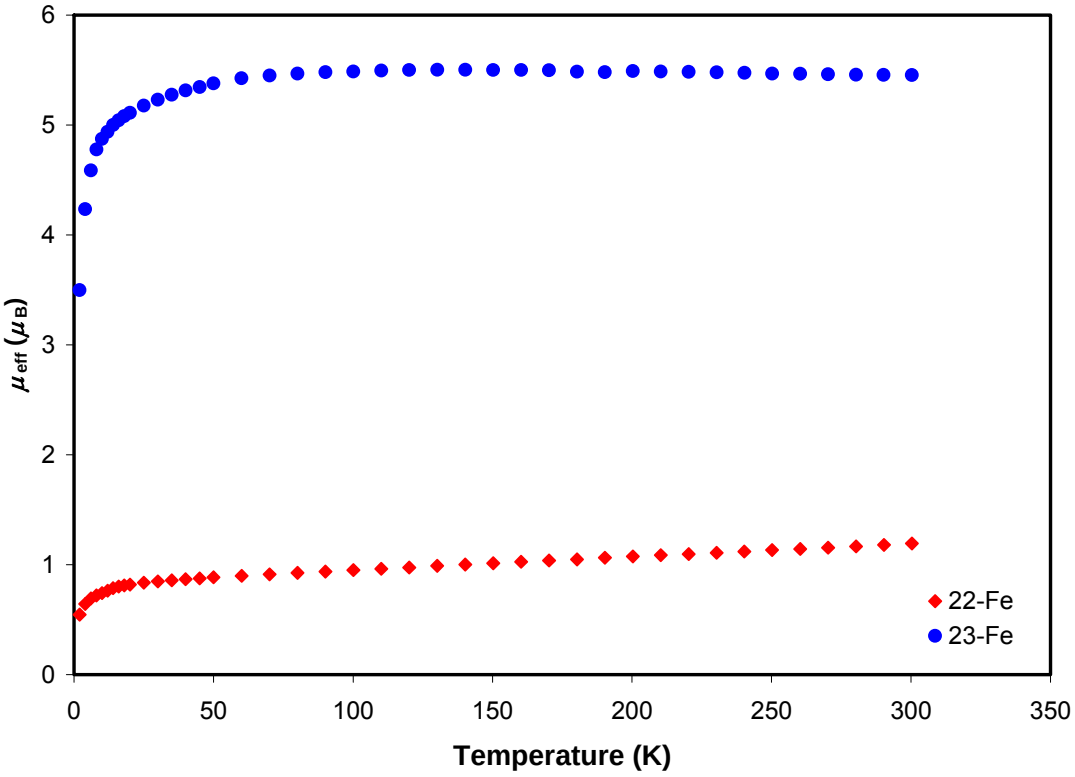

Figure 4.13. SQUID data for (^{o}Mesmif)$_2$Fe (**22-Fe**) and (^{o}Me$_2$smif)$_2$Fe (**23-Fe**) complexes: Magnetic moment (μ_{eff} in μ_B) as a function of T (K).

UV-vis spectroscopy of (^{o}Mesmif)$_2$Fe (22-Fe) and (^{o}Me$_2$smif)$_2$Fe (23-Fe).

Similar to all smif containing complexes, **22-Fe** and **23-Fe** generated colors of unusual intensity in solution. **22-Fe** yields a deep red solution in benzene, and the UV-vis spectrum (Figure 4.14) shows two major features: 425 nm ($\varepsilon \sim 42{,}000$ M^{-1} cm^{-1}) and 533 nm ($\varepsilon \sim 30{,}000$ M^{-1} cm^{-1}). These absorptions may be attributed to intraligand (IL) transitions between azaallyl $CN_{aza}C^{nb}$ orbitals to pyridine π^* orbitals based upon calculations for related smif containing complexes. Additionally, underlying metal-to-ligand charge transfer bands may also be present as the metal 3 d orbitals are energetically close to the azaallyl $CN_{aza}C^{nb}$ orbitals. The transmittance of a deep blue solution of **23-Fe** in benzene is consistent with the strong absorptions in the red and

green regions of the UV-vis spectrum, shown in Figure 4.14. Two major features exist at 399 nm ($\varepsilon \sim 29{,}000\ M^{-1}\ cm^{-1}$) and 598 nm ($\varepsilon \sim 58{,}000\ M^{-1}\ cm^{-1}$) presumably due to IL transitions. It is interesting to note that the addition of *ortho*-CH_3 groups changed not only the spin states of the **6-Fe** derivatives, but it also drastically changes colors and subsequently the wavelengths for the light absorptions in the visible region. With respect to an application in photovoltaic cells, the variations in strong absorptions resulting from the simple addition of a methyl group suggests that mixtures of these complexes may be used to absorb and harvest light from the entire visible region.

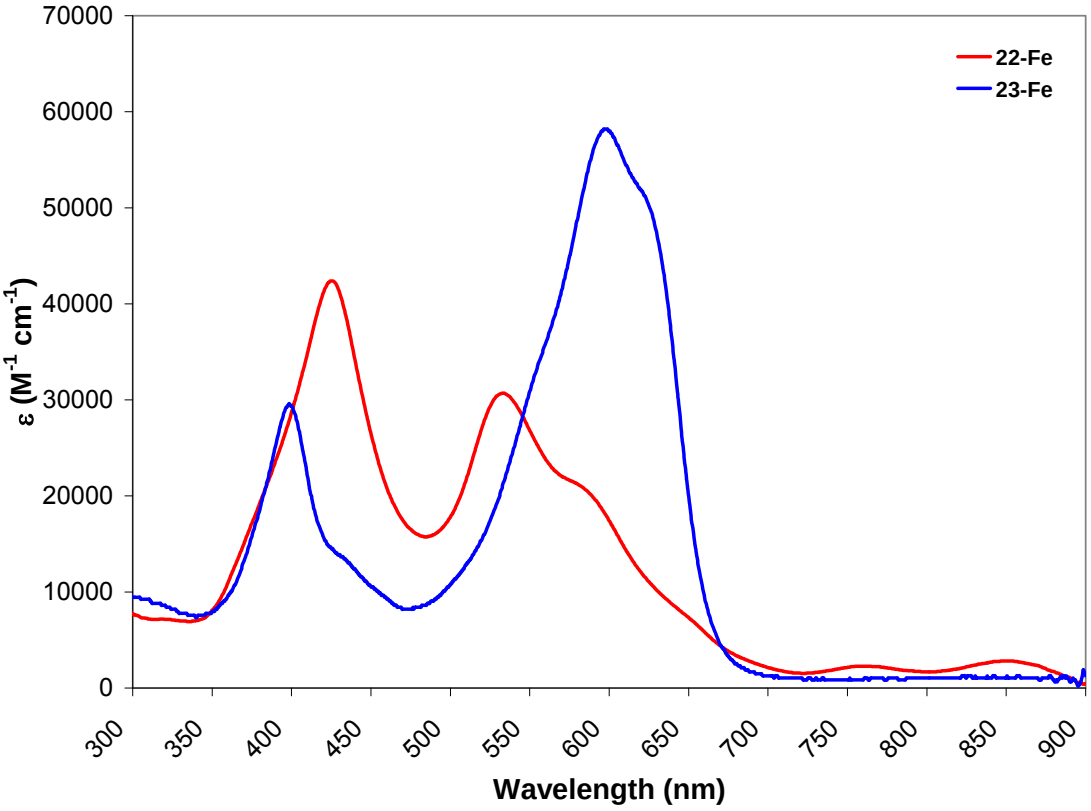

Figure 4.14. UV-vis spectra of (^{o}Mesmif)$_2$Fe (**22-Fe**) and (^{o}Me$_2$smif)$_2$Fe (**23-Fe**) complexes in benzene.

Mössbauer Spectroscopy of (^{o}Mesmif)$_2$Fe (22-Fe) and (^{o}Me$_2$smif)$_2$Fe (23-Fe). Mössbauer spectroscopy permitted another method for investigating the oxidation state, covalency, and overall shape of the iron complexes. Parameters for the complexes can be found in Table 4.3. As previously mentioned, **6-Fe** possesses Mössbauer parameters consistent with a covalent, low spin Fe(II) center at 80 K: δ = 0.30(1) mm/s, ΔE_Q = 0.62(1) mm/s, and Γ_{FWHM} = 0.25(1) mm/s. The addition of one *ortho*-CH_3 group per smif ligand, **22-Fe**, shows similar parameters at 80 K (Figure 4.15), i.e. δ = 0.38 mm/s with a ΔE_Q value of 0.99 mm/s, and Γ_{FWHM} = 0.31 mm/s, suggesting the presence of a covalent, low spin Fe(II) center and an S = 0 GS. Parameters show minimal changes upon warming to 200 K (δ = 0.34 mm/s, ΔE_Q = 1.00 mm/s, and Γ_{FWHM} = 0.28 mm/s). For an NMR spectroscopically pure sample of **23-Fe**, the Mössbauer spectrum at 80 K, shown in Figure 4.15, reveals the presence of two species (82:18). The major species (82 %) is **23-Fe** and has an isomer shift of 1.04 mm/s with a quadrupole splitting of 2.18 mm/s and line widths of 0.39 mm/s. The second species (18 %) is an NMR silent impurity and possesses an isomer shift of 1.02 mm/s with a ΔE_Q of 0.65 mm/s and Γ_{FWHM} of 0.50 mm/s. An independently synthesized sample of **23-Fe** revealed only 5 % of the NMR silent impurity in its Mössbauer spectrum. The quadrupole splitting shows a small temperature dependency as the values increase upon cooling to 15 K. The isomer shift observed for **23-Fe** suggests a less covalent high spin Fe(II) center, and the ΔE_Q value suggests an asymmetry in the electronic field about the iron center.

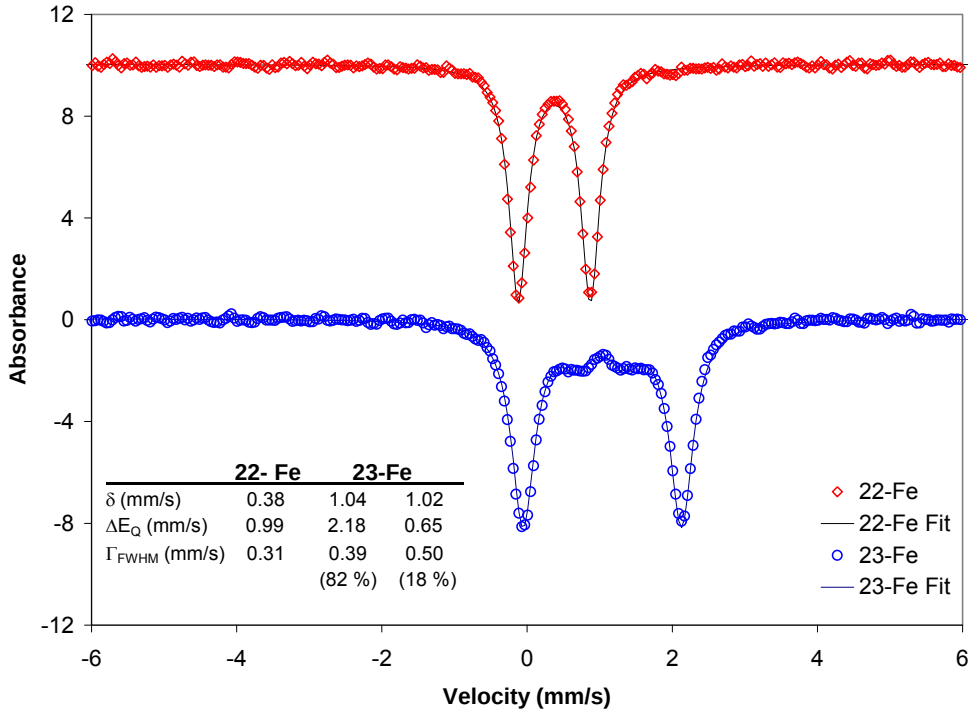

Figure 4.15. Mössbauer spectra of (^{o}Mesmif)$_2$Fe (**22-Fe**) and (^{o}Me$_2$smif)$_2$Fe (**23-Fe**) complexes at 80 K.

Synthesis of (smif)FeN(TMS)$_2$ Analogues with Backbone Methyl Groups. In an attempt to prevent the backbone reactivity, methyl groups were installed on the backbone of **smifH** to yield **^{b}Me$_2$smifH** and **Me$_4$smifH**, as previously described. Treatment of Fe{N(TMS)$_2$}$_2$(THF) in THF with two equivalents of **^{b}Me$_2$smifH** afforded the diamagnetic complex, (^{b}Me$_2$smif)$_2$Fe (**27-Fe**). The mossy green solid of **27-Fe** was obtained in 72 % yield. Small NMR tube scale reactions seemed promising for isolating (^{b}Me$_2$smif)FeN(TMS)$_2$, as only one species was identified by ^{1}H NMR spectroscopy. Unfortunately, challenges arose in scaling up the reaction. All attempts to isolate a pure crystalline product were unsuccessful. ^{1}H NMR spectroscopy of the crystalline solid revealed the presence of more than one complex, which may be attributed to reactivity of the azaallyl backbone.

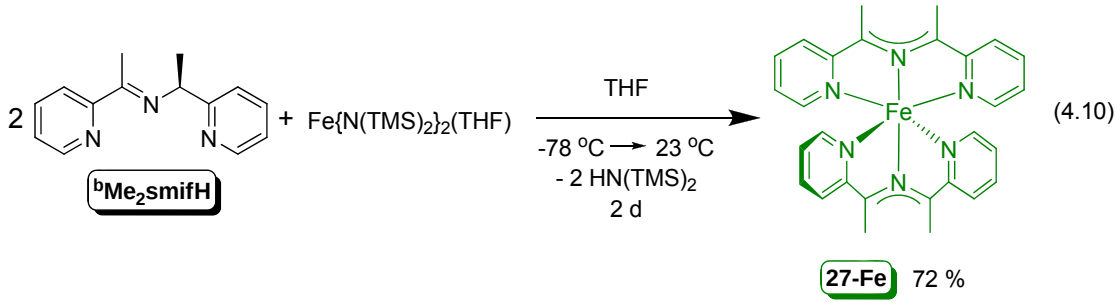

Red-orange crystals of [(μ-C,N^{am},$N^{py}$$_2$-2-(6-methylpyridin-2-yl)-2-(1-(6-methylpyridin-2-yl)ethylamino)ethan-1-ido)Fe{$N(SiMe_3)_2$}]$_2$ ([(Me_4smif)FeN$(TMS)_2$]$_2$, **[28-Fe]$_2$**) precipitated from a bell pepper green solution of (Me_4smif)FeN$(TMS)_2$ (**28-Fe**), which resulted from the addition of **Me_4smifH** to a solution of Fe{$N(TMS)_2$}$_2$(THF) in benzene (eq 4.11). The ^{1}H NMR spectrum possessed paramagnetically shifted peaks consistent with a monomer in solution; however, x-ray crystallographic studies revealed a dimeric structure in the solid state.

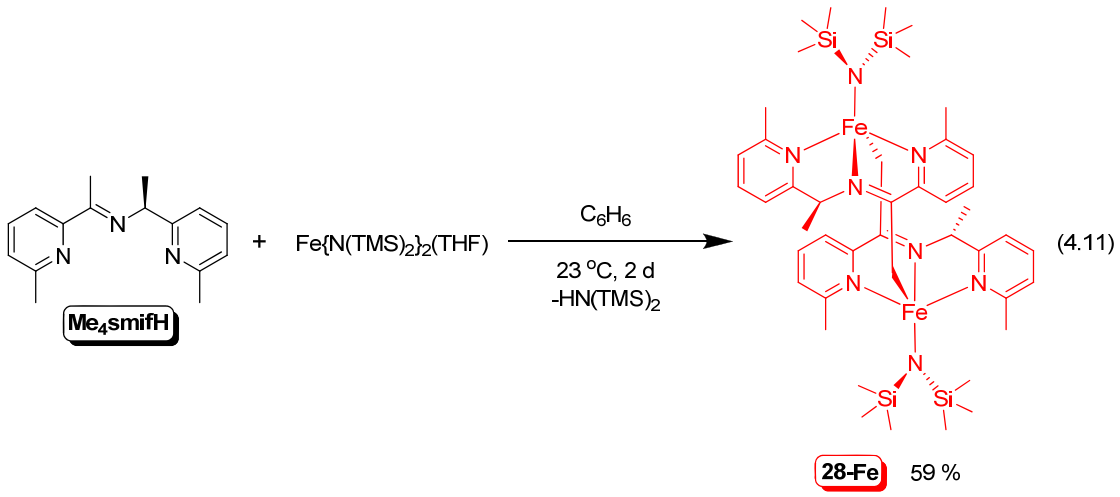

Characterization of [(Me_4smif)FeN$(TMS)_2$]$_2$ (28-Fe): X-ray Crystal Structure. Single crystal, x-ray diffraction quality, red needles of **28-Fe** were obtained from benzene. Select crystallographic and refinement data for **28-Fe** are

listed in Table 4.1, and pertinent distances and angles are listed in Table 4.7. As shown in Figure 4.16, the solid state structure of **28-Fe** reveals a distorted trigonal bipyramidal coordination geometry about the iron center arising from a $N(TMS)_2$ group and the chelation of a tridentate imine with a bridging methylene group. The pyridine nitrogens span an angle of 149.14(6) ° and can be thought of as the pseudo-axis of the trigonal bipyramid. Around the equatorial plane, the $N_{im}FeN_{am}$ angle is 136.76(7) ° (N2-Fe1-N4), thereby causing the $N_{im}FeC$ and $N_{am}FeC$ angles to be less than 120 °: ∠N2-Fe1-C15 = 106.59(7) ° and ∠N4-Fe1-C15 = 116.64(7) °. The $CFeN_{py}$ angles are 91.07(7) ° and 93.39(7) ° for N1-Fe1-C15 and N3-Fe1-C15, respectively. Bite angles for the chelate are smaller than 90 °, i.e. ∠N2-Fe1-N1 = 75.18(6) ° and ∠N2-Fe1-N3 = 74.29(6) °, thereby rendering the corresponding angles, i.e. $N_{py}FeN_{am}$, obtuse (∠N4-Fe1-N1 = 102.19(6) ° and ∠N4-Fe1-N3 = 102.96(6) °). Bond lengths between the iron and nitrogens are normal as iron-pyridine nitrogen bond lengths are 2.3192(17) Å (Fe1-N1) and 2.3538(17) Å (Fe1-N3). The iron-imine nitrogen distance (d(Fe1-N2) = 2.0511(15) Å) is slightly longer than the iron-amide nitrogen bond length (1.9914(16) Å). The iron-carbon bond distance is 2.336(2) Å. Ligand backbone bond distances are standard for a normal imine. An sp^3(N)-sp^2(C) assignment is appropriate for N2-C6, which has a distance of 1.331(2) Å. The N2-C7 bond length is 1.465(3) Å and is consistent with an sp^3(C)-sp^3(N) assignment.

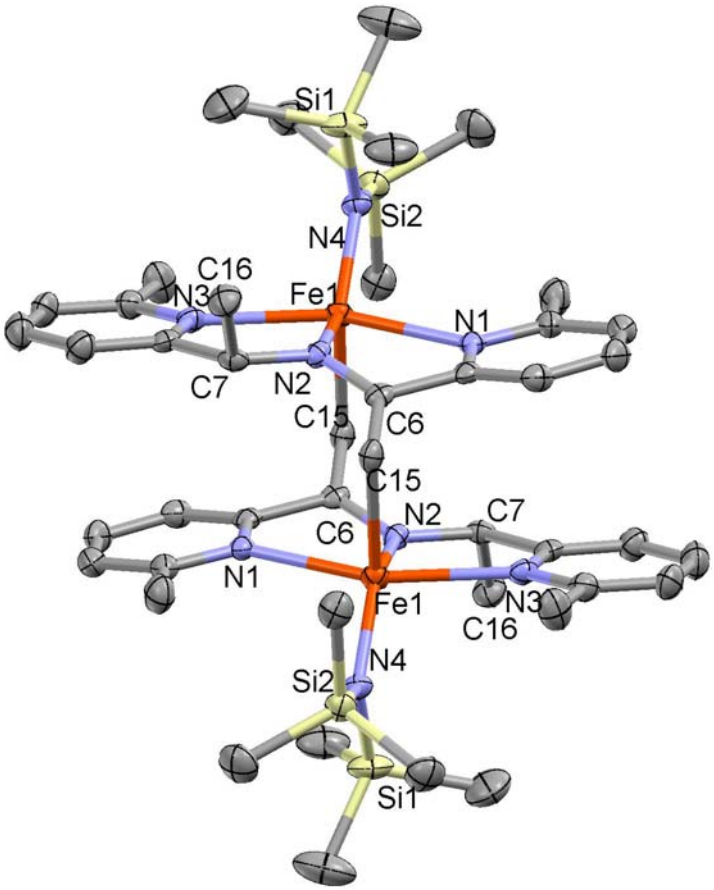

Figure 4.16. Molecular structure of $[(Me_4smif)FeN(TMS)_2]_2$ (**28-Fe**). Thermal ellipsoids are at 50 % probability level, and all hydrogens have been removed for clarity.

Table 4.7. Selected interatomic distances and angles for $[(Me_4smif)FeN(TMS)_2]_2$ (**28-Fe**).

Bond Distances (Å)		Bond Angles (°)	
Fe1 - N1	2.3192(17)	N1 - Fe1 - N2	75.18(6)
Fe1 - N2	2.0511(15)	N1 - Fe1 - N3	149.14(6)
Fe1 - N3	2.3538(17)	N1 - Fe1 - N4	102.19(6)
Fe1 - N4	1.9914(16)	N2 - Fe1 - N3	74.29(6)
Fe1 - C15	2.336(2)	N2 - Fe1 - N4	136.76(7)
N2 - C6	1.331(2)	N3 - Fe1 - N4	102.96(6)
N2 - C7	1.465(3)	N2 - Fe1 - C15	106.59(7)
Fe - Fe	4.7420(5)	N4 - Fe1 - C15	116.64(7)
		N1 - Fe1 - C15	91.07(7)
		N3 - Fe1 - C15	93.39(7)

Magnetism of [(Me$_4$smif)FeN(TMS)$_2$]$_2$ (28-Fe). Temperature dependence studies of the molar susceptibility for **28-Fe** were conducted. SQUID magnetometry data revealed an effective magnetic moment which rises from 2.1 μ_B at 10 K to 6.3 μ_B at 293 K. The moment at 293 K is slightly lower than the expected spin-only value of 6.93 μ_B for two S = 2 centers. A significant amount of ZFS is observed below 50 K. SQUID plots for other dimeric iron complexes are strikingly similar to the one shown in Figure 4.17, and the magnetic behavior may be indicative of antiferromagnetic coupling and/or temperature independent paramagnetism (TIP). In the case of **28-Fe**, it seems appropriate to attribute the magnetism to TIP as the iron-iron distance (4.7420(5) Å) is considerably longer than in other dimeric iron complexes.

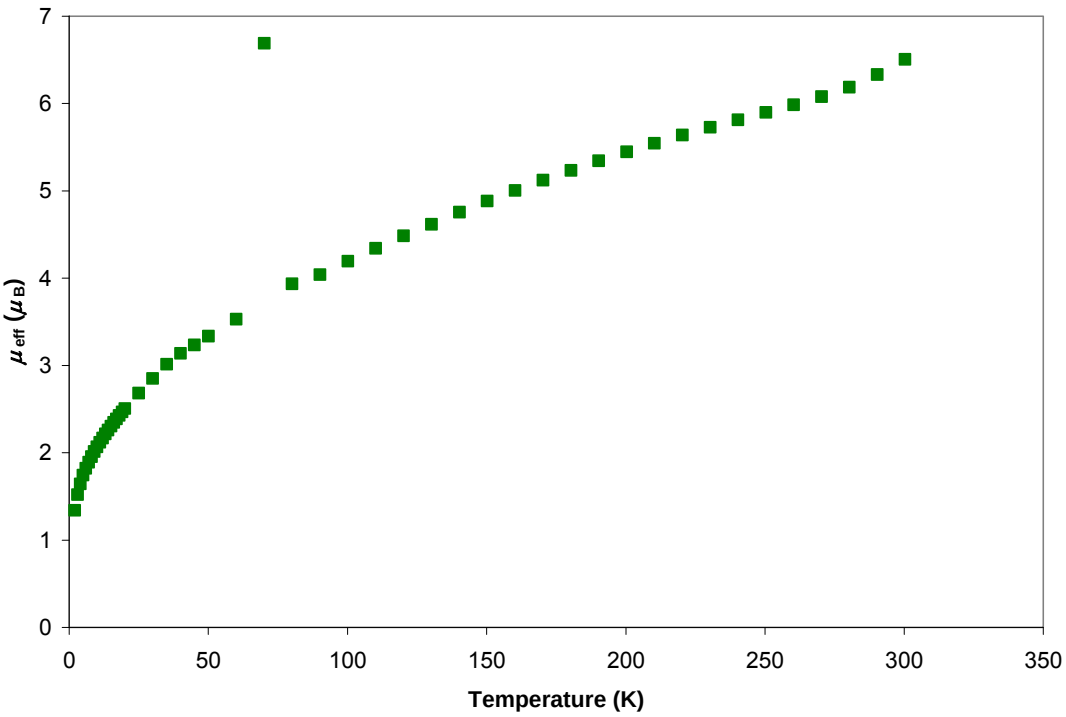

Figure 4.17. SQUID data for [(Me$_4$smif)FeN(TMS)$_2$]$_2$ (**28-Fe**): Magnetic moment (μ_{eff} in μ_B) as a function of T (K).

Proposed Mechanism for the Formation of [(Me$_4$smif)FeN(TMS)$_2$]$_2$ (28-Fe). In order to prevent the formation of a tetra-substituted piperazine ring via the reversible C-C bond formation, substitution was incorporated on the backbone of **smifH**. Unexpectedly, a new dimeric compound, **28-Fe**, was isolated in 59 % yield after exposing a solution of Fe{N(TMS)$_2$}$_2$(THF) to one equivalent of **Me$_4$smifH**. HN(TMS)$_2$ was the only other product observed by ^{1}H NMR spectroscopy. A mechanism similar to that proposed for the formation of (smif)CrN(TMS)$_2$, mentioned in Chapter 1, may be envisioned for the formation of **28-Fe**.

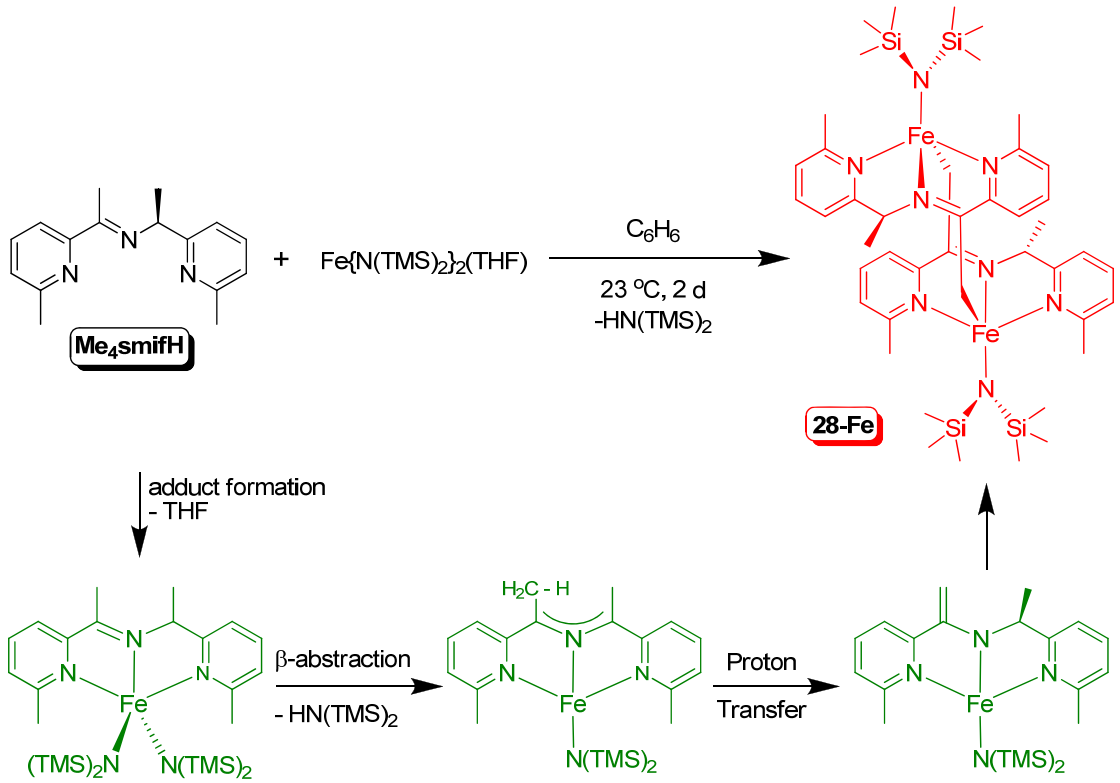

Scheme 4.10. Proposed mechanism for the formation of [(Me$_4$smif)FeN(TMS)$_2$]$_2$ (**28-Fe**).

As shown in Scheme 4.10, the coordination of **Me_4smifH** to $Fe\{N(TMS)_2\}_2(THF)$ generates the 5-coordinate complex, $\{\kappa\text{-}N_{py},N_{py},N_{am}\text{-}(Me_4smifH)Fe\{N(TMS)_2\}_2$, upon the loss of THF. This 5-coordinate adduct may undergo β-abstraction by the internal base, $N(TMS)_2$, with concomitant loss of $HN(TMS)_2$, and the resulting complex would be the proposed square planar complex, (Me4smif)$FeN(TMS)_2$. Proton transfer from one backbone methyl group to the opposite carbon in the smif backbone may result in the formation of a vinyl CH_2 group. The attack of the metal center upon the vinyl CH_2 group results in the formation of the dimeric structure, **28-Fe**.

Reactivity of the Coordinated smif Backbone. Formation of a tetra-substituted piperazine resulting from the dimerization of (smif)$FeN(TMS)_2$ (**16-Fe**) was a particularly interesting transformation. Electronic features of the smif backbone suggest its ability to undergo heterolytic and/or diradical reactivity. In light of these observations, research efforts focused on exploiting the reactive azaallyl ligand with the hope of finding a way to synthesize new heterocycles. **16-Fe** and $(smif)_2Fe$ (**6-Fe**) were treated with a wide variety of unsaturated complexes, shown in Figure 4.18, to effect both potential types of reactivity. The iron complexes either generated a mixture of products or were relatively unreactive towards the substrates even at elevated temperatures. However, two substrates afforded new complexes.

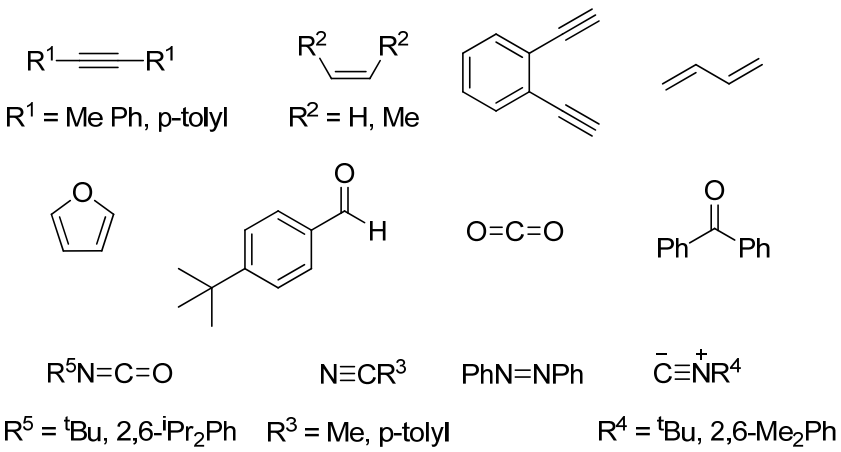

Figure 4.18. Examples of substrates tested for cyclization with the smif backbone.

After 3 d at 50 °C, a benzene solution containing **14-Fe** and di-(*p*-tolyl)acetylene afforded the [3+2] cycloaddition product, [(2,5-di(pyridin-2-yl)-3,4-di-(*p*-tolyl-2,5-dihydropyrrol-1-ide))FeN(TMS)$_2$]$_2$ (**29-Fe**) (eq 4.12). **29-Fe** is a red, paramagnetic complex that was isolated in 19 % yield. X-ray crystallographic studies revealed that **29-Fe** is dimeric in the solid state.

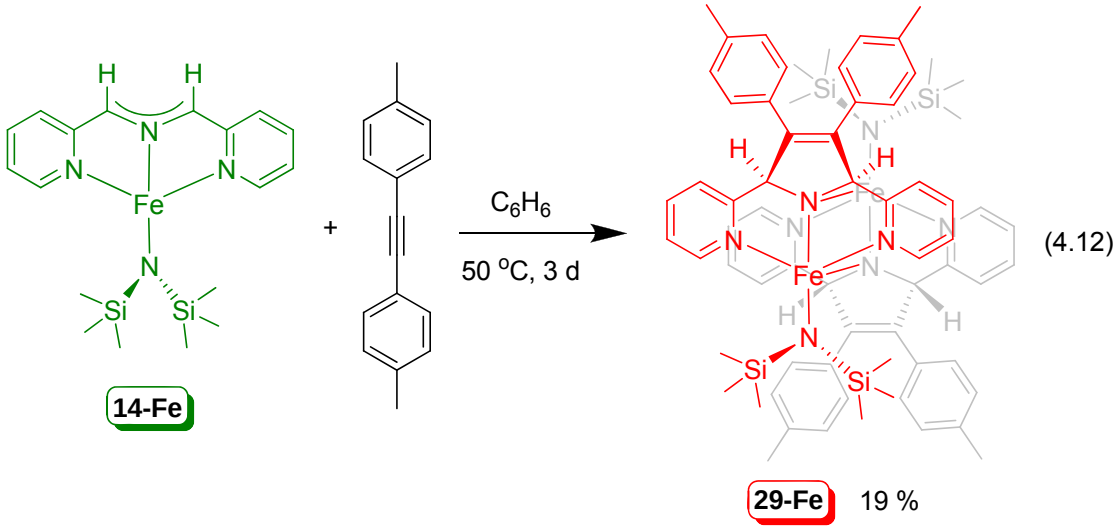

Treatment of a benzene solution of **6-Fe** with two equivalents of 2,6-diisopropylphenylisocyanate afforded the isocyanate insertion product, (2,6-$^{i}Pr_2PhNCOsmif)_2Fe$ (**30-Fe-DIPP**), in 75 % yield as a dark red solid (eq 4.13). 1-D and 2-D NMR spectroscopic studies on this low spin, Fe(II) complex revealed the presence of an NH in addition to two pyridine rings, indicative of an asymmetric smif ligand. The structure of **30-Fe-DIPP** was confirmed by x-ray crystallography.

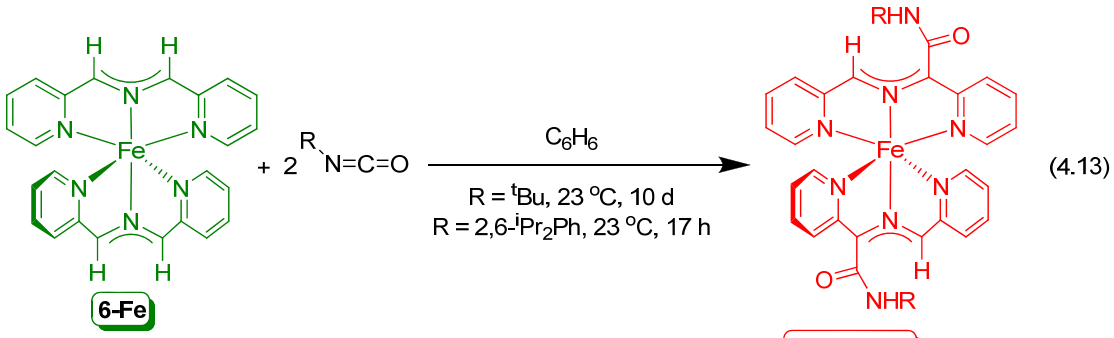

(4.13)

An analogous synthesis afforded (^{t}BuNCOsmif)$_2$Fe (**30-Fe-^{t}Bu**) as a dark red solid in 47 % yield (eq 4.13). **30-Fe-^{t}Bu** is another low spin, Fe(II) complex. The synthesis of **30-Fe-^{t}Bu** was low yielding and particularly sensitive, thus an alternative route was sought. Exposing a THF solution of Na(smif) (**5-Na**) to an equivalent of ^{t}BuNCO yielded a deep red solution of Na(^{t}BuNCOsmif) (**31-Na**) (Scheme 4.11), which was obtained as a metallic green solid in 91 % yield. As shown in Scheme 4.11, the treatment of $FeBr_2(THF)_2$ with two equivalents of **31-Na** generated a deep red-orange solution from which **30-Fe-^{t}Bu** was isolated in 61 % yield.

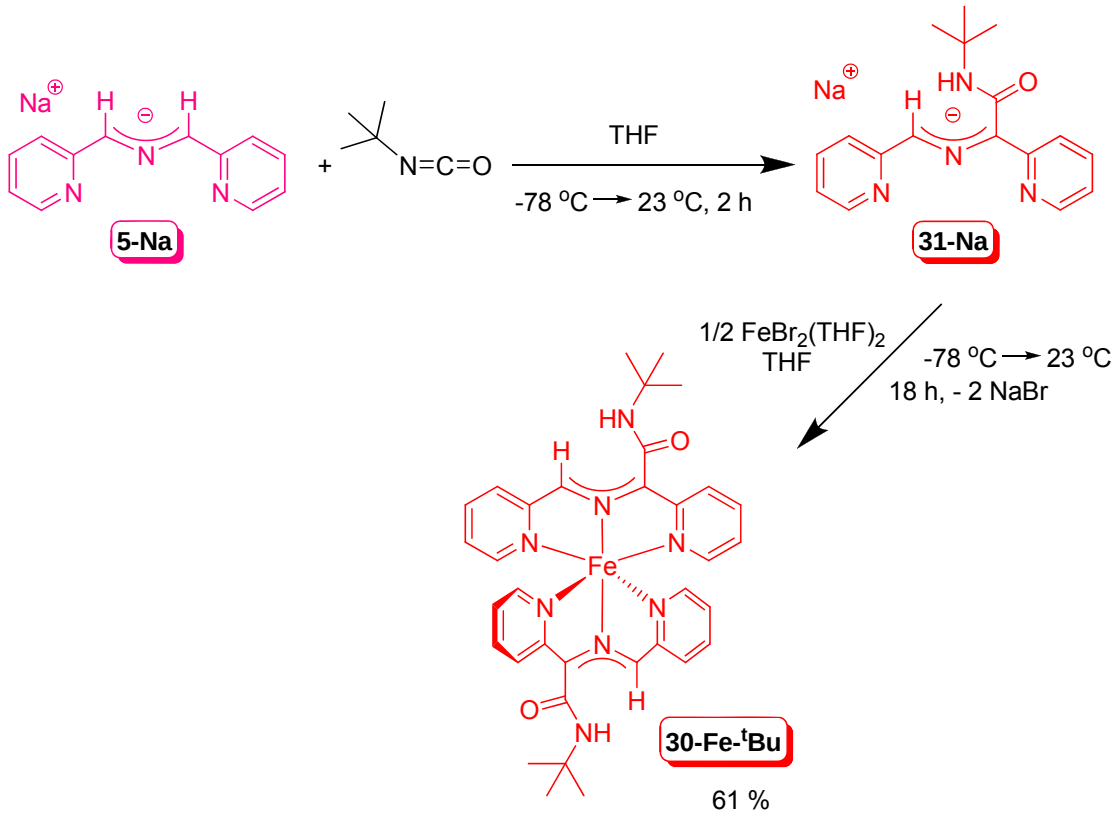

Scheme 4.11. Synthesis of (^{t}BuNCOsmif)$_2$Fe (**30-Fe-^{t}Bu**) via salt metathesis.

Characterization of the [3+2] Cycloaddition Product (29-Fe): X-ray Crystal Structure. X-ray quality, red plates of **29-Fe** were obtained from Et_2O. Select crystallographic and refinement data for **29-Fe** are listed in Table 4.1, and pertinent distances and angles are listed in Table 4.8. As shown in Figure 4.19, the solid state structure of **29-Fe** shows a square pyramidal geometry about the iron center. **29-Fe** is dimeric, and the tetra-substituted pyrroline is coordinated in a κ-N_{py},N_{py},N_{pam} fashion to one iron center and bridges through the pyrroline-nitrogen (N_{pam}) to the other iron center. The pyridine nitrogens span an average angle of 144.04(6) ° around iron, whereas the pyrroline nitrogen-iron-amide nitrogen angle averages 157.1(2) °. Similar to every other tridentate nitrogen chelate mentioned thus far, the $N_{pam}FeN_{py}$ bite angles

in **29-Fe** are also acute, averaging 77.3(8) °. The amide nitrogen-iron-pyridine nitrogen angles are obtuse, i.e. 96.8(4) ° (ave). Almost a perfect square exists between the dimeric complex: $N_{pam}FeN_{pam}$' = 88.3(3) ° (ave), $d(Fe\text{-}N_{pam})_{ave}$ = 2.060(4) Å, and $d(Fe\text{-}N_{pam}')_{ave}$ = 2.107(10) Å. The iron-nitrogen distances are similar to those observed in **[14-Fe]$_2$**, and are consistent with a weaker field invoked by the tetra-substituted pyrroline ligand in comparison to the stronger field smif ligand, which possesses significantly shorter bond lengths. Distances between the iron and amide nitrogens average 2.1624(14) Å and the $Fe\text{-}N_{py}$ bond lengths are slightly shorter, i.e. 2.158(14) Å (ave). The pyrroline nitrogen-carbon distances average a value of 1.467(5) Å, which is consistent with an sp^3(N)-sp^3(C) assignment, whereas the length of the carbon-carbon bond (1.325(6) Å, ave), originally from the alkyne, is typical for an sp^2(C)-sp^2(C) assignment. Metal-metal interactions, i.e. antiferromagnetic coupling, is anticipated in **29-Fe** as the Fe-Fe distance is 3.0539(4) Å.

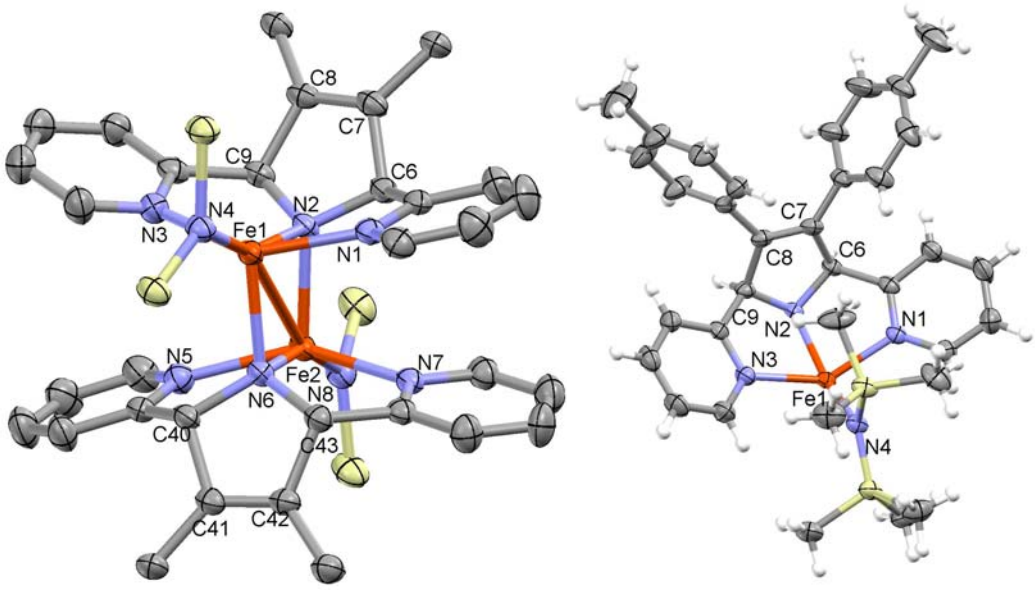

Figure 4.19. Molecular structure of the [3+2] cycloaddition product, **29-Fe**. Thermal ellipsoids are at 50 % probability level. Structural core (**A**) and ½ dimer (**B**).

Table 4.8. Selected interatomic distances and angles for the [3+2] cycloaddition product, **29-Fe**.

Bond Distances (Å)		Bond Angles (°)	
Fe - N_{py}	2.158(14)	N_{py} - Fe - N_{py}	144.04(6)
Fe - N_{am}	2.1624(14)	N_{pam} - Fe - N_{am}	157.1(2)
Fe - N_{pam}	2.060(4)	N_{pam} - Fe - N_{py}	77.3(8)
Fe - N_{am}'	2.107(10)	N_{am} - Fe - N_{py}	96.8(4)
Fe - Fe	3.0539(4)	N_{py} - Fe - N_{pam}'	96.48(5) - 107.18(6)
C_{alk} - C_{alk}	1.325(2)	N_{am} - Fe - N_{pam}'	114.64(13)
N_{pam} - C	1.467(5)	N_{pam} - Fe - N_{pam}'	88.3(3)

N_{pam} = pyrrole amide nitrogen, N_{am} = $N(TMS)_2$, C_{alk} = carbon originally from the alkyne, C = backbone carbon next to N_{pam}.

Magnetism on the [3+2] Cycloaddition Product 29-Fe. A study on the temperature dependence of the molar susceptibility of **29-Fe** was conducted. SQUID magnetometry data revealed a μ_{eff} of 1.7 μ_B at 10 K (Figure 4.20). The magnetic moment rises to 5.2 μ_B at 293 K. A similar behavior was displayed in the magnetism data for **28-Fe** and may be indicative of antiferromagnetic coupling. The data between 20-30 K may result from either a phase change of **29-Fe**, but its origin is ill-defined.

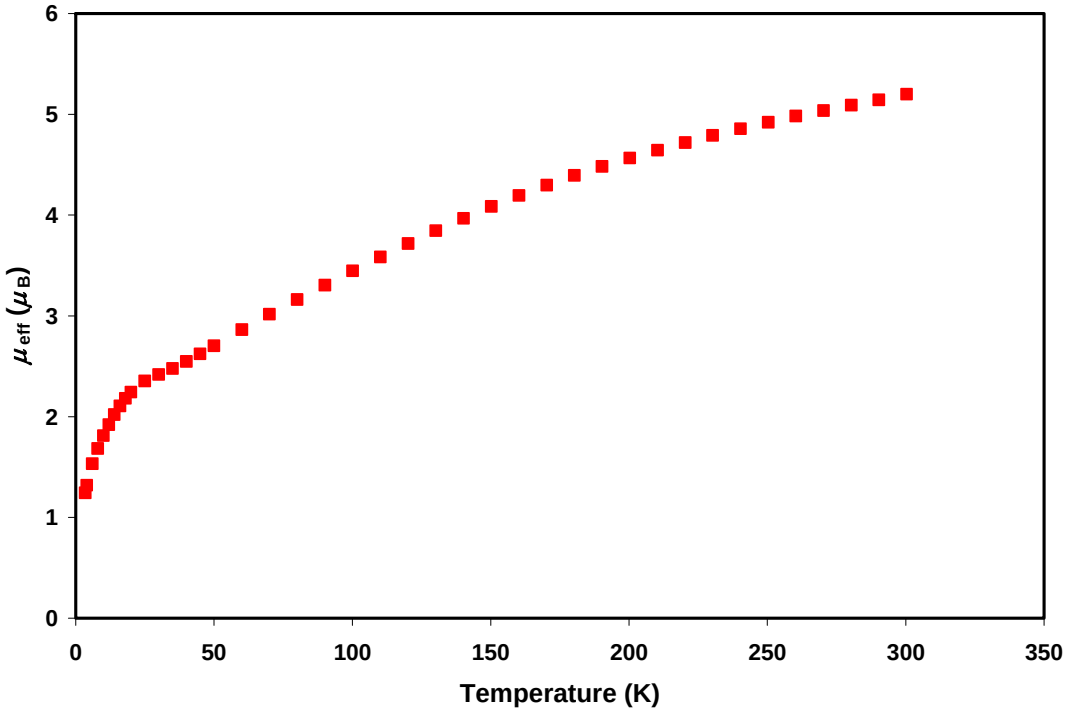

Figure 4.20. SQUID data for [3+2] cycloaddition product, **29-Fe**: Magnetic moment (μ_{eff} in μ_B) as a function of T (K).

Characterization of (RNCOsmif)$_2$Fe Complexes: X-ray Crystal Structure of (2,6-^{i}Pr$_2$PhNCOsmif)$_2$Fe (30-Fe-DIPP). A dark red-black needle, suitable for single crystal x-ray diffraction studies, was obtained from a mixture of THF and pentane. Select crystallographic and refinement data for **30-Fe-DIPP** are listed in Table 4.1, and pertinent distances and angles are listed in Table 4.9. As shown in Figure 4.21, the solid state structure of **29-Fe** possesses two tridentate smif ligands occupying an octahedral geometry similar to the structure of all other (smif)$_2$M complexes. A slight C_s distortion arises from one ligand canting off axis, such that the azaallyl nitrogens span an angle of 176.49(17) ° around iron in contrast to the 179.11(6) ° observed in **6-Fe**. Large $N_{py}FeN_{py}$ angles are observed and average 165.59(12) °. The bite angles of the chelate, i.e. the $N_{aza}FeN_{py}$ angles, are 83.1(4) ° on

average. In contrast to **6-Fe**, the $N_{aza}FeN_{py}$' angles are not identical, i.e. ∠N2-Fe1-N4 = 99.96(16)°, ∠N2-Fe1-N6 = 94.00(16)°, ∠N5-Fe1-N1 = 97.46(16)°, and ∠N5-Fe1-N3 = 96.48(16)°, resulting in a slight C_s distortion. Iron-nitrogen distances are similar to those observed for **6-Fe** and are consistent with the low spin Fe(II) center. The Fe-N_{aza} bond length averages 1.908(11) Å, and the Fe-N_{py} distances are 1.955(15) Å on average. Even though the smif ligand possesses substitution rendering it asymmetric, the N_{aza}-C bond lengths of 1.347(22) Å (ave) are still consistent with a delocalized anion and an sp^2(N)-sp^2(C) assignment.

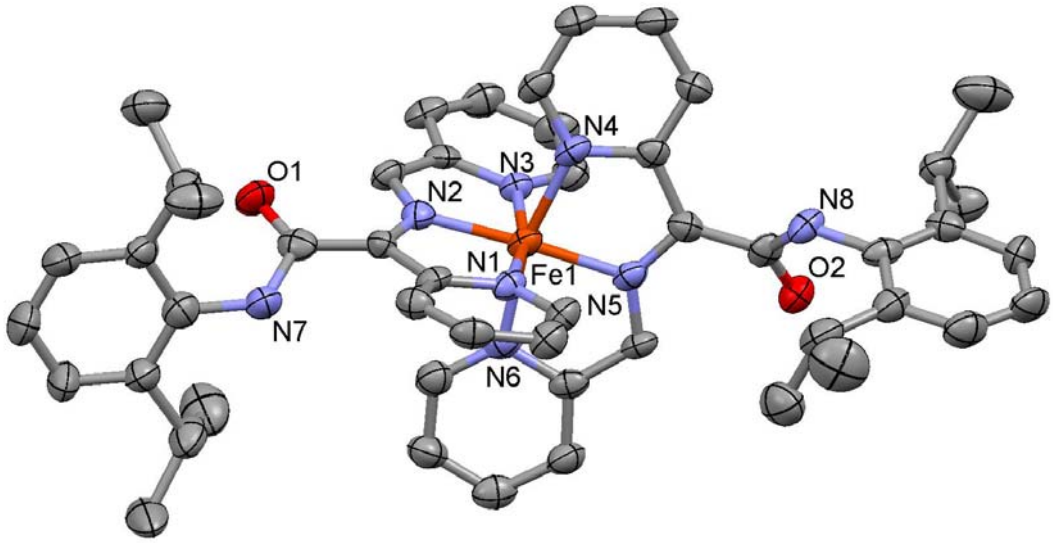

Figure 4.21. Molecular structure of the (2,6-$^{i}Pr_2$PhNCOsmif)$_2$Fe (**30-Fe-DIPP**). Thermal ellipsoids are at 50 % probability level, and all hydrogens have been removed for clarity.

Table 4.9. Selected interatomic distances and angles for $(2,6\text{-}^{i}Pr_2PhNCOsmif)_2Fe$ (**30-Fe-DIPP**).

Bond Distances (Å)		Bond Angles (°)	
Fe - N_{aza}	1.908(11)*	N_{aza} - Fe - N_{aza}	176.49(17)
Fe - N_{py}	1.955(14)*	N_{py} - Fe - N_{py}	165.92(12)*
N_{aza} - C	1.347(22)*	N_{aza} - Fe - N_{py}	83.1(4)*
		N_{aza} - Fe - $N_{py'}$	94.00(16) - 99.96(16)
		N_{py} - Fe - $N_{py'}$	90.8(18)*

* Values averaged.

UV-vis Spectra of $(RNCOsmif)_2Fe$ Complexes. Both isocyanate insertion products, **30-Fe-DIPP** and **30-Fe-^{t}Bu**, produce deep red solutions in benzene. Their UV-vis spectra, shown in Figure 4.22, are virtually identical. They exhibit four main features. The strongest absorption occurs in the low energy regime, i.e. 427 nm ($\varepsilon \sim 46{,}000\ M^{-1}\ cm^{-1}$) and 431 nm ($\varepsilon \sim 42{,}000\ M^{-1}\ cm^{-1}$) for **30-Fe-DIPP** and **30-Fe-^{t}Bu**, respectively. The remaining absorptions in **30-Fe-DIPP** appear at 381 nm ($\varepsilon \sim 33{,}000\ M^{-1}\ cm^{-1}$), 525 nm ($\varepsilon \sim 21{,}000\ M^{-1}\ cm^{-1}$), and 638 nm ($\varepsilon \sim 7{,}000\ M^{-1}\ cm^{-1}$). The corresponding features in **30-Fe-^{t}Bu** occur at 383 nm ($\varepsilon \sim 28{,}000\ M^{-1}\ cm^{-1}$), 534 nm ($\varepsilon \sim 19{,}000\ M^{-1}\ cm^{-1}$), and 644 nm ($\varepsilon \sim 6{,}000\ M^{-1}\ cm^{-1}$). Features observed in these UV-vis spectra may be attributed to intraligand transitions as observed in the UV-vis spectra of all other complexes containing the smif ligand.

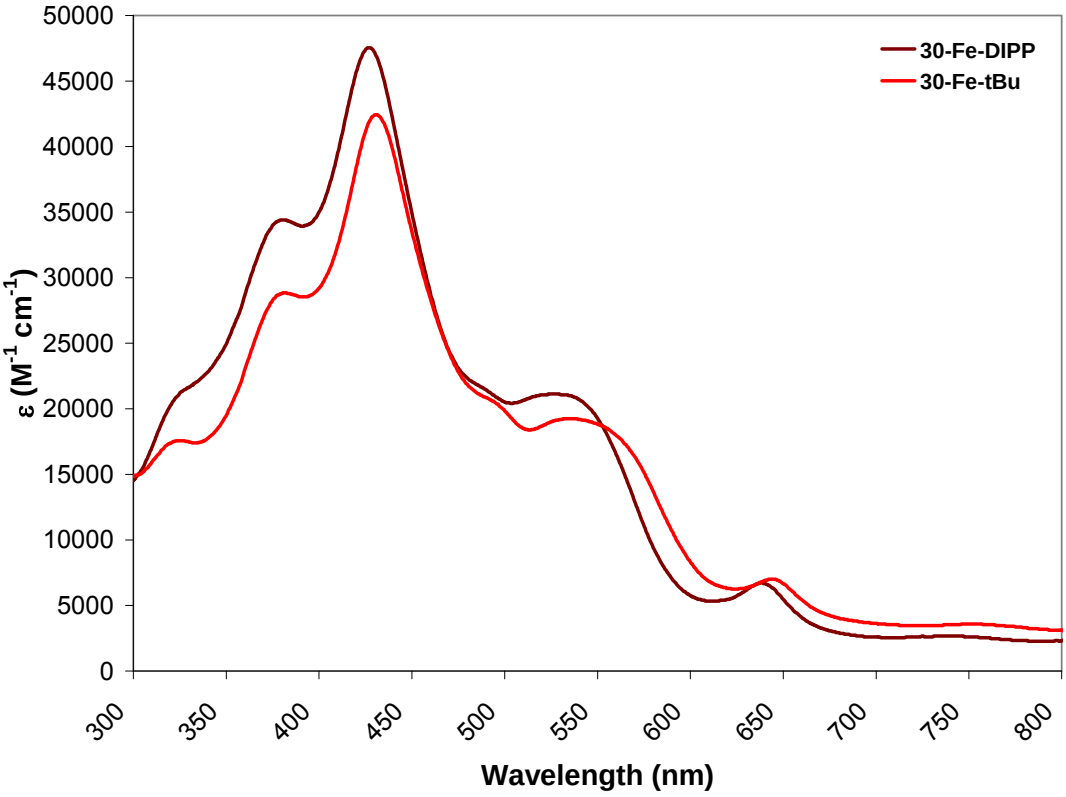

Figure 4.22. UV-vis spectra of $(RNCOsmif)_2Fe$ complexes, where R = 2,6-$^{i}Pr_2Ph$ (**30-Fe-DIPP**) and ^{t}Bu (**30-Fe-^{t}Bu**).

Conclusions

Reversible C-C bond formation was observed while attempting to synthesize the iron analog of $(smif)CrN(TMS)_2$. In solution, $(smif)FeN(TMS)_2$ (**14-Fe**) exists as a monomer and possesses physical properties consistent with an azaallyl backbone; however, dimerization of **14-Fe** to **[14-Fe]$_2$** occurs in the solid state such that C-C bond formation yields a bridging tetra-substituted piperazine ligand. Ligand modifications of **smifH** were explored. Substitution on the *ortho*-position of the pyridine rings with CH_3 groups was implemented to avoid the formation of $(smif)_2Fe$, which may be detrimental for potential catalysis. *Ortho*-CH_3 substitution did not

prevent the formation of $(smif)_2Fe$ derivations; however, it showed how the addition of *ortho*-CH_3 groups changes the ligand field strength. The parent compound, **6-Fe**, is a low spin Fe(II) complex, whereas the fully substituted complex, $(^oMe_2smif)_2Fe$, is high spin (S = 2). Methylation of the **smifH** backbone was designed to prevent reactivity from the chelated azaallyl fragment, yet it did not. Instead, it led to the formation of a new dimeric complex by activating the backbone methyl group.

In light of the inevitable azaallyl backbone reactivity, **14-Fe** and **6-Fe** were treated with a variety of unsaturated organic substrates with the hope of generating new heterocycles. Unfortunately, most substrates tested generated a mess of products or exhibited no reactivity. Interestingly, treatment of **14-Fe** with di-(*p*-tolyl)acetylene led to the [3+2] cycloaddition product, and exposing **6-Fe** to substituted isocyanates afforded insertion products.

$(dpma)FeN(TMS)_2$ (**15-Fe**) and $(dpma)_2Fe$ (**16-Fe**) were synthesized as a means of comparison to **14-Fe** and **6-Fe**. Incidentally, the bis-amide complex, **16-Fe,** differs from **6-Fe** by 4 H^+ and 4 e^-, and the conversion from **16-Fe** to **6-Fe** by the loss of two equivalents of dihydrogen is favored by 12.5 kcal/mol. Therefore, hydrogenation of unsaturated organic substrates by **16-Fe** was also investigated.

Experimental

General Considerations. All manipulations were performed using either glovebox or high vacuum line techniques. Hydrocarbon solvents containing 1-2 mL of added tetraglyme, and ethereal solvents were distilled under nitrogen from purple sodium benzophenone ketyl and vacuum transferred from same prior to use. Benzene-d_6 and toluene-d_8 were dried over sodium, vacuum transferred and stored under N_2. THF-d_8 was dried over sodium benzophenone ketyl. $FeBr_2(THF)_2$,[43]

$Fe\{N(TMS)_2\}_2(THF)$,[27] 6-methyl-2-pyridylmethylamine,[44] and 1,3-(2-pyridyl)-2-azapropene (smifH)[24] were prepared according to literature procedures. All other chemicals were commercially available and used as received. All glassware was oven dried.

NMR spectra were obtained using INOVA 400 and INOVA 500 spectrometers. Chemical shifts are reported relative to benzene-d_6 (^{1}H δ 7.16; ^{13}C{^{1}H} δ 128.39), toluene-d_8 (^{1}H δ 2.09; ^{13}C{^{1}H} δ 20.4), and THF-d_8 (^{1}H δ 3.58; ^{13}C{^{1}H} δ 67.57). Infrared spectra were recorded on a Nicolet Avatar 370 DTGX spectrophotometer interfaced to an IBM PC (OMNIC software). UV-Vis spectra were obtained on a Shimadzu UV-2102 interfaced to an IBM PC (UV Probe software). GC-MS spectra were obtained on a JEOL GCMate 2 mass spectrometer coupled to an Agilent 689 N GC with EI ionization under standard conditions. Solution magnetic measurements were conducted via Evans' method in toluene-d_8.[29] Solid state magnetic measurements were performed using a Johnson Matthey magnetic susceptibility balance calibrated with $HgCo(SCN)_4$. Elemental analyses were performed by Robertson Microlit Laboratories, Madison, New Jersey and the services at the University of Erlangen-Nuremberg, Germany.

Synthesis. 1. *N*-((6-methylpyridin-2-yl)methylene)-1-(pyridine-2-yl)methanamine (^{o}MesmifH). To a suspension of anhydrous $MgSO_4$ (12.421 g, 103.19 mmol) in 40 mL of CH_2Cl_2 was added 6-methyl-2-pyridinecarboxaldehyde (2.500 g, 20.64 mmol) followed by the slow addition of 2-(aminomethyl)pyridine (2.232 g, 20.64 mmol). The suspension stirred at 23 °C for 3 h. The reaction mixture was filtered and washed with CH_2Cl_2. The solvent was removed under vacuum to yield a pale yellow liquid (4.25 g, 97 %). ^{1}H NMR (C_6D_6, 400 MHz): δ 2.39 (s, C*H*$_3$, 3 H), 4.92 (s, C*H*$_2$, 2 H), 6.60 (d, py^{Me}-C^5*H*, 1 H, J = 7.6 Hz), 6.61 (t, py-C^5*H*, 1 H, J =

5.3 Hz), 7.04 (t, py^{Me}-C^4*H*, 1 H, J = 7.6 Hz), 7.08 (td, py-C^4*H*, 1 H, J = 7.5, 1.6 Hz), 7.20 (d, py-C^3*H*, 1 H, J = 7.8 Hz), 8.02 (d, py^{Me}-C^3*H*, 1 H, J = 7.8 Hz), 8.48 (d, py-C^6*H*, 1 H, J = 4.8 Hz), 8.61 (s, im-C*H*, 1 H). ^{13}C{^{1}H} NMR (C_6D_6, 100 MHz): δ 24.62 (CH_3), 67.24 (CH_2), 118.48 (py^{im}-*C*^{3}H), 122.16 (py-*C*^{3}H), 122.53 (py^{im}-*C*^{5}H), 124.39 (py-*C*^{5}H), 136.36 (py-*C*^{4}H), 137.70 (py^{im}-*C*^{4}H), 149.95 (py-*C*^{6}H), 154.25 (py^{im}-*C*^{6}), 158.54 (py^{im}-*C*^{2}), 160.22 (py-*C*^{2}), 164.97 (im-*C*H).

2. 1-(6-methylpyridin-2-yl)-*N*-((6-methylpyridin-2-yl)methylene)methanamine (^{o}Me$_2$smifH). To a suspension of anhydrous $MgSO_4$ (5.036 g, 41.82 mmol) in 16 mL of CH_2Cl_2 was added 6-methyl-2-pyridinecarboxaldehyde (1.014 g, 8.37 mmol) followed by the slow addition of 6-methyl-2-pyridylmethylamine (1.022 g, 8.37 mmol). The yellow suspension stirred at 23 °C for 3 h. The reaction mixture was filtered and washed with CH_2Cl_2. The solvent was removed under vacuum to yield a pale yellow solid (1.73 g, 92 %). ^{1}H NMR (C_6D_6, 500 MHz): δ 2.38 (s, py-C*H*$_3$, 3 H), 2.39 (s, py^{im}-C*H*$_3$, 3 H), 4.93 (s, C*H*$_2$, 2 H), 6.61 (d, py-C^3*H*, py-C^4*H*, 2 H, J = 6.5 Hz), 7.06 (t, py^{im}-C^4*H*, 1 H, J = 7.5 Hz), 7.10 (d, py-C^5*H*, py^{im}-C^5*H*, 2 H, J = 7 Hz), 8.02 (d, py^{im}-C^3*H*, 1 H, J = 8 Hz), 8.62 (s, C*H*, 1 H). ^{13}C{^{1}H} NMR (C_6D_6, 125 MHz): δ 24.62 (py-*C*H$_3$), 24.84 (py^{im}-*C*H$_3$), 67.45 (C*H*$_2$), 118.47 (py-*C*^{3}H), 119.56 (py^{im}-*C*^{3}H), 121.60 (py-*C*^{5}H), 124.36 (py^{im}-*C*^{5}H), 136.70 (py-*C*^{4}H), 136.78 (py^{im}-*C*^{4}H), 155.38 (py^{im}-*C*^{2}), 158.46 (py-*C*^{6}), 158.50 (py^{im}-*C*^{6}), 159.46 (py-*C*^{2}), 164.79 (im-*C*H).

3. 1-(pyridine-2-yl)-*N*-(1-(pyridine-2-yl)ethylidene)ethanamine (^{b}Me$_2$smifH). A solution of **smifH** (1.000 g, 5.07 mmol) in 20 mL THF was slowly added to a suspension of NaH (0.243 g, 10.13 mmol) in 15 mL THF at 0 °C. The reaction mixture turned magenta and was stirred at 0 °C for 3 h prior to the addition of CH_3I (0.63 mL, 10.11 mmol). After stirring at 23 °C for 12 h, the solution appeared

orange-red. The volatiles were removed *in vacuo*, and the residue was filtered in CH_2Cl_2. Methylene chloride was removed, and the solid was triturated with Et_2O and filtered to yield an orange solid (1.138 g, 99 %). ^{1}H NMR (C_6D_6, 500 MHz): δ 1.67 (d, C*H*$_3$, 3 H, J = 7 Hz), 2.37 (s, im-C*H*$_3$, 3 H), 5.19 (q, C*H*, 1 H, J = 6.5 Hz), 6.67 (t, py-C^5*H*, 1 H, J = 5.5 Hz), 6.68 (t, py^{im}-C^5*H*, 1 H, J = 5.5 Hz), 7.17 (t, py-C^4*H*, 1 H, J = 7.5 Hz), 7.19 (t, py^{im}-C^4*H*, 1 H, J = 7.5 Hz), 7.63 (d, py-C^3*H*, 1 H, J = 8 Hz), 8.39 (d, py^{im}-C^3*H*, 1 H, J = 8 Hz), 8.44 (d, py-C^6*H*, 1 H, J = 3.5 Hz), 8.54 (d, py^{im}-C^6*H*, 1 H, J = 4 Hz). ^{13}C{^{1}H} NMR (C_6D_6, 125 MHz): δ 13.97 (*C*H$_3$), 23.52 (im-*C*H$_3$), 62.94 (im-*C*H), 121.37 (py-*C*^{3}H), 121.49 (py^{im}-*C*^{3}H), 122.05 (py-*C*^{5}H), 124.38 (py^{im}-*C*^{5}H), 136.08 (py-*C*^{4}H), 136.50 (py^{im}-*C*^{4}H), 148.81 (py-*C*^{6}H), 149.66 (py^{im}-*C*^{6}H), 158.60 (im-*C*H), 165.95 (py^{im}-*C*^{2}), 166.23 (py-*C*^{2}).

4. 1-(6-methylpyridin-2-yl)-*N*-(1-(6-methylpyridin-2-yl)ethylidene)ethanamine (Me$_4$smifH). A solution of **^{o}Me$_2$smifH** (2.500 g, 11.10 mmol) in 20 mL THF was slowly added to a suspension of NaH (0.533 g, 22.21 mmol) in 15 mL THF at 12 °C. The reaction mixture turned magenta and was stirred at 12 °C for 3 h prior to the addition of CH_3I (1.40 mL, 22.49 mmol). After stirring at 23 °C for 16 h, the volatiles from the orange solution were removed *in vacuo*. The residue was triturated, filtered, and washed with CH_2Cl_2. Methylene chloride was removed, and the solid was triturated with Et_2O and filtered to yield a pale orange solid (1.138 g, 99 %). ^{1}H NMR (C_6D_6, 500 MHz): δ 1.71 (d, C*H*$_3$, 3 H, J = 6.5 Hz), 2.39 (s, py-C*H*$_3$, 3 H), 2.40 (s, py^{im}-C*H*$_3$, 3 H), 2.47 (s, im-C*H*$_3$, 3 H), 5.20 (q, C*H*, 1 H, J = 6.5 Hz), 6.66 (t, py-C^5*H*, py^{im}-C^5*H*, 2 H, J = 7.5 Hz), 7.18 (t, py-C^4*H*, 1 H, J = 7.5 Hz), 7.20 (t, py^{im}-C^4*H*, 1 H, J = 7.5 Hz), 7.54 (d, py-C^3*H*, 1 H, J = 7.5 Hz), 8.31 (d, py^{im}-C^3*H*, 1 H, J = 8 Hz). ^{13}C{^{1}H} NMR (C_6D_6, 125 MHz): δ 14.02 (*C*H$_3$), 23.74 (im-*C*H$_3$), 24.80 (py-*C*H$_3$), 24.98 (py^{im}-*C*H$_3$), 63.12 (im-*C*H), 118.34 (py-*C*^{3}H), 118.66

(py^{im}-C^3H), 121.41 (py-C^5H), 123.72 (py^{im}-C^5H), 136.48 (py-C^4H), 136.93 (py^{im}-C^4H), 157.26 (im-*C*H), 158.02 (py-C^6), 158.23 (py^{im}-C^6), 165.44 (py^{im}-C^2), 166.24 (py-C^2).

5. D-$d_4$dpma/D_2-$d_2$pma. To a 50 mL round bottom flask containing a solution of 2-cyanopyridine (1.658 g, 15.93 mmol) in 16 mL CH_3OD was added sodium borodeuteride (2.000 g, 47.78 mmol). The resulting cloudy suspension was refluxed under argon for 16 h. The yellow suspension was cooled to 23 °C, filtered, and washed with CH_3OD. Volatiles were removed from the yellow filtrates *in vacuo* yielding a yellow solid which was dissolved in 10 mL D_2O, stirred for 1 h at 23 °C, and extracted with CH_2Cl_2 (3 x 10 mL). Organic layers were combined, dried over Na_2SO_4, filtered, and volatiles were removed *in vacuo* to yield an orange-yellow liquid containing both **D_2-$d_2$pma** and **D-$d_4$dpma** which were separated via distillation under dynamic vacuum: **D_2-$d_2$pma** (0.479g, 28%) and **D-$d_4$dpma** (0.698 g, 44%). **D_2-$d_2$pma**: ^{1}H NMR (C_6D_6, 400 MHz): δ 6.62 (dd, py-C^5*H*, 1 H, J = 7.5, 4.8 Hz), 6.88 (dt, py-C^3*H*, 1 H, J = 7.8, 1.2 Hz), 7.05 (td, py-C^4*H*, 1 H, J = 7.7, 1.8 Hz), 8.47 (d, py-C^6*H*, 1 H, J = 4.8 Hz). $^{13}C\{^1H\}$ NMR (C_6D_6, 100 MHz): δ 121.31 (py-C^3H), 121.79 (py-C^5H), 136.24 (py-C^4H), 149.77 (py-C^6H), 163.44 (py-C^2). **D-$d_4$dpma**: ^{1}H NMR (C_6D_6, 400 MHz): δ 6.62 (t, py-C^5*H*, 1 H, J = 5.6 Hz), 7.08 (m, py-C^3*H*, py-C^4*H*, 2 H), 8.47 (d, py-C^6*H*, 1 H, J = 4.7 Hz). $^{13}C\{^1H\}$ NMR (C_6D_6, 100 MHz): δ 122.98 (py-C^3H), 123.32 (py-C^5H), 137.21 (py-C^4H), 150.82 (py-C^6H), 162.27 (py-C^2).

6. (smif)FeN(SiMe$_3$)$_2$ (14-Fe) (in solution) and **[{(Me$_3$Si)$_2$N}Fe]$_2$(μ-N$^{am}_2$,N$^{py}_4$-2,3,5,6-tetrakis(pyridin-2-yl)piperazyl) ([14-Fe]$_2$)** (solid state). A solution of **smifH** (0.700 g, 3.55 mmol) in 10 mL Et_2O was added dropwise to a stirring solution of Fe{N(SiMe$_3$)$_2$}$_2$(THF) (1.592 g, 3.55 mmol) in Et_2O (10 mL) at 23 °C. The solution immediately became dark emerald green. The reaction was degassed, allowed

to stir at 23 °C for 3 h, and volatiles were removed. The orange crystalline solid was triturated with pentane, stripped, and filtered in Et_2O to produce 1.090 g of **[14-Fe]$_2$** (74 %). ^{1}H NMR (THF-d_8, 400 MHz): δ -0.01 ($\upsilon_{1/2} \approx 9$ Hz, C*H*, 1 H), 34.57 ($\upsilon_{1/2} \approx 380$ Hz, Si(C*H*$_3$)$_3$, 9 H), 46.70 ($\upsilon_{1/2} \approx 35$ Hz, py-C*H*, 1 H), 46.99 ($\upsilon_{1/2} \approx 110$ Hz, py-C*H*, 1 H), 86.21 ($\upsilon_{1/2} \approx 790$ Hz, py-C*H*, 1 H), 165.40 ($\upsilon_{1/2} \approx 620$ Hz, py-C*H*, 1 H). ^{1}H NMR (C_6D_6, 400 MHz): δ -14.34 ($\upsilon_{1/2} \approx 270$ Hz, Si(C*H*$_3$)$_3$, 9 H), -10.83 ($\upsilon_{1/2} \approx 100$ Hz, C*H*, 1 H), 71.49 ($\upsilon_{1/2} \approx 130$ Hz, py-C*H*, 1 H), 79.24 ($\upsilon_{1/2} \approx 200$ Hz, py-C*H*, 1 H), 136.99 ($\upsilon_{1/2} \approx 500$ Hz, py-C*H*, 1 H), 203.24 ($\upsilon_{1/2} \approx 430$ Hz, py-C*H*, 1 H). UV-vis (pentane) = 399 nm (ε ~ 37,000 M^{-1} cm^{-1}), 633 nm (ε ~ 52,000 M^{-1} cm^{-1}). Mössbauer parameters (80 K): $\delta = 0.86$ mms^{-1}, $\Delta E_Q = 1.07$ mms^{-1}, $\Gamma_{FWHM} = 0.46$ mms^{-1}. μ_{eff} dimer (SQUID, 300 K) = 7.34 μ_B.

7. (dpma)FeN(SiMe$_3$)$_2$ (15-Fe). To a solution of Fe{N(SiMe$_3$)$_2$}$_2$(THF) (0.500 g, 1.11 mmol) in Et_2O (10 mL) at -78 °C was added di-(2-picolyl)amine (0.222 g, 1.11 mmol) in 10 mL Et_2O via syringe under argon. Upon warming to 23 °C, the solution became red and continued to stir for 3 h. The reaction was degassed, cooled to -78 °C, and filtered. Red needles of **15-Fe** (0.297 g, 64 %) were washed with cold Et_2O. ^{1}H NMR (C_6D_6, 400 MHz): δ 12.73 ($\upsilon_{1/2} \approx 1900$ Hz, Si(C*H*$_3$)$_3$, 9 H), 25.20 ($\upsilon_{1/2} \approx 520$ Hz, C*H*$_2$, 2 H), 36.57 ($\upsilon_{1/2} \approx 1200$ Hz, py-C*H*, 1 H), 81.90 ($\upsilon_{1/2} \approx 2400$ Hz, py-C*H*, 1 H), 130.74 ($\upsilon_{1/2} \approx 2200$ Hz, py-C*H*, 1 H), 182.06 ($\upsilon_{1/2} \approx 3100$ Hz, py-C*H*, 1 H). UV-vis (benzene) = 549 nm (ε ~ 1,500 M^{-1} cm^{-1}). Anal. Calcd. $H_{30}C_{18}N_4Si_2Fe$: C, 52.16; H, 7.30; N, 13.52. Found: C, 52.32; H, 7.32; N, 13.49. μ_{eff} (SQUID, 293 K) = 3.0 μ_B.

8. (dpma)$_2$Fe (16-Fe). To a solution of Fe{N(SiMe$_3$)$_2$}$_2$(THF) (0.250 g, 0.56 mmol) in Et_2O (10 mL) at -78 °C was added di-(2-picolyl)amine (0.222 g, 1.11 mmol) in 5 mL Et_2O via syringe under argon. The solution became dark blue after 30 min at 23 °C and was stirred for 12 h. The volatiles were removed *in vacuo*. The residue was

dissolved in benzene and filtered through Celite. Addition of pentane facilitated the crystallization of **16-Fe** as dark blue-metallic purple crystals (0.188 g, 75 %). ^{1}H NMR (C_6D_6, 400 MHz): δ 8.47 ($\upsilon_{1/2} \approx 40$ Hz, py-C*H*, 1 H), 41.31 ($\upsilon_{1/2} \approx 70$ Hz, py-C*H*, 1 H), 50.37 ($\upsilon_{1/2} \approx 100$ Hz, py-C*H*, 2 H), 56.60 ($\upsilon_{1/2} \approx 180$ Hz, py-C*H*, 1 H), 163.05 ($\upsilon_{1/2} \approx 2900$ Hz, py-C*H*, 1 H). Mössbauer parameters (80 K): $\delta = 0.94$ mms^{-1}, $\Delta E_Q = 0.86$ mms^{-1}, $\Gamma_{FWHM} = 0.39$ mms^{-1}. UV-vis (pentane) = 360 nm ($\varepsilon \sim 5{,}000$ M^{-1} cm^{-1}), 708 nm ($\varepsilon \sim 3{,}700$ M^{-1} cm^{-1}). Anal. Calcd. $H_{24}C_{24}N_6Fe$: C, 63.73; H, 5.35; N, 18.58. Found: C, 65.35; H, 5.05; N, 17.69. μ_{eff} (Evans' method, C_6D_6, 293 K) = 5.0 μ_B. μ_{eff} (SQUID, 293 K) = 5.2 μ_B.

9. (smif)(dpma)Fe (17-Fe). A) To a stirred suspension of **[14-Fe]$_2$** (0.300 g, 0.36 mmol) in 20 mL Et_2O at -78 °C was slowly added a solution of di-(2-picolyl)amine (0.145 g, 0.73 mmol) in Et_2O (10 mL) under argon. The suspension immediately changed from emerald green to red. The reaction was degassed and allowed to stir at 23 °C for 3 h while dark red crystals precipitated from solution. The reaction mixture was concentrated, filtered cold, and washed with cold Et_2O to yield a mixture of **17-Fe** and **6-Fe** (16:1, 0.225 g, representing 63 % of **17-Fe**). **B)** To a stirred solution of **15-Fe** (0.300 g, 0.72 mmol) in 20 mL Et_2O at -78 °C was slowly added a solution of **smifH** (0.143 g, 0.72 mmol) in Et_2O (10 mL) under argon. The reaction was degassed. The reaction mixture changed color from cherry red to dark blue to purple to dark red as the solution warmed to 23 °C. Dark red crystals precipitated from solution while it stirred at 23 °C for 3 h. The reaction mixture was concentrated, filtered cold, and washed with cold Et_2O to yield a mixture of **17-Fe** and **6-Fe** (2:1, 0.260 g, representing 51 % **17-Fe**). ^{1}H NMR (C_6D_6, 400 MHz): δ 8.70 ($\upsilon_{1/2} \approx 19$ Hz, CH_2, 2 H), 14.98 ($\upsilon_{1/2} \approx 40$ Hz, py-C*H*, 1 H), 16.95 ($\upsilon_{1/2} \approx 40$ Hz, py-C*H*, 1 H), 19.48 ($\upsilon_{1/2} \approx 60$ Hz, py-C*H*, 1 H), 21.80 ($\upsilon_{1/2} \approx 80$ Hz, py-C*H*, 1 H), 30.37 ($\upsilon_{1/2} \approx 187$ Hz,

py-C*H*, 1 H), 32.02 ($\upsilon_{1/2} \approx 234$ Hz, py-C*H*, 1 H), 47.34 ($\upsilon_{1/2} \approx 388$ Hz, C*H*, 1 H), 81.73 ($\upsilon_{1/2} \approx 1900$ Hz, py-C*H*, 1 H), 183.55 ($\upsilon_{1/2} \approx 3500$ Hz, py-C*H*, 1 H).

10. (dpma)FeOCHPh$_2$ (18-Fe). To a 50 mL round bottom flask charged with **15-Fe** (0.500 g, 1.21 mmol) and diphenylmethanol (0.222 g, 1.21 mmol) was vacuum transferred 35 mL Et_2O at -78 °C resulting in a red solution. The solution darkened to red-purple and was stirred at 23 °C for 3 h. The solution was concentrated, filtered, and washed with cold Et_2O yielding plum crystals of **18-Fe** (0.449 g, 85 %). ^{1}H NMR (C_6D_6, 400 MHz): δ 9.30 ($\upsilon_{1/2} \approx 53$ Hz, py-C*H*, 1 H), 11.20 ($\upsilon_{1/2} \approx 78$ Hz, py-C*H*, 1 H), 12.67 ($\upsilon_{1/2} \approx 219$ Hz, CH_2, 2 H), 13.81 ($\upsilon_{1/2} \approx 92$ Hz, ArC*H*, 2 H), 20.83 ($\upsilon_{1/2} \approx 107$ Hz, py-C*H*, 1 H), 24.28 ($\upsilon_{1/2} \approx 76$ Hz, ArC*H*, 2 H), 65.23 ($\upsilon_{1/2} \approx 800$ Hz, py-C*H*, 1 H), 132.81 ($\upsilon_{1/2} \approx 2190$ Hz, py-C*H*, 1 H).

11. (smif)FeOCHPh$_2$ (19-Fe). To a 25 mL round bottom flask charged with **[14-Fe]$_2$** (0.200 g, 0.24 mmol) and diphenylmethanol (0.089 g, 0.48 mmol) was vacuum transferred 15 mL THF at -78 °C resulting in an emerald green solution. After stirring at 23 °C for 2.5 d, volatiles were removed *in vacuo* from the dark kelly green solution. The solid was washed with pentane to remove excess diphenylmethanol before filtering and crystallizing **19-Fe** from Et_2O (0.125 g, 59 %). ^{1}H NMR (C_6D_6, 400 MHz): δ -29.46 ($\upsilon_{1/2} \approx 365$ Hz, Ar-C*H*, 4 H), -0.77 ($\upsilon_{1/2} \approx 61$ Hz, Ar-C*H*, 4 H), 1.49 ($\upsilon_{1/2} \approx 20$ Hz, C*H*,1 H), 3.40 ($\upsilon_{1/2} \approx 38$ Hz, Ar-C*H*, 2 H), 3.74 ($\upsilon_{1/2} \approx 30$ Hz, C*H*, 1 H), 35.55 ($\upsilon_{1/2} \approx 47$ Hz, py-C*H*, 1 H), 66.47 ($\upsilon_{1/2} \approx 73$ Hz, py-C*H*, 1 H), 125.50 ($\upsilon_{1/2} \approx 861$ Hz, py-C*H*, 1 H), 254.92 ($\upsilon_{1/2} \approx 554$ Hz, py-C*H*, 1 H).

12. (d$_4$-dpma)$_2$Fe (16-Fe-d$_4$). To a solution of Fe{N(SiMe$_3$)$_2$}$_2$(THF) (0.329 g, 0.73 mmol) in Et_2O (10 mL) at -78 °C was added Dd$_4$-dpma (0.300 g, 1.47 mmol) in 9 mL Et_2O via syringe under argon. The solution changed color from pale green to dark blue after 30 min at 23 °C and was stirred for 20 h. The volatiles were removed *in*

vacuo. The solid was taken up and filtered in Et_2O. The filtrates were concentrated, cooled to -78 °C, filtered, and resulting dark blue crystals, **16-Fe-d_4**, were washed with cold Et_2O (0.220 g, 66 %).

13. (^{o}Mesmif)FeN(TMS)$_2$ (20-Fe) (in solution) and **[{(Me$_3$Si)$_2$N}Fe]$_2$(μ-N$^{am}_2$,N$^{py}_4$-2,5-bis(6-methylpyridin-2-yl)-3,6-bis(pyridin-2-yl)piperazyl) ([20-Fe]$_2$)** (solid state). To a stirring solution of Fe{N(SiMe$_3$)$_2$}$_2$(THF) (0.500 g, 1.11 mmol) in 10 mL Et_2O was slowly added a solution of **^{o}MesmifH** (0.235 g, 1.11 mmol) in Et_2O (8 mL) at 23 °C. The reaction mixture became emerald-teal green. The reaction was degassed, warmed to 23 °C, and stirred for 20 h while yellow-orange crystals precipitated from solution. The suspension was concentrated, and yellow-orange crystals were isolated by filtration to yield **[20-Fe]$_2$** (0.225, 47 %). ^{1}H NMR (C_6D_6, 400 MHz): δ -21.82 ($\upsilon_{1/2}$ ≈ 38 Hz, C*H*, 1 H), -26.10 ($\upsilon_{1/2}$ ≈ 38 Hz, C*H*, 1 H), -13.23 ($\upsilon_{1/2}$ ≈ 413 Hz, CH_3, 3 H), 0.75 ($\upsilon_{1/2}$ ≈ 300 Hz, Si(CH_3)$_3$, 18 H), 14.26 ($\upsilon_{1/2}$ ≈ 131 Hz, py-C*H*, 1 H), 40.95 ($\upsilon_{1/2}$ ≈ 23 Hz, py-C*H*, 1 H), 46.13 ($\upsilon_{1/2}$ ≈ 374 Hz, py-C*H*, 1 H), 47.74 ($\upsilon_{1/2}$ ≈ 23 Hz, py-C*H*, 1 H), 59.84 ($\upsilon_{1/2}$ ≈ 96 Hz, py-C*H*, 1 H), 64.39 ($\upsilon_{1/2}$ ≈ 96 Hz, py-C*H*, 1 H), 252.29 ($\upsilon_{1/2}$ ≈ 1000 Hz, py-C*H*, 1 H).

14. (^{o}Me$_2$smif)FeN(SiMe$_3$)$_2$ (21-Fe). To a stirring solution of Fe{N(SiMe$_3$)$_2$}$_2$(THF) (0.398 g, 0.89 mmol) in 8 mL Et_2O was slowly added a solution of **^{o}Me$_2$smifH** (0.200 g, 0.89 mmol) in Et_2O (8 mL) at 23 °C. The reaction mixture turned teal blue, was degassed, warmed to 23 °C, and stirred for 12 h while gold crystals precipitated from solution. The suspension was concentrated, and gold crystals were isolated by filtration to yield 0.152 g **21-Fe** (39 %). ^{1}H NMR (C_6D_6, 400 MHz): δ -25.33 ($\upsilon_{1/2}$ ≈ 812 Hz, CH_3, 3 H), -2.12 ($\upsilon_{1/2}$ ≈ 53 Hz, C*H*, 1 H), 22.30 ($\upsilon_{1/2}$ ≈ 507 Hz, Si(CH_3)$_3$, 9 H), 32.55 ($\upsilon_{1/2}$ ≈ 154 Hz, py-C*H*, 1 H), 37.80 ($\upsilon_{1/2}$ ≈ 57 Hz, py-C*H*, 1 H), 150.52 ($\upsilon_{1/2}$ ≈ 974 Hz, py-C*H*, 1 H). μ_{eff} (SQUID, 293 K) = 5.1 μ_B.

15. (^{o}Mesmif)$_2$Fe (22-Fe). To a solution of Fe{N(SiMe$_3$)$_2$}$_2$(THF) (0.500 g, 1.11 mmol) in 15 mL Et$_2$O was slowly added a solution of **^{o}MesmifH** (0.471 g, 2.22 mmol) in Et$_2$O (10 mL) at 23 °C. The solution immediately changed from pale green to a brilliant blue. The reaction was degassed and warmed to 23 °C. Purple-mauve crystals began to precipitate from the deep blue solution while stirring for 20 h. The volatiles were removed, and the solid was triturated and filtered in Et$_2$O to yield purple-mauve crystals of **22-Fe** (0.311 g, 59 %). ^{1}H NMR (C$_6$D$_6$, 400 MHz): δ 2.04 (s, py^{Me}-C*H*$_3$, 3 H), 6.44 (t, py^{Me}-C^4*H*, 1 H, J = 6.8 Hz), 6.51 (t, py-C^5*H*, 1 H, J = 6.8 Hz), 6.83 (d, py^{Me}-C^5*H*, 1 H, J = 6.8 Hz), 6.97 (br s, py^{Me}-C^3*H*, py-C^4*H*, 2 H), 7.59 (d, py-C^6*H*, 1 H, J = 6 Hz), 11.43 ($\upsilon_{1/2} \approx$ 29 Hz, C*H*, 1 H), 12.04 ($\upsilon_{1/2} \approx$ 46 Hz, C*H*, 1 H), 13.31 ($\upsilon_{1/2} \approx$ 52 Hz, py-C^3*H*, 1 H). ^{13}C{^{1}H} NMR (C$_6$D$_6$, 100 MHz): δ 25.93 (py^{Me}-*C*H$_3$), 100.75 (py^{Me}-*C*^{3}H), 103.26 (py^{Me}-*C*^{5}H), 107.54 (py-*C*^{3}H), 112.22 (py-*C*^{5}H), 114.11 (py^{Me}-*C*^{4}H), 119.50 (*C*H), 123.66 (py-*C*^{4}H), 132.93 (*C*H), 136.73 (py-*C*^{6}H), 149.10 (py^{Me}-*C*^{6}H), 160.93 (py^{Me}-*C*^{2}), 170.83 (py-*C*^{2}). UV-vis (benzene) = 425 nm (ε ~ 42,000 M^{-1} cm^{-1}), 533 nm (ε ~ 30,000 M^{-1} cm^{-1}), 576 nm (sh, ε ~ 22,000 M^{-1} cm^{-1}). Mössbauer parameters (80 K): δ = 0.38 mms^{-1}, ΔE_Q = 0.99 mms^{-1}, Γ_{FWHM} = 0.31 mms^{-1}. (200 K): δ = 0.34 mms^{-1}, ΔE_Q = 1.00 mms^{-1}, Γ_{FWHM} = 0.28 mms^{-1}. Anal. Calcd. H$_{24}$C$_{26}$N$_6$Fe: C, 65.56; H, 5.08; N, 17.64. Found: C, 65.58; H, 5.25; N, 17.17. μ_{eff} (Gouy, 296 K) = 1.53 μ_B. μ_{eff} (SQUID, 5K) = 0.5 μ_B to μ_{eff} (SQUID, 293 K) = 1.2 μ_B.

16. (^{o}Me$_2$smif)$_2$Fe (23-Fe). To a solution of Fe{N(SiMe$_3$)$_2$}$_2$(THF) (0.747 g, 1.66 mmol) in 12 mL Et$_2$O was slowly added a solution of **^{o}Me$_2$smifH** (0.750 g, 3.33 mmol) in Et$_2$O (10 mL) at 23 °C. The solution immediately changed from pale green to deep forest green. The reaction was degassed and warmed to 23 °C. Gold-bronze crystals began to precipitate from the deep cobalt blue solution after stirring for 30 min. The reaction mixture was stirred for an addition 15.5 h. The volatiles were

removed, and the solid was triturated and filtered in Et_2O to yield gold-bronze crystals of **23-Fe** (0.712 g, 85 %). ^{1}H NMR (C_6D_6, 400 MHz): δ -9.64 ($\upsilon_{1/2} \approx 110$ Hz, C*H*, 1 H), 7.44 ($\upsilon_{1/2} \approx 17$ Hz, CH_3, 3 H), 36.73 ($\upsilon_{1/2} \approx 20$ Hz, py-C*H*, 1 H), 52.87 ($\upsilon_{1/2} \approx 15$ Hz, py-C*H*, 1 H), 167.44 ($\upsilon_{1/2} \approx 53$ Hz, py-C*H*, 1 H). UV-vis (benzene) = 399 nm (ε ~ 29,000 M^{-1} cm^{-1}), 598 nm (ε ~ 58,000 M^{-1} cm^{-1}). Mössbauer parameters (15 K): $\delta_{major\ (81\ \%)}$ = 1.05 mms^{-1}, ΔE_Q = 2.24 mms^{-1}, Γ_{FWHM} = 0.36 mms^{-1}; $\delta_{minor\ (19\ \%)}$ = 1.01 mms^{-1}, ΔE_Q = 0.77 mms^{-1}, Γ_{FWHM} = 0.49 mms^{-1}. (80 K): $\delta_{major\ (82\ \%)}$ = 1.04 mms^{-1}, ΔE_Q = 2.18 mms^{-1}, Γ_{FWHM} = 0.39 mms^{-1}; $\delta_{minor\ (18\ \%)}$ = 1.02 mms^{-1}, ΔE_Q = 0.65 mms^{-1}, Γ_{FWHM} = 0.50 mms^{-1}. Anal. Calcd. $H_{28}C_{28}N_6Fe$: C, 66.67; H, 5.60; N, 16.66. Found: C, 66.54; H, 5.47; N, 16.19. μ_{eff} (Gouy, 295 K) = 5.0 μ_B. μ_{eff} (SQUID, 293 K) = 5.5 μ_B.

17. (^{o}Mesmif)(smif)Fe (24-Fe). To a solution of **20-Fe** (0.050 g, mmol) in 2 mL of Et_2O was slowly added a solution of **smifH** (0.023 g, mmol) in Et_2O (2 mL) resulting in a deep teal solution. The reaction was degassed. Metallic-purple crystals began to precipitate from solution after stirring at 23 °C for 2.5 h, and the reaction was stirred for an addition 13.5 h. Volatiles were removed *in vacuo* from the red-brown suspension. ^{1}H NMR spectroscopy on the solid showed a 1 : 2.8 : 2 ratio of **6-Fe**, **24-Fe**, and **22-Fe**, respectively. ^{1}H NMR (C_6D_6, 400 MHz) for **24-Fe**: δ 2.83(s, py^{oMe}-CH_3, 3 H), 5.56 (d, py$^{oMe\text{-}py}$-C^3*H*, 1 H, J = 7.0 Hz), 5.75 (t, py-C^5*H*, 2 H, J = 6.4 Hz), 5.77 (t, py^{oMe}-C^5*H*, 1 H, J = 6.3 Hz), 6.08 (d, py$^{oMe\text{-}py}$-C^3*H*, 1 H, J = 8.0 Hz), 6.12 (t, py$^{oMe\text{-}py}$-C^4*H*, 1 H, J = 5.4 Hz), 6.14 (d, py^{smif}-C^3*H*, 2 H, J = 8.1 Hz), 6.34 (t, py^{smif}-C^4*H*, 1 H, J = 7.6 Hz), 6.44 (t, py$^{oMe\text{-}py}$-C^5*H*, py^{oMe}-C^4*H*, 2 H, J = 6.7 Hz), 7.17 (d, py$^{oMe\text{-}py}$-C^6*H*, 1 H, J = 6.2 Hz), 7.51 (s, smif-C*H*, 2 H), 7.71 (s, ^{o}Mesmif-C*H*, 1 H), 7.76 (d, py^{smif}-C^6*H*, 2 H, J = 5.5 Hz), 7.90 (s, ^{o}Mesmif-C*H*, 1 H). ^{13}C{^{1}H} NMR (C_6D_6, 100 MHz): δ 22.40 (py^{oMe}-*C*H$_3$), 110.80 (py^{oMe}-*C*^{3}H), 112.08 (py$^{oMe\text{-}py}$-*C*^{5}H), 112.26 (smif-*C*H), 114.62(py^{oMe}-*C*^{4}H), 115.94 (py^{smif}-*C*^{3}H), 116.49 (py^{oMe}-*C*^{5}H),

119.04 (py^{smif}-*C*^{5}H), 119.93 (^{o}Mesmif-*C*H), 120.78 (py$^{oMe\text{-}py}$-*C*^{4}H), 132.93 (^{o}Mesmif-*C*H), 134.86 (py^{smif}-*C*^{4}H), 135.52 (py^{oMe}-*C*^{2}), 136.73 (py$^{oMe\text{-}py}$-*C*^{6}H), 151.07 (py^{oMe}-*C*^{6}), 151.81 (py^{smif}-*C*^{6}H), 152.42 (py$^{oMe\text{-}py}$-*C*^{2}), 166.48 (py^{smif}-*C*^{2}).

18. (smif)(^{o}Me$_2$smif)Fe (25-Fe). To a solution of **[14-Fe]$_2$** (0.050 g, mmol) in 2 mL of Et_2O was slowly added a solution of **^{o}Me$_2$smifH** (0.027 g, mmol) in Et_2O (2 mL) resulting in a deep blue solution. The reaction was degassed. A mauve solid began to precipitate from solution after stirring at 23 °C for 2 h, and the reaction was stirred for an addition 4 h. Volatiles were removed *in vacuo* from the dark blue suspension yielding a mauve solid. ^{1}H NMR spectroscopy on the solid showed a 1:8:2 ratio of **6-Fe**, **25-Fe**, and **23-Fe**, respectively. ^{1}H NMR (C_6D_6, 400 MHz) for **25-Fe**: 4.41 ($\upsilon_{1/2} \approx 51$ Hz, C*H*$_3$, 3 H), 6.47 ($\upsilon_{1/2} \approx 16$ Hz, py-C*H*, 1 H), 7.28 ($\upsilon_{1/2} \approx 16$ Hz, py-C*H*, 1 H), 18.91 ($\upsilon_{1/2} \approx 24$ Hz, py-C*H*, 1 H), 19.70 ($\upsilon_{1/2} \approx 26$ Hz, py-C*H*, 1 H), 20.35 ($\upsilon_{1/2} \approx 28$ Hz, py-C*H*, 1 H), 23.06 ($\upsilon_{1/2} \approx 34$ Hz, py-C*H*, 1 H), 50.88 ($\upsilon_{1/2} \approx 243$ Hz, py-C*H*, 1 H), 53.78 ($\upsilon_{1/2} \approx 154$ Hz, py-C*H*, 1 H), 79.58 ($\upsilon_{1/2} \approx 290$ Hz, py-C*H*, 1 H).

19. (^{o}Mesmif)(^{o}Me$_2$smif)Fe (26-Fe). To a solution of **20-Fe** (0.050 g, mmol) in 2 mL of Et_2O was slowly added a solution of **^{o}Me$_2$smifH** (0.026 g, mmol) in Et_2O (2 mL) resulting in a deep teal-blue solution. The reaction was degassed. Metallic gold crystals precipitated from solution after stirring at 23 °C for 2.5 h, and the reaction was stirred for an addition 13.5 h. Volatiles were removed *in vacuo* from the deep blue suspension. ^{1}H NMR spectroscopy on the solid showed a 2:4:1 ratio of **22-Fe**, **26-Fe**, and **23-Fe**, respectively. ^{1}H NMR (C_6D_6, 400 MHz) for **26-Fe**: -50.83 ($\upsilon_{1/2} \approx 210$ Hz, C*H*$_3$, 3 H), -7.43 ($\upsilon_{1/2} \approx 101$ Hz, py-C*H*, 2 H), -1.55 ($\upsilon_{1/2} \approx 75$ Hz, py-C*H*, 1 H), 3.84 ($\upsilon_{1/2} \approx 16$ Hz, py-C*H*, 1 H), 4.39 ($\upsilon_{1/2} \approx 54$ Hz, py-C*H*, 1 H), 4.61 ($\upsilon_{1/2} \approx 20$ Hz, py-C*H*, 1 H), 7.63 ($\upsilon_{1/2} \approx 93$ Hz, py-C*H*, 1 H), 8.28 ($\upsilon_{1/2} \approx 103$ Hz, py-C*H*, 1 H), 8.87 ($\upsilon_{1/2} \approx 64$ Hz, py-C*H*, 1 H), 9.97 ($\upsilon_{1/2} \approx 44$ Hz, py-C*H*, 2 H), 10.72 ($\upsilon_{1/2} \approx 175$ Hz, C*H*$_3$, 6

H), 26.71 ($\upsilon_{1/2} \approx 58$ Hz, py-C*H*, 1 H), 43.97 ($\upsilon_{1/2} \approx 45$ Hz, py-C*H*, 3 H), 52.90 ($\upsilon_{1/2} \approx$ 49 Hz, py-C*H*, 1 H), 55.24 ($\upsilon_{1/2} \approx 53$ Hz, py-C*H*, 4 H), 56.72 ($\upsilon_{1/2} \approx 68$ Hz, py-C*H*, 1 H), 157.77 ($\upsilon_{1/2} \approx 102$ Hz, py-C*H*, 2 H), 166.94 ($\upsilon_{1/2} \approx 94$ Hz, py-C*H*, 1 H).

20. (^{b}Me$_2$smif)$_2$Fe (27-Fe). To a 50 mL round bottom flask charged with Fe{N(SiMe$_3$)$_2$}$_2$(THF) (0.996 g, 2.22 mmol) and **^{b}Me$_2$smifH** (1.000 g, 4.44 mmol) was vacuum transferred 25 mL THF at -78 °C. The reaction mixture became dark green and was stirred at 23 °C for 2 d. The volatiles were removed *in vacuo*. The solid was first triturated with pentane (2 x 15 mL) and then Et$_2$O prior to filtering and washing with cold Et$_2$O to yield a mossy green solid **27-Fe** (0.802 g, 72 %). ^{1}H NMR (C$_6$D$_6$, 400 MHz): δ 2.54 (s, C*H*$_3$, 3 H), 5.87 (t, py-C^4*H*, 1 H, J = 8 Hz), 6.03 (d, py-C^3*H*, 1 H, J = 8.4 Hz), 6.49 (t, py-C^5*H*, 1 H, J = 4 Hz), 7.80 (d, py-C^6*H*, 1 H, J = 5.2 Hz). ^{13}C{^{1}H} NMR (C$_6$D$_6$, 100 MHz): δ 17.55 (*C*H$_3$), 111.83 (*C*CH$_3$), 115.80 (py-*C*^{5}H), 119.79 (py-*C*^{3}H), 134.70 (py-*C*^{4}H), 152.12 (py-*C*^{6}H), 165.98 (py-*C*^{2}).

21. (Me$_4$smif)FeN(SiMe$_3$)$_2$ (28-Fe) (in solution) and **[(μ-C,N^{am},N^{py})$_2$-2-(6-methylpyridin-2-yl)-2-(1-(6-methylpyridin-2-yl)ethylamino)ethan-1-ido)Fe{N(SiMe$_3$)$_2$}]$_2$ ([28-Fe]$_2$).** A small tube fitted to a 180° needle valve was charged with Fe{N(SiMe$_3$)$_2$}$_2$(THF) (0.105 g, 0.23 mmol) and Me$_4$smifH (0.025 g, 0.30 mmol). A bell pepper green solution appeared immediately upon addition of benzene. The reaction was degassed, sealed under vacuum, and allowed to sit for 2 d at 23 °C. The tube was opened, and benzene was decanted. Red-orange crystals of **[28-Fe]$_2$** were washed with Et$_2$O. (0.069 g, 63 %). ^{1}H NMR (C$_6$D$_6$, 400 MHz): δ -50.62 ($\upsilon_{1/2} \approx 370$ Hz, C*H*$_3$, 3 H), 18.23 ($\upsilon_{1/2} \approx 600$ Hz, Si(C*H*$_3$)$_3$, 9 H), 21.94 ($\upsilon_{1/2} \approx$ 350 Hz, py-C*H*, 1 H), 48.25 ($\upsilon_{1/2} \approx 44$ Hz, py-C*H*, 1 H), 57.31 ($\upsilon_{1/2} \approx 310$ Hz, py-C*H*, 1 H), 69.57 ($\upsilon_{1/2} \approx 440$ Hz, C*H*$_3$, 3 H). Anal. Calcd. H$_{22}$C$_{36}$N$_4$Si$_2$Fe: C, 56.39; H, 7.74; N, 11.96. Found: C, 56.62; H, 7.84; N, 12.04. μ_{eff} (SQUID, 293K) = 4.3 μ_B.

22. [(2,5-di(pyridin-2-yl)-3,4-di-(*p*-tolyl-2,5-dihydropyrrol-1-ide))FeN(TMS)$_2$]$_2$ (29-Fe). To a small glass bomb reactor charged with [(smif)FeN(TMS)$_2$]$_2$ (0.600 g, 0.73 mmol) and di(*p*-tolyl)acetylene (0.300 g, 1.45 mmol) was added 12 mL benzene generating a dark emerald green solution that was degassed. The bomb was placed in a 50 °C oil bath for 3 d. Volatiles were removed *in vacuo*. Any unreacted **14-Fe** was washed away in pentane. The filter cake was washed with Et_2O, and the filtrates were concentrated. Cooling the solution to -78 °C yielded red crystals (0.175 g, 19 %) of **29-Fe** that were filtered, and washed with cold Et_2O. ^{1}H NMR (C_6D_6, 400 MHz): δ 7.97 ($\upsilon_{1/2}$ ≈ 105 Hz, Si(C*H*$_3$)$_3$, 9 H), 17.59 ($\upsilon_{1/2}$ ≈ 40 Hz, py-C*H*/ArC*H*, 1 H), 27.39 ($\upsilon_{1/2}$ ≈ 230 Hz, C*H*$_3$, 3 H), 31.89 ($\upsilon_{1/2}$ ≈ 77 Hz, py-C*H*/ArC*H*, 1 H), 35.96 ($\upsilon_{1/2}$ ≈ 52 Hz, py-C*H*/ArC*H*, 1 H), 98.84 ($\upsilon_{1/2}$ ≈ 1100 Hz, py-C*H*/ArC*H*, 1 H), 194.18 ($\upsilon_{1/2}$ ≈ 1100 Hz, py-C*H*/ArC*H*, 1 H). Anal. Calcd. $H_{84}C_{68}N_8Si_4Fe_2$: C, 66.00; H, 6.84; N, 9.05. Found: C, 67.40; H, 6.45; N, 7.59. μ_{eff} (SQUID, 293 K) = 5.3 μ_B.

23. (2,6-^{i}Pr$_2$PhNCOsmif)$_2$Fe (30-Fe-DIPP). To a 25 mL round bottom flask charged with **6-Fe** (0.500 g, 1.12 mmol) was added 20 mL C_6H_6. The flask was cooled to -78 °C and 2,6-diisopropylphenylisocyanate (0.48 mL, 2.24 mmol) was added via syringe under argon. The reaction was degassed, and slowly warmed to 23 °C as the solution turned deep red-orange. The reaction stirred at 23 °C for 17 h. Volatiles were removed *in vacuo*, and the reaction mixture was triturated with pentane (3 x 5 mL). After filtering and washing with pentane, **30-Fe-DIPP** was isolated as a dark red solid (0.719 g, 75 %). ^{1}H NMR (C_6D_6, 400 MHz): δ 1.38 (s, CH(C*H*$_3$)$_2$, 12 H), 3.56 (sept, C*H*(CH$_3$)$_2$, 2 H, J = 6.9 Hz), 5.84 (t, py-C^5*H*, py'-C^5*H*, 2 H, J = 5.3 Hz), 6.33 (d, Ar-C^3*H*, 2 H, J = 3.8 Hz), 6.54 (t, Ar-C^4*H*, 1 H, J = 7.3 Hz), 6.98 (s, N*H*, 1 H), 7.31 (m, py-C^3*H*, py-C^4*H*, py'-C^4*H*, 3 H), 7.44 (d, py'-C^3*H*, 1 H, J = 8.4 Hz), 7.77 (d, py-C^6*H*,

1 H, J = 5.4 Hz), 7.99 (d, py'-C^6*H*, 1 H, J = 5.2 Hz), 10.15 (s, C*H*, 1 H). ^{13}C{^{1}H} NMR (C_6D_6, 100 MHz): δ 24.36 (CH(*C*H$_3$)$_2$), 24.38 (CH(*C*H$_3$)$_2$), 30.07 (*C*H(CH$_3$)$_2$), 114.11 (py'-*C*^{3}H), 117.00 (py'-*C*^{5}H), 117.98 (py-*C*^{3}H), 118.34 (py-*C*^{5}H), 119.89 (*C*(C=O)), 124.07 (*C*H), 127.92 (Ar-*C*^{3}H), 133.02 (Ar-*C*^{4}H), 134.18 (py-*C*^{4}H), 135.24 (py'-*C*^{4}H), 136.08 (Ar-*C*^{1}), 145.41 (Ar-*C*^{2}), 151.42 (py-*C*^{6}H), 151.88 (py'-*C*^{6}H), 163.97 (py'-*C*^{2}), 164.55 (*C*=O), 165.51 (py-*C*^{2}). UV-vis (benzene) = 381 nm (ε ~ 33,000 M^{-1} cm^{-1}), 427 nm (ε ~ 46,000 M^{-1} cm^{-1}), 525 nm (ε ~ 21,000 M^{-1} cm^{-1}), 638 nm (ε ~ 7,000 M^{-1} cm^{-1}). Anal. Calcd. $H_{54}C_{50}N_8O_2Fe$: C, 70.25; H, 6.37; N, 13.11. Found: C, 70.25; H, 6.37; N, 13.11.

24. (^{t}BuNCOsmif)$_2$Fe (30-Fe-^{t}Bu). A) To a small glass bomb reactor charged with **6-Fe** (0.150 g, 0.33 mmol) was added 10 mL C_6H_6. The bomb was cooled to -78 °C and *tert*-butylisocyanate (76 μL, 0.66 mmol) was added via GC syringe under argon. The reaction was degassed and slowly warmed to 23 °C. The solution turned deep red-orange after stirring at 23 °C for 18 h. The reaction was stirred at 23 °C for 10 d. Volatiles were removed *in vacuo*, and the reaction mixture was triturated with pentane (3 x 5 mL). After filtering and washing with pentane, **30-Fe-^{t}Bu** was isolated as a dark red solid (0.102 g, 47 %). **B)** To a 25 mL round bottom flask charged with $FeBr_2(THF)_2$ (0.141 g, 0.39 mmol) and **31-Na** (0.250 g, 0.79 mmol) was vacuum transferred 20 mL THF at -78 °C. The solution turned red-orange upon warming to 23 °C and was stirred for 18 h. Volatiles were removed *in vacuo*, and the resulting solid was triturated with Et_2O prior to filtering in toluene. A dark red microcrystalline solid, **30-Fe-^{t}Bu**, was obtained (0.154 g, 61 %). ^{1}H NMR (C_6D_6, 500 MHz): δ 1.53 (s, C(C*H*$_3$)$_3$, 9 H), 5.37 (s, N*H*, 1 H), 5.71 (t, py-C^5*H*, 1 H, J = 6.2 Hz), 5.76 (t, py'-C^5*H*, 1 H, J = 6.3 Hz), 6.32 (t, py-C^4*H*, 1 H, J = 7.3 Hz), 6.36 (d, py-C^3*H*, 1 H, J = 7.9 Hz), 6.48 (t, py'-C^4*H*, 1 H, J = 6.3 Hz), 7.03 (d, py'-C^3*H*, 1 H, J = 8.5 Hz), 7.75 (d, py-C^6*H*,

1 H, J = 5.3 Hz), 7.98 (d, py'-C^6*H*, 1 H, J = 5.1 Hz), 9.91 (s, C*H*, 1 H). ^{13}C{^{1}H} NMR (C_6D_6, 125 MHz): δ 30.08 (C(*C*H$_3$)$_3$), 51.35 (*C*(CH$_3$)$_3$), 113.33 (py'-*C*^{3}H), 116.31 (py'-*C*^{5}H), 116.79 (py-*C*^{3}H), 119.27 (py-*C*^{5}H), 119.95 (*C*(C=O)), 130.04 (*C*H), 135.01 (py-*C*^{4}H), 135.42 (py'-*C*^{4}H), 151.70 (py-*C*^{6}H), 152.06 (py'-*C*^{6}H), 164.40 (py'-*C*^{2}), 164.47 (*C*=O), 165.62 (py-*C*^{2}). UV-vis (benzene) = 383 nm (ε ~ 28,000 M^{-1} cm^{-1}), 431 nm (ε ~ 42,000 M^{-1} cm^{-1}), 534 nm (ε ~ 19,000 M^{-1} cm^{-1}), 644 nm (ε ~ 6,000 M^{-1} cm^{-1}). Anal. Calcd. $H_{38}C_{34}N_8O_2Fe$: C, 63.16; H, 5.92; N, 17.33. Found: C, 63.16; H, 5.92; N, 17.33.

25. Na(^{t}BuNCOsmif) (31-Na). To a solution of **5-Na** (0.300 g, 1.37 mmol) in 20 mL THF was added *tert*-butylisocyanate (156 μL, 1.37 mmol) via syringe at -78 °C under argon. The solution was warmed to 23 °C and turned red. Volatiles were removed *in vacuo* after 2 h, and the resulting film was triturated with Et_2O to remove residual THF. **31-Na** was isolated as a metallic green solid (0.396 g, 91 %). ^{1}H NMR (C_6D_6, 500 MHz): δ 1.39 (s, C(C*H*$_3$)$_3$, 9 H), 6.33 (t, py-C^5*H*, 1 H, J = 5.8 Hz), 6.43 (t, py'-C^5*H*, 1 H, J = 5.8 Hz), 6.55 (d, py-C^3*H*, 1 H, J = 8.1 Hz), 6.94 (t, py-C^4*H*, 1 H, J = 7.0 Hz), 7.17 (t, py'-C^4*H*, 1 H, J = 7.7 Hz), 7.81 (d, py'-C^3*H*, 1 H, J = 8.1 Hz), 8.18 (s, N*H*, 1 H), 8.20 (d, py-C^6*H*, 1 H, J = 5.4 Hz), 8.44 (d, py'-C^6*H*, 1 H, J = 3.9 Hz), 10.58 (s, C*H*, 1 H). ^{13}C{^{1}H} NMR (C_6D_6, 125 MHz): δ 30.58 (C(*C*H$_3$)$_3$), 50.26 (*C*(CH$_3$)$_3$), 111.02 (py'-*C*^{3}H), 116.24 (py'-*C*^{5}H), 116.94 (py-*C*^{3}H), 118.74 (py-*C*^{5}H), 121.24 (*C*(C=O)), 123.58 (*C*H), 135.18 (py-*C*^{4}H), 136.52 (py'-*C*^{4}H), 148.28 (py-*C*^{6}H), 150.40 (py'-*C*^{6}H), 157.79 (*C*=O), 160.47 (py'-*C*^{2}), 169.93 (py-*C*^{2}).

Magnetic Susceptibility Measurements. Magnetic susceptibility measurements of crystalline powdered samples (10-30 mg) were performed on a Quantum Design MPMS-5 SQUID magnetometer at 10 kOe between 5 and 300 K for all samples. All sample preparations and manipulations were performed under an inert

atmosphere to due to the air sensitivity of the samples. The samples were either measured in a flame sealed NMR tube or a custom machine sealed Teflon capsule. The diamagnetic contribution from the sample container was subtracted from the experimental data. Pascal's constants[45] were used to subtract diamagnetic contributions, yielding paramagnetic susceptibilities.

Mössbauer Spectroscopy. ^{57}Fe Mössbauer spectra were recorded on a SEE Co. Mössbauer spectrometer (MS4) at 80 K in constant acceleration mode. ^{57}Co/Rh was used as the radiation source. WMOSS software was used for the quantitative evaluation of the spectral parameters (least squares fitting to Lorentizian peaks). The minimum experimental line widths were 0.23 mm s^{-1}. The temperature of the sample was controlled by a Janis Research Co. CCS-850 He/N_2 cryostat within an accuracy of ±0.3 K. Isomer shifts were determined relative to α-iron at 298 K.

Equilibrium study. **14-Fe ≡ [14-Fe]$_2$.** A series of five NMR tubes were charged with known concentrations of (smif)FeN(SiMe$_3$)$_2$. The solutions (3.4 x 10^{-3} to 2.4 x 10^{-2} M) of (smif)FeN(SiMe$_3$)$_2$ in THF-d_8 were prepared in a 5 mL volumetric flask, and ^{1}H NMR spectra were obtained at ambient temperature. The chemical shift associated with the smif 'backbone' CH was monitored as it exhibited the largest change as concentrations varied. The equilibrium constant, ~ 4 x 10^{-4} M^{-1}, was fit using the least squares method developed by Tan for determining the NMR monomer shift and equilibrium constant for self-associating systems.[28]

Hydrogenation & Deuteration Studies. Flame-dried NMR tubes, sealed to 14/20 ground glass joints, were charged with **16-Fe** (0.015 g, 0.033 mmol), two equivalents (0.066 mmol) of the appropriate organic substrate, and 0.5 mL C_6D_6. The tube was fitted with a 180° needle valve and freeze-pump-thaw degassed 3 times before sealing. Reaction progress was monitored via ^{1}H NMR spectroscopy.

Deuteration studies were performed in flame-dried J-Young NMR tubes. Several deuteration experiments were performed in flame-dried and silylated J-Young tubes. Results are summarized in Scheme 4.5 and Table 4.5.

Cyclotrimerization Studies. Flame dried NMR tubes, sealed to 14/20 ground glass joints, were charged with 0.5 mL solutions of known concentrations of an iron compound in the glovebox. The tubes were attached to a calibrated gas bulb and degassed on the vacuum line via freeze-pump-thaw cycle. After condensing 2-butyne at 77 K, the tubes were sealed with a torch. Reaction progress was monitored via ^{1}H NMR spectroscopy by observing the disappearance of 2-butyne (δ 1.50 ppm) and appearance of hexamethylbenzene (δ 2.13 ppm). Upon completion, the tube was opened in the glovebox and contents were transferred into a J Young tube containing 0.010 g ferrocene. A ^{1}H NMR spectrum was obtained, and integrations permitted quantification of hexamethylbenzene produced, turnover number, and turnover frequency. The C_6D_6 stock solutions (4.5×10^{-3} to 1.3×10^{-2} M for $Fe\{N(TMS)_2\}(THF)$ and 4.8×10^{-3} to 1.5×10^{-2} M for **14-Fe**) were prepared using 2 mL or 5 mL volumetric flasks.

Single Crystal X-Ray Diffraction Studies. Upon isolation, the crystals were covered in polyisobutenes and placed under a 173 K N_2 stream on the goniometer head of a Siemens P4 SMART CCD area detector (graphite-monochromated MoK_α radiation, $\lambda = 0.71073$ Å). The structures were solved by direct methods (SHELXS). All non-hydrogen atoms were refined anisotropically unless stated, and hydrogen atoms were treated as idealized contributions (Riding model).

26. [14-Fe]$_2$. An orange parallelpiped crystal (0.40 x 0.20 x 0.15 mm) was obtained after recrystallization from pentane at 80 °C. A total of 32,284 reflections were collected with 7,293 determined to be symmetry independent ($R_{int} = 0.0488$), and

5,519 were greater than 2σ(I). A semi-empirical absorption correction from equivalents was applied, and the refinement utilized $w^{-1} = \sigma^2(F_o^2) + (0.0511p)^2 + 0.0000p$, where $p = ((F_o^2 + 2F_c^2)/3)$.

27. 16-Fe. A dark blue-metallic purple plate (0.60 x 0.15 x 0.05 mm) was obtained from a mixture of benzene and pentane (1:1) at 23 °C. A total of 37,723 reflections were collected with 7,419 determined to be symmetry independent (R_{int} = 0.0594), and 6,031 were greater than 2σ(I). A semi-empirical absorption correction from equivalents was applied, and the refinement utilized $w^{-1} = \sigma^2(F_o^2) + (0.0307p)^2 + 0.4679p$, where $p = ((F_o^2 + 2F_c^2)/3)$.

28. 28-Fe. A red needle (0.60 x 0.10 x 0.03 mm) was obtained from benzene at 23 °C. A total of 20,055 reflections were collected with 4,095 determined to be symmetry independent (R_{int} = 0.0609), and 3,085 were greater than 2σ(I). A semi-empirical absorption correction from equivalents was applied, and the refinement utilized $w^{-1} = \sigma^2(F_o^2) + (0.0368p)^2 + 0.3358p$, where $p = ((F_o^2 + 2F_c^2)/3)$.

29. (29-Fe). A red plate (0.60 x 0.30 x 0.05 mm) was obtained from ether at 23 °C. A total of 69,998 reflections were collected with 15,480 determined to be symmetry independent (R_{int} = 0.0467), and 10,139 were greater than 2σ(I). A semi-empirical absorption correction from equivalents was applied, and the refinement utilized $w^{-1} = \sigma^2(F_o^2) + (0.0606p)^2 + 0.0000p$, where $p = ((F_o^2 + 2F_c^2)/3)$.

30. (30-Fe-DIPP). A dark red-black needle (0.45 x 0.10 x 0.03 mm) was obtained from a mixture of tetrahydrofuran and pentane at 23 °C. A total of 57,325 reflections were collected with 5,564 determined to be symmetry independent (R_{int} = 0.1560), and 2,984 were greater than 2σ(I). A semi-empirical absorption correction from equivalents was applied, and the refinement utilized $w^{-1} = \sigma^2(F_o^2) + (0.0911p)^2 + 0.0000p$, where $p = ((F_o^2 + 2F_c^2)/3)$.

REFERENCES

1 Louie, J.; Hartwig, J. F. *Tetrahedron Lett.* **1995**, *36*, 3609-3612.

2 Guram, A. S.; Rennels, R. A.; Buchwald, S. L. *Angew. Chem. Int. Ed. Engl.* **1995**, *34*, 1348-1350.

3 Christensen, H.; Kiil, S.; Dam-Johansen, K.; Nielsen, O.; Sommer, M. B. *Org. Process Res. Dev.* **2006**, *10*, 762-769.

4 Pearson, W. H.; Lian, B. W. *Angew. Chem. Int. Ed.* **1998**, *37*, 1724-1726.

5 Kauffmann, T. *Angew. Chem., Int. Ed. Engl.* **1974**, *13*, 627-638.

6 Pearson, W. H.; Stoy, P. *Synlett* **2003**, *7*, 903-921.

7 Kauffmann, T.; Berg, H.; Koppelmann, E. *Angew. Chem. Int. Ed. Engl.* **1970**, *9*, 380-381.

8 Kauffmann, T.; Koppelmann, E. *Angew. Chem. Int. Ed. Engl.* **1972**, *11*, 290-293.

9 Kauffmann, T.; Habersaat, K.; Koppelmann, E. *Angew. Chem. Int. Ed.* **1972**, *11*, 291-292.

10 Kauffmann, T.; Habersaat, K.; Koppelmann, E. *Chem. Ber.* **1977**, *110*, 638-644.

11 Kauffmann, T.; Ahlers, H.; Hamsen, A.; Schulz, H.; Tilhard, H.-J.; Vahren, A. *Angew. Chem.* **1977**, *89*, 107-108.

12 Kauffmann, T.; Ahlers, H.; Echsler, K.-J.; Schulz, H.; Tiljard, H.-J. *Chem. Ber.* **1985**, *118*, 4496-4506.

13 Pearson, W. H.; Szura, D. P.; Postich, M. J. *J. Am. Chem. Soc.* **1992**, *114*, 1329-1345.

14 Pearson, W. H.; Mans, D. M.; Kampf, J. W. *J. Org. Chem.* **2004**, *69*, 1235-1247.

15 Kauffmann, T.; Berg, H.; Ludorff, E.; Woltermann, A. *Angew. Chem. Int. Ed. Engl.* **1970**, *9*, 960-961.

16 Kauffmann, T.; Eidenschink, R. *Angew. Chem. Int. Ed. Engl.* **1973**, *12*, 568-569.

17 Kauffmann, T.; Busch, A.; Kabersaat, K.; Koppelmann, E. *Angew. Chem. Int. Ed. Engl.* **1973**, *12*, 569-570.

18 Kauffmann, T.; Eidenschink, R. *Chem. Ber.* **1977**, *110*, 651-655.

19 Kauffmann, T.; Busch, A.; Habersaat, K.; Koppelmann, E. *Chem. Ber.* **1983**, *116*, 492-499.

20 Kauffmann, T.; Koch, U.; Steinseifer, F.; Vahrenhorst, A. *Tetrahedron Lett.* **1977**, *38*, 3341-3344.

21 Kauffmann, T.; Beissner, G.; Maibaum, R. *Angew. Chem. Int. Engl. Ed.* **1970**, *10*, 739-740.

22 Kauffmann, T.; Eidenschink, R. *Chem. Ber.* **1977**, *110*, 645-650.

23 Mayr, H.; Heigl, U. W.; Baran, J. *Chem. Ber.* **1993**, *126*, 1913-1916.

24 Incarvito, C.; Lam, M.; Rhatigan, B.; Rheingold, A. L.; Qin, C. J.; Gavrilova, . L.; Bosnich, B. *J. Chem. Soc., Dalton Trans.* **2001**, 3478-3488.

25 Goodwin, H. A.; Lions, F. *J. Am. Chem. Soc.* **1959**, *81*, 6415-6422.

26 Basak, A. K.; Martell, A. E. *Inorg. Chem.* **1986**, *25*, 1182-1190.

27 (a) Olmstead, M. M.; Power, P. P.; Shoner, S. C. *Inorg. Chem.* **1991**, *30*, 2547-2551. (b) Andersen, R. A.; Faegri, K.; Green, J. C.; Haaland, A.; Lappert, M. F.; Leung, W. P.; Rypdal, K. *Inorg. Chem.* **1988**, *27*, 1782-1786.

28 Tan, H. K.S. *J. Chem. Soc. Faraday Trans.*, **1994**, *90*, 3521-3525.

29 (a) Evans, D. F. *J. Chem. Soc.* **1959**, 2003-2005. (b) Schubert, E. M. *J. Chem. Educ.* **1992**, *69*, 62.

30 Becke, A. D. *J. Chem. Phys*. **1993**, *98*, 5648 - 5652.

31 Lee, C. ; Yang, W. ; Parr, R. G. *Phys. Rev. B* **1988**, *37*, 785-789.

32 GAUSSIAN'03, Revision C.02, Gaussian, Inc., Carnegie Office Park, Building 6, Suite 230, Carnegie, PA 15106, Frisch, M. J.; Trucks, G. W.; Schlegel, H. B.; Scuseria, G. E.; Robb, M. A.; Cheeseman, J. R.; Montgomery, J. A.,Jr.; Vreven, T.; Kudin, K. N.; Burant, J. C.; Millam, J. M.; Iyengar, S. S.; Tomasi, J.; Barone, V.; Mennucci, B.; Cossi, M.; Scalmani, G.; Rega, N.; Petersson, G. A.; Nakatsuji, H.; Hada, M.; Ehara, M.; Toyota, K.; Fukuda, R.; Hasegawa, J.; Ishida, M.; Nakajima, T.; Honda, Y.; Kitao, O.; Nakai, H.; Klene, M.; Li, X.; Knox, J. E.; Hratchian, H. P.; Cross, J. B.; Adamo, C.; Jaramillo, J.; Gomperts, R.; Stratmann, R. E.; Yazyev, O.; Austin, A. J.; Cammi, R.; Pomelli, C.; Ochterski, J. W.; Ayala, P. Y.; Morokuma, K.; Voth, G. A.; Salvador, P.; Dannenberg, J. J.; Zakrzewski, V. G.; Dapprich, S.; Daniels, A. D.; Strain, M. C.; Farkas, O.; Malick, D. K.; Rabuck, A. D.; Raghavachari, K.; Foresman, J. B.; Ortiz, J. V.; Cui, Q.; Baboul, A. G.; Clifford, S.; Cioslowski, J.; Stefanov, B. B.; Liu, G.; Liashenko, A.; Piskorz,

P.; Komaromi, I.; Martin, R. L.; Fox, D. J.; Keith, T.; Al-Laham, M. A.; Peng, C. Y.; Nanayakkara, A.; Challacombe, M.; Gill, P. M. W.; Johnson, B.; Chen, W.; Wong, M. W.; Gonzalez, C.; Pople, J. A.

33 Nakano, H. *J. Chem. Phys.* **1993**, *99*, 7983 - 7992.

34 Schmidt, M.W.; Baldridge, K.K.; Boatz, J.A.; Elbert, S.T.; Gordon, M.S.; Jensen, J.J.; Koseki, S.; Matsunaga, N.; Nguyen, K.A.; Su, S.; Windus, T.L.; Dupuis, M.; Montgomery, J.A. *J. Comput. Chem.* **1993**, *14*, 1347 - 1363.

35 Higham, L. T.; Konno, K.; Scott, J. L.; Strauss, C. R.; Yamaguchi, T. *Green Chem.* **2007**, *9*, 80-84.

36 Han, C.-C.; Balakumar, R.; Thirumalai, D.; Chung, M.-T. *Org. Biomol. Chem.* **2006**, *4*, 3511-3516.

38 Fabbian, M.; Marsich, N.; Farnetti, E. *Inorg. Chim. Acta* **2004**, *357*, 2881-2888.

39 Farnetti, E.; Filipuzzi, S. *Inorg. Chim. Acta* **2010**, *363*, 467-473.

40 (a) Yoshida, K.; Morimoto, I.; Mitsudo, K.; Tanaka, H. *Tetrahedron* **2008**, *64*, 5800-5807. (b) Yoshida, K.; Morimoto, I.; Mitsudo, K.; Tanaka, H. *Chem. Lett.* **2007**, *36*, 998-999.

41 Hilt, G.; Vogler, T.; Hess, W.; Galbiati, F. *Chem. Commun.* **2005**, 1474-1475.

42 Cadierno, V.; Garcia-Garrido, S. E.; Gimeno, J. *J. Am. Chem. Soc.* **2006**, *128*, 15094-15095.

43 Ittel, S. D.; English, A. D.; Tolman, C. A.; Jesson, J. P. *Inorg. Chim. Acta.* **1979**, *33*, 101-106.

44 Gultneh, Y.; Yisgedu, T. B.; Tesema, Y. T.; Butcher, R. J. *Inorg. Chem.* **2003**, *42*, 1857-1867.

45 Carlin, R. L. *Magnetochemistry*; Springer-Verlag: Berlin; New York, 1986.